Quantum simulation of many-body physics with neutral atoms, molecules, and ions

by

Michael Foss-Feig

B.A., Amherst College, 2006

A thesis submitted to the

Faculty of the Graduate School of the

University of Colorado in partial fulfillment

of the requirements for the degree of

Doctor of Philosophy

Department of Physics

2013

This thesis entitled:
Quantum simulation of many-body physics with neutral atoms, molecules, and ions
written by Michael Foss-Feig
has been approved for the Department of Physics

_____

Ana Maria Rey

_____

Prof. Mike Hermele

Date _____

The final copy of this thesis has been examined by the signatories, and we find that both the content and the form meet acceptable presentation standards of scholarly work in the above mentioned discipline.

Foss-Feig, Michael (Ph.D., Physics)

Quantum simulation of many-body physics with neutral atoms, molecules, and ions

Thesis directed by Prof. Ana Maria Rey

Real materials are extremely complicated, and any attempt to understand their bulk properties must begin with the appropriate choice of an idealized model, or Hamiltonian. There are many situations where such models have furnished a decisive understanding of complex quantum phenomena, such as BCS superconductivity and quantum magnetism. There are also cases, for instance the unconventional superconductivity of doped cuprates or heavy-fermion metals, where even the simplest conceivable models are intractable to current theoretical techniques. A promising route toward understanding the physics of such models is to simulate them directly with a highly controlled quantum system. Ultracold neutral atoms, polar molecules, and ions are in many ways ideally suited to this task.

In this thesis, we emphasize how the unique features of particular atomic and molecular systems can be leveraged to access interesting physics in experimentally feasible temperature regimes. In chapter 3, we consider prospects for simulation of the Kondo lattice model using alkaline-earth atoms. In particular, we show how groundstate properties—for instance anomalous mass enhancement—can be probed by looking at far-from equilibrium dynamics, which are a standard diagnostic tool in ultracold atom experiments. Chapter 4 describes a realistic implementation of a bosonic version of the Kondo lattice model, and we show how the Kondo interaction qualitatively changes the superfluid to Mott insulator phase transition. Chapters 5, 6, and 7 are unified through an attempt to understand the effects of dissipation in many-body quantum systems. In chapter 5, our goal is mainly to understand the detrimental effects of two-body reactive collisions on dipolar molecules in a 3D optical lattice. Chapter 6 takes a rather different perspective, and shows that this type of loss naturally induces quantum correlations in the steady state of reactive fermionic molecules or alkaline earth atoms. In chapter 7, we develop an exact analytic solution for the

non-equilibrium dynamics of long-ranged Ising models with Markovian decoherence. We apply our solution to the benchmarking of dynamics in an existing trapped-ion quantum simulator, which due to its large size and long-ranged, frustrated, interactions is well beyond the reach of a brute force numerical description.

Dedication

Dedicated to my parents.

Acknowledgements

This thesis is made possible by more than ten years of learning physics (not all of them in grad school, thankfully!) from many wonderful teachers and colleagues. Since I don't really remember when the beginning of that process was, I'll just begin with the most important part, and thank Ana Maria Rey. As my advisor for the past four years she is, without a doubt, the foremost reason why this research was possible. Working with Ana Maria has been humbling, challenging (in a good way), productive, and fun. Thanks are also deserved by the entirety of Ana Maria's research group: Javier Von Stecher, Shuming Li, Chester Rubbo, Salvatore Manmana, Kaden Hazzard, Gang Chen, Bihui Zhu, and Andrew Koller. Kaden and Salvatore, in particular, have graciously tolerated (and answered) many questions about physics. They are frighteningly good at what they do, which as far as I can tell consists in equal parts of physics and coffee consumption, and I have benefited greatly from this.

JILA, NIST, and the University of Colorado have been a productive and enjoyable environment in which to work, entirely because of the friendliness, collaborative spirit, and skill of the many people who work there. To name just some of the many people who have contributed directly to my understanding of the work in this thesis, if not to the work itself (omitting those already mentioned): Mike Hermele, Victor Gurarie, Leo Radzihovsky, Amodsen Chotia, Brian Neyenhuis, Steven Moses, Bo Yan, Jacob Covey, Debbie Jin, Jun Ye, Andrew Daley, James Thompson, Joe Britton, Brian Sawyer, John Bollinger, Goulven Quéméner, John Bohn, Murray Holland, Jinx Cooper, Dominic Meiser, Cindy Regal, and Adam Kaufman.

Even though it is long after the fact, I feel obligated to thank Michael Fowler, William Loinaz,

Contents

Chapter 1

Quantum simulation: goals and feasibility

The standard procedure for modeling a many-body quantum system consists of two basic parts: (1) deciding on some set of degrees of freedom, which we call the system, and (2) establishing a set of rules for the behavior of these degrees of freedom. For solid state systems, these are not easy choices. On one extreme, one could approach part (1) by trying to include *everything*, i.e. all of the atomic nuclei and all of the electrons. By some accounting, this leads to the simplest result in part (2); Coulomb's law is just about all there is. Nevertheless, the shear complexity of the system makes such an approach entirely hopeless. And, even if it were numerically tractable, it's not clear what one would actually learn by solving such a complex model; would the behaviors found for one type of atom allow one to predict the behaviors for another type without just starting over?

Typically one operates more toward the opposite extreme by trying to minimize the number of degrees of freedom included in the model. But the effect of ignoring degrees of freedom is sometimes very difficult to predict. For example, in describing a metal, it is often a good starting point to assume that the nuclei and core electrons are frozen in space, thus comprising a crystal lattice in which the valence electrons move. Part (1) has been greatly simplified, because now the system contains only one—or maybe a small number of—electrons per atom. In reality, these nuclei can vibrate around their equilibrium positions; these lattice vibrations, called phonons, couple to the electric charge of the valence electrons (simply because they are vibrations of charged ions). One might quite reasonably ask: Is this coupling important for describing the qualitative behavior of the valence electrons? In many situations, the answer is no, but in some metals this coupling

mediates a weak effective attraction between electrons that, at sufficiently low temperatures, leads to superconductivity. There are many other similar situations, where the inclusion of complexities that exist in real materials—disorder, anisotropy, magnetic impurities, etc.—give rise to interesting and unexpected physics. In other words, when modeling a particular material, seemingly innocuous omissions of detail can cause one to overlook qualitatively important aspects of the material's properties.

The above example is meant to illustrate an essential difficulty in condensed matter physics. The enormous complexity of the systems we would like to understand forces us to make many— sometimes uncontrolled—approximations in order to define a workable model of the system. In the end, the appropriate model is often chosen by experience, or intuition, or luck, and its ability to describe the correct physical properties of a material are verified afterwards.

To date, there are many physical properties of materials that are both useful and lacking of a "good" description, i.e. one that is simple and contains only the essential ingredients. Such instances provide some of the most interesting, important, and difficult questions in modern condensed-matter theory. In the particular case of high-T_c superconductivity in the cuprates [33, 30, 110], a very difficult situation exists. The model that most people believe affords a minimal description of this behavior, the repulsive Fermi Hubbard model, has resisted decades of theoretical attacks. The seemingly simple question: does the repulsive Fermi-Hubbard model admit superconductivity? cannot yet be answered. One possible approach to answering such questions, which was introduced in 1982 by Feynman [49] and formalized over a decade later by Lloyd [113], is to simulate the model in a physical system. A "quantum simulation" of this sort could probe the physics of such a model by actually putting it to work, so to speak. Quantum simulation, then, is not *directly* aimed at understanding real materials at all. Rather, it is a program to understand simple models, or Hamiltonians, and to determine whether they do or do not describe the physical properties found in those materials. This knowledge, in turn, is expected to aid in the long term goal of deterministically producing materials with desired physical properties. The basic idea behind building a quantum simulator is to find a physical system in which certain approximations—which

perhaps we are forced to make when describing more complicated systems—are essentially exact. Then one can experimentally answer well posed mathematical questions, such as does (insert some simple Hamiltonian) have a groundstate with (insert some interesting property).

Ultracold atomic and molecular gases in optical lattices comprise a uniquely versatile toolbox for addressing such questions because: (1) The system is intrinsically clean and simple: optical lattices are almost perfectly free of defects, atoms interact with each other in simple and well understood ways, and isolation from the environment is typically exquisite. (2) The geometry of the optical lattice, the strength (and often even structure) of inter-atomic interactions, the statistics of the particles—bosons or fermions, their internal degrees of freedom, even the number of dimensions in which they exist, are all mutable in modern experiments. One significant disadvantage is that ultracold atoms in optical lattices need to be, well, *extremely* cold. On dimensional grounds, the only intrinsic temperature scale for a particle of mass m moving in a lattice with period d should scale as $T \sim \hbar^2/(d^2 m)$. Taking into account that atoms are $\gtrsim 10^4$ times heavier than electrons $(m_\mathrm{a}/m_\mathrm{e} \sim 10^4)$, while interparticle separations in typical ultracold-atom experiments are $\sim 10^4$ times larger than lattice constants in crystals $(d_\mathrm{a}/d_\mathrm{e} \sim 10^4)$, we find that atomic temperatures of

$$T_\mathrm{a} \sim \left(\frac{m_\mathrm{e} d_\mathrm{e}^2}{m_\mathrm{a} d_\mathrm{a}^2}\right) T_\mathrm{e} \sim 10^{-12} T_\mathrm{e} \tag{1.1}$$

are needed to simulate electron systems at temperatures T_e. If the goal is to simulate electrons in a crystal-lattice at room temperature $(\sim 10^2 K)$, which may seem modest, ultracold atom experiments need to operate at $\lesssim$ nK temperatures. If the goal is to simulate superconductivity, which often occurs at temperatures one order of magnitude lower, prospects really look quite grim. Luckily, there are many reasons to be optimistic:

(1) Temperatures in atomic physics *are* extremely low, and get lower all the time. State-of-the-art cooling techniques bring fermionic atoms in a 3D optical lattice about an order of magnitude below the bandwidth of the lattice in which they move[89, 151, 167] (or, continuing to speak loosely, the Fermi-temperature). These low temperatures bring within reach the physics observed in many

room-temperature solid-state systems, including local-moment antiferromagnetism. Another order of magnitude or so in temperature would bring these systems close to where the superconducting instability is believed to exist in the Hubbard model [110, 30].

Furthermore, while the temperatures mentioned above sound fantastically low, any honest discussion ought to bring the physical content of these small numbers into question. If one wants to characterize the proximity of a system to its groundstate (and one often does), especially in the ultracold-atom context it is more meaningful to talk about the system's entropy. One reason is that, if one wants to use low temperature as a characterization of groundstate-proximity, the temperature must be specified to be low compared to, e.g., the energy gap to excitations (or more generally the characteristic energy scales in the model). In ultracold-atom quantum simulators, these energy scales are typically tunable, and hence one needs to be very careful about what is meant by low temperature. Another closely related reason is that the various manipulations that experimentalists typically make in ultracold atomic systems are *isentropic*, but certainly *not* isothermic. We are almost always dealing with a closed system, and so there is no thermal bath to enforce isothermic behavior.

One possible approach to achieving a low entropy equilibrium state of an interesting Hamiltonian is to start in a low entropy state of an uninteresting Hamiltonian, and then adiabatically make the Hamiltonian interesting (i.e. tune some parameters which, at their final values, cause the groundstate to be nontrivial). It turns out that there are many excellent ways to produce uninteresting low entropy states of atomic gases.[1]   Therefore, often the most important question to ask is whether a Hamiltonian can be made interesting slowly enough to be adiabatic, without other bad things happening (decoherence or heating). The timescale for adiabaticity, τ_{a}, will typically be inversely proportional to the relevant energy scales of the system. These are small for cold atoms, and that is generically bad. But the timescale for decoherence, τ_{d}, is typically quite large in cold atom systems (*many* orders of magnitude larger than in solid state systems), and that is generically

---

[1] To what extent these techniques can be generalized to directly preparing low-entropy equilibrium states of nontrivial Hamiltonians is an extremely interesting question, which has just begun to be addressed. See Chapter 6 for more discussion of these prospects.

good. The important question is often whether the situation $\tau_a < \tau_d$ can be achieved. This depends very much on the details of the quantum simulator and the Hamiltonian one is trying to simulate; sometimes the answer is yes, sometimes it is no, but it is never possible to answer this question just by looking at the temperature.

(2) Cold atoms are *not* solid state systems, and they offer many attractive ways to alleviate temperature constraints. First of all, many interesting behaviors of real materials occur at low temperatures for detailed microscopic reasons, and this does not mean that the models describing such systems can't support the same interesting behavior at higher temperatures. This argument applies to a number of crucially important condensed matter phenomena, including high-T_c superconductivity [110] and heavy fermion physics [29]. In both cases, the temperature scale below which interesting physics emerges is controlled by an "effective interaction" strength, which because of its perturbative origin is *necessarily* parametrically small compared to the Fermi temperature. This certainly does *not* imply that the interesting physics cannot remain when the interaction scales are comparable to the Fermi energy; cold atoms implementations of these models can often implement these interactions in a direct, non-perturbative manner [70, 68, 56], and hence can in principle access this regime.

Another remarkable example of this idea—which has been realized in a series of beautiful experiments[72, 73]—is the BCS superconductivity of attractively interacting fermions[65]. In BCS theory, the transition temperature to a superconducting state is suppressed by a factor that is exponentially small in the interaction strength between these fermions. In solid-state BCS superconductors [9], this attraction is mediated by phonons and tends to be weak, resulting in critical temperatures deep below the Fermi temperature.[2] In an ultracold gas of fermionic atoms, the interaction strength can be tuned via a Feshbach resonance [25]. As a fermionic gas approaches unitarity, where the interactions become as strong as quantum mechanics will allow, the interparticle

---

[2] Strictly speaking, the critical temperature in a metal is low compared to the Debye temperature, which is typically one or two orders of magnitude below the Fermi temperature.

separation is the only length scale left in the problem. The Fermi energy is therefore the only intrinsic energy scale and, perhaps not surprisingly, the superconducting instability occurs not much below the Fermi temperature (which is well within the reach of modern Fermi-gas experiments). Such behavior has *never* been observed in solid-state system (it would certainly be very interesting if it were!).

(3) Long time-scales and sophisticated diagnostic tools, both of which exist for cold atoms, open the possibility of asking—and hopefully answering—entirely different types of questions than people typically ask in solid-state physics. In particular, the ability to controllably bring these systems out of equilibrium, and the slow timescales for dynamics/relaxation, have made possible the study of transport in confined geometries [48], light-cone like spreading of correlations [23], far-from equilibrium spin physics [17], and thermalization in closed systems [98, 74]. With the advent of ultrafast pulsed lasers, progress has been made in characterizing the real-time dynamics of electrons in solid state systems (e.g., via transient absorption spectroscopy), but the fast timescales ($\sim 10^{-16}$s) make such experiments extremely challenging. In cold atoms experiments, timescales of dynamics are $\sim 10^{12}$ times longer—for the same reason that the temperatures are similarly lower—and hence spatially resolved real-time dynamics can be studied with inexpensive and widely available tools.

There are, of course, many other application specific ultracold-atom tools that allow for measurements not possible (or at least much more difficult) in the solid state context. For instance, the rich internal structure of atoms and decades of expertise in high precision atomic clocks and interferometers have allowed numerous energy [19, 73] (and sometimes momentum [161])-resolved measurements of many-body quantum systems. Most recently, the advent of quantum-gas microscopy [8, 154] has enabled experimenters to image ultracold atoms in optical lattices with resolution comparable to the size of an individual lattice site. In principle, such techniques give experimentalists access to essentially all information (by way of measuring n^{th}-order correlation functions) contained in the many-body wavefunction.

Outline of this thesis:

Quantum simulation with ultracold atomic systems lies at the intersection of two enormous and well established fields: atomic, molecular, and optical (AMO) physics on the one hand, and solid-state physics on the other. This thesis begins with a basic review of several important concepts in ultracold atomic gases and solid-state systems. The review is by necessity cursory—however, I hope that it will at least help to orient people who are grounded in just one of these two fields toward the essential details of the other field that are necessary to understand their intersection. In section 2.1 I give a general overview of ultracold gas experiments, and some details of the atomic structure on which they rely. Ultracold collisions are discussed in section 2.2, with a particular emphasis on the approximations implicit in using a contact potential. I then move on to discuss the optical trapping of atoms in standing-wave laser fields—optical lattices—in section 2.3. Section 2.4 reviews the basic strategy for describing particles moving in a periodic potential, which will be very familiar to anyone with a solid-state physics background. I close with a brief discussion of open-quantum systems in section 2.5, a topic which is extremely relevant to both solid-state and AMO systems, and will be instrumental to understanding the final three chapters of this thesis.

The rest of the thesis is based on a variety of original research—and by original I mean, of course, done in collaboration with many other people—which is unified by an attempt to controllably add back in degrees of freedom that are typically ignored in the simplest optical lattice simulations (e.g., the Bose- and Fermi- Hubbard models).

Chapter 3 introduces the Kondo lattice model (KLM)—a canonical model of strongly-correlated electron physics—and discusses a promising strategy for its realization in experiments with ultracold fermionic alkaline-earth atoms. The KLM is one of the simplest models of interacting fermions with both spin and orbital degrees of freedom,[3] and is widely accepted to be an appropriate model

---

[3] Here spin refers to any internal degree of freedom, and orbital refers to the motional degrees of freedom *within* a single lattice site.

for heavy-fermion materials [40, 29]. The "heaviness" of charge carriers in these materials manifests in a large linear coefficient of the specific heat; measurements of specific heat in optical lattices systems are not currently feasible, but we show that the same heaviness *can* be probed via non-equilibrium dynamics in a harmonic trap [56, 55]. Chapter 4 will extend these ideas to bosonic models [57]. Such an extension is motivated in part by experimental accessibility, but we will also show that the Kondo interaction leads to qualitatively new physics in a bosonic system, significantly modifying the phase diagram of ultracold bosons in an optical lattice.

In chapter 5 we discuss the creation and reactive-collisional dynamics of KRb molecules in a 3D optical lattice reported in Ref. [27]. Based on a variety of experimental observations, we put forward a phenomenological model for the loss of molecules in a corrugated 1D tube based on a two-stage mechanism where: (1) molecules are promoted into higher bands by lattice instabilities, and then (2) these molecules, now mobile due to the increased tunneling rates in the excited bands, seek out and react with other molecules in the same tube. This process can be viewed as the coupling of a discrete level (the initial ground-band molecule) into a lossy continuum (the excited bands), and we derive the expected behavior in a more rigorous fashion from a detailed microscopic theory of this process. This work implicates lattice instabilities as the leading cause of molecule loss in lattices deep enough to suppress nearest-neighbor interactions, but not so deep that inelastic photon scattering sets the molecule lifetime.

Almost always, reactive two-body collisions are considered to be undesirable, and many ingenious schemes exist to prevent them [138, 69]. Chapter 6 takes a rather different perspective on reactive collisions. Rather than asking the question: how can reactive collisions be avoided? we demonstrate that they can be harnessed as a filtering mechanism for the production of highly entangled Dicke states [53], which may find applications in enhanced quantum metrology [82, 15]. In particular we show that spin-$\frac{1}{2}$ fermionic particles, starting in an incoherent spin mixture and undergoing reactive s-wave collisions, seek steady-states in which the spin wavefunction is a highly entangled Dicke state. The initial state is required to be ultracold but non-degenerate, a situation which can already be achieved experimentally for groundstate molecules [126] and alkaline earth

atoms [61, 35] (both of which can be made to have reactive s-wave collisions). We emphasize that, unlike in other proposals to use dissipation to create entanglement, in this case the necessary structure of the dissipative mechanism is endowed by nature. Namely, (1) s-wave scattering dominates at low temperatures, and (2) the Pauli exclusion principle forces s-wave colliding fermions to have correlations in their spin wavefunction.

In the final chapter, we consider the dynamics of Ising spin models subject to local decoherence. This model is perhaps the simplest example of an interacting many-body system where the coherently driven development of quantum correlations competes with decoherence. We incrementally introduce a solution of the model under extremely general conditions [54], which we believe is the only example of an exact (closed-form analytic) expression for the dynamics of a spin-model in $D > 1$ *and* in the presence of decoherence. We then use this solution to understand the behavior of current (and near-future) trapped-ion experiments.

Publications that this work is based on:

Probing the Kondo lattice model with alkaline-earth-metal-atoms. M. Foss-Feig, M. Hermele, and A. M. Rey, *Phys. Rev. A* **81**, 051603(R) (2009).

Heavy fermions in an optical lattice. M. Foss-Feig, M. Hermele, V. Gurarie, and A. M. Rey, *Phys. Rev. A* **82**, 053624 (2010).

Phase diagram of the bosonic Kondo-Hubbard model. M. Foss-Feig and A. M. Rey, *Phys. Rev. A* **82**, 053619 (2011).

Long-lived Dipolar Molecules and Feshbach Molecules in a 3D Optical Lattice. A. Chotia, B. Neyenhuis, S. A. Moses, B. Yan, J. P. Covey, M. Foss-Feig, A. M. Rey, D. S. Jin, and J. Ye *Phys. Rev. Lett.* **108**, 080405 (2012).

Steady-state many-body entanglement of hot reactive fermions. M. Foss-Feig, A. J. Daley, J. K. Thompson, and A. M. Rey, PRL (in press), (2012).

Far from equilibrium quantum magnetism with ultracold polar molecules. K. R. A. Hazzard, S. Manmana, M. Foss-Feig, and A. M. Rey, arXiv:1209.4076, (2012).

An exact solution to the open-system dynamics of long-ranged Ising models. M. Foss-Feig, K. R. A. Hazzard, J. J. Bollinger, and A. M. Rey, arXiv:1209.5795, (2012).

Chapter 2

Ultracold atoms in optical lattices

2.1   Ultracold atoms

2.1.1   From room temperature to ultracold

Most ultracold atomic gas experiments work with alkali atoms, mainly because they have a single valence electron, and thus have a simple electronic level structure admitting a variety of useful spectroscopic manipulations. When the atoms first enter the experiment, they are hot—sometimes room temperature, sometimes hotter, so we'll say 10^3K. By exposing the atoms to laser light that is slightly lower in frequency than an atomic resonance, the Doppler effect promotes the absorption of photons with momentum opposite to the velocity of the absorbing atom. The photon is reemitted in a random direction, and thus on average the translational kinetic energy of an atom is reduced. This process, called laser cooling, brings down the temperature of these initially hot gases by many orders of magnitude, but it cannot stop their translation completely. The momentum kicks suffered due to spontaneous emission of photons from the excited level push the atom around randomly, causing heating and giving rise to a "Doppler cooling limit" (set by the decay rate from the atomic excited state). For alkali atoms, where the excited electronic states used for laser cooling have line widths $\gtrsim$ MHz, the minimum achievable temperatures from laser cooling are in the vicinity of $\sim$mK. By combining the cooling lasers with an inhomogeneous magnetic field (in what's called a magneto-optical trap, or MOT), the radiation pressure can also confine the atoms, and so these mK atoms become trapped.

These cold gases can then be further cooled toward the ultracold regime[1] by forced evaporation [94]: the hottest atoms are allowed to escape, carrying away entropy and reducing the average energy of the remaining atoms. For alkali atoms, the evaporation is usually carried out in a magnetic trap, but for alkaline earth atoms—which have no electronic angular momentum in their groundstate—optical traps must be used instead (see Section 2.3.1 for a discussion of optical trapping). Eventually, as the atoms become colder and move more slowly, the typical de Broglie wavelength of the atoms,

$$\lambda_{\mathrm{D}} = \sqrt{\frac{2\pi\hbar^2}{mk_{\mathrm{B}}T}} \qquad (2.1)$$

(where m is the atomic mass), becomes comparable to the inter-particle spacing. For typical densities and masses, this happens at $\lesssim \mu K$ temperatures. At this point, the quantum nature of the particles becomes important, and depending on whether the atoms are bosons or fermions something very different happens. For bosons, there is an abrupt change at the so-called *condensation temperature* T_{BEC}, and suddenly a finite fraction of the atoms begin to occupy the lowest energy state. At this point, we say there is a Bose Einstein condensate (BEC) [14, 44]. For fermions, the Pauli exclusion principle forbids this from happening. We find instead that as the temperature is lowered, the gas shrinks toward the center of the trap until we reach the Fermi temperature T_{F}, at which point the Pauli exclusion principle (which can be viewed as a type of quantum pressure) prevents the gas from shrinking any further. Notice that for fermions, nothing sudden happens when T falls below T_{F} (this is in stark contrast to a Bose gas when the temperature drops below T_{BEC}). Nevertheless, below this temperature we say that the Fermi gas is degenerate. These BECs and degenerate Fermi gases are the starting point for almost all of the physics we will talk about (with the exception of the trapped ions in Chapter 7).

---

[1] Often, an intermediate stage of polarization gradient cooling is applied first to reach temperatures in the 10's of μK range.

2.1.2   Basic atomic structure

We will not attempt to do any justice to the extensive topic of atomic structure, but instead will simply introduce a few key ideas, notations, and energy scales, which should help guide the unfamiliar reader through the rest of this thesis. Along the way, we will also point out some of the key differences between alkali atoms and alkaline earth atoms, both of which will be considered at various points throughout this thesis.

The low-energy level structure of an alkali atom, and the spectroscopic notation used to describe it, is shown for ^{87}Rb in the left pannel of Fig. 2.1. The core electrons are assumed to be inert, and the electronic state of the one valence electron is written in terms of the associated quantum numbers as $n^{2S+1}L_J$. Here n is the principle quantum number, S is the electronic spin, L is the electronic orbital angular momentum, specified as $S, P, D, \ldots$ for $L = 0, 1, 2, \ldots$, and J is the total electronic angular momentum ($\boldsymbol{J} = \boldsymbol{L} + \boldsymbol{S}$). For any neutral alkali atom in its groundstate, the electronic configuration is $n^2 S_{1/2}$, with $n = 5$ for Rb. For a Coulomb potential we expect the S and P states to have the same energy, but screening due to the core electrons causes there to be a large energy splitting between the groundstate and the lowest lying excited states $n^2 P_J$. This splitting is the largest energy scale typically addressed in experiments on alkali atoms,[2] and corresponds to optical photon frequencies. In an alkali atom there are two of these $5^2 P$ levels, with $J = \frac{1}{2}, \frac{3}{2}$, depending on whether the electron spin aligns parallel to or antiparallel to its orbital angular momentum (fine-structure splitting). The transitions from $n^2 S_{1/2}$ to $n^2 P_{1/2}$ and $n^2 P_{3/2}$ are referred to as the D$_1$ and D$_2$ lines, respectively, and are used for almost all spectroscopic manipulations on alkali atoms (cooling, imaging, optical trapping).

The excited electronic states have short lifetimes ($< \mu$s), and so are never populated for quantum simulations (they are coupled to off resonantly, however, for the creation of optical potentials). Hyperfine coupling between the nuclear spin ($\boldsymbol{I}$) and the total electronic angular momentum ($\boldsymbol{J}$) causes a splitting between states with different total angular momentum $\boldsymbol{F} = \boldsymbol{I} + \boldsymbol{J}$ (these are

---

[2] There are certainly exceptions to this rule, in particular experiments on Rydberg atoms regularly excite the valence electron to states with large principle quantum number n.
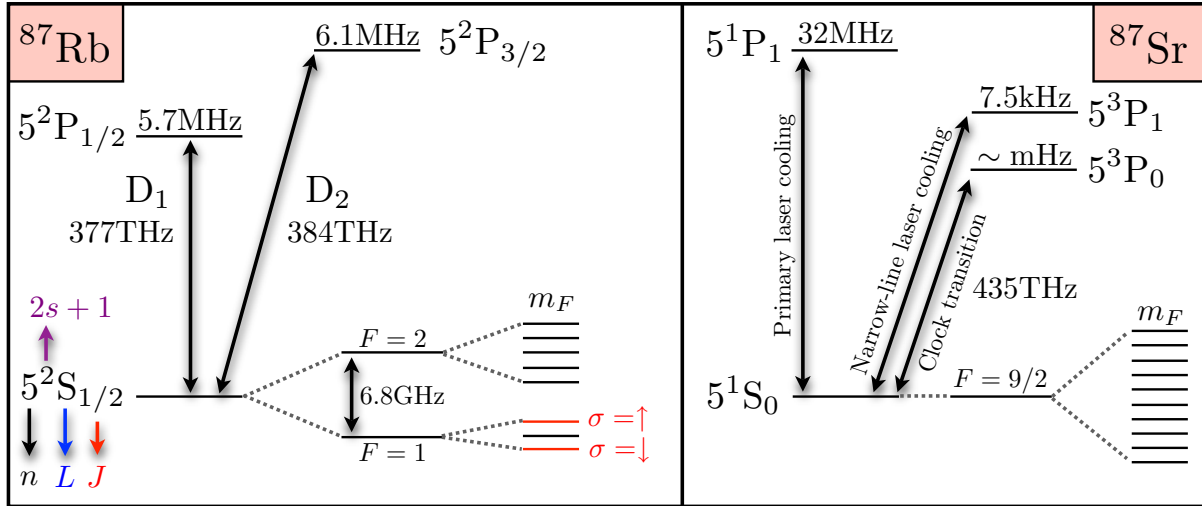
Figure 2.1: Left pannel: some relevant features of the spectrum for a prominent bosonic alkali atom (^{87}Rb). Up to the magnitude of the nuclear spin $\boldsymbol{I}$ (and hence the maximal possible size of the total angular momentum $\boldsymbol{F} = \boldsymbol{I} + \boldsymbol{J}$) and the energy scales, the structure for other alkalis is similar. Right pannel: some relevant features of the spectrum for a prominent fermionic alkaline earth atom (^{87}Sr).

shown for the electronic groundstate in the left pannel of Fig. 2.1). Unlike the excited electronic states, hyperfine states within the ground-electronic manifold have long life times, and hence *can* be used as internal degrees of freedom for quantum simulation. In Chapter 4 we will discuss the implementation of a spin-$\frac{1}{2}$ model using the two levels of the $F = 1$ manifold labeled as $\sigma = \uparrow, \downarrow$ in Fig. 2.1.

Recently, a variety of bosonic and fermionic *alkaline earth atoms* have also been cooled to quantum degeneracy [61, 60, 159, 103, 121, 166, 35]. In these two-electron atoms, the total electronic angular momentum in the groundstate vanishes (the two valence electrons pair into a singlet, and $L = 0$). As a result, the $^1S_0$ groundstate is insensitive to magnetic fields, and hence magnetic trapping is ineffective. These atoms can still be trapped optically, however, and all of the discussion of optical lattices (in Section 2.3.1) applies equally well to both alkali and alkaline earth atoms. Laser cooling on the broad ($\sim$ MHz) $^1S_0$ to $^1P_1$ transition gives temperatures comparable to those achievable in alkali atoms. Subsequent cooling on the relatively narrow ($\sim$ kHz) $^3P_1$ line

can access much colder ($\lesssim \mu$K) temperatures, since the Doppler cooling limit is set by the line width of the cycling transition used.

While the cooling of alkaline earth atoms is still in its infancy (relative to alkali atoms), they have a number of remarkable properties that render them useful for quantum information [31], quantum simulation [68, 79, 21, 175, 56, 55], and precision spectroscopy [16, 164, 112]. First of all, the lowest lying excited electronic state is the $^3P_0$ level (right pannel, Fig 2.1), and the decay into the $^1S_0$ groundstate is doubly dipole forbidden.[3]   As a result, the line width for the transition is tiny ($\sim$mHz, compared to typical line widths of $\sim$MHz for electronic excited states). For this reason, the (optical) splitting between these so-called "clock states" is extremely useful as a frequency standard in atomic clocks. This narrow line width also ensures that, in the absence of collisions, the $^3P_0$ state is metastable on timescales longer than nearly any quantum simulation. Furthermore, because the clock states are optically separated, it is possible to simultaneously couple them through some other excited electronic levels such that both states have large but different detunings. This enables the application of independent and far-detuned optical lattices for each state, greatly enhancing the flexibility of quantum simulations[4] [31].

For fermionic isotopes, which have nuclear spin, another key feature of these two $J = 0$ clock states is that there is effectively no hyperfine coupling (which arises from $\boldsymbol{J} \cdot \boldsymbol{I}$, as discussed above). As a result, the nuclear spin is just a spectator to atom-atom collisions; more precisely, we can say that the scattering length for $^3P_0 - {}^3P_0$, $^3P_0 - {}^1S_0$, and $^1S_0 - {}^1S_0$ collisions are almost perfectly independent of the nuclear spin degree of freedom, m_I [68]. Defining the nuclear spin degeneracy $N = 2I + 1$, this gives rise to an SU(N) symmetry of the atomic interactions [68], which has a number of interesting implications for quantum simulation. This symmetry, along with the ability to create independent optical lattices for the $^1S_0$ and $^3P_0$ states [31], is the basis for quantum simulation of the Kondo lattice model discussed in Chapter 3.

---

[3] In the dipole approximation for atomic transitions, both $J = 0 \to J' = 0$ and $S \neq S'$ transitions are forbidden by selection rules.

[4] See section 2.3 for more discussion. Hyperfine-state dependent lattices can also be made for alkali atoms, but because the hyperfine splitting is in the GHz range, these lattices must be near-detuned (i.e. made from a laser with frequency close to the D_1 and D_2 lines) and hence suffer from spontaneous photon emission.
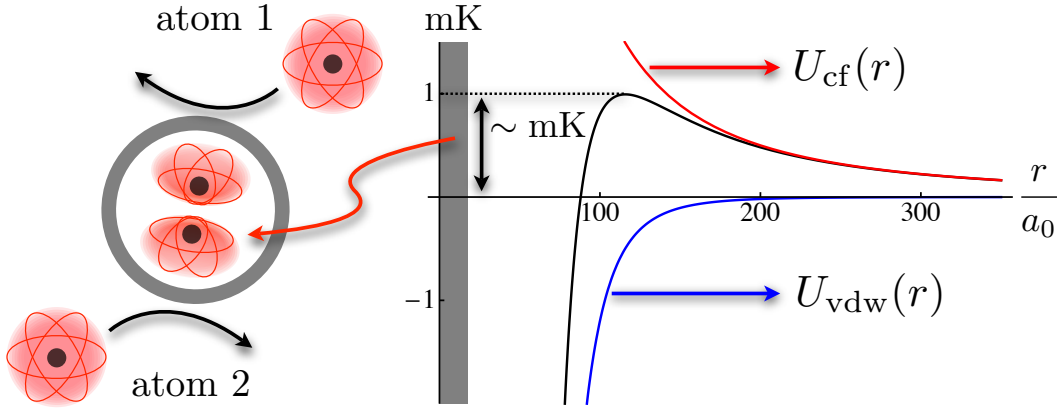
Figure 2.2: At short range, collisional physics is extremely complicated, but at long range the interatomic potential is to a good approximation a Van der Waals potential. The competition between U_{vdw} and the centrifugal potential U_{cf} determines the height of the barrier for collisions with non-zero angular momentum (typically this barrier height is in the mK range).

2.2   Ultracold collisions

In general, the collision of two atoms is an extremely complicated process: in a close-range encounter, the electronic wavefunctions of the atoms are severely distorted, and a full description of this dynamics is a very difficult task. At the low temperatures and densities that are common in ultracold atom experiments, however, many simplifications can be made. In particular, many important features of low-energy atomic scattering owe to the long-range Van der Waals potential, $U_{\text{vdw}}(r) = -\alpha/r^6$ (where $r = |\boldsymbol{r}|$ is the magnitude of the relative coordinate $\boldsymbol{r}$), and hence are *universal* in the sense that they do not depend in detail on the complicated short-range physics.

Let's suppose that the height and location of the centrifugal barrier (for collisions with angular momentum $l\hbar$, $l \geq 1$) is determined by competition between the repulsive centrifugal potential $U_{\text{cf}}(r) = l(l+1)\hbar^2/2mr^2$ and the attractive $U_{\text{vdw}}(r)$. Setting these two energy scales equal to each other, and taking $l = 1$, we find a characteristic radius of the centrifugal barrier[5]

$$r_0 = \left(\frac{\alpha m}{\hbar^2}\right)^{1/4}. \tag{2.2}$$

For alkali atoms, this estimate typically yields $r_0 \sim 10^2 a_0$, with a_0 the Bohr radius (the size of

---

[5] Note that this length scale is actually more general, in the sense that it emerges from the Schrödinger equation at zero energy for $l = 0$ as well (by dimensional analysis). Hence, even in the absence of a centrifugal barrier r_0 is a good order of magnitude estimate for emergent length scales of the problem, e.g. the *s*-wave scattering length.

the atom). We take this estimate as post-facto justification that U_{vdw} does indeed determine the centrifugal barrier, since the potential at this distance *is* well described by Van der Waals attraction. The height of the centrifugal barrier can now be estimated as $E_{\text{cf}} = \hbar^2/(mr_0^2)$, which determines a minimum characteristic temperature $T_{\text{cf}} \sim$ mK below which scattering with $l \neq 0$ (when the centrifugal barrier exists) is suppressed. Ultracold atomic gases are several orders of magnitude colder (typically sub-μK), and hence only s-wave scattering needs to be considered.[6]

On general grounds, the s-wave scattering of two particles can be characterized by a momentum dependent scattering amplitude $f(k)$ (basically the strength of the outgoing spherical wave). When the relative momentum k satisfies $kr_0 \ll 1$, $f(k)$ can be parameterized by the s-wave scattering length a_s as[7]

$$f(k) \approx \frac{-a_s}{1 + ika_s}. \tag{2.3}$$

This is a fairly remarkable result: despite the very complicated close-ranged potential, which we may not even know, the low energy scattering is parameterized by a *single number*, a_s. Calculation of a_s from first principles, however, requires a more detailed knowledge of the short range part of the potential, and in general is a very difficult task.

Because the low-energy scattering of two atoms is characterized by the scattering length a_s, it is possible to model this scattering using *any* short-ranged potential that has the same scattering length. A key result, which is put to work in almost all many-body treatments of cold gases, is that this scattering amplitude in Eq. (2.3) is *exactly* reproduced (i.e. the $\approx$ can be replaced with a strict equality) by scattering from an s-wave *pseudopotential* $U_s(\boldsymbol{r})$, which is defined by its action on the relative coordinate wavefunction [47, 85]

$$U_s(\boldsymbol{r})\psi = \frac{4\pi\hbar^2 a_s}{m}\delta(\boldsymbol{r}) \times \partial_r(r\psi). \tag{2.4}$$

This pseudopotential gives the low-energy result Eq. (2.3) for arbitrary k (which is not surprising, since the potential is zero-range). However, it should be kept in mind that for sufficiently large

---

[6] There are notable exceptions to this statement, the most important being when s-wave collisions are forbidden by symmetry, for instance when two spinless fermions collide. In such situations, the dominant contribution to low-energy scattering is in the p-wave channel, and though it is small it can sometimes be important.

[7] We will take this dependence of the scattering amplitude as the definition of the s-wave scattering length.

k, in particular for $k \sim 1/r_0$, the pseudopotential does not reproduce the scattering of the Van der Waals potential [for which the true amplitude $f(k)$ no longer obeys Eq. (2.3)]. When acting on wavefunctions that are regular at the origin, the regularization operator $\partial_r(r...)$ has no effect and can be dropped.[8] As a result, the unregularized pseudopotential can be used when treating an interacting gas at mean-field theory or in first-order perturbation theory, where one takes the expectation value of $U_s(\boldsymbol{r})$ in well-behaved wavefunctions.

In second quantization, a two-body interaction of the form $U(\boldsymbol{x} - \boldsymbol{y})$ (here $\boldsymbol{x}$ and $\boldsymbol{y}$ are the positions of the two interacting atoms) is written

$$\mathcal{U} = \frac{1}{2} \int d^3\boldsymbol{x} d^3\boldsymbol{y} \hat{\psi}^\dagger(\boldsymbol{x}) \hat{\psi}^\dagger(\boldsymbol{y}) U(\boldsymbol{x} - \boldsymbol{y}) \hat{\psi}(\boldsymbol{y}) \hat{\psi}(\boldsymbol{x}), \tag{2.5}$$

where $\hat{\psi}^\dagger(\boldsymbol{x})[\hat{\psi}(\boldsymbol{x})]$ creates[annihilates] a particle at point $\boldsymbol{x}$ in space (see Appendix A). Inserting the un-regularized pseudopotential $U_s(\boldsymbol{x} - \boldsymbol{y}) = \frac{4\pi\hbar^2 a_s}{m}\delta(\boldsymbol{x} - \boldsymbol{y})$ and integrating over $\boldsymbol{y}$, the interaction becomes

$$\mathcal{U}_s = \frac{4\pi\hbar^2 a_s}{m} \frac{1}{2} \int d^3\boldsymbol{x} \hat{\psi}^\dagger(\boldsymbol{x}) \hat{\psi}^\dagger(\boldsymbol{x}) \hat{\psi}(\boldsymbol{x}) \hat{\psi}(\boldsymbol{x}). \tag{2.6}$$

One should always keep in mind, however, that this interaction is explicitly designed to give the correct physics when treated at first-order in perturbation theory, or in a mean-field approximation. Any attempt to extend perturbative expressions to higher order using Eq. (2.6) is liable to produce unphysical results, and one must be more careful.

Note that the above interaction Hamiltonian vanishes for fermions, because $\hat{\psi}(\boldsymbol{x})\hat{\psi}(\boldsymbol{x}) = 0$ (the Pauli exclusion principle). This is an artifact of treating only s-wave scattering, which cannot occur for identical fermions (since it implies a wavefunction that is even under particle exchange). In reality, identical fermionic atoms interact in the p-wave channel; we could have included this by using a p-wave pseudopotential [91]. But, as mentioned above, at ultracold temperatures these p-wave interactions are severely suppressed, and degenerate Fermi gases (with all atoms in the same

---

[8] A somewhat technical aside: It is not difficult to show that the asymptotic wavefunction (i.e. for $r \gg r_0$) contains contributions from functions that are both regular (do not diverge) and irregular (diverge as r^{-1}) at the origin. For a real atomic potential, these wavefunctions change their behavior completely as they approach the origin ($r \lesssim r_0$), and hence the irregular piece of the asymptotic wavefunction does not cause any pathological behavior. For a zero-ranged pseudo-potential, where $r_0 = 0$, the wavefunction maintains its asymptotic behavior all the way in to $r = 0$. If the pseudopotential is to reproduce the correct asymptotic wavefunction, with its irregular piece included, the regularization operator is needed to deal with the r^{-1} divergence at the origin.

internal state) are essentially collisionless.[9]   One way to obtain interactions between fermionic atoms is to populate two internal states (for instance, two hyperfine states of an alkali atom). As long as scattering does not populate other states in the hyperfine manifold, and denoting these two internal degrees of freedom by $\sigma = \pm$, we obtained an interaction term

$$\mathcal{U}_s = \frac{4\pi\hbar^2 a_s}{m} \sum_{\sigma\sigma'} \frac{1}{2} \int d^3\boldsymbol{x}\, \hat{\psi}_\sigma^\dagger(\boldsymbol{x})\hat{\psi}_{\sigma'}^\dagger(\boldsymbol{x})\hat{\psi}_{\sigma'}(\boldsymbol{x})\hat{\psi}_\sigma(\boldsymbol{x}). \tag{2.7}$$

For simplicity, in the rest of this chapter we will (mainly) focus on bosons, for which s-wave interactions between spinless particles are allowed, and the simpler interaction Hamiltonian in Eq. (2.6) does not vanish.

Before moving on, we note that as long as only two internal states are allowed, which we'll associate with spin-up and spin-down of a spin-$\frac{1}{2}$, Eq. (2.7) is pretty much the most general interaction that we will encounter. The reason is that for bosons (fermions) interacting in the s-wave channel, the addition of the two spin-$\frac{1}{2}$ degrees of freedom in the problem is forced to yield a spin triplet (singlet) in order to give the proper symmetrization of the two-body wavefunction under particle exchange. Hence, despite the internal degrees of freedom, the combined internal state of two interacting atoms is completely determined by the knowledge that they interact at all (in the s-wave channel). In chapter 3 we will encounter situations where there are more than two internal degrees of freedom, and we'll see exactly how Eq. (2.7) generalizes.

2.3   Optical lattices

An optical lattice is the standing wave created by the retro-reflection of a laser beam onto itself. The simplest case is a one dimensional (1D) optical lattice, which for light of wavelength λ generates an intensity pattern $I(x) = 2I_x \cos^2(kx)$, where I_x is the root-mean-square intensity of the beam and $k = 2\pi/\lambda$. Lattices in the orthogonal direction can be added, and kept from interfering with each other by either (a) using orthogonal polarizations of light, (b) detuning the

---

[9] While this is usually true, one should keep in mind that p-wave scattering can sometimes be resonantly enhanced.

1D lattice   2D lattice   3D lattice

2D geometry   1D geometry   0D geometry
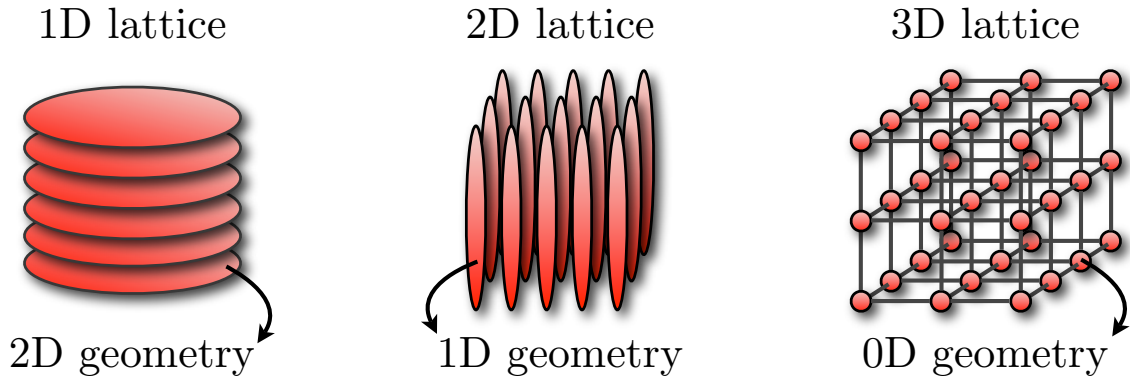
Figure 2.3: Various separable lattice geometries obtainable by superimposing one, two, or three or-thogonal 1D optical lattices. Note that the individual lattice sites can be made to have a quasi-2D, quasi-1D, or quasi-0D geometry. Thus, in addition to enabling lattice physics (when tunneling be-tween wells in a 3D lattice is possible), deep optical lattices enable experiments to probe continuum physics in various dimensions.

lasers such that the interference terms are time-averaged away, or both. The total intensity is then

$$I(x, y, z) = 2I_x \cos^2(kx) + 2I_y \cos^2(ky) + 2I_z \cos^2(kz). \tag{2.8}$$

By taking advantage of interference between the various beams, much more complicated lattice structures can also be made. So far, we have said nothing to indicate that an atom actually experiences a force due to this spatially varying intensity pattern; a brief explanation of how this arises is given in the next section.

2.3.1 AC stark shift

The ability to confine atoms in an optical lattice relies on the AC stark shift, which causes the energy of an atom in its ground electronic state to depend on the intensity of a laser field with which the atom interacts. The physics behind the AC stark shift is actually quite simple, though a full quantitatively correct treatment requires quite a bit of work. In the absence of an electric field, a neutral alkali atom has a single valence electron that is uniformly distributed around the nucleus, and hence there is no dipole moment. In the presence of an electric field $\mathcal{E} = \boldsymbol{\epsilon}\mathcal{E}$, a dipole moment $\boldsymbol{d}$ is induced, and the energy of the atom is reduced by $\Delta E \propto \boldsymbol{d} \cdot \boldsymbol{\mathcal{E}}$. The magnitude of the induced dipole moment depends on how tightly bound the electron is to the atom. This is

encapsulated mathematically by defining a polarizability α, in terms of which the dipole moment satisfies $\boldsymbol{d} = \alpha \boldsymbol{\mathcal{E}}$, and the energy shift can be written as $\Delta E = -\frac{1}{2}\alpha \boldsymbol{\mathcal{E}} \cdot \boldsymbol{\mathcal{E}}$. Because the electron is in equilibrium for $\boldsymbol{\mathcal{E}} = 0$, it's excursions from equilibrium in weak applied fields are harmonic. If we assume it has a characteristic oscillation frequency ω_{eg} (the meaning of the subscript eg will become clear below), and a frequency dependent polarizability $\alpha(\omega)$, perturbing the atom with the AC electric field $\boldsymbol{\mathcal{E}} \cos \omega t$ induces an oscillating dipole moment of strength $\boldsymbol{d}(\omega) = \alpha(\omega)\boldsymbol{\mathcal{E}}$. Just as for a classical driven harmonic oscillator, if the drive is below(above) resonance [$\Delta = \omega - \omega_{eg}$ is less(greater) than zero], the electron will oscillate in(out) of phase with the field, and hence the energy of the atom will be shifted down(up) by $\frac{1}{2}|\alpha(\omega)|\mathcal{E}^2$.

To understand this effect slightly more quantitatively, and from an approach that is more amenable to incorporating details of the actual atomic level structure, we make the approximation of a two-level atom, with ground electronic state $|g\rangle$ and excited electronic state $|e\rangle$ (with difference energy $\hbar\omega_{eg}$). It is possible to proceed by treating the electric field classically and using time-dependent perturbation theory. However, we find it conceptually simpler to treat the field quantum mechanically, as a collection of photons of energy $\hbar\omega$. If we imagine that the atom sits in a cavity[10] supporting a single (normalized) mode $\Xi(\boldsymbol{r})$, then the coupling between the atom and the photon field is given by $\mathcal{V} = \hat{\boldsymbol{\mathcal{E}}} \cdot \hat{\boldsymbol{d}}$, where now

$$\hat{\boldsymbol{\mathcal{E}}} = \Xi(\boldsymbol{r})\boldsymbol{\epsilon}\sqrt{\hbar\omega/2\epsilon_0}(\hat{a}^\dagger + \hat{a}) \tag{2.9}$$

is an operator corresponding to the electric field ($\hat{a}^\dagger$ creates a photon in the mode Ξ) and $\hat{\boldsymbol{d}}$ is the dipole operator of the atom. For a two level atom we can rewrite $\boldsymbol{\epsilon} \cdot \hat{\boldsymbol{d}}$ in terms of its only non-vanishing matrix elements as

$$\boldsymbol{\epsilon} \cdot \hat{\boldsymbol{d}} = |g\rangle\langle e|\mu_{ge} + |e\rangle\langle g|\mu_{eg}, \tag{2.10}$$

with $\mu_{eg} = \boldsymbol{\epsilon} \cdot \langle e|\hat{\boldsymbol{d}}|g\rangle$,[11] and the atom-photon coupling can be written

$$\mathcal{V} = \Xi(\boldsymbol{r})\sqrt{\frac{\hbar\omega}{2\epsilon_0}}(\hat{a}^\dagger + \hat{a})\left(|g\rangle\langle e|\mu_{ge} + |e\rangle\langle g|\mu_{eg}\right). \tag{2.11}$$

---

[10] The cavity is just a convenient way of dealing with the mode normalization, which for a plane wave in free space is more confusing. Nothing discussed in this section actually requires the existence of a cavity.

[11] We will assume that $|g\rangle$ and $|e\rangle$ have well-defined parity, so that the diagonal elements of $\hat{\boldsymbol{d}}$ vanish.
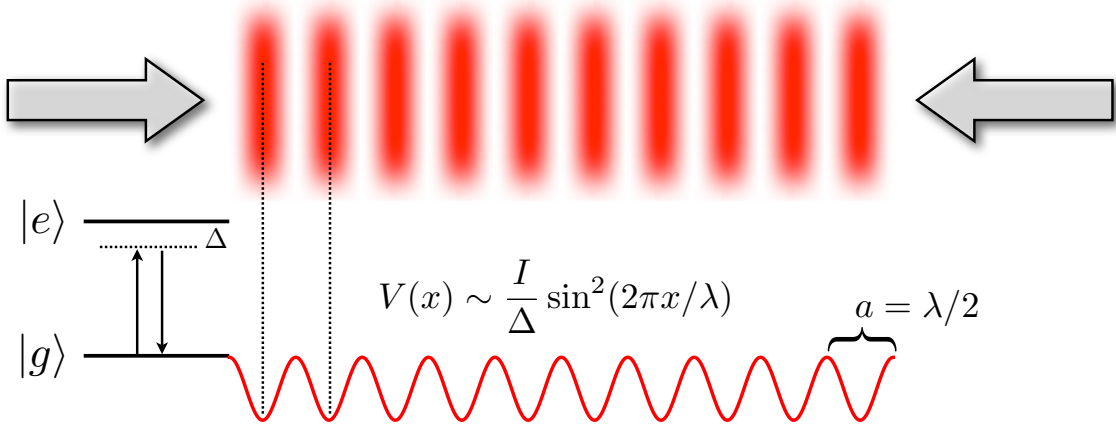
Figure 2.4: A 1D lattice is created from the interference pattern of two counter-propagating laser beams. A sinusoidal intensity pattern is created, and the energy of an atom in its groundstate is shifted in proportion to this intensity due to the AC-stark effect. Depending on whether the atom is driven below or above resonance (in this picture it is driven below resonance, i.e. $\Delta < 0$), the atoms are attracted to either the intensity maxima or the intensity minima.

We now imagine an atom sitting in this cavity, in its groundstate and in the presence of N photons (denoted by $|g, N\rangle$), and ask how the introduction of the atom-photon coupling $\mathcal{V}$ shifts the groundstate energy. Defining the detuning $\Delta = \omega - \omega_{eg}$, we see that the two states $|g, N\rangle$ and $|e, N - 1\rangle$ are degenerate when $\Delta = 0$. For non-zero Δ, but $\langle g, N|\mathcal{V}|e, N - 1\rangle \ll \hbar\Delta$, we expect that the shift in energy to the state $|g, N\rangle$ to second order in perturbation theory, denoted δ, is dominated by the term

$$\delta \quad = \quad \frac{\langle g, N|\mathcal{V}|e, N - 1\rangle\langle e, N - 1|\mathcal{V}|g, N\rangle}{\hbar\Delta} \tag{2.12}$$

$$= \quad \frac{\hbar\Omega^2}{\Delta}. \tag{2.13}$$

Here we have defined the Rabi frequency

$$\Omega = |\Xi(\boldsymbol{r})||\mu_{eg}|\sqrt{\frac{N\omega}{2\hbar\epsilon_0}}, \tag{2.14}$$

and the factor of N comes from the application of the photon annihilation operator to the state $|g, N\rangle$ ($\hat{a}|g, N\rangle = \sqrt{N}|g, N-1\rangle$). There are also contributions to the ground-state energy shift that arise from the term

$$\frac{\langle g, N|\mathcal{V}|e, N + 1\rangle\langle e, N + 1|\mathcal{V}|g, N\rangle}{\hbar(\Delta - 2\omega)}, \tag{2.15}$$

but for $\Delta \ll \omega$ these terms are ignored because of the large denominator (if we had used time-dependent perturbation theory, these terms would have been dropped by making the *rotating wave approximation*). In general it is straightforward to calculate the matrix elements μ_{eg}, but in order to do so we would need to specify what the states $|e\rangle$ and $|g\rangle$ are. In order to avoid this specification, and because it will be useful for the discussion that follows, we simply parametrize these matrix elements in terms of the decay rate from the excited state[12]

$$\Gamma = \frac{\omega_{eg}^3 |\langle e|\boldsymbol{d}|g\rangle|^2}{3\pi\epsilon_0 \hbar c^3}. \tag{2.16}$$

Remembering that the time averaged intensity is given by $I = \frac{1}{2}\epsilon_0 c\mathcal{E}^2$, we can also write the energy shift as

$$\delta = \left(\frac{2\pi c^2 \Gamma}{\omega_{eg}^3}\right) \frac{I}{\Delta}. \tag{2.17}$$

In a simple cubic optical lattice, the intensity varies in space according to Eq. (2.8), resulting in a spatially varying AC stark shift

$$V(\boldsymbol{r}) = \delta(\boldsymbol{r}) = \left(\frac{2\pi c^2 \Gamma}{\omega_{eg}^3}\right) \frac{I(\boldsymbol{r})}{\Delta}. \tag{2.18}$$

Plugging in $I(\boldsymbol{r})$ from Eq. (2.8) and defining $V_\mu = (4\pi c^2 \Gamma I_\mu)/(\omega_{eg}^3 \Delta)$ ($\mu \in \{x, y, z\}$), the 3D cubic lattice potential is then given by

$$V(\boldsymbol{r}) = V_x \cos^2(kx) + V_y \cos^2(ky) + V_z \cos^2(kz). \tag{2.19}$$

Non-interacting ground-state atoms moving in this potential[13] are described by the Hamiltonian $V(\boldsymbol{r}) - \hbar^2 \nabla^2 /(2m)$, which in second quantization becomes

$$\mathcal{H}_0 = \int d^3 \boldsymbol{r}\, \hat{\psi}^\dagger(\boldsymbol{r}) \left[V(\boldsymbol{r}) - \frac{\hbar^2 \nabla^2}{2m}\right] \hat{\psi}(\boldsymbol{r}). \tag{2.20}$$

The wavelength of the lattice light affords a natural length scale. If we pull out the characteristic length scale $\lambda/2\pi = k^{-1}$ by defining a dimensionless coordinate $\tilde{\boldsymbol{r}} = k\boldsymbol{r}$, dimensionless Laplacian

---

[12] This decay rate can be calculated using Fermi's golden rule, and it arises from the coupling of the atomic dipole operator to vacuum fluctuations in the quantized electromagnetic field. This coupling induces matrix elements between the states $|e\rangle$ and $|g\rangle$, and naturally these matrix elements are proportional to μ_{eg}.

[13] Notice that we are assuming a Born-Oppenheimer style approximation, in which the atoms are assumed to adiabatically follow the groundstate of the atom plus field as they move around in space.

$\tilde{\nabla}^2 = k^{-2}\nabla^2$, and dimensionless field operators $\tilde{\psi}^\dagger(\boldsymbol{r}) = k^{-3/2}\psi^\dagger(\boldsymbol{r})$, Eq. (2.20) can be rewritten

$$\mathcal{H}_0 = E_R \int d^3\tilde{\boldsymbol{r}} \, \tilde{\psi}^\dagger(\tilde{\boldsymbol{r}}) \left[\sum_\mu \frac{V_\mu}{E_R} \cos^2(\tilde{r}^\mu) - \tilde{\nabla}^2 \right] \tilde{\psi}(\tilde{\boldsymbol{r}}), \qquad (2.21)$$

where $E_R = \frac{\hbar^2 k^2}{2m} = \frac{h^2}{2m\lambda^2}$. The energy scale E_R, called the "recoil energy", is the zero-point energy of an atom moving in a box the size of one lattice site. Not surprisingly, this is a natural unit for describing the kinetic energy of atoms in a lattice.[14]

2.3.2 Extensions and limitations

Two questionable approximations have to be made in order to derive the above results: (1) the rotating wave approximation [i.e. ignoring the term in Eq. (2.15)] and (2) the two-level atom approximation. If one makes the detuning Δ very large, to the point where it is an appreciable fraction of ω_{eg}, the rotating wave approximation begins to break down. Indeed, in many experiments operating with far-detuned optical lattices these corrections are important. If one makes the detuning Δ too small, to the point where it becomes comparable to the fine-structure splitting (between the D_1 and D_2 lines), then the two-level atom approximation breaks down. Once the fine-structure can be spectroscopically resolved, the lattice becomes spin-dependent, in that it couples different hyperfine levels differently.

This spin-dependence is not necessarily a bad thing: There are many theoretical proposals to take advantage of it [122, 1, 41], and a number of experiments that do so [2, 119, 118]. However, it should be kept in mind that the probability for an atom to be in the excited state (which has a decay rate Γ) is equal to $(\Omega/\Delta)^2$. As a result, the rate at which a groundstate atom in an optical lattice spontaneously emits photons is given by

$$\gamma = \Gamma \left(\frac{\Omega}{\Delta} \right)^2 = \hbar^{-1} V(\boldsymbol{r}) \frac{\Gamma}{\Delta}. \qquad (2.22)$$

---

[14] The name "recoil energy" comes from another physical meaning: By conservation of momentum, it's not hard to see that E_R is the kinetic energy imparted to an atom of mass m upon spontaneously emitting a photon of wavelength λ. This connection is useful, for instance, when computing heating rates do to inelastic photon scattering, where E_R sets the typical energy imparted per scattered photon. Notice that E_R is *much* smaller than the photon energy $E_\gamma = hc/\lambda$.

The spontaneous emission of a photon causes the atom to recoil, gaining kinetic energy E_R. Thus, near-detuned lattices typically suffer from large heating rates. It is a common misconception that this heating rate can be suppressed by working in a blue-detuned ($\Delta > 0$) optical lattice, the reasoning being that the atoms sit at the intensity minima of the optical lattice, and hence are exposed to fewer photons. While the absolute scattering rate of photons *is* lower (for this exact reason) in a blue detuned lattice, the heating that results due to this scattering is actually identical for blue- and red-detuned lattices [132].

2.4   Physics in a lattice: choice of basis

As with any problem in quantum mechanics, the best choice of basis depends on the problem one is trying to solve. For a particle moving in a periodic potential, the discrete translational invariance of the problem allows one to construct plane-wave-like wavefunctions, called Bloch states. The energies of these states can be grouped into distinct *bands*, which are separated by *band gaps*. In terms of these Bloch states the single-particle Hamiltonian takes on a particularly simple, diagonal form, which we derive in Section 2.4.1. This delocalized basis is, in principle, amenable to the treatment of two-body interactions. However, we will show by explicit construction of the interaction operator that such a description is extremely unwieldy (Section 2.4.2). This motivates the introduction of Wannier functions in Section 2.4.3. Within a given band, Wannier functions are as localized as possible around the individual lattice sites. Writing the interaction in this basis is the starting point for a number of controlled simplifications known collectively as the *tight-binding approximation*, which we introduce in Section 2.4.4. In the end we will see how, under typical experimental conditions, an extremely simple real-space description of an interacting lattice gas emerges.

2.4.1 Single particle eigenstates in a periodic potential

The eigenstates of a particle in free space (we will work exclusively in 1D here) are plane waves

$$\psi_k(x) = \frac{1}{\sqrt{L}}e^{-ikx}, \tag{2.23}$$

where we assume the length of space L is finite in order to introduce a proper normalization. We would like to know what happens to these eigenstates in the presence of a periodi lattice potential $V(x)$ with periodicity $a = \lambda/2$.[15]   Because of the periodicity of the lattice potential, it can be decomposed into discrete Fourier components as

$$V(x) = \sum_{n=-\infty}^{\infty} c_n e^{i2\pi nx/a}. \tag{2.24}$$

If we would like to calculate the eigenfunctions in the lattice by working in the plane wave basis, we will need to calculate matrix elements of the form

$$\mathcal{H}_{k',k} = \frac{1}{L}\int dx\,\psi_{k'}^*(x)V(x)\psi_k(x) - \frac{1}{L}\int dx\,\psi_{k'}^*(x)\frac{\hbar^2\partial_x^2}{2m}\psi_k(x). \tag{2.25}$$

$$= \frac{1}{L}\int dx\,e^{ix(k'-k)}V(x) - \frac{\hbar^2 k^2}{2m}\frac{1}{L}\int dx\,e^{ix(k'-k)}. \tag{2.26}$$

We can see from the Fourier expansion of $V(x)$ that the first term will only be nonzero when $k - k' = 2\pi r/a$ for some integer r, motivating the substitutions $k \to q + 2\pi r/a$ and $k' \to q + 2\pi s/a$, where $q \in (-\pi/a, \pi/a]$ (q must be restricted in this way to avoid redundancy). This allows us to rewrite the above matrix elements as

$$\mathcal{H}_{rs}(q) = \frac{1}{L}\int dx\,e^{i2\pi(s-r)x/a}V(x) - \frac{\hbar^2(q+2\pi r/a)^2}{2m}\frac{1}{L}\int dx\,e^{i2\pi(s-r)x/a} \tag{2.27}$$

$$= c_{r-s} - \frac{\hbar^2(q+2\pi r/a)^2}{2m}\delta_{rs} \tag{2.28}$$

If we diagonalize this matrix, which is now discrete but with a parametric dependence on q, we find eigenvectors $v_\alpha^r(q)$ and eigenvalues $\varepsilon_\alpha(q)$. The eigenfunctions can then be obtained by summing

---

[15] While an optical lattice is often sinusoidal, it need not be, and for the time being we will keep things more general.

the amplitudes $v_\alpha^r(q)$ over the real-space basis elements they correspond to, $e^{-i(q+2\pi r/a)x}$. We thus obtain the eigenfunctions

$$\varphi_{\alpha q}(x) = \sum_r v_\alpha^r(q)e^{-i(q+2\pi r/a)x} = e^{-iqx}\overbrace{\sum_r v_\alpha^r(q)e^{-i2\pi r/ax}}^{\equiv u_{\alpha q}(x)} \tag{2.29}$$

$$= e^{-iqx}u_{\alpha q}(x). \tag{2.30}$$

Notice that the functions $u_{\alpha q}(x)$ have the periodicity of the lattice. That the wavefunctions $\varphi_{\alpha q}(x)$ have the above form is called Bloch's theorem, and can be argued for (without going through all of the manipulations above) on the basis of discrete translational symmetry. The above constructive derivation, however, has the advantage of demonstrating how these functions are actually calculated, rather than just proving that they have a particular form. One can simply truncate the matrix $\mathcal{H}_{rs}(q)$ to be finite,[16] and then obtain the $\varepsilon(q)$ and $v_\alpha^r(q)$ by numerically diagonalizing this finite matrix, and then construct the Bloch functions according to Eq. (2.29).

At this point several things are in need of saying. First of all, we normally refer to q as a quasi-momentum (unlike the momentum k), and we call the range in which it sits, $(-\pi/a, \pi/a]$, the first Brillouin zone. Just as the quantum number k reflects the continuous translational symmetry of free space, q reflects the discrete translational symmetry of the lattice Hamiltonian (which is invariant under $x \to x + a$). While the spectrum of a free particle is continuous, even an arbitrarily weak lattice causes gaps to appear in the single-particle spectrum. These gaps can be understood from the lifting of degeneracy between free particle states with momentum $k = \pm(2m+1)\pi/a$ in the presence of a lattice with period a (which in general introduces matrix elements between such states). The continuous set of energies $\varepsilon_\alpha(q)$ between two such gaps is called a band, and we often call α a band index. We will use the convention that $\alpha = 0$ for the ground-band, $\alpha = 1$ for the first excited band, etc.

In second quantization, the single particle Hamiltonian $\mathcal{H}_0 = V(x) - \hbar^2\partial_x^2/(2m)$ is given by

$$\mathcal{H}_0 = \int dx\, \hat{\psi}^\dagger(x)\left[V(x) - \frac{\hbar^2\partial_x^2}{2m}\right]\hat{\psi}(x). \tag{2.31}$$

---

[16] This truncation limits the ability to get the short-wavelength behavior of these functions correct. Hence, for deep lattices, where we expect these functions to be sharply peaked about the minima of the potential, many values of m may need to be included.

By expanding the field operators $\hat{\psi}(x)$ in terms of operators $\hat{\varphi}_{\alpha q}$ that create particles in the single-particle eigenstates $\varphi_{\alpha q}(x)$,

$$\hat{\psi}(x) = \sum_{\alpha,q} \varphi_{\alpha q}(x) \hat{\varphi}_{\alpha q}, \tag{2.32}$$

and substituting this expression into Eq. (2.31), we obtain

$$\mathcal{H}_0 = \sum_{\alpha,q} \varepsilon_\alpha(q) \hat{\varphi}_{\alpha q}^\dagger \hat{\varphi}_{\alpha q}. \tag{2.33}$$

The diagonal form of the Hamiltonian, of course, simply reflects the fact that we are working in the eigen-basis.

2.4.2   Interactions in the quasi-momentum basis

When adding in the effects of a contact interaction, there is nothing to stop us from working in the quasi-momentum basis defined by the operators $\hat{\varphi}_{\alpha q}$. Because the interaction between atoms is local in real space, however, it will couple eigenstates with many different quasi-momenta. Substituting this expression into the 1D interaction Hamiltonian[17] $\mathcal{U}_s^{1D} = g_{1D} \frac{1}{2} \int dx \, \hat{\psi}^\dagger(x) \hat{\psi}^\dagger(x) \hat{\psi}(x) \hat{\psi}(x)$, we obtain an awful mess:

$$\mathcal{U}_s^{1D} = \frac{1}{2} \sum_{q_1,\alpha} \sum_{q_2,\beta} \sum_{q_3,\gamma} \sum_{q_4,\delta} \hat{\varphi}_{\alpha q_1}^\dagger \hat{\varphi}_{\beta q_2}^\dagger \hat{\varphi}_{\gamma q_3} \hat{\varphi}_{\delta q_4} U_{q_1,q_2,q_3,q_4}^{\alpha,\beta,\gamma,\delta}. \tag{2.34}$$

Here

$$U_{q_1,q_2,q_3,q_4}^{\alpha,\beta,\gamma,\delta} = g_{1D} \int dx \, \varphi_{\alpha q_1}^*(x) \varphi_{\beta q_2}^*(x) \varphi_{\gamma q_3}(x) \varphi_{\delta q_4}(x), \tag{2.35}$$

and because the functions $\varphi_{\alpha q}(x)$ are delocalized over a lattice, most of these integrals are finite and need to be retained. If we can find a basis in which each state is localized around a particular lattice site, such that the spatial overlap between different states is small, we expect that the interaction will be (predominantly) diagonal in this basis.

---

[17] The 1D coupling strength g_{1D}, which has dimensions of (energy×length), is left arbitrary here. This 1D interaction might arise, for instance, by putting atoms a very elongated trap and keeping the temperature small compared to the transverse level spacing, so that the physics is effectively 1D. In this case g_{1D} can be calculated explicitly in terms of the 3D scattering length [129].

quasi-momentum space ←——→ real space

$V = 13E_R$

energy

Δ_{01}

$w_1(x)$

$w_0(x)$

$-\pi/a$ 0 π/a

quasi-momentum   position
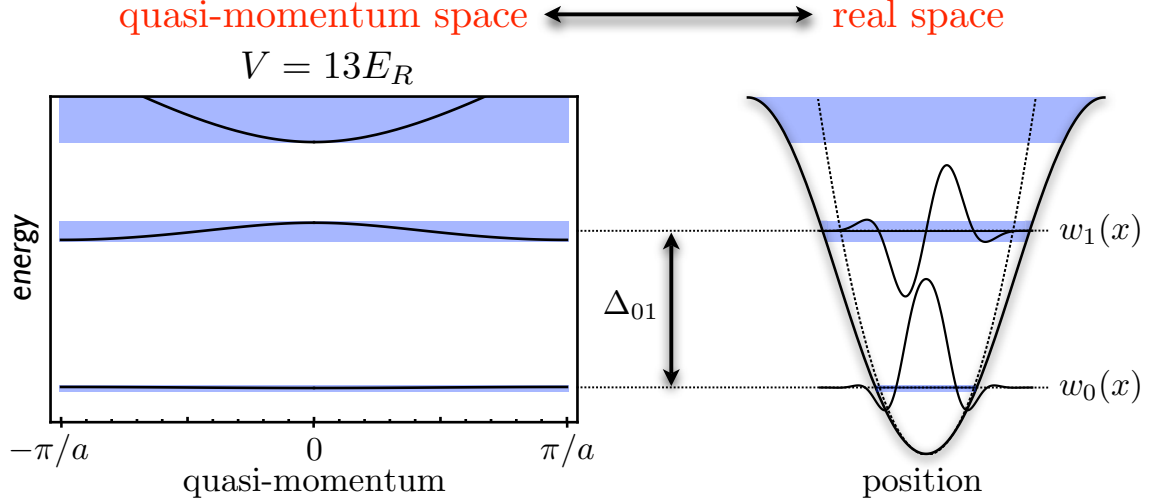
Figure 2.5: Illustration of the correspondence between bands (in quasi-momentum space) and the localized wavefunctions they are built from (in real space). If the lattice were infinitely deep, the Wannier functions would be harmonic oscillator levels. For a finite lattice depth, the Wannier functions are no longer eigenstates, and so the once infinitely narrow harmonic oscillator levels develop a finite lifetime set by the band-width (blue shaded region).

2.4.3   Local basis (Wannier functions)

In the absence of a lattice, we would construct a wave function maximally localized about the point x_0 by adding up plane waves $\psi_k(x) = \frac{1}{\sqrt{2\pi}}e^{ikx}$

$$\delta(x - x_0) = \frac{1}{\sqrt{2\pi}} \int dk \; e^{-ikx_0} \psi_k(x). \tag{2.36}$$

Analogously, in a lattice we can add up the delocalized Bloch-states within a given band to form maximally localized Wannier functions, defined[18]

$$w^\alpha(x - x_j) = \frac{1}{\sqrt{L}} \sum_q e^{-iqx_j} \varphi_{\alpha q}(x). \tag{2.37}$$

Here we have implicitly assumed that the lattice has L sites, so that q is a discrete index with spacing $2\pi/(aL)$, and for notational simplicity we will define $w_j^\alpha(x) = w^\alpha(x - x_j)$.

These Wannier functions furnish a natural real-space description of atoms in an optical lattice, with each w_j^α describing an atom in the αth band and on the jth site. In a very deep lattice, the

---

[18] Note that there is an ambiguity here, because $\varphi_{\alpha q}(x)$ is only defined up to an overall phase, and clearly the function $w^n(x - x_j)$ will depend on how we make this choice for the many different q entering the sum. At least in 1D, it is known that there is a well defined phase convention that produces maximally localized Wannier functions [100].

low lying Wannier functions are localized near the center of each lattice site, where the potential is to a good approximation harmonic (see Fig. 2.5). This approximately harmonic potential has frequency $\omega = 2E_R\hbar^{-1}\sqrt{V/E_R}$, and hence the low-lying band gaps are well approximated by $\hbar\omega$. In this real-space picture, the kinetic energy of an atom is due to tunneling from one site of the lattice to another. As we will see below, this tunneling depends on the matrix elements of $\mathcal{H}_0$ in neighboring Wannier functions. The Wannier functions $w_j^\alpha(x)$ have oscillatory tails extending in each neighboring well (which are needed to ensure their orthogonality between neighboring Wannier functions in the same band) and these matrix elements are sensitive to the oscillations. Hence the harmonic-oscillator approximation of w_j^α generally does not provide a good estimate of the tunneling of atoms between sites.

Before continuing, we note briefly that for any lattice potential that is *separable* in cartesian coordinates, i.e. the simple cubic lattice often used in experiments

$$V(\boldsymbol{r}) = V_x \cos^2(kx) + V_y \cos^2(ky) + V_z \cos^2(kz), \tag{2.38}$$

all of the above discussion generalizes trivially to more than one dimension. For example, in 2D (where we can easily picture the results), we simply solve for the Wannier functions of the lattice in each direction, $w_{\alpha_x}^x(x)$, and $w_{\alpha_y}^y(y)$, and then compose the 2D Wannier functions as

$$w_{\alpha_x \alpha_y}(x,y) = w_{\alpha_x}^x(x) w_{\alpha_y}^y(y), \tag{2.39}$$

as shown in Fig. 2.6.

2.4.4 Hamiltonian in the Wannier basis (tight binding model)

Just as we did before with the Bloch-states, we can expand the field operators in the Wannier basis as

$$\hat{\psi}(x) = \sum_{j,\alpha} w_j^\alpha(x) \hat{a}_{j\alpha}, \tag{2.40}$$

$$w_{00}(x,y) = w_0(x)w_0(y) \qquad w_{01}(x,y) = w_0(x)w_1(y) \qquad w_{10}(x,y) = w_1(x)w_0(y) \qquad w_{11}(x,y) = w_1(x)w_1(y)$$
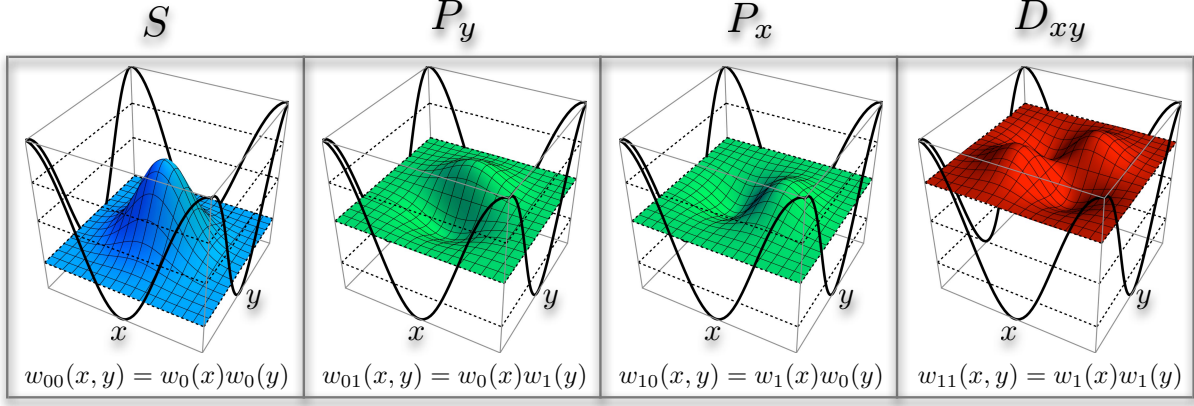
Figure 2.6: Examples of Wannier functions in 2D and the language used to describe them.

where now $\hat{a}_{j\alpha}^\dagger$ creates an atom in the Wannier function $w_j^\alpha(x)$. Substituting this expression into Eq. (2.31) we obtain

$$\mathcal{H}_0 = -\sum_{\alpha,i}\sum_{\beta,j}\hat{a}_{i\alpha}^\dagger\hat{a}_{j\beta}J_{i,j}^{\alpha,\beta}, \qquad (2.41)$$

where

$$J_{i,j}^{\alpha,\beta} = -\int dx\, w_i^{*\alpha}(x)\left[V(x) - \frac{\hbar^2\partial_x^2}{2m}\right]w_j^\beta(x). \qquad (2.42)$$

$$= -\int dx\, w_i^{*\alpha}(x)\left[V(x) - \frac{\hbar^2\partial_x^2}{2m}\right]w_j^\alpha(x)\delta_{\alpha,\beta}. \qquad (2.43)$$

The second equality follows because the noninteracting Hamiltonian (in the square brackets) is block-diagonal in the band index (note that here δ is the Kronecker-δ, not an index). In what follows we will therefore drop one of the two band indices on J, defining $J_{i,j}^\alpha = J_{i,j}^{\alpha,\beta}\delta_{\alpha,\beta}$. Notice that the single particle Hamiltonian is more complicated (not diagonal) when expanded in the Wannier basis, which simply reflects the fact that Wannier functions are not eigenstates of $\mathcal{H}_0$.

Similarly, we write the interaction Hamiltonian as

$$\mathcal{U}_s^{1D} = \frac{1}{2}\sum_{\alpha,i}\sum_{\beta,j}\sum_{\gamma,k}\sum_{\delta,l}\hat{a}_{i\alpha}^\dagger\hat{a}_{j\beta}^\dagger\hat{a}_{k\gamma}\hat{a}_{l\delta}U_{i,j,k,l}^{\alpha,\beta,\gamma,\delta}, \qquad (2.44)$$

where

$$U_{i,j,k,l}^{\alpha,\beta,\delta,\gamma} = g_{1D}\int dx\, w_i^{*\alpha}(x)w_j^{*\beta}(x)w_k^\gamma(x)w_l^\delta(x). \qquad (2.45)$$

Figure 2.7: Illustration of the two terms in the Bose Hubbard model. The hopping term, proportional to J, hops a boson from one site to the other, delocalizing the particles and thus contributing to their kinetic energy. The term proportional to U enforces an energy penalty for putting more than one boson on the same site, and thus tends to localize the particles.

It may not seem that we are any better off than before, when we used the Bloch-basis, but the current form of the Hamiltonian is amenable to a series of well controlled (and often extremely well justified) approximations, collectively referred to as the *tight-binding approximation*. The basic idea is that, because $w_j^\alpha(x)$ is exponentially localized around the jth lattice site, we set all integrals $U_{i,j,k,l}^{\alpha,\beta,\gamma,\delta}$ to zero unless $i = j = k = l$, and set all integrals $J_{i,j}^\alpha$ to zero unless $|i - j| \leq 1$. Defining nearest-neighbor tunneling matrix elements $J^\alpha = J_{i,i+1}^\alpha$, onsite energies $\varepsilon_\alpha = -J_{ii}^\alpha$, and the onsite interaction parameters $U^{\alpha,\beta,\delta,\gamma} = U_{i,i,i,i}^{\alpha,\beta,\delta,\gamma}$, the full Hamiltonian $\mathcal{H} = \mathcal{H}^0 + \mathcal{U}_s^{1D}$ then simplifies to

$$\mathcal{H} = \sum_{\alpha,j} \varepsilon_\alpha \hat{a}_{j\alpha}^\dagger \hat{a}_{j\alpha} - \sum_{\alpha,\langle i,j \rangle} J^\alpha \hat{a}_{i\alpha}^\dagger \hat{a}_{j\alpha} + \frac{1}{2} \sum_j \sum_{\alpha,\beta,\gamma,\delta} U^{\alpha,\beta,\gamma,\delta} \hat{a}_{j\alpha}^\dagger \hat{a}_{j\beta}^\dagger \hat{a}_{j\gamma} \hat{a}_{j\delta}. \tag{2.46}$$

Here the notation $\langle i, j \rangle$ implies that the sum should be restricted to pairs of sites that are nearest neighbors. It nearly all experiments where cold atoms have been loaded into optical lattices for the purpose of quantum simulation, the temperature of the atoms is much smaller than the band gap $\Delta_{01} = \varepsilon_1 - \varepsilon_0$. In this case this case (and when all of the $U^{\alpha,\beta,\gamma,\delta}$ are small compared to Δ_{01}, see the next section), the density of atoms in the excited bands is negligible. Defining $J = J^0$, $U = U^{0,0,0,0}$, and $\hat{a}_j^\dagger = \hat{a}_{j0}^\dagger$, we have

$$\mathcal{H} = -J \sum_{\langle i,j \rangle} \hat{a}_i^\dagger \hat{a}_j + \frac{1}{2} U \sum_j \hat{a}_j^\dagger \hat{a}_j^\dagger \hat{a}_j \hat{a}_j. \tag{2.47}$$

The Hamiltonian we are left with, called the single-band Bose-Hubbard model [50], describes the nearest-neighbor hopping of bosons (J), in a single band, with an energy penalty (U) when two bosons are on the same site. Note that by using the commutation relations for bosonic operators, the interaction term can (and often is) be written $\frac{1}{2} U \hat{n}_j (\hat{n}_j - 1)$, where $\hat{n}_j = \hat{a}_j^\dagger \hat{a}_j$ counts the number

of bosons on the site j. Therefore, more generally, this term assigns an energy U to all pairwise interactions of multiple bosons on the same site. Despite the apparent simplicity, there is no exact solution for, e.g., the groundstate correlation functions, finite temperature correlation functions, or dynamics, even in 1D. A great deal of qualitative understanding of the model, however, can be obtained in mean-field theory, as we will show in Chapter 4. Moreover, while analytic solutions are not available, this model is amenable to a variety of very powerful numerical techniques (DMRG for 1D [107] and Monte Carlo one [150] and two [106] dimensions), and thus many of its properties have been determined in a numerically exact fashion.

2.4.5   A note on energy scales

Besides the recoil energy, there are a number of other energy scales that appear when treating cold atoms in optical lattices, and therefore there is no *a priori* reason to expect the relevant energy scales to be comparable to the recoil energy. For instance one can change the lattice depth V, which is in principle completely independent of E_R. However, one can show via WKB-type arguments that tunneling between lattice sites in the lowest band obeys $J \sim e^{-\sqrt{V/E_R}}$, and hence in situations where this tunneling is non-negligible, lattice depths are given in small numbers of ($\lesssim 20$) E_R. The lowest band gap can be estimated as $\Delta_{01} \approx 2E_R\sqrt{V/E_R}$, and hence it too is naturally expressed in recoil energies (typically $\lesssim 10E_R$). The extent of the lowest band Wannier function is given by $x_0 \approx \sqrt{\hbar/m\omega}$, from which one can estimate (in a 3D lattice) $U \approx (\hbar^2 a_s)/(\sqrt{2\pi}x_0^3)$. Once again, for typical alkali-atom scattering lengths ($a_s \sim 1 - 10$nm) this is naturally expressed in recoil energies ($U \lesssim 1E_R$). As a general rule of thumb, J, U, and Δ_{01} satisfy

$$J < U < \Delta_{01}, \tag{2.48}$$

with both inequalities being replaceable by $\ll$ in many cases. Notable exceptions are that (typically) $J \sim U$ at the onset of the tight-binding regime (lattice depths of a few E_R), and $U \sim \Delta_{01}$ is possible if the scattering length is made artificially large via a Feshbach resonance.

2.5   Open quantum systems

The description of a quantum system always requires the choice of a boundary, i.e. a devision between degrees of freedom we will explicitly treat (the system) and those that we will not (the reservoir). Formally, we can say that the Hilbert space of the Universe is a direct product of a System Hilbert space and an Reservoir Hilbert space:

$$\mathscr{H}_U = \mathscr{H}_S \otimes \mathscr{H}_R \tag{2.49}$$

The Hamiltonian describing the Universe can always be written

$$\mathcal{H}_U = \mathcal{H}_S \otimes I_R + I_S \otimes \mathcal{H}_R + v\mathcal{H}_{S-R}, \tag{2.50}$$

where I is the identity operator, $\mathcal{H}_S$ contains operators acting only on the system, $\mathcal{H}_R$ contains operators acting only on the reservoir, and $\mathcal{H}_{S-R}$ contains products of both (and hence couples the system to the reservoir). One possible approach to obtaining system dynamics, which is often valid in atomic systems (at least on experimentally relevant timescales), is to completely ignore the coupling between system and reservoir, i.e. to put $v = 0$ in Eq. (2.50). In this case, and if the system and reservoir are initially unentangled so that $|\Psi\rangle = |\Psi_S\rangle \otimes |\Psi_R\rangle$, then the system wavefunction $|\Psi_S\rangle$ obeys a Schrödinger equation

$$\frac{d}{dt}|\Psi_S\rangle = -i\mathcal{H}_S|\Psi_S\rangle. \tag{2.51}$$

The extent to which this approximation is valid in ultracold atomic systems is often quite remarkable. However, even in these carefully isolated atomic systems, the system and reservoir are nevertheless always coupled to *some* extent. Especially in ions and dipolar molecules, which typically couple to their environment more strongly than neutral atoms, this approximation can break down on experimentally relevant timescales.

In the presence of even a weak system-reservoir coupling, the two become entangled, and the notion of a system wavefunction is no longer well defined (in the full Hilbert space $\mathscr{H}_U$, however, a wavefunction description is of course still valid). Let's define the density matrix of the universe

$\rho_U = |\Psi\rangle\langle\Psi|$, in terms of which the expectation value of an arbitrary operator $\mathcal{O}$ is given by $\langle\mathcal{O}\rangle = \langle\Psi|\mathcal{O}|\Psi\rangle = \text{Tr}\,[\mathcal{O}\rho]$. The trace is over states $|u\rangle$ in the Hilbert space $\mathscr{H}_U$. Notice that we don't *need* to introduce a density operator to calculate observables, but there is nothing to stop us. If we only care to calculate expectation values of operators that act on the system ($\mathcal{O}_S$), we can write

$$\langle\mathcal{O}_S\rangle = \text{Tr}\,[\rho_U\mathcal{O}_S] \;=\; \sum_{s,r} \left((\langle s|\otimes\langle r|)\,\rho_U\mathcal{O}_S\,(|r\rangle\otimes|s\rangle)\right) \tag{2.52}$$

$$= \sum_{s}\langle s|\text{Tr}_R[\rho_U]\mathcal{O}_S|s\rangle \tag{2.53}$$

$$= \text{Tr}_S[\rho_S\mathcal{O}_S]. \tag{2.54}$$

In the second line we have defined the partial trace $\text{Tr}_{R(S)}[\mathcal{A}] = \sum_{r(s)}\langle r(s)|\mathcal{A}|r(s)\rangle$, and in the third line we have defined the reduced density operator of the system $\rho_S \equiv \text{Tr}_R[\rho_U]$. The important point emerging from this algebra is that the expectation value of system operators can be obtained by tracing just over the system degrees of freedom, as long as one uses the reduced-system density matrix (this is *the* reason why reduced density matrices are useful). Notice that unless $\rho_U = \rho_S\otimes\rho_R$, which only remains true in time if $v = 0$, the system reduced density matrix is not pure. Hence, if we don't want to make explicit mention of the reservoir, we are now *forced* to describe the system with a density matrix. This is the price we pay for formally eliminating the reservoir.

At this point, everything we have said is exact, but if we want to derive an equation of motion for ρ_S that does not explicitly involve the reservoir degrees of freedom, we will need to make some approximations. This is the main goal in the field of *open quantum systems*. There are two very common and broadly applicable approximations that are employed to make progress:

(1) The system-reservoir coupling is treated in the Born approximation, which means the resulting equations are valid to second-order in v.

(2) The reservoir is assumed to be Markovian, meaning two things: (a) The time it takes for the reservoir to relax to equilibrium after being perturbed by the system, called the correlation time,

is small compared to the relaxation rate of the system and (b) The physical size of the reservoir is large enough that, once it has relaxed, its density matrix is essentially unchanged.

For a system-reservoir interaction of the form

$$\mathcal{H}_{S-R} = \sum_\alpha \sqrt{\frac{\gamma_\alpha}{2}} \left(\mathcal{J}_\alpha^\dagger \mathcal{R}_\alpha + \mathcal{J}_\alpha \mathcal{R}_\alpha^\dagger \right), \tag{2.55}$$

and assuming that the effects of the various couplings add incoherently, these approximations lead to the following master equation for the reduced system density matrix ρ_S

$$\hbar \dot{\rho}_S = i \left[\rho_S, \mathcal{H}_S \right] + \sum_\alpha \frac{\gamma_\alpha}{2} \left(2\mathcal{J}_\alpha \rho_S \mathcal{J}_\alpha^\dagger - \mathcal{J}_\alpha^\dagger \mathcal{J}_\alpha \rho_S - \rho_S \mathcal{J}_\alpha^\dagger \mathcal{J}_\alpha \right). \tag{2.56}$$

Obviously many details have been left out, but excellent pedagogical reviews exist [20]. Before moving on, we simply note a few very general features of the master equation. First of all, the γ_α are all assumed to be real and positive, in which case a valid density matrix remains a valid density matrix ($\mathrm{Tr}\,[\rho] = 1$, ρ is a positive operator, and $\rho = \rho^\dagger$). It can be explicitly checked, however, that $\mathrm{Tr}\,[\rho^2]$ is not in general conserved, and hence an initially pure state will in general become mixed.

For a finite-dimensional system Hilbert space [dimension $D = \dim(\mathscr{H}_S)$] spanned by states $|\mu\rangle$, a pure-state $|\psi_S\rangle$ can be represented with D complex numbers as

$$|\psi_S\rangle = \sum_{\mu=1}^{D} c_\mu |\mu\rangle. \tag{2.57}$$

The most general representation of a density matrix, however, is furnished by D^2 complex numbers

$$\rho_S = \sum_{\mu,\nu=1}^{D} c_{\mu\nu} |\mu\rangle\langle\nu|. \tag{2.58}$$

Hence solving the master equation numerically is more difficult than solving the Schrödinger equation.[19] There are techniques, broadly called Monte Carlo wavefunction simulations [133], that can greatly speed up the solution of the master equation. In these techniques, one effectively reduces

---

[19] As a result, for a many body system in which D scales exponentially with the particle number $\mathcal{N}$, a good rule of thumb is that the difficulty of solving the master equation is roughly comparable to that of solving a Schrödinger equation with twice the number of particles.

the solution to a stochastic sampling of wavefunctions, or "quantum trajectories", the production of which only requires solving the Schrödinger equation. A particular implementation of such methods, which will be used extensively in Chapters 6 and 7.

Chapter 3

Quantum simulation of the Kondo lattice model with alkaline earth atoms

Like the Hubbard model, the Kondo lattice model (KLM) has served for decades as a canonical example of interacting-electron physics [40]. It is similarly difficult in the sense that its emergent physical properties demand the proper incorporation of electron-electron correlations. While it can be derived from a particular limit of a two-band Hubbard model [76], it differs fundamentally in that the charge degrees of freedom (i.e. the hopping of electrons between lattice sites) in one of those bands have been completely frozen out. Electrons in this band act as localized spins that scatter itinerant electrons residing in the remaining (conduction) band, and in most treatments the interaction between the conduction electrons is ignored. Hence the KLM is, on a formal level, a model of electrons interacting with spins. In the most common presentation of the model there is one localized spin on each lattice site, and the only interaction considered is an on-site Heisenberg exchange between the conduction electrons and the localized spins (see Fig. 3.1). For different values of the exchange coupling the KLM gives rise to very different physics [76, 169]. We focus exclusively on the case of antiferromagnetic exchange (favoring anti-alignment of the localized spin and a conduction electron on the same site), which has been studied for over three decades as a model for inter-metallic compounds with anomalously massive quasiparticle excitations, termed *heavy fermion materials* [40, 160, 29]. While heavy fermion physics is interesting in its own right, the discovery of unconventional superconductivity in these materials [158] in 1979 has ensured intense interest in the Kondo lattice model over the last several decades. Despite the wealth of theoretical machinery developed for and brought to bear on the antiferromagnetic KLM, however,

the structure of the ground-state phase diagram (in $D > 1$) is not yet well understood.

The layout of this chapter is as follows. Before delving into the details, we give a brief historical overview of the KLM, with the simple intention of orienting the unfamiliar reader to its context and importance. We will briefly review some of what is known about the groundstate phase diagram, both in 1D and in 2D, and in so doing introduce the qualitative picture that has emerged for understanding heavy-fermion materials. We then review the details of an experimentally realistic scheme for simulating the Kondo lattice model using alkaline-earth atoms in an optical lattice, which was originally proposed in [68].

Before there can be any prospect for the exploration of unknown aspects of the phase diagram via quantum simulation, it is imperative that we understand the manifestation of relatively well understood KLM physics in an inhomogeneous setting—the ubiquitous cold-atom trap. With this goal in mind, we spend the rest of the chapter exploring the behavior of the Kondo lattice model in a harmonic potential. We will begin by introducing an extension to the trap of a well known mean-field theory (MFT) appropriate for describing the *heavy Fermi liquid* [109]. Some ground-state properties can be determined with relatively little effort within the local-density approximation (LDA). Already at this level several hallmarks of Kondo physics can be observed in the trap. For example, the Kondo insulator phase induces a shell structure in the trapped density distribution, and the emergence of heavy quasiparticles in the heavy Fermi liquid phase shifts conduction atom weight out to the so called "large Fermi surface".[1]

The harmonic trap is also a valuable tool for studying out of equilibrium dynamics [48]. After a brief review of single particle dynamics in a lattice plus confining potential [144], we consider three distinct parameter regimes where signatures of Kondo physics are manifest in dynamics after a sudden trap displacement. The first two are in 1D, at weak coupling [155] and at strong coupling [128, 156]. Such dynamics could be studied experimentally by making the optical lattice extremely

---

[1] When the Kondo coupling is absent, the conduction electrons form a noninteracting Fermi sea. The volume of this Fermi sea is determined by the number of conduction electrons, a scenario that is referred to in the literature as the existence of a "small Fermi surface". In the heavy Fermi liquid phase, it is well established that the localized electrons (spins) should be included when determining the Fermi volume, and this scenario is referred to as the existence of a "large Fermi surface".
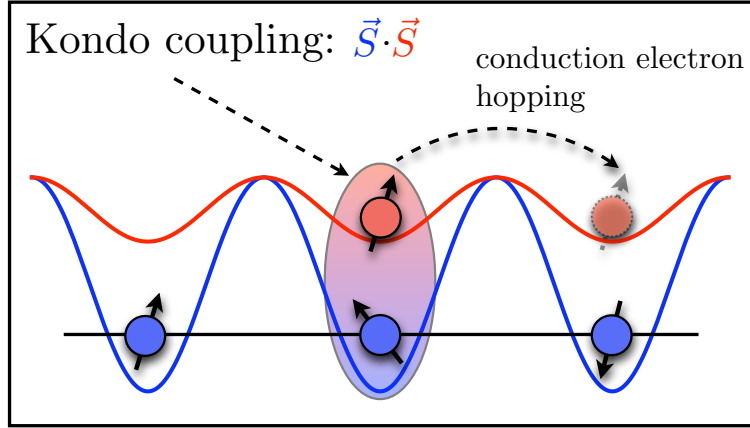
Figure 3.1: In the Kondo Lattice Model the conduction electrons (red) can hop from site to site, and they interact with localized spins (blue) via a Heisenberg exchange.

deep in two directions, resulting in an array of independent 1D chains, and would be a sensible starting point for simulations wishing to verify the model (especially with regards to the strong coupling dynamics, which can be calculated quite rigorously and have a simple signature). Outside of 1D, we employ a numerical self-consistent diagonalization of the MFT discussed above. Using the exact mean-field wave function we explore center-of-mass oscillations resulting from a sudden displacement of the trap center, and find a clear signature of the heavy fermion mass enhancement.

3.1 Introduction to the Kondo lattice model

The Kondo Lattice model (KLM) has a rich and elaborate history, and it would be difficult to overemphasize its importance to the field of condensed-matter theory [80, 29]. An essential piece of physics involved in the model is the spin-screening of localized magnetic impurities by itinerant electrons. For a lattice of localized spins ($\boldsymbol{S}_{ej}$) interacting with a tight-binding band of electrons ($c^{\dagger}_{gj\sigma}$) via spin-exchange, the Hamiltonian is

$$\mathcal{H}_{\mathrm{K}} = -J \sum_{\langle i,j\rangle\sigma} \hat{c}^{\dagger}_{gi\sigma}\hat{c}_{gj\sigma} - 2V_{\mathrm{ex}} \sum_{j} \boldsymbol{S}_{ej} \cdot \boldsymbol{S}_{gj}. \tag{3.1}$$

Here the spin density of the conduction electrons on site j is given by $\boldsymbol{S}_{gj} = \sum_{\sigma\sigma'} \hat{c}^{\dagger}_{gj\sigma}\boldsymbol{\tau}_{\sigma\sigma'}\hat{c}_{gj\sigma'}$. That the conduction band is tight-binding is largely irrelevant, but it simplifies the real space

description. A negative exchange coupling $V_{\text{ex}} < 0$ leads to an antiferromagnetic coupling, and we will exclusively consider this case, and will often use the positive dimensionless quantity

$$v = -2V_{\text{ex}}/J \tag{3.2}$$

as a measure of strong ($v \gg 1$) and weak ($v \ll 1$) coupling. The localized spins can also be written in terms of fermionic operators as $\boldsymbol{S}_{ej} = \sum_{\sigma\sigma'} \hat{c}^\dagger_{ej\sigma} \boldsymbol{\tau}_{\sigma\sigma'} \hat{c}_{ej\sigma'}$, in which case, dropping constant energy shifts, we can write

$$\mathcal{H}_{\text{K}} = -J \sum_{\langle i,j \rangle \sigma} \hat{c}^\dagger_{gi\sigma} \hat{c}_{gj\sigma} + V_{\text{ex}} \sum_{i\sigma\sigma'} \hat{c}^\dagger_{ig\sigma} \hat{c}^\dagger_{ie\sigma'} \hat{c}_{ig\sigma'} \hat{c}_{ie\sigma}. \tag{3.3}$$

Historically, the screening of magnetic impurities in a metal was first studied for just a single impurity (on site $j = 0$) [3, 102], such that the Hamiltonian takes the form

$$\mathcal{H}_{\text{K}} = -J \sum_{\langle i,j \rangle \sigma} \hat{c}^\dagger_{gi\sigma} \hat{c}_{gj\sigma} - 2V \boldsymbol{S}_{e0} \cdot \boldsymbol{S}_{g0}. \tag{3.4}$$

The apparent simplicity of the *Kondo impurity model* defined in Eq. (3.4) is misleading: A full understanding of the low-temperature physics of this model took decades of work by numerous researchers, and encouraged the development of a variety of new theoretical techniques [4, 173, 28, 141]. If the impurity did not interact via spin exchange, i.e. if the problem reduced to pure potential scattering off of an energy barrier on site $j = 0$, the model would indeed be quite trivial.[2] The essential difficulty arrises because the spin-spin interaction has terms like $S^+_{e0} S^-_{g0}$, which cause a scattered electron to exchange its spin with the local impurity. This electron, we'll call it electron 1, then goes off with a knowledge of the state of the impurity, i.e. they are correlated. When another electron comes in, we'll call it electron 2, and scatters off the impurity, the result of this scattering depends on the state of the impurity. In this way, electrons 1 and 2 become correlated, despite the fact that they do not interact directly.

Interest in this model originated soon after the experimental observation that in some non-magnetic metals, the existence of a small concentration of magnetic impurities was connected with a minimum in the resistance at low temperatures [148] (in most metals that don't superconduct, the

---

[2] By trivial, we mean only that there would be no correlation effects, and one could solve the problem by looking at a single-electron scattering process.

resistance is expected to decrease monotonically and then saturate as the temperature $T \to 0$). Jun Kondo, for whom the model is named, calculated the scattering rate of electrons in perturbation theory to third order in V [102]. The end result of this calculation was a contribution to the resistivity $\propto V_{\mathrm{ex}} \log(T)$, which for $V_{\mathrm{ex}} < 0$ causes the resistivity to grow as $T \to 0$. While this calculation cemented the notion that magnetic impurities were central to the resistance minimum, it was just the beginning of a long effort to understand the low temperature physics of the Kondo model [which clearly is not captured by the $\log(T)$ term, which diverges]. At this point, as a result of numerical scaling analyses [173] and even an exact solution [4], the model has been very extensively understood. The modern picture, due in large part to the work of Anderson [], Wilson [], and Nozieres [], is that, at low energies, the scattering

The Kondo lattice model was subsequently proposed by Doniach [40] in the late 1970s as a possible explanation for the enormous linear specific heat term in the recently discovered *heavy-fermion metals'* [5]. Unlike for the Kondo impurity model, the Kondo lattice model is far from understood. At strong coupling, $v \gg 1$, it is clear that all conduction electrons should bind to the localized spins as singlets, and in 2D this leads to a paramagnetic state called the *heavy Fermi liquid*. In analogy to the single-impurity model, the energy scale associated with this singlet formation is called the Kondo temperature, and obeys

$$T_{\mathrm{K}} \sim J e^{-J/|V_{\mathrm{ex}}|}. \tag{3.5}$$

One essential problem with having a lattice of impurities is that, as the coupling v is reduced, the conduction electrons mediate an effective magnetic interaction between the localized spins, known as the RKKY interaction [146, 93, 176], which causes them to develop magnetic order. Because this interaction arrises perturbatively from the scattering of conduction electrons (by the exchange interaction) out of and then back into the Fermi sea, it has a characteristic strength

$$T_{\mathrm{RKKY}} \sim V_{\mathrm{ex}}^2/J. \tag{3.6}$$

This magnetic ordering competes with the tendency toward singlet formation at larger V_{ex}, and

eventually destabilizes the heavy Fermi liquid when the characteristic temperature scale of magnetism becomes comparable to the Kondo temperature ($T_K \approx T_{RKKY}$).

3.1.1 Groundstate Phase Diagram

Determining the groundstate phase diagram of the Kondo Lattice model is an active area of current research. As is typical for many-body systems, the physics of the model in 1D is quite different from in higher dimensions. Nevertheless the availability of numerical and analytical techniques for treating 1D systems has prompted intensive study of the 1D phase diagram, which at this point is basically known (a good review can be found in [169]). In $D > 1$, much less is known. A number of approximate techniques, both numerical and analytical, have helped to form some consensus about the basic structure, but there are many open questions. At zero temperature (i.e. in the groundstate), the physics is entirely determined by the dimensionless ration v and the average number of conduction electrons per unit cell, n_g.

In 1D there are three distinct phases: (1) a ferromagnetic phase at large v, (2) a paramagnetic phase at small v, and (3) an insulating state at $n_g = 1$, for any value of the coupling. The ferromagnetism at strong coupling may be surprising, given that the coupling is antiferromagnetic. Strictly speaking, for $n_g < 1$ and in the limit $v \to \infty$, there are no processes (to first order in the hopping J) within the low-energy Hilbert space that change the ordering of the unpaired localized spins, and hence the groundstate energy is independent of the ordering of the unpaired localized spins [128]. Working to second order in the hopping, however, the unpaired spins can change their order, and a careful analysis of the matrix elements for such processes shows that the energy is lowered when all unpaired spins are aligned, and hence the groundstate is ferromagnetic [156]. The weak coupling phase is much more difficult to understand analytically, but extensive numerical studies have helped clarify a number of its properties. It is known to be a paramagnetic metal, with gapless spin and charge excitations [169]. Exactly at $n_g = 1$, the system becomes insulating (with finite spin and charge gaps) for *any* non-zero value of the coupling v.

In 2D, the groundstate phase diagram is much less well known. For $n_g = 1$ and large v, the
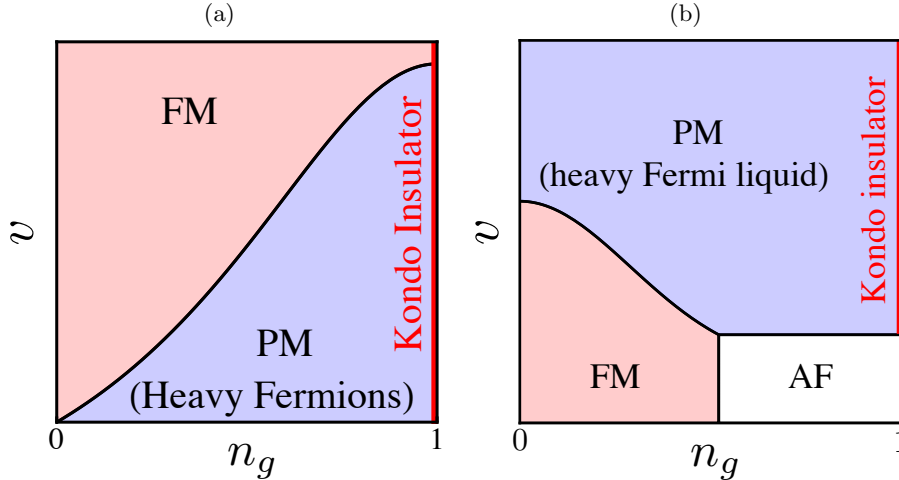
Figure 3.2: (a) Schematic zero temperature phase diagram for the 1-D KLM [169, 76]. FM is a ferromagnetic phase, and PM is a paramagnetic phase closely related to heavy fermions in higher dimensions. (b) 2D mean-field ground-state phase diagram as constructed in [109], n_g being conduction electron density and v being a dimensionless measure of the interaction strength. PM is a paramagnetic phase, in which the heavy Fermi liquid behavior is expected. The FM (AFM) phase is where RKKY interactions [146, 93, 176] generate ferromagnetic (antiferromagnetic) order among the localized spins. Exactly at $n_g = 1$ the AF phase gives way to a non-magnetic insulating state for sufficiently large v [7].

system is insulating and has both spin and charge gaps. This phase is referred to as the Kondo insulator. Unlike in 1D, the limit $v \to 0$ with $n_g = 1$ eventually causes a phase transition to a magnetically ordered state [7], as has been confirmed by numerous numerical studies. As discussed above, at $n_g < 1$ the behavior is expected to be determined by a competition between the Kondo effect—favoring a paramagnetic heavy Fermi liquid at strong coupling—and the RKKY mediated magnetic ordering at weak coupling. The type of magnetic ordering that develops at weak coupling depends on both the filling n_g and the details of the lattice structure, but is generically expected to range from ferromagnetic at $n_g \ll 1$ to antiferromagnetic (or something more complicated) for $n_g \lesssim 1$. This picture is confirmed by numerous mean-field studies [109, 46], but a rigorous picture of the phase diagram is non-existent. A major outstanding challenge in KLM research is to understand the quantum phase transition that separates these two regimes, and this challenge could in principle be addressed by careful analysis of an optical lattice emulator.

3.2   Advantages of alkaline-earth atoms

Recently it has been proposed that several unique properties of fermionic alkaline-earth atoms (AEAs) make them particularly well suited for the simulation of a broad class of condensed matter Hamiltonians describing the interplay between internal (spin) and external (orbital) electronic degrees of freedom [68, 79, 21, 175, 52]. These two-electron atoms are more complicated than their one-electron alkali counterparts, however in the last few years a great deal of progress has been made in cooling a variety of bosonic and fermionic isotopes to quantum degeneracy [61, 60, 159, 103, 121, 166, 35]. There are two primary features of AEAs that make them suitable for simulation of the KLM: (1) The long-lived $^1S_0$ (g) and $^3P_0$ (e) clock states can be trapped independently by two different but spatially commensurate optical lattices [31]. (2) Both clock states have total electronic angular momentum $J = 0$, and as a result there is essentially no coupling between the different nuclear spin states and therefore no spin changing collisions (in contrast to alkali metal atoms) [68]. This enables us to consider an ensemble where just two states in the hyperfine manifold are populated, since to a very good approximation no transfer of states into the rest of the manifold can occur, and these two states are identified with spin up and spin down of the electrons in the KLM.

3.2.1   Independent lattices

The ability to engineer independent lattices for the $^1S_0$ and $^3P_0$ states of an AEA relies on the optical frequency separations between these two states [31]. As a result, an optical lattice of a given frequency can induce entirely different polarizabilities for these two states (since their detunings from various other electronic levels are completely different), even in the limit where both are far detuned from any transition. We denote the lattice potential for the atomic state $\alpha \in \{g, e\}$ by V_α, and we note that, despite their different wavelengths, V_e and V_g can be made to have the same periodicity by increasing the angle between the counter-propagating beams for the shorter wavelength lattice. We denote the lowest Wannier orbital of the lattice V_α by w_α, and then define

hopping energies

$$J_\alpha = \int d^D \mathbf{r} w_\alpha (\mathbf{r}_i - \mathbf{r}) \left(-\frac{\hbar^2}{2m} \nabla^2 + V_\alpha \right) w_\alpha (\mathbf{r}_j - \mathbf{r}) \tag{3.7}$$

(m is the atomic mass, and $(\mathbf{r}_i, \mathbf{r}_j)$ are the centers of two nearest neighbor lattice sites). The situation we have in mind is when the lattice for the e atoms is very deep (driving these atoms into a Mott insulator), while the independent lattice for the g atoms is kept shallow (though still deep enough for the tight-binding approximation to be valid). In this arrangement, we can justify (see the next section for details) the scenario where there is one e atom in each site of the lattice; these will be our localized spins. The g atoms will be the equivalent of the conduction electrons in the KLM.

3.2.2   Interactions

In order to understand the origin of the exchange coupling, it will suffice to consider the s-wave scattering of two fermionic AEAs, one in the $^1S_0(\alpha = g)$ electronic state and the other in the $^3P_0(\alpha = e)$ electronic state, where each can have any nuclear spin $-I \leq m \leq I$. Because the collisional physics only depends on the electronic state, the possible collision processes can be categorized by the two possible two-particle combinations of electronic states, $\frac{1}{\sqrt{2}}(|ge\rangle \pm |eg\rangle)$ (note that both are possible because the nuclear spins can still be used to properly antisymmetrize the fermionic wavefunction). Each of these possibilities we'll call a channel, and we denote the s-wave scattering lengths in these channels by $a_{eg}^\pm$. At this level, the lack of coupling between the nuclear spin and the electronic angular momentum appears as a lack of nuclear-spin dendence of these scattering lengths. Defining $g^\pm = \frac{4\pi\hbar^2 a_{eg}^\pm}{m}$, the total (unregularized) s-wave pseudopotential can be written as

$$U(\mathbf{r}) = \left(g^+ \mathcal{P}^+ + g^- \mathcal{P}^- \right) \delta(\mathbf{r}), \tag{3.8}$$

where $\mathcal{P}^\pm$ is a projector on the electronic state $\frac{1}{\sqrt{2}}(|ge\rangle \pm |eg\rangle)$.

If we temporarily employ a spin-$\frac{1}{2}$ description of the two-level system comprised of the electronic states,[3] these projection operators can be written as $\mathcal{P}^+ = \frac{3}{4} + \mathbf{S}_1 \cdot \mathbf{S}_2$ and $\mathcal{P}^- = \frac{1}{4} - \mathbf{S}_1 \cdot \mathbf{S}_2$.

---

[3] Note that these are *not* the spin operators that will appear in the context of the Kondo-exchange interaction

Both of the two particle states we are considering have $S_1^z S_2^z = -\frac{1}{4}$. Hence, remembering that

$\boldsymbol{S}_1 \cdot \boldsymbol{S}_2 = S_1^z S_2^z + \frac{1}{2}\left(S_1^+ S_2^- + S_1^- S_2^+\right)$, we can write

$$U(\boldsymbol{r}) = \left[\frac{g^+ + g^-}{2}\right]\delta(\boldsymbol{r}) + \left[\frac{g^+ - g^-}{2}\left(S_1^+ S_2^- + S_1^- S_2^+\right)\right]\delta(\boldsymbol{r}) \tag{3.9}$$

The first term is a density-density interaction, which in second-quantization can be written

$$\mathcal{U}_{\mathrm{d}} = \frac{g^+ + g^-}{2}\sum_{m,m'}\int d^3\boldsymbol{r}\,\hat{\psi}_{gm}^\dagger(\boldsymbol{r})\hat{\psi}_{gm}(\boldsymbol{r})\hat{\psi}_{em'}^\dagger(\boldsymbol{r})\hat{\psi}_{em'}(\boldsymbol{r}), \tag{3.10}$$

where $\hat{\psi}_{\alpha m}^\dagger(\boldsymbol{r})$ creates an atom in electronic state α and nuclear spin state m at position $\boldsymbol{r}$. The second term is an exchange term, which swaps the electronic state of the two interacting atoms while leaving their nuclear spins untouched. In second quantization the operator $S^+ = \sum_m \hat{\psi}_{em}^\dagger(\boldsymbol{r})\hat{\psi}_{gm}(\boldsymbol{r})$, and the whole exchange term is given by

$$\mathcal{U}_{\mathrm{ex}} = \frac{g^+ - g^-}{2}\sum_{m,m'}\int d^3\boldsymbol{r}\,\hat{\psi}_{gm}^\dagger(\boldsymbol{r})\hat{\psi}_{em'}^\dagger(\boldsymbol{r})\hat{\psi}_{gm'}(\boldsymbol{r})\hat{\psi}_{em}(\boldsymbol{r}), \tag{3.11}$$

In an $e-g$ collision, if we restrict the nuclear spin Hilbert space to contain just two possible values $m = \uparrow, \downarrow$, the exchange term causes there to be a difference in energy between the states $\frac{1}{\sqrt{2}}(|\uparrow\downarrow\rangle \pm |\downarrow\uparrow\rangle)$. If we treat the two nuclear spin degrees of freedom as our spin-$\frac{1}{2}$ (rather than the electronic states), this term has the structure $\boldsymbol{S}_g \cdot \boldsymbol{S}_e$, and is the origin of the Kondo-exchange in what follows. Note that, even for an atom with $I > 1/2$, it is possible to initially populate just two nuclear-spin levels and thereby obtain a spin-$\frac{1}{2}$ model; the exchange interaction conserves independently the population in each level m_I, and so the spin $\frac{1}{2}$ model will remain valid at any later time. In the rest of the chapter, we will make the assumption that only two levels are populated, and denote them by $\sigma = \uparrow, \downarrow$.

Both the direct and exchange interactions above arise from the collision between a g-atom and an e atom, but there can also be collisions between two e (or g) atoms in the s-wave channel. These are exactly analogous to the interaction in Eq. (2.7), and are given by

$$\mathcal{U}_{\alpha\alpha} = \frac{g_{\alpha\alpha}}{2}\sum_{m,m'}\int d^3\boldsymbol{r}\,\hat{\psi}_{\alpha m}^\dagger(\boldsymbol{r})\hat{\psi}_{\alpha m'}^\dagger(\boldsymbol{r})\hat{\psi}_{\alpha m'}(\boldsymbol{r})\hat{\psi}_{\alpha m}(\boldsymbol{r}), \tag{3.12}$$

---

later on.

where $g_{\alpha\alpha} = 4\pi\hbar^2 a_{\alpha\alpha}/m$, and $a_{\alpha\alpha}$ is the scattering length for collisions between two α atoms.

As in Chapter 2, to describe physics at temperatures much less than the lowest band gap (of both lattices) we project these interactions into the lowest bands of the e and g lattices, and we will ignore interaction terms involving atoms on more than one site. Defining creation operators

$$\hat{c}_{\alpha j\sigma}^\dagger = \int d^3 \boldsymbol{r}\, \hat{\psi}_{\alpha\sigma}^\dagger(\boldsymbol{r}) w_\alpha^*(\boldsymbol{r}_j - \boldsymbol{r}) \tag{3.13}$$

and the onsite interaction parameters

$$V_{\text{ex}} = \frac{g^+ - g^-}{2} \int d^3 \boldsymbol{r}\, |w_g(\boldsymbol{r})|^2 |w_e(\boldsymbol{r})|^2 \tag{3.14}$$

$$V_{\text{d}} = \frac{g^+ + g^-}{2} \int d^3 \boldsymbol{r}\, |w_g(\boldsymbol{r})|^2 |w_e(\boldsymbol{r})|^2 \tag{3.15}$$

$$V_{\alpha\alpha} = g_{\alpha\alpha} \int d^3 |\boldsymbol{r} w_\alpha(\boldsymbol{r})|^4, \tag{3.16}$$

we obtain the (projected) interactions

$$\tilde{\mathcal{U}}_{\text{ex}} = V_{ex} \sum_{j,\sigma,\sigma'} c_{jg\sigma}^\dagger c_{je\sigma'}^\dagger c_{jg\sigma'} c_{je\sigma} \tag{3.17}$$

$$\tilde{\mathcal{U}}_{\text{d}} = V_{\text{d}} \sum_{j,\sigma,\sigma'} c_{jg\sigma}^\dagger c_{jg\sigma} c_{je\sigma'}^\dagger c_{je\sigma'} \tag{3.18}$$

$$\tilde{\mathcal{U}}_{\alpha\alpha} = V_{\alpha\alpha} \sum_{j,\sigma,\sigma'} c_{j\alpha\sigma}^\dagger c_{j\alpha\sigma} c_{j\alpha\sigma'}^\dagger c_{j\alpha\sigma'} \tag{3.19}$$

We are interested in the case where $V_{ee} \gg J_e$ and $V_{gg} \ll J_g$. Under these conditions, and with a sufficiently weak confining potential $\Omega(i)$, the e atoms form a unit filled Mott insulator at the center of the trap and the g atoms are to a good approximation non-interacting. We choose the e atoms to represent the localized spins because they would otherwise suffer lossy collisions [68]. At temperatures well below V_{ee}, to lowest order we can drop both V_{ee} and J_e and simply constrain the Hilbert space to have one e atom per site. Certainly to higher order in J_e/V_{ee} there would be super-exchange interactions, but we assume these to be negligible compared to all other terms in the Hamiltonian. Neglecting terms ($\propto V_{\text{d}}$) which are constant in consideration of the constraint on

the e atom density, what remains is an inhomogeneous version of the Kondo Lattice Hamiltonian:

$$\begin{aligned}
\mathcal{H}_{\mathrm{K}} &= -J_g \sum_{\langle i,j \rangle, \sigma} c_{ig\sigma}^\dagger c_{jg\sigma} + V_{\mathrm{ex}} \sum_{i\sigma\sigma'} c_{ig\sigma}^\dagger c_{ie\sigma'}^\dagger c_{ig\sigma'} c_{ie\sigma} \\
&+ \sum_i \Omega(i) \, \hat{n}_{ig}.
\end{aligned} \tag{3.20}$$

In Eq (3.20) $\hat{n}_{i\alpha} = \sum_\sigma c_{i\alpha\sigma}^\dagger c_{i\alpha\sigma}$. In the rest of the chapter we will consider only D-dimensional hypercubic lattices, with a particular focus on $D = 2$. In the first term of the Hamiltonian we have used the convention that $\langle i, j \rangle$ restricts the summation to nearest-neighbor sites. It is important to observe that satisfaction of the inequalities $V_{ee} \gg J_e$ and $V_{gg} \ll J_g$ places no fundamental constraint on V_{ex}/J_g. This independence of parameters is a unique feature of the alkaline earth atom simulations proposed in Ref. [68]. Previous proposals to study the KLM using alkali-metal atoms lack this tunability because they either populate multiple bands of a single lattice (Ref. [42], in which case V_{ee}, V_{gg} and V_{ex} all scale with the lattice depth), or generate Eq (3.20) as an effective Hamiltonian which necessarily operates at weak coupling ($|V_{\mathrm{ex}}|/J_g \ll 1$) [130]. In the present scheme, V_{ex} will vary from one isotope to another, and can be further adjusted by offsetting the two lattices with respect to each other (to decrease the overlap between Wannier orbitals).

3.3   Mean-Field Theory

There is no nontrivial parameter regime in which Eq. (3.20) can be solved exactly, and approximations have to be made. In the heavy Fermi liquid phase a qualitative understanding can be gained by treating the interaction term at mean-field level [109]:

$$\begin{aligned}
V_{\mathrm{ex}} c_{ig\sigma}^\dagger c_{ie\sigma'}^\dagger c_{ig\sigma'} c_{ie\sigma} &\rightarrow V_{\mathrm{ex}} \sum_{\sigma'} \tilde{V}_i \left(c_{ig\sigma'}^\dagger c_{ie\sigma'} + c_{ie\sigma'}^\dagger c_{ig\sigma'} \right) \\
&- V_{\mathrm{ex}} \tilde{V}_i^2
\end{aligned} \tag{3.21}$$

where we have defined the on-site hybridizations

$$\tilde{V}_i = \frac{1}{2} \sum_\sigma \left\langle c_{ie\sigma}^\dagger c_{ig\sigma} + c_{ig\sigma}^\dagger c_{ie\sigma} \right\rangle. \tag{3.22}$$

This expectation value, along with all others in this section, is taken in the ground state of the mean-field Hamiltonian [see Eq. (3.23) below]. Because the mean-field Hamiltonian is quadratic,

the ground state is a Slater determinant of the lowest $(N_e + N_g)/2$ single particle states (half the total number of atoms due to spin degeneracy), where N_α is the total number of α atoms. This decoupling is not unique, for instance there could be terms that mix different spin states, but if the KLM is generalized to allow the spin index σ to run from 1 to N ($N = 2$ for the KLM), then the above decoupling is exact in the limit[4] $N \to \infty$ [28, 141]. One should keep in mind, however, that the decision not to keep any spin mixing terms in the decoupling guarantees that this MFT cannot capture a transition to a magnetically ordered state, and therefore cannot remain valid for arbitrarily small v (where RKKY-induced magnetic order should exist). The resulting quadratic Hamiltonian is

$$\mathcal{H}_{\mathrm{M}} = -J_g \sum_{\langle i,j \rangle, \sigma} c^\dagger_{ig\sigma} c_{jg\sigma} + \sum_i \left[\Omega\left(i\right) \hat{n}_{ig} + \mu_{ie}\left(\hat{n}_{ie} - 1\right) \right]$$
$$+ V_{\mathrm{ex}} \sum_{i\sigma} \tilde{V}_i \left(c^\dagger_{ig\sigma} c_{ie\sigma} + c^\dagger_{ie\sigma} c_{ig\sigma} \right) - V_{\mathrm{ex}} \sum_i \tilde{V}_i^2, \tag{3.23}$$

where the μ_{ie} are local chemical-potentials needed to enforce the constraint of one e atom per site on average (in the exact KLM we have the much stronger constraint $\langle (\hat{n}_{ie} - 1)^2 \rangle = 0$, but in the MFT this must be relaxed to $n_{ie} \equiv \langle \hat{n}_{ie} \rangle = 1$). The theory is now paramagnetic, because $\mathcal{H}_{\mathrm{M}}$ does not couple different spin states, and the eigenstates are created by quasiparticle operators:

$$\alpha^\dagger_{q\sigma} = \sum_i \left(u^i_q c^\dagger_{ig\sigma} + v^i_q c^\dagger_{ie\sigma} \right). \tag{3.24}$$

Here $q \in \{1, 2, ...\}$ is an index that labels the different quasiparticle eigenstates, and not a wave vector. Solving the MFT then means finding the above mode coefficients u^i_q and v^i_q, but this needs to be done self-consistently: As parameters in the Hamiltonian the $\tilde{V}_i$ determine the mode coefficients, but in turn the mode coefficients determine the $\tilde{V}_i$ via the definition

$$\tilde{V}_i = \frac{1}{2} \sum_\sigma \left\langle c^\dagger_{ie\sigma} c_{ig\sigma} + c^\dagger_{ig\sigma} c_{ie\sigma} \right\rangle$$
$$= \sum_{q=1}^{(N_g+N_e)/2} \left(u^i_q \bar{v}^i_q + v^i_q \bar{u}^i_q \right). \tag{3.25}$$

---

[4] In order not to obtain a trivial limit it is important to hold the proper quantities fixed as $N \to \infty$. In particular, one should hold JN constant and adjust the filling of localized electrons such that $n_e/N = \frac{1}{2}$.

We sum over a number of modes equal to half of the total number of particles, but put two particles in each mode to account for the degeneracy of spin. Similarly, the onsite g and e atom densities are given by

$$n_{ig} = \sum_\sigma \left\langle c^\dagger_{ig\sigma} c_{ig\sigma} \right\rangle = 2 \sum_{q=1}^{(N_g+N_e)/2} u^i_q \bar{u}^i_q$$

$$n_{ie} = \sum_\sigma \left\langle c^\dagger_{ie\sigma} c_{ie\sigma} \right\rangle = 2 \sum_{q=1}^{(N_g+N_e)/2} v^i_q \bar{v}^i_q. \tag{3.26}$$

If we define the ground-state energy $E = \langle \mathcal{H}_\mathrm{M} \rangle$, the self-consistency condition and the local constraints $n_{ie} = 1$ can be written compactly as

$$\partial E / \partial \tilde{V}_i = 0 \quad \text{and} \quad \partial E / \partial \mu_{ie} = 0 \tag{3.27}$$

respectively.

3.3.1 Translationally Invariant Case

Before solving the MFT in the presence of a trap, it is useful to review known results for the translationally invariant case ($\Omega = 0$) [109]. It is common to assume that the hybridizations and chemical potentials retain the discrete translational invariance of the exact KLM Hamiltonian ($\tilde{V}_i, \mu_{ie} \to \tilde{V}, \mu_e$), in which case the Hamiltonian in Eq. (3.23) reduces to

$$\begin{aligned} \mathcal{H}_\mathrm{T} &= -J_g \sum_{\langle i,j \rangle \sigma} c^\dagger_{ig\sigma} c_{jg\sigma} + \mu_e \left(\sum_i \hat{n}_{ie} - \mathcal{N} \right) \\ &+ V_\mathrm{ex} \sum_{i\sigma} \tilde{V} \left(c^\dagger_{ig\sigma} c_{ie\sigma} + c^\dagger_{ie\sigma} c_{ig\sigma} \right) - \mathcal{N} V_\mathrm{ex} \tilde{V}^2, \end{aligned} \tag{3.28}$$

$\mathcal{N}$ being the total number of lattice sites. It is common to include a g atom chemical potential by adding a term $-\mu_g \sum_i \hat{n}_{ig}$ in Eq. 3.28, but we find it conceptually simpler to work at a fixed n_g for the time being (we will trade in n_g for μ_g in the next section to apply the LDA). Due to the translational invariance the nonconstant part of $\mathcal{H}_\mathrm{T}$ (those terms containing operators) can easily be diagonalized for general $\tilde{V}$ and μ_e by going to Fourier space. Defining $c_{k\alpha\sigma} = \frac{1}{\sqrt{\mathcal{N}}} \sum_j c_{j\alpha\sigma} e^{i r_j \cdot k}$ (where r_j is the position of site j and k is a quasi-momentum vector in the first Brillouin zone),

we find quasiparticles

$$\alpha^\dagger_{\boldsymbol{k}\sigma} = c^\dagger_{\boldsymbol{k}g\sigma}u(\boldsymbol{k}) + c^\dagger_{\boldsymbol{k}e\sigma}v(\boldsymbol{k}) \tag{3.29}$$

and the quasiparticle spectrum

$$\mathcal{E}_\pm(\boldsymbol{k}, \tilde{V}, \mu_e) = \frac{\epsilon(\boldsymbol{k}) + \mu_e}{2} \pm \frac{1}{2}\sqrt{4V_{\mathrm{ex}}^2 \tilde{V}^2 + (\epsilon(\boldsymbol{k}) - \mu_e)^2}. \tag{3.30}$$

Here $\epsilon(\boldsymbol{k}) = -2J_g \sum_{i=1}^D \cos(k_i a)$ (a being the lattice spacing) is the tight-binding dispersion for the g atoms in a D-dimensional hyper-cubic lattice, and the two branches of the quasiparticle spectrum are called the upper and lower hybridized bands. If $\mathcal{N}$ is large then the energy per site of the translationally invariant system, given by $E(\tilde{V}, \mu_e, n_g) = \langle \mathcal{H}_\mathrm{T} \rangle / \mathcal{N}$, can be written as an integral over the Fermi volume $\mathcal{F}$. For example, on a D dimensional lattice with $n_g < 1$ the total energy per site is:

$$E(\tilde{V}, \mu_e, n_g) = -V_{\mathrm{ex}}\tilde{V}^2 - \mu_e + \frac{1}{(2\pi)^D} \int_{\mathcal{F}} d^D k \; \mathcal{E}_-(\boldsymbol{k}, \tilde{V}, \mu_e), \tag{3.31}$$

with the dependence on n_g hidden in the limits of integration. Only the lower hybridized band is populated because $n_g = 1$ corresponds to completely filling the first Brillouin zone (since there is also one localized atom per site). For $1 < n_g < 2$ the lower hybridized band will be completely full and the upper band will be partially integrated over. For a given n_g, the correct μ_e and self consistent $\tilde{V}$ can be found by solving the coupled equations

$$\frac{\partial E(\tilde{V}, \mu_e, n_g)}{\partial \tilde{V}} = 0 \;\; \text{and} \;\; \frac{\partial E(\tilde{V}, \mu_e, n_g)}{\partial \mu_e} = 0. \tag{3.32}$$

It will be useful for later application of the LDA to appreciate that the only knob we can turn to determine the MFT solutions (beyond the couplings J_g and V_{ex} in the Hamiltonian) is a choice of the g atom density. Once n_g is chosen, the correct $\tilde{V}$ and μ_e are fixed by Eq (3.32).

Defining the dimensionless coupling

$$v \equiv -2V_{\mathrm{ex}}/J_g, \tag{3.33}$$

one finds that for small v the hybridization $\tilde{V}$ will also be small. The two hybridized bands track the e and g atom bands closely, however mixing due to finite $\tilde{V}$ causes the crossing to be avoided
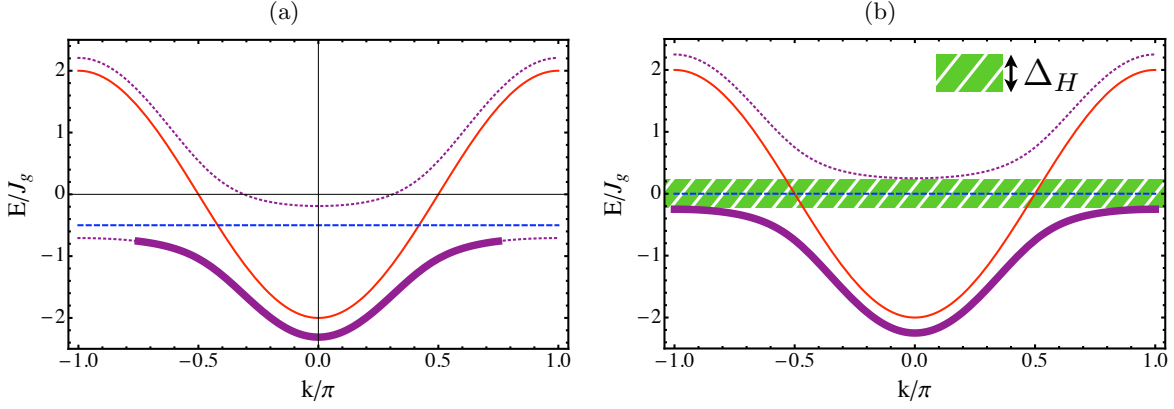
Figure 3.3: Spectrum of the translationally invariant MFT for $n_g < 1$ (a) and for $n_g = 1$ (b), shown in 1D for clarity. The blue dashed line is the e atom band ($E = \mu_e$), and the red solid curve is the g atom band ($E = -2J_g \cos(k)$). The purple dotted lines are the hybridized bands $\mathcal{E}_{\pm}$, with the thicker solid section covering the Fermi volume. In (b) the lower band is filled and separated from the upper band by the hybridization gap Δ_H (green slashed region), causing the system to be insulating for $n_g = 1$.

[Fig. (3.3)]. For less than unit filling of the g atoms, the ground state is obtained by filling the lower hybridized band with quasiparticles out to the Fermi surface ($k_F = \frac{\pi}{2}(1 + n_g)$ in 1D). The part of the lower hybridized band running nearly parallel to the line $E = \mu_e$ [blue line in Fig. 3.3(a)] holds most of the e atom weight, which indicates that for decreasing n_g we must pull μ_e down below the center of the g atom band in order to satisfy $n_e = 1$. This pins the Fermi surface to the flattened part of the hybridized band (called the Kondo resonance), which is the origin of the quasiparticle mass enhancement.

When $n_g = 1$ the lower hybridized band is completely full, and $\mu_e = 0$ because of a particle hole symmetry [169]. The system is an insulator with a gap Δ_H [Fig. 3.3(b)]. Despite having the appearance of a band gap in the MFT, this gap should be understood as arising from correlation effects: Filling the lower hybridized band means having one conduction atom per unit cell, so non-interacting band theory of the conduction atoms would predict a metallic state. From Eqs. (3.23) and (3.25) one can see that at $v = \infty$ and $\mu_e = 0$ we have $\tilde{V} = 1$. It then follows from Eq (3.30) that the MFT predicts $\Delta_\mathrm{H} \sim J_g v$ at strong coupling. At weak coupling, more careful analysis shows that the MFT predicts a non analytic gap scaling $\Delta_\mathrm{H} \sim J_g e^{-1/v}$. This weak coupling expression should

be understood as correct for v small but not less than some critical $v_c > 0$. The critical coupling v_c marks the phase transition between the heavy Fermi liquid and a (presumably) magnetically ordered phase, in which the MFT is not valid [see Fig. 3.2(b)].

It has been implicit in the discussion above that both the e and g atoms are to be included in the Fermi volume of the MFT ground state. However, one should keep in mind that the actual size of the Fermi surface is a subtle and important issue in the KLM [120, 169]. Looking at Eq. (3.20), one might expect the volume of the Fermi sea in any KLM ground state to be determined by the number of g atoms, since the e atoms represent localized spins with no charge degrees of freedom. However, the KLM at small v is an effective model for the Periodic Anderson Model at large U, for which Luttinger's theorem [117] is expected to hold [120] (meaning that the Fermi volume should be determined by the number of g and e atoms). These two scenarios are referred to respectively as a small and large Fermi surface. The heavy Fermi liquid ground state, which is described by our MFT, is known to have a large Fermi surface. The Kondo insulator is a cousin of the heavy Fermi liquid, which arises when the density of g atoms increases to unity, and the large Fermi surface of the heavy Fermi liquid completely fills the Brillouin zone. Our focus in this section is on the heavy Fermi liquid and Kondo insulator, largely because we believe it is likely that the heavy Fermi liquid and Kondo insulator phases will occupy a significant part of the paramagnetic region of the phase diagram [PM in Fig. 3.2(b)]. Indeed, on the square lattice that we consider the Kondo insulator is known to occur for $v \gtrsim 1.45$ (when $n_g = 1$) [7]. Given the close relationship between heavy Fermi liquid and Kondo insulator, the heavy Fermi liquid most likely *at least* exists nearby (i.e. for $v \gtrsim 1.45$ and $n_g \lesssim 1$).

3.3.2   Local-Density Approximation

The simplest way to extend the MFT to an inhomogeneous system is via the local density approximation (LDA). The idea is that on a given site, we consider the trapping potential to be a

chemical potential in a translationally invariant system with Hamiltonian

$$\mathcal{H}_{\mathrm{T}} - \mu_{jg} \sum_{i\sigma} c_{ig\sigma}^{\dagger} c_{ig\sigma}, \tag{3.34}$$

with $\mu_{jg} = \mu_g - \Omega(j)$. On physical grounds one might argue that the local chemical potential should be applied to the e atoms as well. However this is unnecessary; the e atom density is fixed to be one per site, so including the effect of the trap on them simply provides an overall constant energy shift (more technically, if it were applied to the localized atoms as well the local μ_{je} would simply readjust to absorb it). We now have one translationally invariant problem per lattice site, each of which can be solved as described in Section 3.3. There is a minor complication owing to the choice in Section 3.3 to work at fixed density, not fixed chemical potential. But this can be resolved easily by remembering that at zero temperature the chemical potential is the energy required to add one quasiparticle at the Fermi surface. Solving the translationally invariant model at fixed μ_{jg} simply means finding the n_{jg} satisfying

$$\frac{dE(\tilde{V}, \mu_e, n_{jg})}{dn_{jg}} = \mu_{jg}, \tag{3.35}$$

since the left hand side is the energy cost of adding one quasiparticle at the Fermi surface. The derivative on the left hand side can be expanded as

$$\frac{\partial E}{\partial \tilde{V}} \frac{d\tilde{V}}{dn_{jg}} + \frac{\partial E}{\partial \mu_e} \frac{d\mu_e}{dn_{jg}} + \frac{\partial E}{\partial n_{jg}}, \tag{3.36}$$

and the first two terms are zero for the MFT solution by Eq. (3.32). The last term is the change in the energy, at fixed $\tilde{V}$ and μ_e, due to the addition of a single quasiparticle at the Fermi surface, so we conclude that

$$\mu_{jg} = \mathcal{E}_{\pm}(\boldsymbol{k}_F(n_{jg}), \tilde{V}(n_{jg}), \mu_e(n_{jg})) \tag{3.37}$$

Here $\boldsymbol{k}_F$ is any vector falling along the Fermi surface consistent with the filling n_{jg}, and the $\pm$ means to choose the branch that yields a solution: there will only be one, since both branches are monotonic functions of n_g and they are separated by a gap. Solving Eq. (3.37) for n_{jg} on each lattice site, while adjusting μ_g to obtain the correct total number of particles, constitutes the LDA
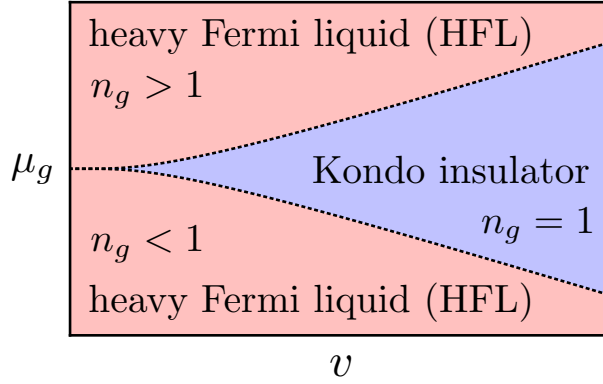
Figure 3.4: Schematic ground-state mean-field phase diagram of the KLM as a function of chemical potential μ_g and dimensionless coupling v. The black dotted lines are given by $\mu_g = \pm\Delta_{\mathrm{H}}/2$, which crosses over from Kondo like scaling ($\Delta_{\mathrm{H}} \sim J_g e^{-1/v}$) at small v to linear scaling ($\Delta_{\mathrm{H}} = J_g v$) at large v.

solution. The LDA gives us immediate access to many important groundstate properties, such as the real-space and momentum-space density distributions.

3.3.3 Real space g atom density distribution

In order to understand the qualitative features of trapped g atom density distributions it is helpful to plot the ground-state mean-field phase diagram in the $\mu_g - v$ plane [Fig. 3.4]. Moving from the outside of the g atom cloud towards the center of the trap corresponds to moving from the bottom to the top of the phase diagram along a line of fixed v. For sufficiently small N_g, we will reach the trap center before entering the region of Kondo insulator, and therefore we expect to be everywhere in the $n_g < 1$ heavy fermion metallic state. If, however, we choose N_g sufficiently large, we will breach the $n_g = 1$ Kondo insulator phase and a unit filling plateau should develop at the center of the trap. Increasing N_g further we will find that near the center of the trap we exit the Kondo insulator phase into the $n_g > 1$ heavy fermion metallic phase. This behavior is very similar to the Mott plateaus of the Hubbard model [18, 51], only here we have a Kondo insulator and not a Mott insulator. We also emphasize an unusual feature of the shell structure, that it exists in the density distribution of g atoms, which *do not interact with each other directly.*

In Fig. 3.5(a) we demonstrate such a plateau for a symmetric trap geometry $\Omega(i) = \Omega r^2$
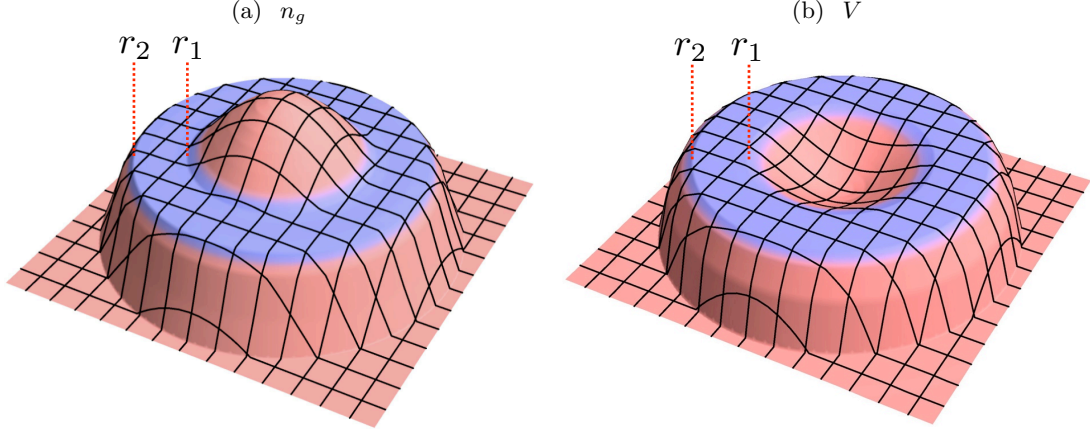
Figure 3.5: (a) The formation of a Kondo plateau between r_1 and r_2 at high trap fillings, obtained within LDA. (b) The hybridization also displays the plateau, but as the density increases past $n_g = 1$ the hybridization goes back down. In both (a) and (b) the parameters used are $N_g \approx 550$, $\Omega/J_g = 45/1000$, and $v = 8$.
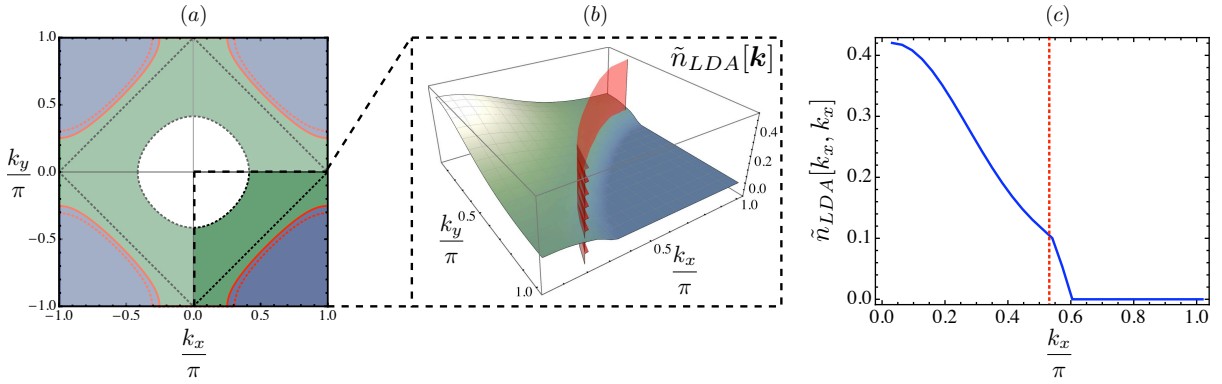
Figure 3.6: (a) The first Brillouin zone of a 2D square lattice. The central white region (within the dotted circle) is the small Fermi sea of the translationally invariant KLM with a conduction atom density $n_g \approx 0.19$. The shaded green region (within the solid red line) fills out the large Fermi sea (the red solid line is the large Fermi surface, as defined in Section 3.3.4). The red dotted line (just outside of the red solid line) is the large Fermi surface corresponding to a uniform filling equal to the density at the center of the trap. Even when there are no conduction atoms the large Fermi sea occupies half of the zone (within the dotted diamond), since there is still one localized atom per site contributing to the volume. (b) Quasi-momentum distribution of the conduction atoms plotted over one quadrant of the Brillouin zone, showing a prominent feature at the large Fermi surface (red ribbon). (c) A 1D cut along the line $k_y = k_x$ in (b), $\tilde{n}_{LDA}[k_x, k_x]$ is the blue solid line, and the large Fermi surface is the red dotted line. For all plots the parameters used are $N_g \approx 116$, $\Omega/J_g = 5/1000$, and $v = 8$.

(where r is the distance of site i from the origin, in lattice units). This result was obtained by

exploiting the rotational symmetry and solving a simpler 1D problem in the radial coordinate r. We are still solving Eq (3.37), but now instead of μ_{jg} we use $\mu_{rg} = \mu_g - \Omega r^2$, and we rotate the solution around the axis of cylindrical symmetry to obtain the plot in Fig. 3.5(a). Of course for this to work the g atom cloud radius must be relatively large in lattice units, otherwise the lack of rotational symmetry of the lattice itself would be relevant. The plateau also shows up in the hybridization profile [Fig. 3.5(b)], however near the center of the trap the hybridization dips back down. Physically this occurs because for $n_g > 1$ some g atoms are forced to pair with each other into singlets, reducing the number available to hybridize with the localized atoms.

Defining $r_{1(2)}$ to be the interior (exterior) radius of the plateau, it is clear from the argument used to link Fig. 3.4 to Fig. 3.5 that $\Omega \left(r_2^2 - r_1^2 \right) = \Delta_{\mathrm{H}}$. More generally, in an exact treatment of the KLM the LDA solution will predict $\Omega \left(r_2^2 - r_1^2 \right) = 2\Delta_{\mathrm{qp}}$, where Δ_{qp}, called the quasiparticle gap, is the difference in energy between the unit-filled ground state and the lowest energy state with one g atom added or removed (these are both the same because of particle hole symmetry) [169]. Physically this result reflects the LDA assumption that transfer of density from one site to another does not affect the energy to first order ($dE(n_{jg})/dn_{jg} + \Omega(j) = \mu_g$ is constant across the trap). Therefore the energy needed to add a quasiparticle at r_1 ($\Delta_{\mathrm{qp}} - \mu_g + \Omega r_1^2$) must be opposite to the energy needed to remove one at r_2 ($\Delta_{\mathrm{qp}} + \mu_g - \Omega r_2^2$), giving $\Omega \left(r_2^2 - r_1^2 \right) = 2\Delta_{\mathrm{qp}}$.

At strong coupling, where the plateau is most visible, the exact quasiparticle gap of the KLM can be calculated by considering a single site (due to the relatively small hopping) [169]. If on one site we have $n_g = n_e = 1$ initially, adding or subtracting a g atom costs $(3/4)J_g v = \Delta_{\mathrm{qp}}$. Therefore we can be certain that for large v the plateau size should satisfy $\Omega(r_2^2 - r_1^2) = (3/2)J_g v$. In this limit $\Delta_{\mathrm{H}} = J_g v$, so the MFT underestimates the size of the plateau in the strong-coupling limit.

3.3.4 g atom quasi-momentum distributions

At mean-field level a large Fermi surface arrises by assumption: By assigning a nonzero value to the hybridization matrix element $\tilde{V}$, the e atoms are liberated into the Fermi sea. This is well known, and proves nothing about the Fermi surface in the actual KLM ground state. However,

as an example of how the structure of the large Fermi surface survives in the trap, we proceed to calculate the quasi-momentum distribution in the LDA [64]. In the translationally invariant MFT, there is a unique g atom quasi-momentum distribution

$$\tilde{n}[\boldsymbol{k}, n_g] = f[\boldsymbol{k}, n_g]\,|u(\boldsymbol{k})|^2 \tag{3.38}$$

associated with every possible filling n_g, where $f[\boldsymbol{k}, n_g]$ is the zero temperature Fermi function for non-interacting electrons at a filling $1 + n_g$. The LDA approximation to the quasi-momentum distribution is then obtained by summing $\tilde{n}$ over the densities on each lattice site

$$\tilde{n}_{LDA}[\boldsymbol{k}] = \sum_j \tilde{n}[\boldsymbol{k}, n_{jg}], \tag{3.39}$$

where the n_{jg} are calculated as discussed in the previous section.

The existence of the trap introduces an unavoidable ambiguity in the definition of the small and large Fermi surfaces, since the filling is affected by what one chooses as the system size (i.e. should the sites outside of the g atom cloud be included?). However we find it reasonable, for the sake of comparison, to choose the system size to be defined by the diameter of the g atom cloud. Then the trap can be considered as a perturbation on the translationally invariant system that is sufficiently small as to not force the density to zero anywhere. The large Fermi surface then belongs to a translationally invariant system of this size containing the same number of conduction atoms as there are in the trap. Applying this definition to ~ 116 conduction atoms in the symmetric trap of Section 3.3.3 (this time with $\Omega = 5J_g/1000$), we plot the large Fermi surface as a solid red line in Fig. 3.6(a). In Fig. 3.6(b) we plot the quasi-momentum distribution $\tilde{n}_{LDA}[\boldsymbol{k}]$ for the trapped system alongside the large Fermi surface of the translationally invariant system.

It is worth appreciating that the large Fermi surface actually survives smearing by the trap better than it would for free fermions. This is in part because in the averaging over the trap only Fermi surfaces between the black and red dotted lines of Fig. 3.6(a) contribute (for free fermions the averaging would contain arbitrarily small Fermi surfaces). Another reason is that, as we approach the edge of the conduction atom cloud and the local Fermi surface recedes toward the line $|k_x| + |k_y| = \pi$, the height of the discontinuity also decreases to zero.

3.4   Self-Consistent Diagonalization

In order to probe mass enhancement in the heavy fermion state we would like to study dynamics of the conduction atom cloud in response to a trap displacement. This type of dynamics has been shown to be an excellent diagnostic tool for strongly correlated systems in experiments using bosonic as well as fermionic atoms [48, 163, 123]. At mean-field level this requires us to know the self-consistent ground state; we must move beyond the LDA and self-consistently diagonalize $\mathcal{H}_{\mathrm{M}}$. Analytic progress is made difficult by the necessity to maintain site dependent hybridizations, and we proceed numerically. We start by making an initial guess for the $\tilde{V}_i$ and μ_{ie} using LDA. We then diagonalize $\mathcal{H}_{\mathrm{M}}$ numerically, calculate new $\tilde{V}_i$ from Eq. (3.22), and repeat until the $\tilde{V}_i$ converge to a self consistent value. This process is complicated by the need to repeatedly determine the μ_{ie} that satisfy the constraint of one e atom per site on average (these will change every time the $\tilde{V}_i$ are updated). A discussion of the procedure we use to determine the correct μ_{ie} can be found in Appendix C.

To simplify the numerics, we consider a geometry where the potential changes only in the *longitudinal* direction (length aL_l and g atom hopping J_l), while the *transverse* direction (length aL_t and g atom hopping J_t) is homogenous with periodic boundary conditions. The motivation for this unusual geometry is to retain a number of constraint equations equal to the longitudinal length, thereby accessing relatively large system sizes (up to ~ 1000 sites is reasonable). Adopting a notation $c^{\dagger}_{mn\alpha\sigma}$ for the creation operators, where m labels the site in the longitudinal direction and n labels the site in the transverse direction, we define partially Fourier decomposed operators

$$c^{\dagger}_{mk\alpha\sigma} = \frac{1}{\sqrt{L_t}} \sum_n e^{-ikn} c^{\dagger}_{mn\alpha\sigma}. \tag{3.40}$$

Rewriting the nonconstant part of the mea- field Hamiltonian [Eq. (3.23)] in terms of these new operators, it decouples into the sum of L_t effectively 1D Hamiltonians, which we label by the

transverse quasi-momentum $k \in \left\{ \frac{2\pi}{L_t a}, ..., \frac{2\pi}{a} \right\}$:

$$
\begin{aligned}
\mathcal{H}_{\mathrm{M}} &= \sum_k \mathcal{H}_k \\
\mathcal{H}_k &= -J_l \sum_{\langle i,j \rangle \sigma} c_{ikg\sigma}^\dagger c_{jkg\sigma} + V_{\mathrm{ex}} \sum_{i\sigma} \tilde{V}_i \left(c_{ikg\sigma}^\dagger c_{ike\sigma} \right. \\
&+ \left. c_{ike\sigma}^\dagger c_{ikg\sigma} - \tilde{V}_i/2 \right) + \sum_{i\sigma} (\mu_{ie} - 1) c_{ike\sigma}^\dagger c_{ike\sigma} \\
&+ \sum_{i\sigma} \left(-2J_t \cos(ka) + \Omega i^2 \right) c_{ikg\sigma}^\dagger c_{ikg\sigma}.
\end{aligned}
\tag{3.41}
$$

One can give a simple physical interpretation to these new Hamiltonians: the energy gained by a g atom dispersing with quasi-momentum k in the transverse direction $[2J_t \cos(ka)]$ has been incorporated as a chemical potential in a 1D model describing hopping in the longitudinal direction. The eigenstates are created by quasiparticle operators

$$
\alpha_{qk\sigma}^\dagger = \sum_i \left(u_{qk}^i c_{ikg\sigma}^\dagger + v_{qk}^i c_{ike\sigma}^\dagger \right).
\tag{3.42}
$$

Similar to Eq. (3.24), here $q \in \{1, 2, ...\}$ is an index labeling the eigenstates in order of increasing energy (for a given k). Unless the transverse bandwidth is smaller than the level spacing of the harmonic potential $(4J_t < 2\sqrt{\Omega J_l})$, the different k modes cannot be expected to have the same occupation numbers, which leads us to define k-dependent Fermi levels q_F^k. For a given k, q_F^k is the smallest q for which the mode labeled by q and k is unoccupied. The ground state is

$$
|\Psi\rangle = \prod_{k\sigma} \prod_{q < q_F^k} \alpha_{qk\sigma}^\dagger |0\rangle,
\tag{3.43}
$$

and the expectation value in Eq. (3.22) becomes

$$
\tilde{V}_i = \sum_k \sum_{q < q_F^k} (u_{qk}^i \bar{v}_{qk}^i + \bar{u}_{qk}^i v_{qk}^i).
\tag{3.44}
$$

3.5   Dynamics

3.5.1   Single particle dynamics in a trap

Before introducing dynamics in the MFT, we briefly mention some important details of single-particle dynamics in a lattice plus harmonic potential [144, 134, 83, 145]. If there are no

interactions, the trapping potential is parabolic with curvature Ω, and we work in 1D for simplicity, then the g atoms are described by the Hamiltonian

$$\mathcal{H}_0 = -J_g \sum_{\langle i,j \rangle, \sigma} c_{ig\sigma}^\dagger c_{jg\sigma} + \Omega \sum_{i\sigma} i^2 c_{ig\sigma}^\dagger c_{ig\sigma}. \tag{3.45}$$

A single particle eigenstate $|\psi_\sigma^n\rangle = \sum_i \psi_i^n c_{ig\sigma}^\dagger |0\rangle$ has coefficients ψ_i^n given by the Fourier components of periodic Mathieu functions, with the corresponding eigenvalue E_n determined by the function's characteristic parameter [144]. The solutions are complicated, but in certain limits they have a very simple form. We will exclusively consider the limit where $q \equiv 4J_g/\Omega \gg 1$. Then $1/\sqrt{q}$ is a natural small parameter for expanding both the eigenfunctions and eigenvalues, and to lowest non-trivial order one obtains:

$$\psi_i^n \sim \sqrt{\frac{\sqrt{2}}{2^n n! \, (q\pi^2)^{1/4}}} \exp\left(-\frac{\xi^2}{2}\right) H_n(\xi)$$

$$E^n \sim \frac{\Omega}{4}\left(-2q + 4\sqrt{q}\left[n + \frac{1}{2}\right] - \frac{(2n+1)^2 + 1}{8}\right), \tag{3.46}$$

where $\xi \equiv i\,(4/q)^{1/4}$ and H_n are Hermite polynomials. In this approximation the expectation value for the center of mass (COM) of the ground state, evolving due to a small displacement δ (measured in lattice units), can be obtained in closed form (the motion of excited states is similar but slightly complicated by various combinatorial factors):

$$\langle X(t) \rangle = \delta \exp\left[-\frac{\delta^2}{x^2}\sin\left(\frac{\Omega t}{8\hbar}\right)^2\right] \times$$

$$\cos\left[\left(\omega^* - \frac{\Omega}{4\hbar}\right)t - \frac{\delta^2}{2x^2}\sin\left(\frac{\Omega t}{4\hbar}\right)\right]. \tag{3.47}$$

In the above $x \equiv (q/4)^{1/4}$ is a characteristic oscillator length (in lattice units) and $\omega^* \equiv \Omega\sqrt{q}/\hbar$ is the characteristic frequency. It is interesting to note that there is periodic (non-dissipative) damping of the oscillation amplitude. In the absence of the lattice this damping would be forbidden by the generalized Kohn theorem [101], according to which COM oscillations in a harmonic potential should be undamped under fairly general conditions.

It is important for our purpose in what follows to observe that the tunneling matrix element is inversely proportional to the lattice-effective mass $m^* = (2J_g a^2/\hbar^2)^{-1}$. Therefore, the effective

oscillator period (at which, for sufficiently large q, all low lying single particle modes oscillate) is related to the mass as $\tau^* = \frac{2\pi}{\omega^*} \sim \sqrt{m^*}$. In what follows, we take the periodicity ($\tilde{\tau}$) of oscillations to define the effective mass for the interacting system ($\tilde{m}$): $\tilde{m}/m^* = (\tilde{\tau}/\tau^*)^2$.

3.5.2 Dynamics in 1D

In 1D, there are two limits in which dynamics can be calculated exactly: (1) $v = \infty$, where the model can be mapped onto free fermions, and (2) the extreme dilute limit, in particular $N_g = 1$. For a finite system, the results for a single conduction electron can be applied for at weak coupling even for $N_g > 1$, as we discuss below.

3.5.2.1 Strong coupling

When $v = \infty$ the ground state is formed by pairing each g atom into a spin singlet with one e atom. For $n_g < 1$, the singlets become mobile at first order in J_g, and there is an exact mapping of the unpaired e atoms to the fermions of a $U = \infty$ Hubbard model (the singlets are the holes) [108]. Because nearest neighbor hopping cannot exchange up and down spins, we can think of the fermions as spinless [128], perform a particle hole transformation (now the singlets are the spinless fermions), and thereby arrive at a simple Hamiltonian describing the g atoms:

$$\mathcal{H}_\infty = -\frac{J_g}{2} \sum_{\langle i,j \rangle} c_{ig}^\dagger c_{jg} + \Omega \sum_i i^2 n_{ig}. \tag{3.48}$$

The reduction of the hopping energy is the result of projecting out the high energy triplet states. To highlight this strong coupling behavior, we again consider dynamics ensuing from a sudden displacement of the trap center. If the system is strongly interacting, Eq. (3.48) avails a simple treatment of these dynamics based on the non-interacting solutions in Ref. [144]. There the authors found that for $q \gg 1$ and $N_g \lesssim 4\sqrt{2J_g/\Omega}$ the dynamics involved *delocalized*, free space harmonic oscillator like states with level spacing $\omega^* = \Omega\sqrt{q}$. At $v = \infty$ we effectively have $N_g \to 2N_g$ (because the fermions become spinless) and $J_g \to J_g/2$, therefore the inequality can be violated at strong coupling even when satisfied for the non-interacting system; *localized* states become populated, and
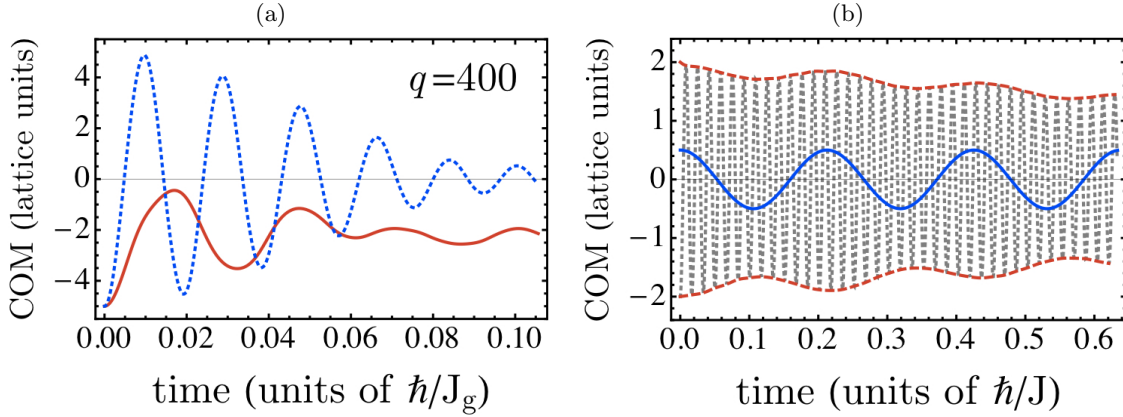
Figure 3.7: (a) The blue line shows non interacting dynamics of 16 g atoms after displacement of the trap by 5 lattice sites. The red line shows the same dynamics except now with $v = \infty$ (calculated using $\mathcal{H}_\infty$). (b) ($q = 800, v = 0.02$) Polaron COM (grey solid line) oscillating after trap displacement by 2 lattice sites. For comparison we plot $\cos(V_{ex}t)$ (blue solid line), showing that the energy gap determines the time scale of amplitude modulation. The overall decay is a finite size effect, and eventually revives.

transport is strongly inhibited [Fig. 3.7(a)].

3.5.2.2   Weak coupling

Another limit which is well understood in the FM phase of the translationally invariant model is $N_g = 1$. Sigrist et al. [155] proved that the ground state of the KLM with L sites and one conduction electron has total spin $S = \frac{1}{2}(L-1)$ even in the absence of translational symmetry, and they described the excitations for the homogenous case as bound states between the g atom and a flipped spin in the deep lattice (spin polaron). For a weak trap ($q \gg 1$) and at sufficiently small coupling ($V_{ex} \ll \omega^*$), we characterize the polaron spectrum to lowest order in degenerate perturbation theory and find that one eigenvalue separates from the rest by a gap of approximately $|V_{ex}|$. As seen in Fig. 3.7(b), this energy scale is manifest in the COM oscillations of a single g atom as strong modulation of the oscillation amplitude with periodicity $\tau \approx \frac{2\pi}{|V_{ex}|}$, as verified by dynamics calculated from the exact eigenstates.

For the finite system under consideration, we expect this behavior will persist for $N_g > 1$ whenever N_g is odd. This can be seen by noting that a single unpaired g atom at the Fermi

level gains energy at first order in perturbation theory when coupling to the e atoms is turned on, whereas the doubly occupied levels below it do so only at second order. It is worth noting that the condition $V_{ex} \ll \omega^*$ is equivalent to demanding the perturbation stay smaller than the finite size gap. For fixed lattice depth and peak g atom density, the gap scaling is $\omega^* \sim 1/R$, with R the Thomas Fermi radius of the g atom cloud ($R \propto \sqrt{N_g J_g/\omega^*}$). This means that the demonstrated modulations will be washed out with increasing $|V_{ex}|$ or with increasing g atom number, and are manifestly a finite size effect.

3.5.3   MFT dynamics

In D$>$ 1, we study dynamics in mean-field theory with the intention of capturing the mass enhancement of the heavy Fermi liquid phase. Once we have solved for the MFT groundstate, calculating dynamics is relatively straightforward. One can easily write down a time dependent Schrödinger equation for the mode coefficients. Just as $\psi_q(x) \to \psi_q(x,t)$ in continuum quantum mechanics, here we have a discrete analogy $u_{qk}^j \to u_{qk}^j(t)$, and likewise for the v_{qk}^j. The time dependent discrete Schrödinger Eq. reads

$$
\begin{aligned}
-i\hbar \frac{du_{qk}^j}{dt} &= J_l\left(u_{qk}^{j-1} + u_{qk}^{j+1}\right) - \Omega\,(j-\delta)^2\,u_{qk}^j \\
&\quad + 2J_t\left[\cos(ka)\right]u_{qk}^j - V_{ex}\tilde{V}_j v_{qk}^j \\
-i\hbar \frac{dv_{qk}^j}{dt} &= -\Omega\,(j-\delta)^2\,v_{qk}^j - \mu_{je}v_{qk}^j - V_{ex}\tilde{V}_j u_{qk}^j.
\end{aligned}
\tag{3.49}
$$

Eq (3.49) can be obtained formally by considering the coefficients in Eq (3.42) to carry the time dependence and then solving the Heisenberg equations of motion for the quasiparticles

$$
\hbar \frac{d}{dt}\alpha_{qk\sigma}^\dagger = i\left[\mathcal{H}_k^\delta, \alpha_{qk\sigma}^\dagger\right]
\tag{3.50}
$$

($\mathcal{H}_k^\delta$ being a shift of $\mathcal{H}_k$ by δ lattice sites).

There is one subtlety in the time evolution: although the exact KLM Hamiltonian has a local U(1) symmetry to conserve the e atom density distribution, the MFT we have used does not: the occupation of the localized band will certainly evolve in time, which we cannot allow. The

solution is to let the chemical potentials be time dependent.[5] It is easy to check that the first time derivative of the e atom density does not depend on the chemical potentials, and hence the constraints $dn_{ie}/dt = 0$ cannot determine the μ_{ie}. Instead they must be chosen to satisfy the second order constraints $d^2 n_{ie}/dt^2 = 0$. It follows directly from Eqs. (3.49) that $dn_{ie}/dt = 0$ initially, since all the mode coefficients can be chosen to be real. Keeping the second derivative zero at all times means the first derivative does not change; it will always be zero and the local constraints will be obeyed. To find an explicit formula for the chemical potentials we first express the constraints in terms of the mode coefficients:

$$\frac{d^2}{dt^2} n_{ie} = 2 \sum_k \sum_{q < q_F^k} \left(\ddot{v}_{qk}^i \bar{v}_{qk}^i + v_{qk}^i \ddot{\bar{v}}_{qk}^i + 2 \dot{v}_{qk}^i \dot{\bar{v}}_{qk}^i \right). \tag{3.51}$$

Using the Schrödinger equation to evaluate the time derivatives in Eq. (3.51), some algebra leads to:

$$\mu_{ie} = \frac{-2 V_{\mathrm{ex}} \Re\left[d_i\right]^2 (c_i - f_i) - J_l \Re\left[d_i\left(a_i + b_i\right)\right] + \Re\left[d_i x_i\right]}{\Re\left[d_i\right]^2 - \Im\left[d_i\right]^2}, \tag{3.52}$$

where $\Re$ and $\Im$ are the real and imaginary parts respectively. The latin letters are defined as:

$a_i = \frac{1}{L_t} \sum' \bar{v}_{qk}^i u_{qk}^{i-1}$	$b_i = \frac{1}{L_t} \sum' \bar{v}_{qk}^i u_{qk}^{i+1}$
$d_i = \frac{1}{L_t} \sum' \bar{v}_{qk}^i u_{qk}^i$	$f_i = \frac{1}{L_t} \sum' \bar{v}_{qk}^i v_{qk}^i$
$c_i = \frac{1}{L_t} \sum' \bar{u}_{qk}^i u_{qk}^i$	$x_i = -\frac{2 J_t}{L_t} \sum' \bar{v}_{qk}^i u_{qk}^i \cos(ka)$

where $\sum' \equiv \sum_k \sum_{q < q_F^k}$.

Using Eq. (3.44) and (3.52) to write the $\tilde{V}_i$ and μ_{ie} in terms of the mode coefficients reduces Eq (3.49) to a system of $4 L_t L_l^2$ coupled first order differential equations, which can be integrated with standard methods. We calculate the dynamics resulting from displacement of the trap by one lattice site for fixed J_l, J_t, and Ω at several different values of V_{ex}, and extract the period of

---

[5] The time dependence of the chemical potentials can be traced back to the choice to make the hybridizations real [Eq. (3.22)], and amounts formally to a choice of gauge. See Ref. [141] for a detailed discussion of gauge symmetry in the mean-field theory we are using.
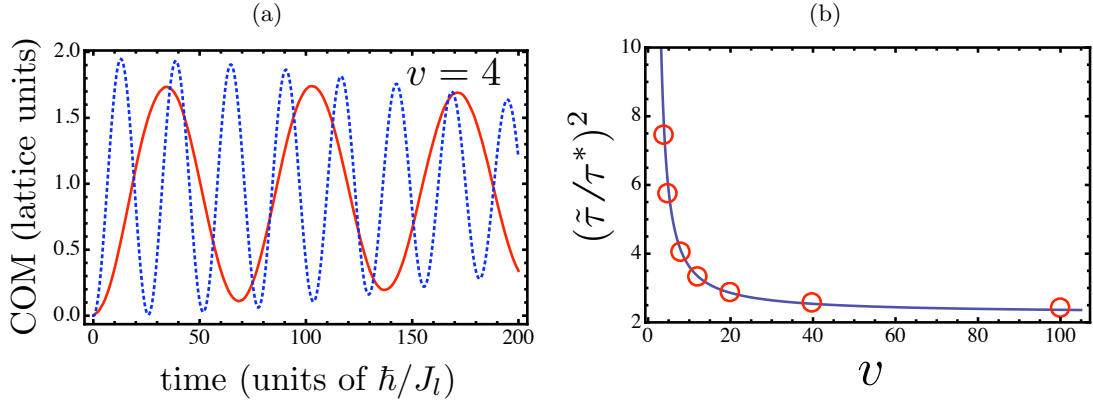
Figure 3.8: (a) Here we plot the time evolution of the COM after displacement of the trap by one lattice site (red line). The blue dashed line is the noninteracting dynamics for comparison. The parameters used in this plot are $q = 235$, $v = 4$, $L_t = 8$, $N_g = 40$, and $J_l/J_t = 2$. (b) The effective mass scales like $\tilde{m}/m^* \sim (\tilde{\tau}/\tau^*)^2$ (see the vertical axis): by extracting the period of oscillation from several traces like the one in (a) at several different values of v we find significant enhancement of the effective mass as $v \rightsquigarrow 1$. The red circles are from self-consistent diagonalization of the MFT, and the blue line is a guide to the eye.

COM oscillations (see Fig. 3.8). Since $\tilde{m}/m^* = (\tilde{\tau}/\tau^*)^2$, Fig. 3.8(b) demonstrates the emergence

of heavy quasiparticles as we decrease v.

In the thermodynamic limit of the translationally invariant MFT, the density-of-states effec-

tive mass truly diverges as $v \to 0$. This divergence is not physical, because for sufficiently small

v RKKY interactions lead to the development of magnetic order, at which point the paramag-

netic MFT is no longer valid [40]. In the trap, however, the effective mass does not diverge in

the small v limit, even within the MFT. This follows from the discreteness of the spectrum in the

non-interacting theory; when the hybridization energy $\tilde{V}V_{\mathrm{ex}}$ becomes smaller than the energy spac-

ing, it cannot significantly change the system properties. Instead, as we decrease v the relatively

fast free particle oscillations emerge on top of the slow quasiparticle oscillations. Eventually, the

dynamics converges to that of the noninteracting system, as shown in Fig. 3.9.
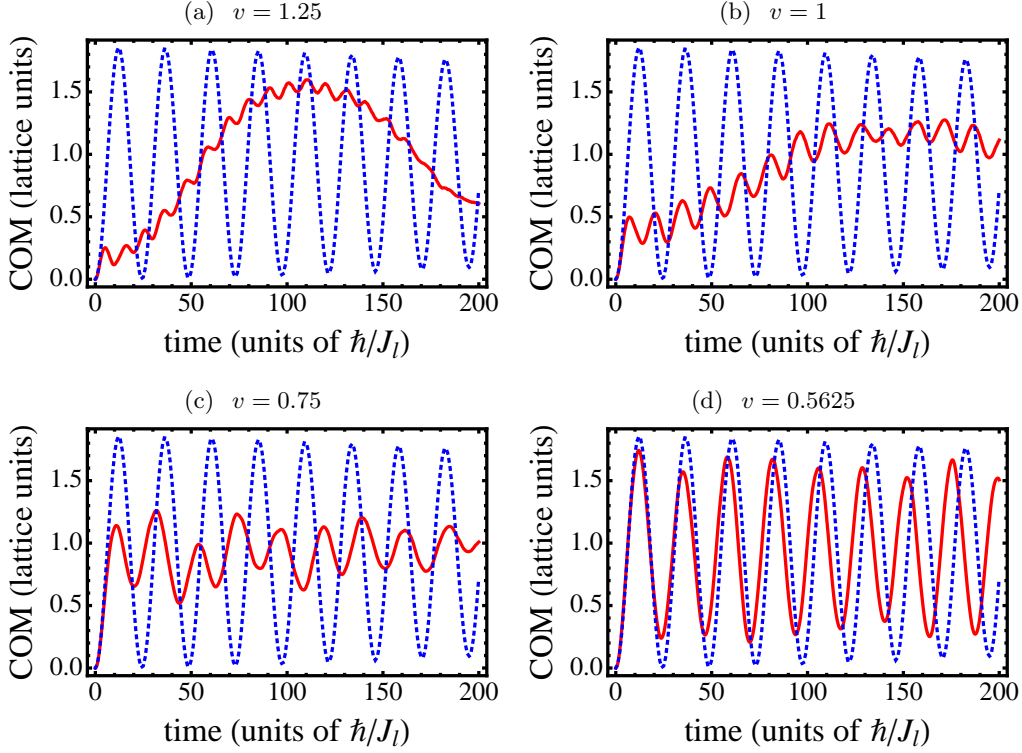
Figure 3.9: COM oscillations for decreasing values of v, showing how the fast free-particle dynamics emerge on top of the slow quasiparticle dynamics. The red solid line is from MFT dynamics, and the blue dotted line is the noninteracting solution. The parameters used in this plot are $q = 235$, $L_t = 1$, $N_g = 6$, and $J_l/J_t = 2$.

3.6   Experimental Considerations and Outlook

In order to obtain the heavy fermion metallic groundstate, it is necessary to prepare a Mott insulator of e atoms coexisting with a dilute cloud of g atoms. To realize the SU(2) symmetry of the KLM under consideration only two hyperfine states should be initially populated. In consideration of the lossy nature of e-e scattering, the starting point we envision is a Mott insulator of g atoms with doubly occupied sites in the center of the trap. Such a configuration can be obtained by making the lattice for g atoms sufficiently deep and the parabolic trap sufficiently tight. The deep lattice for the e atoms is unoccupied but already established. Taking advantage of the mean-field energy shift associated with double occupied sites, it is in principle possible to make the transfer $|gg\rangle \rightarrow (|eg\rangle + |ge\rangle)/\sqrt{2}$ with high efficiency. The sites occupied by a single g atom (at the edge of

the trap) can also be addressed independently, transferring the atoms on them into the e lattice. If the g lattice is adiabatically lowered, we are left with the configuration desired. For sufficiently large v this procedure can also yield a unit filling plateau at the trap center (the Kondo insulator), but to observe the second layer in the shell structure discussed in Section 3.3.3 (which has 3 atoms per site in the center of the trap, 1 e and 2 g), the trap should be adiabatically tightened until $n_g > 1$ at the trap center.

The observation of dipole oscillations over a small number of lattice sites ($\lesssim 8$) has precedent in several experiments done with alkali-metal atoms [48, 163]. Usually the COM velocity of the cloud as a function of time is measured directly by TOF imaging, and the COM position is inferred from simple kinematics. There are also promising proposals to measure the COM expectation value in a non-destructive and precise manner by coupling the atomic motion to unpumped cavity modes [131] (the COM motion is inferred indirectly by its relationship to measurable quadratures of the photon field.)

For the above mentioned experiments to be feasible, it is important that the requisite temperatures are within the reach of current technology. In real metals heavy fermion behavior develops only below the Kondo temperature $T_K \sim J_g e^{-1/v}$. For $v \ll 1$, which is always the case in heavy fermion metals, the exponential suppression guarantees that T_K is always well below the Fermi temperature of the non-interacting conduction electrons, and that the mass enhancement (which scales as T_K^{-1}) is extremely large. However one should not think of the smallness of T_K as being fundamental to heavy fermion behavior, but simply as the result of the bare parameters ($v \ll 1$) which happen to exist in real metals. A larger Kondo temperature can always be obtained by choosing a larger v, at the cost of reducing the mass enhancement. By artificially creating the KLM in an optical lattice and choosing $v \sim 1$ the Kondo temperature could be estimated as $T_K \sim J_g \sim V_{\text{ex}}$. Therefore the temperature need only be smaller than the interaction energy, which is a much better situation than one encounters in proposals to observe super-exchange or RKKY type physics.

Chapter 4

A bosonic Kondo lattice model with alkali atoms

4.1   Introduction

In this chapter we will revisit a version of the KLM first proposed in Ref. [42], in which the electrons are replaced by spin-$\frac{1}{2}$ bosons, with the spin degree of freedom encoded in two hyperfine states of an alkali atom. There are primarily two reasons for doing so: (1) experiments with bosonic alkali atoms are in many ways the most advanced of all ultracold atom experiments, and the technologies involved in cooling and manipulating these atoms are the best developed. (2) As we will see, obtaining an antiferromagnetic Kondo-like interaction using repulsively interacting alkali atoms (being repulsive makes them stable against collapse or pairing) with only two internal degrees of freedom demands that we use repulsively interacting bosons. Moreover, by using bosons we might hope to retain some remnants of Kondo-like physics in a situation where calculations are more tractable than for fermions.

Our primary new finding is that, for any small but nonzero Kondo coupling, the typically continuous superfluid (SF) to Mott insulator (MI) phase transition becomes first-order. The qualitative difference between the pure Hubbard and Kondo-Hubbard model, even at arbitrarily weak Kondo coupling, is reminiscent of similar results for the Fermi Kondo-Hubbard model obtained in Ref. [7]. That the inclusion of small inter-band interactions (which are often relevant in real materials) can have such a dramatic effect on the Bose Hubbard phase diagram underscores the importance of generalizing optical lattice simulations to include orbital degrees of freedom.

The structure of this chapter is as follows. The experimental implementation of the Bose

Kondo-Hubbard model is discussed in Sec. 4.2. This section deviates from the original proposal [42] in that we emphasize the essential role of lattice non-separability in obtaining the model in more than one spatial dimension. We begin our investigation of the model's phase diagram in Sec. 4.3, where we derive effective spin Hamiltonians valid in the weak coupling (Sec. 4.3.1) and strong coupling (Sec. 4.3.2) limits in order to understand the magnetic properties of the SF and MI phases. We then employ an analytic treatment of Gutzwiller mean-field theory (MFT) in Sec. 4.4 to map out the ground state phase diagram. At mean-field level, one can observe the interplay of two competing tendencies: Superfluidity of the conduction bosons tends to spontaneously break SU(2) symmetry, whereas the Kondo interaction prefers a rotationally symmetric ground state composed of localized singlets. While the rigidity of the superfluid protects it from magnetic fluctuations, we will see that these fluctuations give rise to a metastable MI of Kondo singlets, causing the MI to SF transition to become first-order. Such a first-order transition has been realized—and confirmed by Quantum Monte Carlo—in the spin-$\frac{1}{2}$ boson model of Ref. [34]. In Sec. 4.5.1 we consider experimental details related to dynamically maintaining a two-band model. In particular we discuss the implementation of the model, and the relevant parameter regimes, using the non-separable lattice of Ref. [153]. In Sec. 4.5.2 we discuss the preparation of the unit-filled MI phase. We then suggest the possibility of experimentally observing the first-order transition by ramping down the lattice to enter the SF regime; due to the discontinuous nature of the phase transition, even an arbitrarily slow ramp should excite collapses and revivals of the superfluid order parameter. In Sec. 4.6 we summarize our findings and their relevance.

4.2   The model

Everything that follows assumes a three dimensional (3D) optical lattice $\mathcal{I}(\boldsymbol{r}) + \mathcal{I}_z(z)$ populated by bosonic alkali atoms with mass m and s-wave scattering length a_s. Here $\boldsymbol{r} = \{x, y\}$ is a vector living in the x-y plane. The model itself will be *two dimensional* (2D), which can be achieved by choosing $\mathcal{I}_z(z)$ to be sufficiently deep (to freeze out tunneling in the z-direction), and loading every atom into a Wannier orbital $w_0^z(z)$ of the lowest band of $\mathcal{I}_z$. With the exception

of the integral $\chi \equiv \int dz\, w_0^z(z)^4$, which will appear in the interaction matrix elements below, we will from now on ignore the existence of the z-direction completely. We assume that all atoms are initially in the $F = 1$ hyperfine manifold and have $m_f = \pm 1$, in which case two colliding atoms can have total $F = 0, 2$ ($F = 1$ is not allowed for s-wave interacting bosons because it implies a wavefunction that is antisymmetric under particle exchange). In ^{87}Rb, the similarity of scattering lengths for total spin $F = 0$ and $F = 2$ collisions (denoted $a_0 \approx a_2 \equiv a_s$), together with the ability to offset the $m_F = 0$ state via the quadratic Zeeman effect [2, 81], strongly suppresses spin changing collisions into the $m_F = 0$ state. This justifies considering only two internal states ($m_F = \pm 1$) for times long after the initial preparation, and we label these two internal (spin) degrees of freedom by $\sigma = \uparrow, \downarrow$. At sufficiently low temperatures, the full interatomic potential can be replaced with an s-wave pseudopotential [47, 85] $V_s(\boldsymbol{r}_{\mathrm{rel}}) = \delta(\boldsymbol{r}_{\mathrm{rel}})4\pi a_s \hbar^2/m$, where $\delta(\boldsymbol{r}_{\mathrm{rel}})$ is the 3D delta function and $\boldsymbol{r}_{\mathrm{rel}}$ is the (3D) relative vector between two colliding atoms.[1]   Neglecting nearest neighbor interactions, but for the time being making no approximations for the band degree of freedom α, the Hamiltonian describing this system is

$$\mathcal{H} = \sum_{ij\alpha\sigma} J_{\alpha ij}\alpha_{i\sigma}^\dagger \alpha_{j\sigma} + \sum_{j\alpha} \frac{U_\alpha}{2}\hat{n}_{j\alpha}(\hat{n}_{j\alpha} - 1) + \sum_{j,\alpha>\beta} V_{\alpha\beta}\hat{n}_{j\alpha}\hat{n}_{j\beta} \tag{4.1}$$

$$+ \sum_{j,\alpha>\beta,\sigma\sigma'} V_{\alpha\beta}\alpha_{j\sigma}^\dagger \beta_{j\sigma'}^\dagger \alpha_{j\sigma'}\beta_{j\sigma} + \sum_{j,\{\alpha,\beta\}\neq\{\gamma,\delta\}} W_{\alpha\beta\gamma\delta}\alpha_{j\sigma}^\dagger \beta_{j\sigma'}^\dagger \gamma_{j\sigma'}\delta_{j\sigma}. \tag{4.2}$$

In general there should also be a term accounting for the mean band-energies. However, in consideration of the forthcoming approximation that there are no band changing collisions, which will render such terms conserved quantities, we ignore them from the outset. In Eq. (4.1), $\alpha_{j\sigma}^\dagger$ creates a spin-σ boson in a Wannier orbital $w_\alpha(\boldsymbol{r} - \boldsymbol{r}_j)$ belonging to the αth band of $\mathcal{I}(\boldsymbol{r})$, located on the lattice site centered at $\boldsymbol{r}_j$. The density operator for bosons on site j in the αth band is

---

[1] In general, the pseudopotential should be regularized and the scattering length should depend on momentum. The regularization can be disregarded when treating the interaction in first-order perturbation theory, which is valid for any lattice model truncated to bands in which the single-particle wave functions oscillate on a length scale l_{sp} that is large compared to the scattering length a_s (which is certainly the case for ^{87}Rb in the first several bands of an optical lattice). The momentum dependence can be ignored whenever the effective range of the true interatomic potential is much smaller than l_{sp} [13], which is also an excellent approximation.

$\hat{n}_{j\alpha} = \sum_\sigma a^\dagger_{j\sigma} a_{j\sigma}$, and the various parameters are given by

$$
\begin{aligned}
J_{\alpha ij} &= \int d^2 \boldsymbol{r} \, w_\alpha(\boldsymbol{r} - \boldsymbol{r}_i) \left[\mathcal{I}(\boldsymbol{r}) - \frac{\hbar^2 \nabla^2}{2m} \right] w_\alpha(\boldsymbol{r} - \boldsymbol{r}_j) \\
U_\alpha &= \frac{4\pi \hbar^2 a_s \chi}{m} \int d^2 \boldsymbol{r} \, w_\alpha(\boldsymbol{r})^4 \\
V_{\alpha\beta} &= \frac{4\pi \hbar^2 a_s \chi}{m} \int d^2 \boldsymbol{r} \, w_\alpha(\boldsymbol{r})^2 w_\beta(\boldsymbol{r})^2 \\
W_{\alpha\beta\gamma\delta} &= \frac{2\pi \hbar^2 a_s \chi}{m} \int d^2 \boldsymbol{r} \, w_\alpha(\boldsymbol{r}) w_\beta(\boldsymbol{r}) w_\gamma(\boldsymbol{r}) w_\delta(\boldsymbol{r}).
\end{aligned}
\tag{4.3}
$$

The notation $\{\alpha, \beta\} \neq \{\gamma, \delta\}$ means that these two sets of indices cannot contain identical elements, and is introduced so that the final term in $\mathcal{H}$ contains all (and only) scattering processes that change the band populations on a given site. The hoppings $J_{\alpha ij}$ are so far unspecified; in order to obtain a 2D model, we only require that, for a given α, all such hoppings emanating from one site to its nearest neighbors are similar in magnitude. To set the overall scale of kinetic energy we define the effective hopping strength $J_\alpha = \frac{1}{4} \sum_i |J_{\alpha ij}|,^2$ which does not depend on the site index j.

We further restrict our attention to an initial state with one atom per site in the lowest vibrational band (b band, or localized band) of $\mathcal{I}(\boldsymbol{r})$, and an average of n atoms per site in a single excited band (a band, or conduction band). The assumption that these conditions will be maintained dynamically, a necessary condition for obtaining a bosonic Kondo model, amounts to disregarding all of the $W_{\alpha\beta\gamma\delta}$ terms in Eq. (4.1). In previous works [86, 125, 157], such an approximation has been justified largely by the restricted density of states in an optical lattice. Very roughly, the argument is that when interactions are small compared to typical band gaps, and if the bands themselves are narrow, then band changing collisions tend to be off resonant and strongly suppressed. Here we point out a notable exception to the validity of this reasoning, which to our knowledge has not been previously described in the literature. This exception affects the implementation of the Kondo-Hubbard model, and also of the multi-flavor models described in Ref. [86].

For a lattice that can be written $\mathcal{I}(\boldsymbol{r}) = \mathcal{I}_x(x) + \mathcal{I}_y(y)$, a Wannier orbital in the a band

---

[2] The factor of $\frac{1}{4}$ is so that J_α agrees with the usual hopping integral in the case of nearest neighbor hopping on an isotropic square lattice.
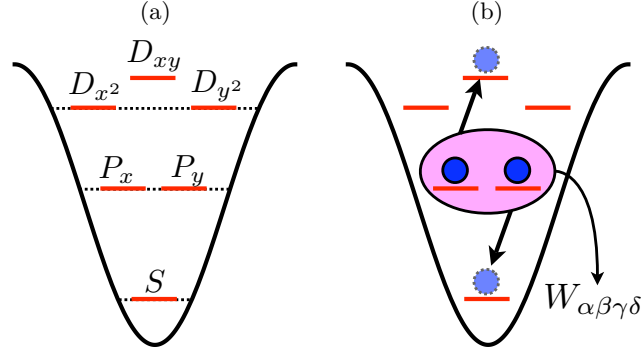
Figure 4.1: In (a) we plot an energy level diagram for states $|00\rangle$ (S band), $|10\rangle$ (P_x band), $|01\rangle$ (P_y band), $|20\rangle$ (D_{x^2} band), $|02\rangle$ (D_{y^2} band), and $|11\rangle$ (D_{xy} band). The resonant scattering process (due to the $W_{\alpha\beta\gamma\delta}$ terms in $\mathcal{H}$) that transfers atoms from the initially populated S and D_{xy} bands into the P_x and P_y bands is shown in (b).

can be written $w_a(\boldsymbol{r}) = w_{a_x}^x(x)w_{a_y}^y(y)$, whereas a Wannier orbital in the b band can be written $w_b(\boldsymbol{r}) = w_0^x(x)w_0^y(y)$. To have a 2D model, it must be true that hopping in both the x and y directions is greater in the conduction band than in the localized band, and hence $a_x, a_y > 0$. Because of the separability of the non-interacting part of the Hamiltonian in the x-y basis, the state $|00\rangle \otimes |a_x a_y\rangle$ [describing a single site with one atom in $w_0^x(x)w_0^y(y)$ and one atom in $w_{a_x}^x(x)w_{a_y}^y(y)$] is, even in the presence of interactions, *exactly* degenerate with the state $|0a_y\rangle \otimes |a_x 0\rangle$. Furthermore, these states are connected by the interaction term W with a matrix element equal to twice the exchange integral V between the conduction and localized orbitals (see Appendix D). The situation is depicted graphically in Fig. 4.1 for the case where $a_x = a_y = 1$, and the states $|00\rangle$, $|10\rangle$, $|01\rangle$, and $|11\rangle$ belong to the S, P_x, P_y, and D_{xy} bands respectively. The P_x and P_y bands will be populated via collisions on a timescale $\tau = \pi/V$; this is unacceptable, since τ will turn out to be the timescale for singlet formation, and one can't expect to see Kondo like physics if the approximations yielding the model break down so quickly. The way around this problem is to use an optical lattice potential which cannot be separated in cartesian coordinates. In section 4.5.2 we will give an example of an existing non-separable lattice which is favorable for avoiding this problem, but for the time being we continue with the approximation that the $W_{\alpha\beta\gamma\delta}$ can be ignored.

If the atoms in the b band are deep in the unit-filled MI regime, and we drop terms that are

therefore constant, then $\mathcal{H}$ can be reduced to a bosonic Kondo-Hubbard model [42]

$$
\begin{aligned}
\mathcal{H}_{\mathrm{K}} &= -\sum_{ij\sigma} J_{ij} a_{i\sigma}^{\dagger} a_{j\sigma} + \frac{U}{2} \sum_{j} \hat{n}_{ja} (\hat{n}_{ja} - 1) \\
&+ 2V \sum_{j} \boldsymbol{S}_{ja} \cdot \boldsymbol{S}_{jb} - \mu \sum_{j} \hat{n}_{ja}.
\end{aligned}
\tag{4.4}
$$

In Eq. (4.4) a chemical potential has been included to facilitate the forthcoming mean-field treatment, and the spin operators are defined by $\boldsymbol{S}_{j\alpha} \equiv \frac{1}{2} \sum_{\sigma\sigma'} \alpha_{j\sigma}^{\dagger} \boldsymbol{\tau}_{\sigma\sigma'} \alpha_{j\sigma'}$, with $\boldsymbol{\tau}$ being a vector whose components are the Pauli matrices. In order to avoid a clutter of indices, we have defined $V \equiv V_{ab}$, $J_{ij} \equiv J_{ija}$ (and $J \equiv J_a$), and $U \equiv U_a$. Because V has the same sign as a_s, the Kondo interaction is antiferromagnetic (AFM) for repulsive interactions, which is a manifestation of Hund's rule adapted for bosons: Antisymmetrization of the spin wave function for two identical bosons requires the antisymmetrization of their spatial wave function, thus keeping them apart and lowering the energy cost of repulsive interactions.

4.3 Effective spin models

In the presence of the Kondo term, one still expects the conduction bosons to undergo a MI to SF phase transition at unit filling ($n = 1$) as the ratio U/J is varied. However, the magnetic properties of these phases will be heavily influenced. The goal of this section is to study magnetic ordering in the SF and MI phases by deriving effective spin Hamiltonians that are accurate in either the weak coupling or strong coupling limits. The results presented are meant to reinforce and complement the mean-field picture that will subsequently be developed.

4.3.1 Weak coupling

In the fermionic KLM at $V = 0$, the localized spins are decoupled from the conduction electrons, giving rise to a large spin degeneracy in the ground state manifold. The lifting of this degeneracy is the result of virtual excitations of the conduction electrons from below to above the Fermi-surface, which mediate long ranged couplings between the localized spins known as the Rudderman-Kittel-Kasuya-Yosida (RKKY) interaction [146, 93, 176]. In dimensions greater than

one, the RKKY interaction is believed to stabilize long-range magnetic order in the KLM ground state [93]. The primary difference in the bosonic model is that the $V = 0$ spin degeneracy extends to the conduction band, where the ferromagnetic superfluid can point in any direction. Surprisingly, this additional freedom actually simplifies the situation; the degeneracy will now be lifted at first (rather than second) order in V, and at this order the effective Hamiltonian can be solved exactly.

Although we are not considering the presence of a confining potential in this chapter, in order to preserve the greatest generality in the ensuing discussion we will state our results in terms of arbitrary single particle eigenstates $\psi_r(j)$ and eigenvalues ϵ_r for a lattice plus trap. At $V, U = 0$, the ground state is formed by putting all conduction bosons in the single particle wavefunction $\psi_0(j)$ and has a degeneracy of $(N_a + 1) \times 2^\mathcal{N}$, where $\mathcal{N}$ is the number of lattice sites (also the number of b atoms), and N_a is the number of a atoms. It is useful to define the functions $\mathcal{G}_{jl}^r = \psi_r^*(j)\psi_r(l)$, in terms of which the spin density operator for a conduction boson in the single particle groundstate is

$$\boldsymbol{S}_a^0 = \frac{1}{2} \sum_{jl} \mathcal{G}_{jl}^0 \sum_{\sigma\sigma'} a_{j\sigma}^\dagger \boldsymbol{\tau}_{\sigma\sigma'} a_{l\sigma'}. \tag{4.5}$$

Projection of $\mathcal{H}_\mathrm{K}$ onto the degenerate groundstate manifold yields an effective weak coupling Hamiltonian that is first order in the Kondo coupling V

$$\mathcal{H}_\mathrm{wc}^{(1)} = 2V \boldsymbol{S}_a^0 \cdot \sum_j \mathcal{G}_{jj}^0 \boldsymbol{S}_{jb}. \tag{4.6}$$

The first order energy shift due to U has been dropped because it does not lift the spin degeneracy. Equation (4.6) describes the so-called *central spin model*, which is familiar in the context of electron spin decoherence in quantum dots [95]. In the application to quantum dots, the model describes coupling between the spin of an electron in the dot and the nuclear spins of the atomic lattice in which the dot sits, with a coupling function determined by the square of the electron's wavefunction. In the present case, the condensate atoms are Schwinger bosons representing the central spin $\boldsymbol{S}_a^0$, which couples to the mutually non-interacting localized spins with a coupling function given by the square of the condensate wavefunction. The central spin model has been studied extensively in the literature, and exact solutions have been obtained by Bethe ansatz [63]. However, for a

translationally invariant system $\mathcal{H}_{\text{wc}}^{(1)}$ can easily be diagonalized by rewriting it in terms of the conserved quantities s_b, s_a, and s, where s_α is the total spin quantum number of $\boldsymbol{S}_\alpha = \sum_j \boldsymbol{S}_{j\alpha}$, and s is the total spin quantum number of the combine spin $\boldsymbol{S}_a + \boldsymbol{S}_b$. The ground state is formed when the localized spins align fully ferromagnetically ($s_b = \mathcal{N}/2$), and then their total spin $\boldsymbol{S}_b$ couples as antiferromagnetically as possible to the condensate spin $\boldsymbol{S}_a$ ($s = \frac{\mathcal{N}}{2}|n - 1|$).

Second-order perturbation theory in the Kondo exchange generates a correction to the weak coupling Hamiltonian

$$
\begin{aligned}
\mathcal{H}_{\text{wc}}^{(2)} &= -n\mathcal{N}V^2 \sum_{j,l} \mathcal{R}_{jl} \boldsymbol{S}_{jb} \cdot \boldsymbol{S}_{lb} \\
&+ 2V^2 \boldsymbol{S}_a \cdot \sum_j \mathcal{R}_{jj} \boldsymbol{S}_{jb},
\end{aligned}
\tag{4.7}
$$

where $\mathcal{R}_{jl} = \sum_r \mathcal{G}_{jl}^r \mathcal{G}_{lj}^0(\varepsilon_r)^{-1}$ [see Appendix E for a derivation of Eq. (4.7)]. The first term in Eq. 4.7 is the bosonic analog of the RKKY interaction for fermions, and has the same physical origin; a spin at site j scatters an a atom out of the condensate, which then re-enters the condensate upon scattering off the spin at site l, and in this way the two spins talk to each other. The second term, which renormalizes the spin couplings of $\mathcal{H}_{\text{wc}}^{(1)}$, reflects the ability of the scattered boson to return to the condensate with its spin flipped. Such a term is absent for fermions because Pauli exclusion principle prevents a conduction fermion from returning to the Fermi sea with its spin flipped.[3] Unlike the RKKY term this correction is local in space, a property that can be attributed to the cancellation of time reversed scattering processes involving more than one localized spin (the sign for such a scattering process depends on whether the spin flip occurs when the conduction atom is exiting or returning to the condensate).

Although the first term has the same physical origin as RKKY for fermions, an important difference arises due to the structure of the coupling function. In the fermionic case, the Fermi surface introduces a length scale k_F^{-1}, at which the long-range coupling oscillates. For noninteracting bosons there is no such length scale, the coupling function $\mathcal{R}$ does not oscillate, and one can show that it is strictly positive at any finite separation for a translationally invariant system in

---

[3] This is strictly true in the thermodynamic limit. For a finite fermionic system an intensive central spin like term exists whenever the number of conduction fermions is odd.

the thermodynamic limit. Thus any groundstate of $\mathcal{H}_{\mathrm{wc}}^{(1)}$ automatically minimizes $\mathcal{H}_{\mathrm{wc}}^{(2)}$, and the polarization of the localized spins persists to second order in V (note also that the renormalization of the central spin coupling constants by the second term in $\mathcal{H}_{\mathrm{wc}}^{(2)}$ is toward larger positive values). It should be noted, however, that $\mathcal{N}\mathcal{R}_{jj}$ diverges logarithmically with the system size in 2D, suggesting that the energy cannot actually be expanded in powers of V. Nevertheless, the existence of exclusively ferromagnetic (FM) terms in the first two orders of perturbation theory strongly suggests a FM ground state at weak coupling. We note that at unit filling, the true groundstate of $\mathcal{H}_{\mathrm{wc}}$ is a singlet ($s = 0$), but nevertheless the superfluid and the localized spins are aligned ferromagnetically within themselves ($s_a = s_b = \frac{\mathcal{N}}{2}$). That $s_b = \frac{\mathcal{N}}{2}$ means that all off-diagonal elements of the correlation function

$$\chi_{jl} = \langle \boldsymbol{S}_{jb} \cdot \boldsymbol{S}_{lb} \rangle \tag{4.8}$$

obtain the maximum value of $\frac{1}{4}$. Hence when we say that the $n = 1$ superfluid phase is FM, we mean that ferromagnetism exists independently within the superfluid and within the localized spins.

4.3.2   Strong coupling

We will take the strong coupling limit to be defined by $U \gg J$, for any V, and for simplicity we will restrict our discussion to the case of commensurate filling in the conduction band. However, we will see that a similar limit arrises for $V \gg J$ and any U when the a atoms are at unit filling. For integer $n \geq 1$ the ground state is a MI with n conduction bosons per site. The eigenstates on a single site follow from the addition of angular momenta $\boldsymbol{S}_{ja} + \boldsymbol{S}_{jb} \equiv \boldsymbol{S}_j$, and therefore have total spin quantum number $s_j^{\pm} = (n \pm 1)/2$. Because the interaction is AFM, the eigenstate with lower total spin is the ground state, and the MI phase with density n must have total spin $(n-1)/2$ at each site. If on a single site we label the state by its total spin quantum number s_j and the z projection of total spin s_j^z, then the n filling MI at $J = 0$ is given by

$$|\mathrm{MI}_n\rangle = \bigotimes_j |(n-1)/2, s_j^z\rangle, \tag{4.9}$$

and it has energy per site $E_n = \frac{U}{2}n(n-1) - \frac{V}{2}(2+n)$. For $n = 1$ each site contains a singlet $|0,0\rangle_j$, spin excitations are gapped ($\Delta_s = 2V$), and the ground state is PM. We also note that for unit filling the charge gap is $\Delta_c = U + V$, and does not vanish as $U \to 0$. Hence the unit-filled MI exists whenever either U or V is large compared to J.

States with $n \geq 2$ can be obtained from the singlet by repeated application of the a atom creation operators:

$$|s_j^-, s_j^z\rangle \propto (a_{j\uparrow}^\dagger)^{s_j^- + s_j^z}(a_{j\downarrow}^\dagger)^{s_j^- - s_j^z}|0,0\rangle_j. \tag{4.10}$$

It is interesting to note that for a MI phase with $n \geq 2$ the charge gap is given by $\Delta_c = U$, and has no dependence on V. Therefore the limit $V \gg J$ alone does not yield a MI in this case. Because the states $|s_j^-, s_j^z\rangle$ are degenerate ($s_j^z = -s_j^-, ..., s_j^-$), it is possible to derive an effective super-exchange Hamiltonian between the total spins on neighboring sites by perturbation theory in the hoppings J_{ij}. The calculation—though complicated by the existence of virtual excited states with two possible total spin quantum numbers—is straightforward, and yields an effective Hamiltonian that only contains the *total spin operators* $\boldsymbol{S}_j$

$$\mathcal{H}_{\rm sc} = -g(n) \sum_{ij} \frac{J_{ij}^2}{U} \boldsymbol{S}_i \cdot \boldsymbol{S}_j. \tag{4.11}$$

In Eq. (4.11),

$$g(n) = \frac{4n+8}{(n+1)^2} \left(\frac{V(n+1)^2 + U(n+2)^2}{Vn+U} \right) \tag{4.12}$$

is a strictly positive, density dependent coupling constant, and we have dropped an overall density dependent energy shift. The ground state is therefore FM with total spin $\frac{N}{2}(n-1)$, and, unlike for the $n = 1$ MI, there is no spin gap. Notice that this result for the total spin also holds for the weak coupling case, although the nature of the FM state is completely different in the two limits. While the inter-site spin correlations between the localized spins are maximized at weak coupling, in the strong-coupling limit we find the diminished correlation $\chi_{jl} = \frac{1}{4}(\frac{n-1}{n+1})^2$, which vanishes when $n = 1$.
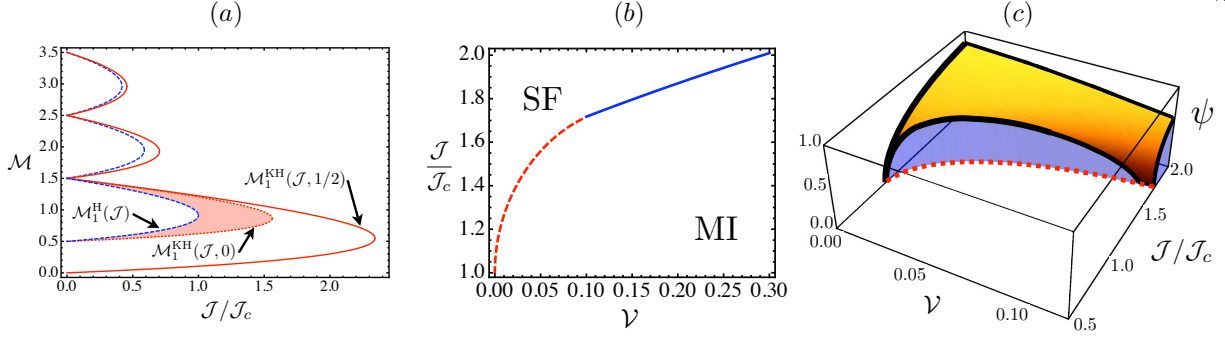
Figure 4.2: (a) Mott lobes in the $\mathcal{M} - \mathcal{J}$ plane, with $\mathcal{J}$ plotted in units of $\mathcal{J}_c = (3 + \sqrt{8})^{-1}$, which is where the single band mean-field transition occurs at unit filling. The red solid lines depict the boundaries of Mott lobes for $V = U/2$, given by $\mathcal{M}_n^{\text{KH}}(\mathcal{J}, 1/2)$. The blue dashed lines are the boundaries of Mott lobes for the single band boson Hubbard model, denoted $\mathcal{M}_n^{\text{H}}(\mathcal{J})$. These have been shifted up by $\mathcal{V} = 1/2$ along the $\mathcal{M}$-axis in order to more easily compare their widths with those of the Kondo-Hubbard lobes. The red dotted line is the boundary $\mathcal{M}_1^{\text{KH}}(\mathcal{J}, 0)$, which does not agree with $\mathcal{M}_n^{\text{H}}(\mathcal{J})$. In Fig. 4.2(b) we plot the phase boundary of the $n = 1$ MI in the $\mathcal{J}$-$\mathcal{V}$ plane. The solid blue line demarks a continuos transition, while the red dotted line demarks a first-order transition. Fig. 4.2(c) shows the superfluid order parameter ψ in the $\mathcal{J}$-$\mathcal{V}$ plane, showing the discontinuity along the first-order portion of the phase transition.

4.4   Mean Field Theory

As was shown by a numerical analysis of the Gutzwiller variational ansatz in Ref. [42], in the presence of the localized spins the a atoms continue to exhibit a MI to SF phase transition at commensurate filling. Here we adopt an alternate but equivalent description of the Gutzwiller variational ansatz as a site-decoupled mean-field theory (MFT) [50], and obtain an analytical description of the phase transition. The motivation for this mean-field treatment is that (1) it semi-quantitatively describes the MI to SF phase transition of bosons in $D > 1$ and (2) the new features of the present model—the Kondo term—are entirely local, and thus are included without further approximation.

The starting point of Gutzwiller mean-field theory is the decoupling of the kinetic energy term

$$a_{i\sigma}^\dagger a_{j\sigma} \rightarrow \langle a_{i\sigma}^\dagger \rangle a_{j\sigma} + a_{i\sigma}^\dagger \langle a_{j\sigma} \rangle - \langle a_{i\sigma}^\dagger \rangle \langle a_{j\sigma} \rangle \tag{4.13}$$

Assuming that the mean-field order parameter $\psi_\sigma = \langle a_{j\sigma} \rangle$ is translationally invariant, and defining

$\mathcal{J} = 4J/U$, $\mathcal{V} = V/U$, and $\mathcal{M} = \mu/U$, we can rewrite the exact Hamiltonian $\mathcal{H}_{\mathrm{K}}$ as a sum over identical Hamiltonians defined at each site (any one of which we call the mean-field Hamiltonian):

$$
\begin{aligned}
\mathcal{H}_{\mathrm{GA}} &= -\mathcal{J} \sum_{\sigma} (\psi_\sigma a_\sigma^\dagger + \psi_\sigma^* a_\sigma) + \mathcal{J} \sum_{\sigma} \psi_\sigma^* \psi_\sigma \\
&+ \frac{1}{2} \hat{n}_a (\hat{n}_a - 1) + 2\mathcal{V} \boldsymbol{S}_a \cdot \boldsymbol{S}_b - \mathcal{M} \hat{n}_a.
\end{aligned}
\tag{4.14}
$$

The mean-field ground state is obtained by minimizing $E_{\mathrm{GA}}(\psi_\sigma) \equiv \langle \mathcal{H}_{\mathrm{GA}} \rangle$ with respect to ψ_σ. The order parameter describes the formation of superfluid coherence; if ψ_σ is finite, then by virtue of having to point somewhere it describes a state that spontaneously breaks SU(2) symmetry, as the superfluid should. On the other hand, $\psi_\sigma = 0$ is the signature of a Mott insulator phase, in which number fluctuations are suppressed and phase coherence vanishes. Because $\mathcal{H}_{\mathrm{GA}}$ is invariant under the U(1) gauge transformations $a_\sigma, \psi_\sigma \to e^{i\theta_\sigma} a_\sigma, e^{i\theta_\sigma} \psi_\sigma$, we are justified to choose both components of our spinor order parameter to be real. Physically, this choice amounts to confining any superfluid that arrises to live in the $x - z$ plane, since the y component of the (vector) superfluid density

$$
\boldsymbol{\rho} = \sum_{\sigma\sigma'} \psi_\sigma^* \boldsymbol{\tau}_{\sigma\sigma'} \psi_{\sigma'}
\tag{4.15}
$$

vanishes when $\psi_\sigma^* = \psi_\sigma$. It should be understood in what follows that this apparent broken symmetry is an artifact maintained for simplicity.

The mean-field Hamiltonian can easily be solved numerically by truncating the single-site Hilbert space to contain no more than some finite number of a atoms. However, much insight can be gained by proceeding as far as possible analytically. If one makes the assumption that the SF to MI transition is continuous, then the mean-field phase boundary is described exactly by perturbation theory in ψ_σ. We want to emphasize from the beginning that this assumption will later be shown to break down in certain parameter regimes. Nevertheless, with this assumption in mind one writes the mean-field energy as

$$
E_{\mathrm{GA}} = \mathcal{A}(\mathcal{J}, \mathcal{V}, \mathcal{M}) + \mathcal{B}(\mathcal{J}, \mathcal{V}, \mathcal{M})\psi^2 + \mathcal{O}(\psi^4),
\tag{4.16}
$$

where $\psi^2 \equiv \sum_\sigma \psi_\sigma^2$ is the superfluid density, and the phase boundary is determined by the condition $\mathcal{B} = 0$. That E_{GA} can be written as an even function of ψ follows from the symmetries of $\mathcal{H}_{\mathrm{GA}}$.

For a Mott lobe of filling n, the groundstate at finite $\mathcal{V}$ is in general degenerate (see Sec. 4.3.2), and $\mathcal{B}$ must be found by calculating the lowest eigenvalue of the effective Hamiltonian

$$\mathcal{H}_{\text{eff}} = \mathcal{J}^2 \sum_{n\sigma\sigma'} \psi_\sigma \psi_{\sigma'} \frac{(a_\sigma^\dagger + a_\sigma)|n\rangle\langle n|(a_{\sigma'}^\dagger + a_{\sigma'})}{E_0 - E_n}. \tag{4.17}$$

When $n = 1$ the MI ground state is unique (the singlet), and while degenerate perturbation theory is unnecessary it is not wrong (we simply end up finding the eigenvalue of a 1×1 matrix, which is of course its only entry). Some algebra reveals that the above effective Hamiltonian can be rewritten in the following sensible form

$$\mathcal{H}_{\text{eff}} = \mathcal{J}^2 c_1(\mathcal{V}, \mathcal{M}, n)\rho - \mathcal{J}^2 c_2(\mathcal{V}, \mathcal{M}, n)\boldsymbol{\rho} \cdot \boldsymbol{S}, \tag{4.18}$$

where $\boldsymbol{S} = \boldsymbol{S}_a + \boldsymbol{S}_b$, the coefficients c_1 and c_2 (obtained by straightforward by tedious algebra) are given by

$$c_1 = \frac{1}{2n} \left(\frac{n^2 + 2n}{\mathcal{M} - \mathcal{V} - n} - \frac{n^2 - 1}{1 + \mathcal{M} - \mathcal{V} - n} - \frac{1}{1 + \mathcal{M} - \mathcal{V} + \mathcal{V}n - n} \right) \tag{4.19}$$

$$c_2 = \frac{-1}{n^2 + n} \left(\frac{n^2 + 2n}{\mathcal{M} - \mathcal{V} - n} - \frac{(n+1)^2}{1 + \mathcal{M} - \mathcal{V} - n} + \frac{1}{1 + \mathcal{M} - \mathcal{V} + \mathcal{V}n - n} \right), \tag{4.20}$$

and the vector superfluid density $\boldsymbol{\rho}$ acts as a magnetic field. It is not hard to show that c_2 is strictly positive,[4] and as a result minimization of $\mathcal{H}_{\text{eff}}$ is achieved when $\boldsymbol{S}$ points along the magnetic field. This result makes perfect sense, since it amounts to self consistency in the direction of the order parameter. Because the quantum number of total spin in the unperturbed groundstate is $s = (n-1)/2$, we find

$$\mathcal{B}(n) = \mathcal{J}^2 \left(\frac{1}{\mathcal{J}} + c_1(\mathcal{V}, \mathcal{M}, n) - c_2(\mathcal{V}, \mathcal{M}, n)\frac{n-1}{2} \right). \tag{4.21}$$

$\mathcal{B}(n) = 0$ determines the boundary of the n-filling Mott lobe, which we will denote by $\mathcal{M}_n^{\text{KH}}(\mathcal{J}, \mathcal{V})$. The first three lobes are shown in Fig. 4.2(a). Notice that the width of the $n = 1$ MI is increased (from 1 to $1 + \mathcal{V}$ along the $\mathcal{M}$ axis), while the widths of the higher filling lobes are unaffected. The reason for this goes back to the discussion in Sec. 4.3.2, where we pointed out that the charge gap is given by $\Delta_{\text{c}} = U(1 + \mathcal{V})$ for the $n = 1$ MI and by $\Delta_{\text{c}} = U$ for an $n \geq 2$ MI.

---

[4] For a given $n > 1$, the Mott lobe is bounded below by $\mathcal{V} + n - 1$ and above by $\mathcal{V} + n$, and it is within these constraints that the coefficient c_2 is strictly positive.
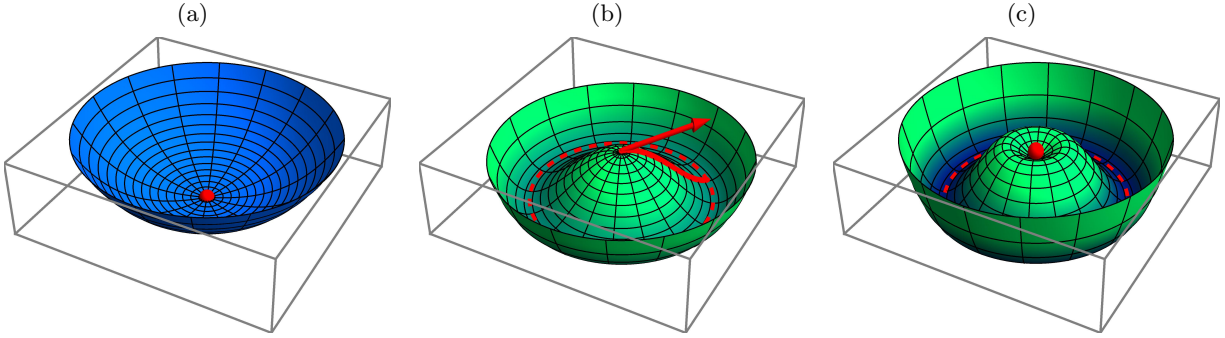
Figure 4.3: Schematic illustration of the mean-field energy, demonstrating the mechanism that drives the SF to MI phase transition first-order. (a) and (b) show the two forms that E_{GA} can take when $\mathcal{V} = 0$, (a) in the MI phase and (b) in the SF phase, with the order parameter spontaneously breaking SU(2) symmetry by choosing a particular direction. In (c) we show a possible scenario for a small nonzero $\mathcal{V}$. The superfluid is weakly affected (being rigid against spin fluctuations), but when the order parameter is small magnetic fluctuations are allowed, reducing the energy and causing the formation of a metastable MI phase.

At this point we are in a position to see that something is wrong with the phase boundaries as they have been presented so far [the solid red lines in Fig. 4.2(a)]. Explicit calculation yields the boundaries at zero Kondo coupling

$$2\mathcal{M}_n^{\mathrm{KH}}(\mathcal{J}, 0) = 2n - 1 - \mathcal{J} \pm \sqrt{(\mathcal{J} - 1)^2 - 4\mathcal{J}n - \frac{4J}{n+1}} \tag{4.22}$$

whereas the mean-field phase boundaries for the single-band Bose Hubbard model are given by

$$2\mathcal{M}_n^{\mathrm{H}}(\mathcal{J}) = 2n - 1 - \mathcal{J} \pm \sqrt{(\mathcal{J} - 1)^2 - 4\mathcal{J}n}, \tag{4.23}$$

which only agree at $\mathcal{J} = 0$. But the conduction bosons of the Kondo-Hubbard model certainly *are* governed by the single band Bose Hubbard model at $\mathcal{V} = 0$, since they don't talk to the localized spins. What has gone wrong? The problem is that Eq. (4.22) was derived by assuming that the mean-field ground state in the MI phase has $s = (n-1)/2$, which is true whenever $\mathcal{V} > 0$. However, there are also the excited spin states with $s = (n+1)/2$, separated from the ground state manifold by $\Delta_n = \mathcal{V}(n+1)$, which have been ignored. Formally, such a procedure is correct for any finite $\mathcal{V}$, so long as $\mathcal{J}\psi \ll \Delta_n$ is satisfied. As $\mathcal{V} \to 0$, the range of validity shrinks, until eventually at $\mathcal{V} = 0$ the perturbative results break down for any finite ψ.

Once this issue is understood, it becomes clear that the phase transition must in fact be first-order, and the argument is as follows. If we sit somewhere in the red shaded region of Fig. 4.2(a), at $\mathcal{V} = 0$ the system is a superfluid (since we are outside of the dashed blue line, which *is* correct at $\mathcal{V} = 0$), and so E_{GA} looks like it does in Fig. 4.3(b). Now as we turn on small but finite $\mathcal{V}$, a local minimum of the energy *must* immediately develop at $\psi = 0$ [see Fig. 4.3(c)], since perturbation theory has a finite range of validity in ψ and predicts $\mathcal{B} > 0$ [a Mott insulator, see the red dotted curve in Fig. 4.2(a)]. As $\mathcal{V}$ becomes larger, the range of validity for the perturbative result Eq. (4.22) increases, until eventually the $\psi = 0$ minimum must be the global minimum; at this point there is a first-order transition into a Mott insulator of Kondo singlets. Notice that the first-order transition is not tied to the development of a cubic term in the energy, as is often the case, but rather results from the negative contributions of even powers of ψ beyond ψ^2. By numerically solving the mean-field Hamiltonian we can obtain the first-order phase boundaries, defined by where the metastable MI and the superfluid become degenerate. The boundary for the first Mott lobe is shown in Fig. 4.2(b), whereas the discontinuous jump in the order parameter across this boundary is shown in Fig. 4.2(c).

While the above argument is quite rigorous, it offers little physical insight into what is really going on; there is a more intuitive argument that explains the existence of the metastable MI phase and pinpoints the general features of our model that give rise to it. The superfluid ground state has, in a sense to be made precise shortly, a certain rigidity against spin fluctuations. Denoting the $\mathcal{V} = 0$ mean-field ground state $|\langle \boldsymbol{S}_b \rangle, \boldsymbol{\rho} \rangle$, and letting $\hat{\boldsymbol{\rho}} = \boldsymbol{\rho}/\psi^2$ be a unit vector in the direction of the superfluid, one might guess that turning on a small $\mathcal{V}$ causes the groundstate to be the singlet-like $|-\frac{1}{2}\hat{\boldsymbol{\rho}}, \boldsymbol{\rho} \rangle - |\frac{1}{2}\hat{\boldsymbol{\rho}}, -\boldsymbol{\rho} \rangle$, gaining $3\mathcal{V}/2$ from the Kondo term. However, it can be seen that such a state actually has $\sim \mathcal{J}\psi^2$ more kinetic energy than the mean-field ground state at $\mathcal{V} = 0$. Hence when $\mathcal{J}\psi^2 \gtrsim \mathcal{V}$, rather than fluctuating its spin the superfluid will just anti-align with the localized spin, gaining only $\mathcal{V}/2$ from the Kondo term. Notice that this rigidity is purely kinetic in origin, and that the mean-field ground state for small $\mathcal{V}$ agrees, both in form and energy, with the lowest order results of Sec. 4.3.2. On the other hand, when $\mathcal{J}\psi^2 \lesssim \mathcal{V}$, the superfluid gains more
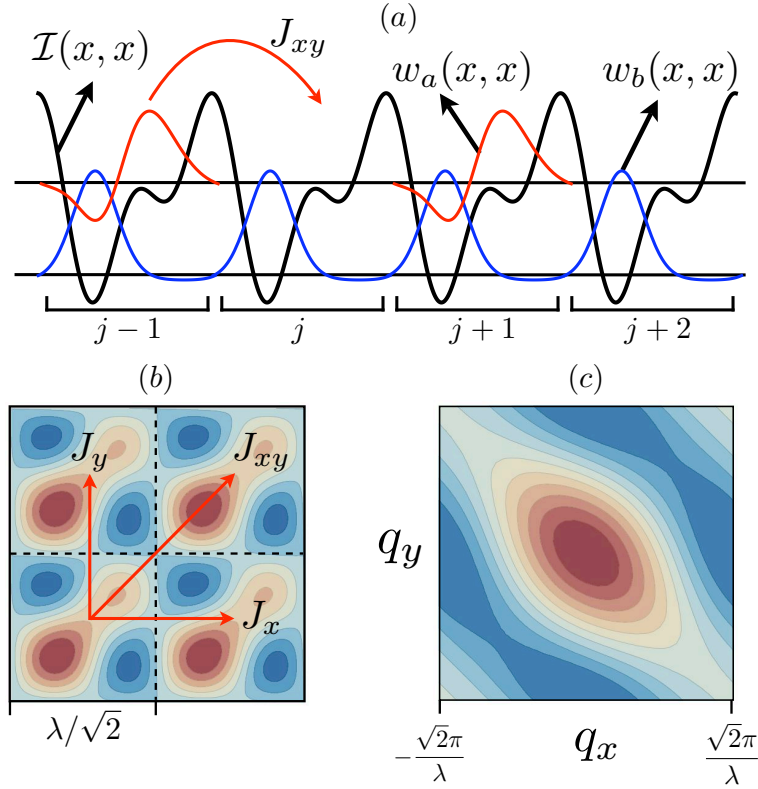
Figure 4.4: (a) Plot of $\mathcal{I}(x,x)$, with the wave functions w_a and w_b shown schematically. (b) A contour plot of $\mathcal{I}(x,y)$, showing the primary hoppings. The resulting spectrum in the a band is plotted as a function of quasi-momenta q_x and q_y (c), and can be fit to a tight-binding model with hoppings J_x, J_y, and J_{xy} [see (b)].

energy from the Kondo term by fluctuating its spin than it looses in kinetic energy, and hence its energy decreases by $3\mathcal{V}/2$. The tendency of the mean-field energy to be lowered more for small ψ than for large ψ is what enables a local minimum at $\psi = 0$ to arise.[5]

4.5   Experimental details

4.5.1   The optical lattice

As a specific example of how the approximations and parameters considered in this chapter can be obtained in an optical lattice, we consider the 2D potential of Ref. [153]

$$
\begin{aligned}
\mathcal{I}(x,y) &= -4\mathcal{I}_o[\cos kx + \cos ky]^2 \\
&- \mathcal{I}_i[2\cos(2kx - 2\varphi) + 2\cos 2ky],
\end{aligned}
\tag{4.24}
$$

and a deep transverse confining lattice with potential $\mathcal{I}_z(z) = \mathcal{I}_\perp \cos^2(k_z z)$. Each unit cell consists of a biased double well [Fig. 4.4(a)], and control of the bias allows for an adjustment of the overlap integral $\int d^2\boldsymbol{r} \, |w_a(\boldsymbol{r})|^2 |w_b(\boldsymbol{r})|^2$ and hence of V. This lattice offers a large parameter space to play with, and here we give just one example of a lattice configuration that could facilitate our model. Defining $E_R = \frac{\hbar^2}{2m\lambda^2}$, we choose the parameters $\{\mathcal{I}_o, \mathcal{I}_i, \varphi\} = \{0.9E_R, 2.52E_R, 0.3\pi\}$, for which the deep well has a depth of $\sim 21E_R$ and the shallow well has a depth of $\sim 11E_R$.

Using a transverse lattice with $\mathcal{I}_\perp = 40E_R$ and $\lambda = 2\pi k_z^{-1} = 780$nm, and the scattering length of ^{87}Rb, we find $U_b/4J_b \approx 2 \times 10^3$, $U_a/4J \approx 10$, and $V/U_a \approx 0.1$. Here J_b is the nearest neighbor hopping matrix element for the b band. This is just inside the $n = 1$ mean-field Mott lobe, with V/U_a in the correct range to observe the first-order phase transition, and these parameters can be adjusted to exit the Mott insulator in the a band, or to change V/U_a. One consequence of this geometry is that the bands are not isotropic. The effect is very small for the b band, but for the a band, by fitting the numerically calculated dispersion [Fig. 4.4(c)] to a tight binding model, we find primary hoppings $J_x = J_y = 0.002E_R$ and $J_{xy} = 0.0035E_R$ [Fig. 4.4(b)].

Other important energy scales are the band gaps, and for the parameters given above the first 4 gaps (all those between the b band and the a band and the gap above the a band) are all at least $1E_R$. This should be compared to the largest relevant interaction energy U_b, and for the parameters given above we find $U_b \approx 0.28E_R$. It should be noted that this comparison is an

---

[5] It is also essential that for a superfluid density ψ^2, the depth of the superfluid minimum can become much smaller than $\mathcal{J}\psi^2$ as $\mathcal{B} \to 0$ (i.e., as the Mott transition is approached). If this were not the case, the larger energy gain from the Kondo term at small ψ might not induce a local minimum at $\psi = 0$.

extremely conservative metric of how the interaction energies compare to the band gaps. After all, U_b is the largest interaction energy in the model, and the band gap separating the b band from the band directly above it is larger than $5E_R$.

4.5.2   Observation of the first-order transition

In order to probe the SF to MI phase transition, an ideal starting point would be a 2D $(x-y$ plane) MI of spin triplet pairs in the lowest vibrational level of the 2D lattice with $\mathcal{I}_i = 0$. The PM MI could then be achieved with high fidelity by ramping up $\mathcal{I}_i$ to establish an array of double wells in the $x - y$ plane, and then using either Raman pulses [125] or the population swapping techniques of Refs. [2, 174] to populate the a band. Standard time-of-flight imaging, combined with band-mapping techniques [2] and spin selective imaging, could be used to resolve both the superfluid coherence and the magnetic ordering in either band.
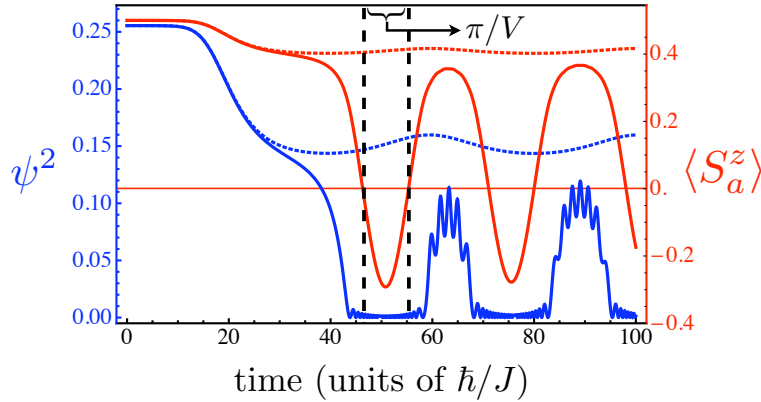
Figure 4.5: Dynamics during a slow ramp of $\mathcal{V}$ from the SF to the MI at fixed conduction band filling $n = 1$ (through a first-order phase transition). The ramping function is $\mathcal{V}(t) = \mathcal{V}_f(\tanh(t/t_0)+1)/2$, with $t_0 \approx 5.7\hbar/J$. For a ramp to $\mathcal{V}_f = \mathcal{V}_c + \delta$ $(\mathcal{V}_f = \mathcal{V}_c - \delta)$, the lower blue solid (dotted) line is ψ^2 and the upper red solid (dotted) line is $\langle S_a^z \rangle$. The fast oscillations of ψ^2 in the non-adiabatic case occur on a time scale of order $\frac{2\pi}{U}$.

As we have discussed in Sec. 4.5.1, $\mathcal{V}$ can be tuned in a double well lattice. Therefore the first-order phase transition should be observable by sitting just outside the unit-filled Mott insulator lobe and increasing $\mathcal{V}$ from 0 to some value $\mathcal{V}_f$ large enough to support a Mott insulating ground state. The discontinuous nature of the phase transition will cause a failure of adiabaticity for even

an arbitrarily slow sweep of $\mathcal{V}$. At the mean-field level, the effect of ramping $\mathcal{V}$ can be explored with no further approximation by solving the time-dependent equations of motion that result from minimization of the Lagrangian [88]

$$\mathcal{L} = \langle i\frac{d}{dt} - \mathcal{H}_{\text{GA}}\rangle, \tag{4.25}$$

where the expectation value is taken in the single site Hilbert space (for practical calculations, this space must be truncated by cutting off the maximum number of allowed bosons). Defining $\mathcal{V}_c$ to be the value of $\mathcal{V}$ at which the metastable SF solution disappears (note that this is *not* where we define the phase boundary in Sec. 4.4), we compare a slow ramp of $\mathcal{V}$ from 0 to $\mathcal{V}_f = \mathcal{V}_c \pm \delta$. For $\mathcal{V}_f < \mathcal{V}_c$, we observe a nearly adiabatic reduction of the SF component, whereas for $\mathcal{V} > \mathcal{V}_c$ we observe collapses and revivals of the SF component. This is reminiscent of the behavior seen in Refs. [71, 172], where a fast quench was studied in the single-band Bose Hubbard model, but here the collapses occur even for very slow lattice ramps. Since the collapses are pinned to a rotation of the magnetization [Fig. 4.5], it is not surprising that they repeat on a time scale $\sim \frac{2\pi}{V}$.

Regarding the experimental feasibility of the proposed dynamics around the MI to SF transition, the total time elapsed in Fig. 4.5 is $100\hbar/J$, which is comparable to the longest excited band decay times measured in Ref. [125] for the $n = 1$ situation. This suggests that dynamical evidence of the first-order transition, e.g. loss of adiabaticity or hysteresis, should be within reach of current experiments. Hysteretic behavior will be limited to temperatures that are comparable to or smaller than the energy barrier between the two metastable phases. This height is set by $V \lesssim 0.1U$, suggesting that the required temperature is cold, but much more favorable than that required for super-exchange physics. A more quantitative determination of the temperature requirements necessitates a more rigorous (numerically exact, rather than mean-field) study, and will be addressed in future research. We also note that the first-order phase transition could be explored by measuring local and static observables in the trap, for instance it could manifest as a discontinuity in the density profile.

4.6   Summary and conclusions

In real metals, it is known that when conduction electrons interact with magnetic impurities their behavior is drastically altered; in order to describe such systems, it is necessary to study many-body Hamiltonians that include spin, charge, and orbital degrees of freedom, such as the KLM. The bosonic analogues of such systems are experimentally accessible using ultracold alkali atoms in *non-separable* optical lattices, motivating this fairly in depth study of the Bose Kondo-Hubbard model. Our primary new finding is that the SF to MI phase transition of the conduction bosons is qualitatively modified by the existence of an arbitrarily small Kondo coupling to a band of localized spins. When approaching the MI, as the superfluid density of the conduction bosons is reduced, magnetic fluctuations driven by the Kondo exchange induce a metastable MI of Kondo singlets, and as a result the associated phase transition becomes first-order. We expect the first-order phase transition to be observable in experiment, making this model a leading candidate for observing entirely new, strongly correlated, multi-band phenomena in optical lattices.

Chapter 5

Ultra cold polar molecules in a 3D optical lattice

The creation of nearly-degenerate gases of polar molecules [126, 127, 27] has generated a tremendous amount of excitement in the fields of quantum simulation, quantum information, and ultracold chemistry. While the production of these molecules has required a number of severe technical challenges to be surmounted, and achieving quantum degeneracy is much more difficult than for atoms, they have several advantages over atoms that make these difficulties worthwhile.

First of all, diatomic molecules have an extremely rich internal structure: beyond the usual electronic and nuclear-spin degrees of freedom found in atoms, molecules can also vibrate and rotate. These extra degrees of freedom make possible, for instance, the implementation of condensed matter models with both spin- and orbital- electronic degrees of freedom (much as alkaline earth atoms can). In addition, experimentally achievable DC electric fields can induce extremely large dipole moments in heteronuclear molecules. Using low-lying rotational levels as spin degrees of freedom, these dipolar interactions can give rise to long-ranged quantum spin models as proposed in Ref. [70]. These spin-models are highly tunable, long-ranged, controllably anisotropic (both in spin space and real space), and have temperature scales that can be orders of magnitude larger than those relevant to spin-models arising from super-exchange in neutral atoms.

The creation of groundstate polar molecules, as realized in [126] for ^{40}K^{87}Rb, involves a two-step process: (1) magneto-association of the atoms into weakly bound Feshbach molecules [142], and (2) coherent transfer of these Feshbach molecules into the rotational, vibrational, and electronic groundstate, via stimulated Raman adiabatic passage (STIRAP) [126]. Under 3D har-

monic confinement, the efficiency of molecule production is primarily limited by step (1). While the reasons for this inefficiency are not completely understood at this time, the poor phase-space overlap between bosons and fermions at low temperatures is almost certainly a contributing factor. One might guess that the detrimental effects of low efficiency are limited to low molecule yield, and therefore could be overcome by simply starting with more atoms. However, low efficiency of Feshbach molecule creation has a more fundamentally detrimental effect. Imagine, for the sake of simplicity, that both the potassium and rubidium are at zero temperature and have perfect spatial overlap. The pairing of one potassium atom and one rubidium atom will in general result in a Feshbach molecule having approximately the momentum of the potassium atom (because the rubidium atoms, which are bosons, will have a much narrower momentum distribution at low temperatures). If the potassium atoms that get paired into molecules are drawn somewhat uniformly from their initial momentum distribution, then typical KRb momenta (and hence energies) are set by the initial Fermi momentum of the potassium distribution, which has no dependence on the creation efficiency. The Fermi temperature of the KRb molecules, on the other hand, does scale with the number of molecules created as $T_{\mathrm{KRb}}^{F} \sim N_{\mathrm{KRb}}^{1/3}$. Defining the molecule creation efficiency relative to the initial potassium number N_{K}, $\eta = (N_{\mathrm{KRb}}/N_{\mathrm{K}})$, and assuming that the temperature of the molecules is set by their typical kinetic energy (which is certainly true for sufficiently small efficiency) we obtain

$$\frac{T_{\mathrm{KRb}}}{T_{\mathrm{KRb}}^{F}} \sim \eta^{1/3}. \tag{5.1}$$

By this argument, it is not possible to directly obtain a degenerate gas of fermionic molecules from a degenerate gas of atoms unless the molecule creation efficiency is large.[1]

One possible route toward a degenerate Fermi gas of molecules is to accept these low efficiencies, and then attempt to remove the resulting entropy via forced evaporation. There are reasons to be optimistic that this might work [138, 139], however it is certainly not clear that it will. Efficient evaporation relies on a large separation of timescales between elastic and inelastic collisions. In an

---

[1] In which case the above argument breaks down, since there is no reason to expect the temperature of the molecules to be determined by their kinetic energy.

atomic gas, inelastic collision processes typically require the participation of at least three atoms (three-body recombination) in order to conserve energy and momentum, and thus the ratio between elastic (two-body) and inelastic collision rates can be driven up by decreasing the density. KRb molecules, on the other hand, suffer from inelastic *two-body* collisions,[2] and hence the scaling cannot be improved by changing the density. On these fairly general grounds, one expects the competition between inelastic and elastic collision rates in reactive molecules to be less favorable than for atoms. The actual outcome of this competition, of course, depends on the detailed microscopic physics of elastic and inelastic collisions. For KRb there is reason to believe that, at low temperature, the ratio is actually quite large, and efficient evaporation may indeed be possible.

Another possible route to quantum degeneracy is to create Feshbach molecules in a 3D optical lattice [59] (rather than in a harmonic trap). The ideal starting point is achieved if the rubidium atoms form a unit filled Mott insulator, which is well overlapped with a unit-filled band insulator of potassium atoms. Then each lattice site has exactly one potassium and one rubidium on it (up to whatever thermal fluctuations persist in the deep lattice limit), and in a deep lattice the efficiency of magneto-association is determined by a single site problem. The creation of Feshbach molecules on a single site can be studied theoretically [99], and there is good reason to believe that it can be extremely efficient. In particular, the adiabaticity time scale through the Feshbach resonance should be set by the harmonic oscillator level spacing on a single site, which can be many kHz. Experimentally, this efficiency for KRb has been shown to exceed 80%, and to be consistent with 100% [27].

5.1   Efficiency of Feshbach molecule creation

The goal of this section is to estimate the creation efficiency for Feshbach molecules in a 3D optical lattice, as realized in Ref. [27]. As mentioned above, a near unity conversion efficiency between two atoms on a single lattice site and a Feshbach molecule has been demonstrated experi-

---

[2] Two body inelastic collisions occur because two KRb molecules can release binding energy while still separating into two pieces at large distances (one ^{2}Rb molecule and one ^{2}K molecule), thereby satisfying energy and momentum conservation.

mentally. It is therefore appropriate to estimate the efficiency of Feshbach molecule creation in a 3D lattice by calculating the number of sites containing exactly one rubidium atom and one potassium atom (a preformed pair). Both below and above the rubidium condensation temperature T_c, we calculate the initial entropy of the combined potassium and rubidium clouds in the optical dipole trap, and extract the equilibrium properties of atoms in the 3D lattice by assuming conservation of entropy until the final lattice depth is reached. However, given the wide temperature range covered by the experimental data, it is convenient to carry out two different calculations, one to capture the physics at temperatures below T_c and one to capture the physics above T_c.

Below T_c we take Rb-Rb interactions into account, but ignore the hopping of atoms between lattice sites[3] as well as the K-Rb interaction. The inclusion of Rb-Rb interactions at these temperatures is critical, because they greatly suppress the number of sites with more than one rubidium, which are not expected to yield molecules. In the presence of differential sag, we expect the attractive K-Rb interaction to pull the clouds slightly closer together, which would push the theory prediction for the number of preformed pairs slightly up at low temperatures [59]. Because the tunneling is ignored, we can focus on the Hilbert space of a single site, which we restrict to have at most four rubidium atoms, and then calculate the energies ϵ_α on that site by assuming the usual s-wave pseudopotential approximation and integrating over the appropriate Wannier orbitals in each band. The grand canonical potential for rubidium, $\Omega_{\mathrm{Rb}} = -\beta^{-1} \sum_j \log[\mathcal{Z}_{\mathrm{Rb}}(j)]$, is obtained from the partition functions at each site

$$\mathcal{Z}_{\mathrm{Rb}}(j) = \sum_\alpha e^{-\beta(\epsilon_\alpha + V(\boldsymbol{r}_j) - \mu)}, \tag{5.2}$$

where β is the inverse temperature, and $V(\boldsymbol{r}_j)$ is the final confining potential resulting from the gaussian beam profiles, evaluated at site j. The grand canonical potential for potassium is obtained trivially, since they are non-interacting and we are ignoring the hopping between lattice sites.

Above T_c it is necessary to retain a large number of bands; at the highest temperature data

---

[3] This approximation is reasonable when all of the atoms are in the lowest band, since at the final lattice depths the lowest band tunneling is always effectively zero on experimentally relevant timescales. In general, we calculate the final distribution at a lattice depth of $20E_R$ for Rb, since at this point we do not expect any further transport of the atoms to be possible.

point, adiabatic heating during the lattice ramp yields a final temperature that is comparable to the first band-gap for potassium. However, because the gases are quite dilute at this temperature, with *peak* densities of rubidium and potassium being approximately 0.6 and 0.1 per lattice site, respectively, we do not expect interactions between the atoms to play an important role. We therefore model the final distribution in the lattice assuming no interactions, but keeping as many bands as are needed for convergence at each data point. In order to efficiently calculate thermodynamic quantities, we evaluate the grand canonical potential in the local density approximation (LDA)

$$\Omega = \pm \beta^{-1} \int d^3\boldsymbol{r} \int d\epsilon \, \rho(\epsilon) \log[1 \pm e^{\beta(\mu-\epsilon-V(\boldsymbol{r}))}], \tag{5.3}$$

where $+$ is for potassium and $-$ is for rubidium, and the integral over $\boldsymbol{r}$ approximates the LDA sum over lattice sites. The $\boldsymbol{r}$ integration can be done analytically, and the remaining integral over energy is carried out by choosing a coarse-grained density of states

$$\rho(\epsilon) = \sum_\alpha g_\alpha \delta(\epsilon - \epsilon_\alpha), \tag{5.4}$$

with $\delta(\epsilon - \epsilon_\alpha)$ the Dirac delta function, g_α the number of states in the αth band per unit cell of the lattice, and ϵ_α once again being the average energy of the αth band. This approach has the advantage of yielding asymptotically correct results in the deep lattice limits, and agrees very well with exact expressions in the case of no lattice (in which case $\epsilon_\alpha \sim E_R \alpha^2$ is the average energy of a free particle with momentum between $\alpha \frac{h}{\lambda}$ and $(\alpha + 1)\frac{h}{\lambda}$, with λ the wavelength of the lattice beams).

From these thermodynamic calculations, we extract the final chemical potential and temperature by assuming conservation of particle number and entropy, respectively. With the temperature and chemical potential in hand, we can extract the distribution of sites (indexed by j) with exactly one rubidium (potassium), denoted $P_1^{\text{Rb(K)}}(j)$, from the associated Boltzmann weights. In terms of the $P_1^{\text{Rb(K)}}(j)$, the total number of preformed pairs is given by

$$\mathcal{N}_{\text{K,Rb}} = \sum_j P_1^{\text{Rb}}(j) P_1^{\text{K}}(j). \tag{5.5}$$
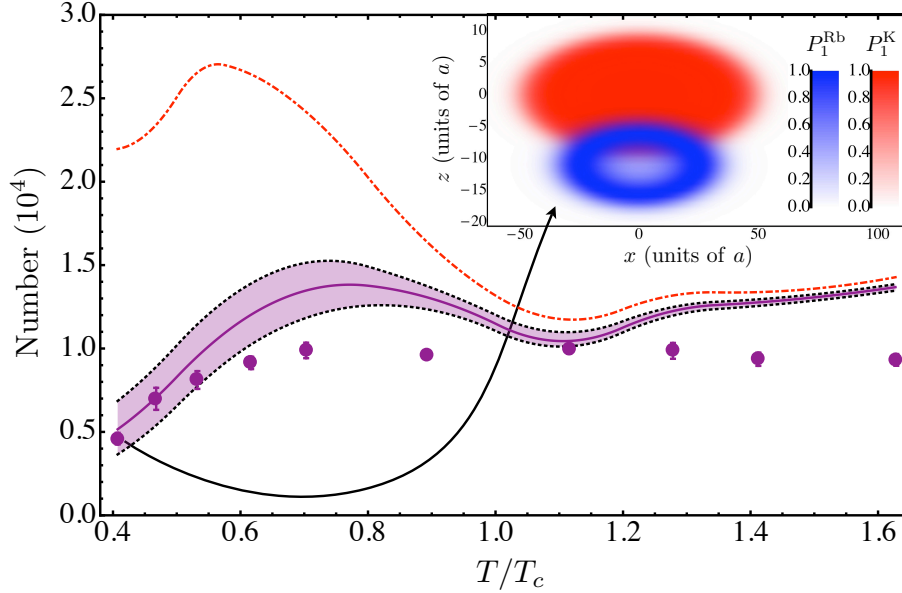
Figure 5.1: Preformed pairs: Purple solid curve is the number of preformed pairs obtained with a no-free-parameter theory, and the black dotted curve below (above) it assumes a differential sag of one lattice site more (less) than the calculated value. The purple circles are experimentally measured numbers of Feshbach molecules in the 3D lattice. The red dashed-dotted line shows the expected number of preformed pairs in the absence of a differential sag. Inset: Slice in the x-z plane of the distribution of sites with a single Rb (blue, lower) and single K (red, upper), with the $n = 1$ Mott insulator shell manifest as a ring of singly occupied Rb sites (the hollow area within the ring has mostly sites with two Rb atoms). The offset along z of about $11a$, where a is the lattice spacing, is caused by the differential gravitational sag in the initial optical dipole trap, and is an important source of inefficiency in the molecule creation.

In Fig. 5.1 we plot the calculated $\mathcal{N}_{\mathrm{K,Rb}}$ (with no free parameters), and we show the theory predictions for $\mathcal{N}_{\mathrm{K,Rb}}$ if there were no differential sag between the clouds. This procedure of counting preformed pairs breaks down at sufficiently high temperatures, for reasons that can be understood semi-classically: Once more highly dispersive bands—with greater velocities—become populated, two atoms must be nearby in momentum space, as well as in position space, in order to form a molecule. Before moving on to discuss molecule loss rates, we note that the low temperature results suggest that the JILA experiments are already close to producing large numbers of densely packed molecules in a 3D optical lattice: The current decrease in efficiency at low temperatures appears to be due almost entirely to differential gravitational sag between potassium and rubidium (due primarily to their different masses).

5.2   Loss rates from ground-state molecule collisions in a corrugated 1D tube

In Ref. [27], the lifetime of groundstate KRb molecules in a 3D optical lattice was probed as a function of the lattice depth in the z direction, with the x and y lattices held at a constant depth (large enough to completely freeze out motion in the x and y direction). By tuning the z lattice depth continuously between zero (an array of 1D tubes) and $\sim 100 E_R$ (where motion in all three directions is completely frozen out), a crossover was observed between: (1) low z-lattice behavior, where the lifetime increased with the lattice depth, and (2) high z-lattice behavior, where the lifetime decreased with the lattice depth. For large lattice depths, the decreasing lifetime was shown to be consistent with inelastic light scattering (which increases with intensity of the lattice beams). For low lattice depths, there is strong evidence that the molecular gas lifetime becomes limited by molecule-molecule inelastic collisions, as we now discuss.

It was observed experimentally that the lifetime of molecules in an array of 1D tubes is sensitive to the strength of an applied electric field. This electric field dependence is expected for collisions between identical dipolar fermions [139, 127], and hence implicates molecule-molecule collisions as the loss mechanism. It was also observed that, at zero electric field, the addition of a weak corrugating lattice along the tubes greatly enhances the molecule lifetime. In order to understand this effect, here we study lossy molecule-molecule collisions in a tube, at zero electric field and in the presence of a lattice along the z direction.

At low temperatures (μK) and in zero electric field, a collision between two ground-state fermionic molecules in the same nuclear spin state occurs primarily in the p-wave channel. We model the lossy part of the molecule-molecule interaction with a p-wave pseudopotential, parametrized by a strictly imaginary p-wave scattering volume [90, 24]:

$$\mathcal{D} = i \frac{6\pi \hbar^2 V_p}{m} \int d^3 \boldsymbol{r} \; \psi^\dagger \left(\vec{\nabla} \psi^\dagger \right) \cdot \left(\vec{\nabla} \psi \right) \psi. \tag{5.6}$$

Everywhere else in this thesis we have considered only s-wave scattering, and the above expression warrants some discussion (for more details about p-wave pseudopotentials, see for example Ref. [90]). First of all, one might naively guess that an operator such as $\psi(\boldsymbol{r}) \vec{\nabla} \psi(\boldsymbol{r})$ would vanish (due

to the anticommutation relations for the annihilation operators), but this is not the case. One way to deal with the derivative of a field operator is to expand it in some complete set of wavefunctions $\varphi_\alpha(\boldsymbol{r})$ as

$$\psi(\boldsymbol{r}) = \sum_\alpha \varphi_\alpha(\boldsymbol{r}) c_\alpha, \tag{5.7}$$

in which case we have

$$\psi(\boldsymbol{r})\vec{\nabla}\psi(\boldsymbol{r}) \;=\; \sum_{\alpha,\beta} c_\alpha c_\beta \varphi_\alpha(\boldsymbol{r})\vec{\nabla}\varphi_\beta(\boldsymbol{r}) \tag{5.8}$$

$$=\; \sum_{\alpha>\beta} c_\alpha c_\beta \left[\varphi_\alpha(\boldsymbol{r})\vec{\nabla}\varphi_\beta(\boldsymbol{r}) - \varphi_\beta(\boldsymbol{r})\vec{\nabla}\varphi_\alpha(\boldsymbol{r}) \right]. \tag{5.9}$$

Notice that if we had calculated $\psi(\boldsymbol{r})\psi(\boldsymbol{r})$ in this way, i.e. we had ignored the derivative, the term in square brackets would have given $[\varphi_\alpha(\boldsymbol{r})\varphi_\beta(\boldsymbol{r}) - \varphi_\beta(\boldsymbol{r})\varphi_\alpha(\boldsymbol{r})] = 0$, as it should. While we will not give a rigorous justification for the form of this pseudopotential, we mention that it does make a lot of sense, for the following reason. For two particles who's relative wavefunction is a plane wave of momentum k, $\psi_{\rm rel}(r) \propto e^{ikr}$, the expectation value of the s-wave pseudopotential of Sec. 2.2 is proportional to the low-energy scattering amplitude a_s. The expectation value of the p-wave pseudopotential in Eq. (5.6), however, is proportional to $V_p k^2$ (because of the two derivatives). This is consistent with the Wigner threshold law for p-wave scattering in a Van der Waals potential, which states that the low energy scattering amplitude in the p-wave channel should scale as k^2 as $k \to 0$ [147].

The magnitude of the imaginary scattering volume, $V_p \approx 350$ nm^3, is obtained by comparing ab initio calculations of the loss rate for two molecules in an isotropic 3D harmonic trap [116] to results using the pseudopotential. Assuming that most molecules are in the transverse ground-state of a tube, two representative loss processes for molecules in the same tube (on two adjacent lattice sites) are shown in Fig. 5.2. The loss rate for two nearest-neighbor molecules within the lowest band (γ_{00}) is rapidly suppressed by Pauli blocking for increasing z-lattice depth. The loss rate for one molecule in the lowest band and one molecule in the first excited band on the same site (γ_{01}) grows with increasing z-lattice depth, due to the increasing localization of the lowest band and first excited band Wannier orbitals [$w_0(z)$ and $w_1(z)$, respectively].
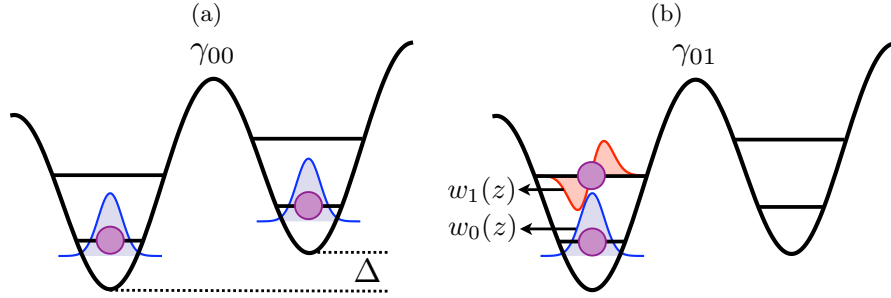
Figure 5.2: Loss processes within the lowest two bands of the z lattice. (a) Lowest band loss rate for two molecules on neighboring lattice sites (γ_{00}). (b) Onsite loss rate for one molecule in the lowest band and one in the first excited-band on the same site (γ_{01}). The offset Δ is in general present, due to the gaussian profile of the lattice beams.

We now address the question of whether the loss rates in Ref. [27] can be understood in terms of the fundamental two-body loss processes shown in Fig. 5.2, and their associated rates γ_{00} and γ_{01}. Two molecules in the lowest band should be lost at a rate proportional to γ_{00}, where the constant of proportionality is determined in a semiclassical picture by the fraction of time those two molecules spend on neighboring sites. Since this fraction is clearly less than one—being driven down both by low density and by single particle localization due to the energy offsets between sites (Δ)—γ_{00} is an upper bound to the actual loss rate of two molecules in the lowest band. As shown in Fig. 5.4, γ_{00} is too small to explain the measured loss rates, so collisions between molecules within the lowest band are clearly not the loss mechanism. When one molecule is in the lowest band and one molecule is in the first excited band, the loss rate is proportional to γ_{01}, so long as $\hbar\gamma_{01} \ll J_1, \Delta$ is satisfied. It is still possible, however, that the loss rate can decrease with increasing lattice depths, since even as γ_{01} is becoming larger the molecules are becoming more localized. When $\hbar\gamma_{01} \gg J_1, \Delta$, in the so-called Zeno suppression regime, the loss rate can actually be inversely proportional to γ_{01} [165] (see the next section for a detailed discussion of Zeno suppression). However, for the experimental data taken at low z-lattice depths (the first four data points in Fig. 5.4), the Zeno suppression scenario can be ruled out, and interband collisions should result in a loss rate that is proportional to γ_{01}.

This result is, however, inconsistent with the experimental observation that losses in corru-
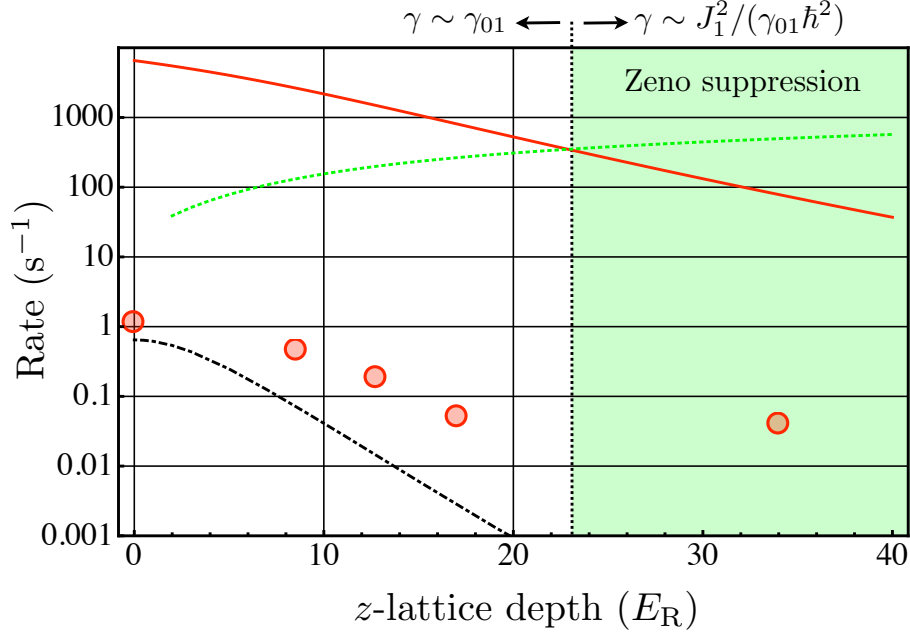
Figure 5.3: Relevant rates for molecules confined to the lowest two bands in the z-direction, as a function of the z-lattice depth. The black dashed-dotted curve is γ_{00}, the red solid curve is $J_1/\hbar$, and the green dotted curve is γ_{01}. It is clear that γ_{00} is too small to explain the measured loss rates (red circles, the error bars are smaller than the plot markers). The rate γ_{01} increases with the z-lattice depth due to the increasing confinement of the lowest two Wannier orbitals, and eventually becomes larger than the first excited-band hopping rate ($J_1/\hbar$) at a z-lattice depth of around 23 E_{R}. For even larger z-lattice depths (green shaded region) one expects Zeno suppression to affect the loss rate of two molecules in different bands.

gated tubes do not exhibit the electric field dependence of losses in uncorrugated tubes: When dipole-dipole interactions are taken into account, both γ_{00} and γ_{01} should increase with electric field strength. The most likely explanation for this lack of electric field dependence is that, in the presence of the z-lattice, collisional physics does not determine the molecule lifetime, despite being ultimately responsible for the loss. Instead, a heating mechanism that promotes molecules from localized to mobile single-particle levels is what sets the time scale for the loss. If the promotion rate into mobile states is slower than the collisional loss rate for the mobile molecules, but faster than the collisional loss rate for the localized molecules—which is suppressed by the diluteness of the molecular gas—then it will determine the molecule lifetime, thereby rendering the lifetime independent of electric field.
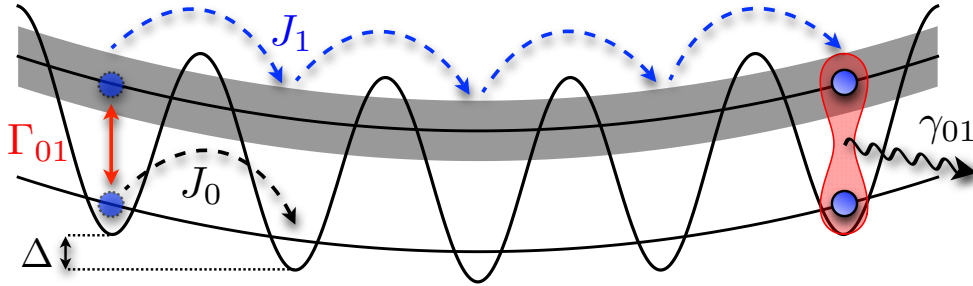
Figure 5.4: Schematic of the loss model: A ground band molecule is essentially completely demobilized by a combination of narrow bandwidth and energy offsets between lattice sites ($J_0 \ll \Delta$). Lattice instabilities couple molecules into higher bands (in this example the first excited band), and if this bandwidth is sufficiently large ($J_1 \sim \Delta$) the molecule becomes mobile. Once mobile, a molecule is rapidly lost due to inelastic collisions (rate γ_{01}).

To model this process phenomenologically, we assume that a heating mechanism imparts energy to the molecules at a fixed rate, and hence the promotion rate between successive bands is inversely proportional to the band gap between them. Microscopically, this picture is motivated by the following reasoning. Fluctuations in the transverse lattice beams—which provide a potential that is only approximately decoupled from the z-direction—should be the dominant source of heating at low z-lattice depths. While a detailed knowledge of these fluctuations is absent, one can in complete generality assume that to first order in z, the motion of a molecule along z couples to a time-dependent perturbation of the form $\mathcal{I}(z,t) = \mathcal{I}_\perp f(t) z$, where the intensity $\mathcal{I}_\perp$ depends primarily on the transverse lattice strength. The resulting transition rate from a localized state $|\alpha\rangle$ (Wannier orbital of the αth band along z) to a localized state $|\alpha + 1\rangle$ (Wannier orbital of the next higher band along z) on the same lattice site is given by [149]

$$\Gamma_{\alpha,\alpha+1} = \frac{\pi S(\omega_\alpha)\mathcal{I}_\perp^2}{\hbar^2}|\langle \alpha + 1|z|\alpha\rangle|^2. \tag{5.10}$$

In the above, $S(\omega_\alpha)$ is the power spectrum of the noise $f(t)$, evaluated at the transition frequency ω_α between $|\alpha\rangle$ and $|\alpha + 1\rangle$. For a power spectrum that is relatively flat over frequency ranges $\Delta\omega \sim E_R/\hbar$, the matrix element $|\langle \alpha + 1|z|\alpha\rangle|^2 \sim \omega_\alpha^{-1}$ gives the dominant scaling of the transition rate on the z-lattice depth, and thus we expect interband transitions of this variety to be suppressed by the band gaps. On a single site, if we take the energies of localized states to be the band centers

$\epsilon_\alpha(v)$ (where v is the z-lattice depth measured in E_R), then we can define interband transition rates

$$\Gamma_{\alpha,\alpha+1}(v) = \mathcal{E}[\epsilon_{\alpha+1}(v) - \epsilon_\alpha(v)]^{-1}, \tag{5.11}$$

where $\mathcal{E}$ is a constant heating rate.

The loss rate for a given molecule can then be obtained by deciding on a localization criteria; for a molecule in the αth band sitting s sites from the trap center (in the z-direction), we consider that it is mobile whenever the bandwidth $4J_\alpha$ provides enough kinetic energy for it to reach the trap center [83]. This criteria sets a critical lattice depth $v_c(\alpha, s)$ in the αth band, below which a molecule at site s is mobile and above which it is localized. Our primary assumption is that, once mobile, a molecule in any excited band suffers lossy collisions on a time scale much shorter than the inter-band transition time, in which case the loss rate of the molecule is given by

$$\gamma_\alpha(s, v) = \mathcal{L}\Theta(v - v_c(\alpha, s)), \tag{5.12}$$

with Θ the step function, and with the collisional loss rate $\mathcal{L}$ chosen to be effectively infinite. Because the current experimental conditions are such that the molecules are very dilute, it is reasonable to think of any remaining molecules (in the same tube) as a dissipative bath for the mobilized molecule, and hence this is really a one-body loss problem, despite the eventual loss mechanism being distinctly two-body. In the ground band we retain the loss rate γ_{00}, calculated using the exact eigenstates of the lattice plus harmonic confinement, in order to capture the correct behavior in the weak z lattice limit. These considerations lead to a model for the decay of probability that a molecule initially at site s is still there after a given time, denoted $\mathcal{P}^s(t)$. Truncating to the lowest three bands along z, and denoting the probability for the molecule to be in band α by $\mathcal{P}_\alpha^s$, $\mathcal{P}^s = \sum_\alpha \mathcal{P}_\alpha^s$ is governed by the rate equations

$$\begin{aligned}
\dot{\mathcal{P}}_0^s &= -\gamma_{00}(v)\mathcal{P}_0^s - \Gamma_{01}(v)(\mathcal{P}_0^s - \mathcal{P}_1^s) \\
\dot{\mathcal{P}}_1^s &= -\gamma_1(s, v)\mathcal{P}_1^s - \Gamma_{01}(v)(\mathcal{P}_1^s - \mathcal{P}_0^s) - \Gamma_{12}(v)(\mathcal{P}_1^s - \mathcal{P}_2^s) \\
\dot{\mathcal{P}}_2^s &= -\gamma_2(s, v)\mathcal{P}_2^s - \Gamma_{12}(v)(\mathcal{P}_2^s - \mathcal{P}_1^s).
\end{aligned} \tag{5.13}$$

For a given lattice depth, the ensemble loss rate, which is the rate measured in the experiment, is extracted by averaging the solution to Eq. (5.13) over s

$$\mathcal{P} \propto \sum_s e^{-2s^2/\xi^2} \mathcal{P}^s, \tag{5.14}$$

and then fitting $\mathcal{P}$ to a decaying exponential decay $e^{-t/\tau(v)}$ with lifetime $\tau(v)$. Here we assume that the initial distribution of molecules in the z direction is gaussian with a $1/e^2$ radius of $\xi = 14$ lattice sites, which is based on experimental measurements of the molecule cloud; the qualitative features of the results are not particularly sensitive to this quantity. We find that heating rates between $\mathcal{E} = 1\ E_R/s$ (66 nK/s) and $\mathcal{E} = 2\ E_R/s$ (132 nK/s) are consistent with the experimental data at low z lattice depths. It should be noted that once the z lattice is sufficiently deep, and molecules remain localized for times comparable to the inelastic light scattering time, this model is no longer valid.

5.3   Microscopic justification of the loss model

In section 5.2, we considered the loss of molecules in a corrugated tube formed by deep optical lattices in the x and y direction and a weak lattice along z. Based on experimental observations, it was inferred that the loss of molecules is most likely due to the promotion of localized molecules into higher bands of the lattice (heating). Once in higher bands, they become deconfined and seek out other molecules, leading to loss via chemical reactions. The primary underlying assumption in the model presented is that it is possible to couple a discrete level (the localized molecule) into a lossy continuum (higher bands), and have the loss rate be independent of γ when γ is much larger than the coupling strength Ω. Notice that it is not immediately obvious that such a situation can occur: If the coupling Ω were to a discrete level, which had a loss rate γ, the actual rate of populations loss is either proportional to γ (in the limit $\gamma \ll \Omega$) or proportional to Ω^2/γ (in the limit $\gamma \gg \Omega$, the so called Zeno-suppressed regime). In neither case is the loss rate independent of γ.

5.3.1 Review of Zeno suppression: coupling to a lossy discrete level

Before tackling the more complicated case of coupling to a continuum, we consider the coupling of a discrete level to a single level with loss rate γ. In order to be concrete, let's take a two-level atom with groundstate $|a\rangle$ and an excited state $|b\rangle$ having a finite decay rate γ. To make the most direct connection with particle loss, we assume the system is not closed under spontaneous emission, and that the excited state relaxes to some state outside of the two level system (never to return). We will start with the atom in its groundstate, and couple it to the excited level with a Rabi frequency Ω, with $\Omega \ll \gamma$. We assume that the two levels are coupled on resonance, and work in the dressed state basis so that $|a\rangle$ and $|b\rangle$ are degenerate. One way to obtain the dynamics is to solve a master equation describing the dynamics of this open system. It turns out, however, that we can obtain the exact same results by simply evolving the initial wavefunction with an effective Hamiltonian[4]

$$\mathcal{H}_{\text{eff}} = \begin{pmatrix} 0 & \Omega \\ \Omega & -i\gamma/2 \end{pmatrix} \tag{5.15}$$

Instead of just solving the dynamics by brute force, we take advantage of $\gamma \gg \Omega$ to calculate the loss rate of population from the two-level system perturbatively. For $\Omega = 0$, there is of course no loss. If we turn on a small $\Omega \ll \gamma$, the eigenstates remain the same to zeroth order, and therefore the loss rate will be determined by the imaginary part of the energy shift to the $|a\rangle$ level. This shift can be calculated in second order perturbation theory, giving a loss rate

$$\Gamma \equiv -2\text{Im}\left(\frac{\langle a|\mathcal{H}_{\text{eff}}|b\rangle\langle b|\mathcal{H}_{\text{eff}}|a\rangle}{i\gamma/2}\right) \tag{5.16}$$

$$= \frac{4\Omega^2}{\gamma}. \tag{5.17}$$

The loss of population occurring at a rate Γ that is *inversely proportional to* the microscopic loss rate γ is what we mean by Zeno suppression of losses.

---

[4] The equivalence between solving the master equation and time evolution with an effective Hamiltonian of this form is *not* general. It holds in this case because of the particularly simple structure of the problem. In particular, the jump operators occurring in the master equation do not couple states within the subsystem we consider, and we do not care about the details of the population that leaves this subspace.

There is another very simple way to understand why Γ has this form. The emission of photons at a rate γ from the excited level (when it is populated) can be thought of as successive projective measurements discerning whether the atom is in state $|a\rangle$ or state $|b\rangle$. After all, we could set up a photodetector to tell us when these photons are emitted, and each time the detector clicks it tells us that the system was in the excited state. At short times, the probability of the atom being in the groundstate begins to evolve (due to the coupling Ω) as $P_a \approx (1 - \Omega^2 t^2)$. A measurement of the state is made at time γ^{-1}, at which point the probability of being in the groundstate (and not having emitted a photon) is $P_a \approx (1 - \Omega^2/\gamma^2)$. If the system is in the groundstate, the dynamics then start over; after a time $t = N\gamma^{-1}$, with N large, the probability of the atom still being in the groundstate is given by

$$
\begin{aligned}
P_a(t) &\approx (1 - \Omega^2/\gamma^2)^N & (5.18) \\
&= (1 - t\frac{\Omega^2}{\gamma}\frac{1}{N})^N & (5.19) \\
&= \exp[-t(\Omega^2/\gamma)]. & (5.20)
\end{aligned}
$$

5.3.2   Coupling to a lossy continuum

Transitions between two degenerate states $|a\rangle$ and $|b\rangle$, induced by a coupling Ω_{ab}, are suppressed if the initially unoccupied state has a loss rate $\gamma \gg \Omega_{ab}$. If there are other states around, this picture remains true when the spectrum is discrete, and when there are no other states within Ω_{ab} of this degenerate pair. We now turn to the case where, instead of the single state $|b\rangle$, we have a continuum of states, and we explain the various behaviors that result in different parameter regimes. As one might guess, since tunneling into a continuum is an inherently incoherent (irreversible) process, the laborious calculation below leads to simple classical rate equations describing loss from the discrete level into the continuum, followed by loss out of the continuum. These rate equations (which, in particular, allow for loss rates $\Gamma \propto \Omega$ when $\Omega \ll \Gamma$) are the formal justification for Eqs. (5.13) in the previous section.

The model:
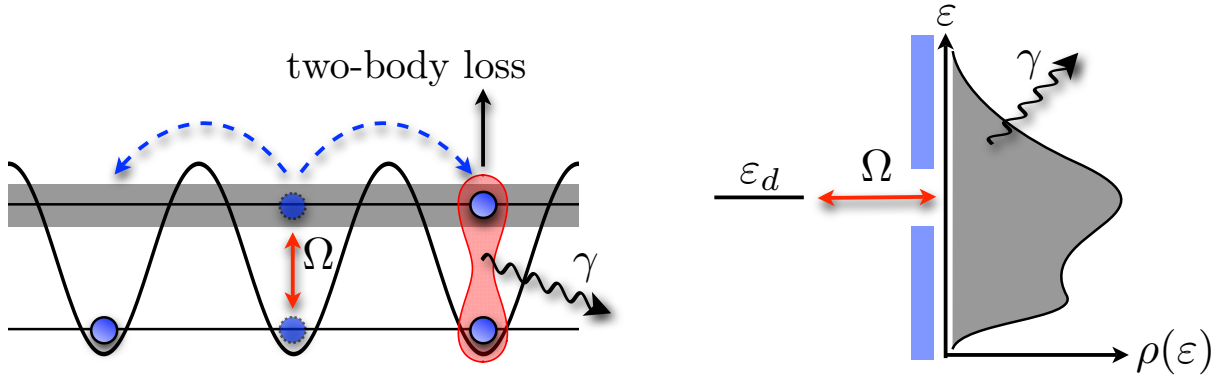
Figure 5.5: The left pannel shows the physical system we would like to study: Initially immobile (and hence long-lived) molecules are coupled to higher bands, where they become mobile and therefore susceptible to reactive collisions. The right pannel distills the essential mathematical structure of the problem: A discrete level is coupled to a continuum, with all states in the continuum being lossy.

We consider a single discrete level $|d\rangle$ with energy ε_d, coupled to a continuum of states $|k\rangle$ with complex energies $\varepsilon(k) = \omega(k) - i\gamma(k)/2$ by coherent couplings $\Omega(k)$. Defining creation operators $c_k^\dagger$ for the states $|k\rangle$ and a creation operator $c_d^\dagger$ for a particle in the state $|d\rangle$, in second quantization the Hamiltonian can be written

$$\mathcal{H} = \varepsilon_d c_d^\dagger c_d + \int dk \left(\Omega(k) c_d^\dagger c_k + \Omega(k)^* c_k^\dagger c_d + \varepsilon(k) c_k^\dagger c_k \right). \tag{5.21}$$

Whether the particles are fermions or bosons is irrelevant, because we will only consider the dynamics of a single particle. In the spirit of Section 5.2, we'll take as our continuum an lattice with tight binding dispersion and bandwidth $\mathcal{D}$. There are three regimes of interest here:

(I) The bandwidth is the largest energy in the problem, and the loss rate is large compared to the coupling ($\mathcal{D} \gg \gamma \gg \Omega$). In this case we might expect Zeno suppression to occur, but we will see that it does not.

(II) The bandwidth is the largest energy in the problem, and the loss rate is small compared to the coupling ($\mathcal{D} \gg \Omega \gg \gamma$). In this case there are two distinct possibilities: Depending on whether γ is small or large compared to $\Omega^2 \rho$, with ρ the density of states in the continuum, the loss rate will be limited either by γ (loss rate from the continuum) or by $\Omega^2 \rho$ (loss rate into the continuum, which will remain essentially empty).

(III) The bandwidth is small compared to the coupling ($\mathcal{D} \ll \Omega$). This case is not directly relevant to the heating and subsequent loss of molecules discussed in section 5.2, but we include it for the sake of completeness.

Case I: $\mathcal{D} \gg \gamma \gg \Omega$

This is the case we have in mind when applying the phenomenological loss model of Sec. 5.2. It appears superficially to be directly analogous to the Zeno suppression regime described above for a discrete spectrum, in that the coupling to any particular level in the continuum is Zeno suppressed by virtue of $\Omega(k) \ll \gamma(k)$. However, we will see that the loss rate is not Zeno suppressed, and is in fact independent of $\gamma(k)$ all together. Instead, the loss rate is determined by Fermi's golden rule as the tunneling rate into the continuum. This is the result one might guess without any knowledge of Zeno suppression: The loss rate hinges on two processes, tunneling into the continuum and then being lost, and the tunneling limits (and therefore sets) the rate for this process when $\Omega(k) \ll \gamma(k)$.

This result can be derived in time-dependent or time-independent perturbation theory. Unlike in the absence of losses, where Fermi's golden rule is normally derived, here the time-independent derivation is actually easier. Moreover, it will make explicit why Zeno suppression—as derived above—does not occur when coupling to a continuum. Because $|\varepsilon(k) - \varepsilon_d| \geq \gamma(k)/2$, the impurity level will remain an eigenstate to zeroth order in $\Omega(k)$ (i.e. there are no degeneracies when the imaginary part of the continuum energies are taken into account). Therefore, the survival probability

of a particle initially in the discrete level is approximately given by

$$P_d(t) = \exp[-\Gamma t]$$

$$\Gamma = 2\text{Im}[\tilde{\varepsilon}_d] \tag{5.22}$$

The factor of two in Γ comes from calculating the norm squared of the wave function, and $\tilde{\varepsilon}_d$ is the energy of the discrete state in the presence of the couplings. The shift in energy of the impurity level can be controllably expanded whenever $\Omega(k) \ll \gamma(k)$. This should be contrasted with the usual situation of $\gamma = 0$, where the discrete level is approximately degenerate with part of the continuum. To second order, we find

$$\tilde{\varepsilon}_d = \varepsilon_d + \int \frac{|\Omega(k)|^2 dk}{\varepsilon_d - \varepsilon(k)} + \mathcal{O}(\Omega^4). \tag{5.23}$$

By introducing the density of states $\rho(\omega) = (d\omega/dk)^{-1}$, this integral becomes

$$\tilde{\varepsilon}_d = \varepsilon_d + \int \frac{|\Omega(\omega)|^2 \rho(\omega) d\omega}{\varepsilon_d - \omega + i\gamma(\omega)/2} + \mathcal{O}(\Omega^4). \tag{5.24}$$

For $\gamma \ll \mathcal{D}^5$ this integral can be evaluated using the well known relation

$$\lim_{\gamma \to 0^+} \frac{1}{\varepsilon_d - \omega + i\gamma/2} = -i\pi\delta(\varepsilon_d - \omega) + \mathcal{P}\frac{1}{\varepsilon_d - \omega}, \tag{5.25}$$

In order to obtain the imaginary part of the energy shift, we can ignore the principle part integral $\mathcal{P}$, and obtain the simple result

$$\text{Im}[\varepsilon_d^{(2)}] = -\pi|\Omega(\varepsilon_d)|^2\rho(\varepsilon_d). \tag{5.26}$$

According to Eq. (5.22), we find that to second order in $\Omega(k)$ a particle initially occupying the discrete level will be lost at a rate

$$\Gamma = 2\pi|\Omega(\varepsilon_d)|^2\rho(\varepsilon_d). \tag{5.27}$$

This is the same as the tunneling rate into a lossless continuum given by Fermi's golden rule (more on this later).

---

[5] Really the criteria should be that both $\rho(\omega)$ and $\Omega(\omega)$ vary on energy scales that are large compared to γ. In that case, the integral is well approximated by taking the limit $\gamma \to 0$.

The technical manipulations above can also be described in a simple picture. By coupling to a particular continuum level labeled by k, the discrete level gets an energy shift $\sim \Omega(k)^2/[i\gamma(k)/2 + (\omega(k) - \varepsilon_d)]$, the imaginary part of which is simply

$$\frac{1}{2}\left(\frac{\gamma(k)|\Omega(k)|^2}{\gamma(k)^2/4 + (\omega(k) - \varepsilon_d)^2}\right). \tag{5.28}$$

This function is a Lorentzian peaked around $\omega(k) = \varepsilon_d$, with height $2|\Omega(k)|^2/\gamma(k)$ and width $\gamma(k)/2$. To obtain the total shift in energy to the discrete level, we must take into account the coupling to all $\sim \gamma\rho(\varepsilon_d)$ states that fall within the peak: hence we have $\sim \gamma$ states that contribute an imaginary energy $\sim \gamma^{-1}$, causing the dependence of the loss rate on γ to drop out of the problem.

Case II: $\mathcal{D} \gg \Omega \gg \gamma$

If we were working with a single final state rather than a continuum, it is clear that γ would set the loss rate. Here, however, it is not so clear. In fact, $\gamma(k) \ll \Omega(k)$ is not sufficient to determine the dependence of the loss rate on $\gamma(k)$: one should really compare $\gamma(k)$ to $\Omega(k)^2/\mathcal{D}$, since in the absence of losses the latter quantity sets the time scale for tunneling out of the discrete level. And indeed, since $\mathcal{D} \gg \Omega(k)$, it is possible to have either $\gamma(k) \ll \Omega(k)^2\mathcal{D}^{-1}$ or $\gamma(k) \gg \Omega(k)^2\mathcal{D}^{-1}$ while simultaneously satisfying $\gamma(k) \ll \Omega(k)$.

In this limit the $\gamma(k)$ are not large enough to justify non-degenerate time-independent perturbation theory as above, so we will proceed as one does for Fermi's golden rule. This derivation actually subsumes the discussion in the last section, in that it recovers the behavior of the large $\gamma(k) \gg \Omega(k)$ limit, but it connects more weakly with the Zeno suppression picture.

We begin by writing down the time dependent Schrödinger equation

$$\begin{aligned}\dot{\psi}_d &= i\int dk\, \Omega(k)\psi_k \\ \dot{\psi}_k &= -i\varepsilon(k)\psi_k + i\Omega(k)\psi_d,\end{aligned} \tag{5.29}$$

where the meaning of the ψ's is self evident. Setting $\varepsilon_d = 0$ for notational simplicity, these equations

are equivalent to integro-differential equations that read

$$\psi_k(t) = i\Omega(k)\int_0^t \psi_d(\tau)e^{i\varepsilon(k)(\tau-t)}d\tau \tag{5.30}$$

$$\dot{\psi}_d(t) = -\int_0^t d\tau\; \psi_d(\tau)\int dk\; \Omega(k)^2 e^{i\varepsilon(k)(\tau-t)}. \tag{5.31}$$

An approximation necessary to continue is that the k integral in Eq. (5.31) is very sharply peaked in time around $\tau = t$ (this will be true if both the bandwidth and the energy range of the couplings $\Omega(k)$ are large). In that case, and choosing to keep $\gamma(k) = \gamma$ independent of k, we can set $\psi_d(\tau) = \psi_d(t)$ and $e^{\gamma(\tau-t)} = 1$, and complete the time integration to obtain

$$\begin{aligned}
\dot{\psi}_d(t) &= i\psi_d(t)\int dk\; \Omega(k)^2 \left(\frac{1-e^{i\omega(k)t}}{\omega(k)}\right) \\
&= i\psi_d(t)\int d\omega\; \rho(\omega)\Omega(\omega)^2 \left(\frac{1-e^{i\omega t}}{\omega}\right)
\end{aligned} \tag{5.32}$$

The imaginary part of the term in parentheses is $\sin(\omega t)/\omega$, and becomes $\pi\delta(\omega)$ in the limit $t \to \infty$. Restoring ε_d we obtain the result

$$\dot{\psi}_d(t) = -\psi_d(t)\pi\Omega^2(\varepsilon_d)\rho(\varepsilon_d), \tag{5.33}$$

which leads to Fermi's golden rule for decay of probability to be found in the discrete state:

$$P_d(t) = |\psi_d(t)|^2 = e^{-\Gamma t}, \tag{5.34}$$

$$\Gamma = 2\pi\Omega(\varepsilon_d)^2\rho(\varepsilon_d). \tag{5.35}$$

Now it remains to calculate the time dependence of the continuum population

$$P_c(t) = \int dk\; |\psi_k(t)|^2. \tag{5.36}$$

To do this we return to Eq. (5.30) and, plugging in the result for $\psi_d(t)$, obtain

$$\psi_k(t) = i\Omega(k)\int_0^t e^{-\Gamma\tau/2}e^{i\varepsilon(k)(\tau-t)}d\tau. \tag{5.37}$$

Here we are ignoring that the discrete level, in addition to a lifetime, also inherits a real energy shift from coupling to the continuum. At the end of the calculation this will shift the point at
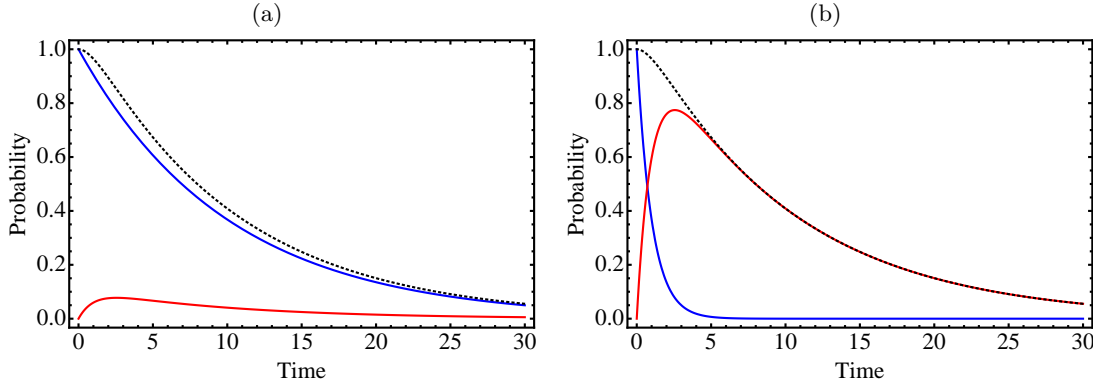
Figure 5.6: Plots of discrete level population $P_d(t)$ (blue line), continuum population $P_c(t)$ (red line), and total population $P(t) = P_d(t) + P_c(t)$ (black dotted line). In (a) $\gamma \gg \Gamma$: the continuum population is suppressed at all times (just as we deduced in the previous section for $\gamma \ll \Omega$) and the discrete level population decays at the limiting rate Γ. In (b) $\gamma \ll \Gamma$: population is quickly transferred into the continuum, where it then decays at the limiting rate γ.

which we evaluate the density of states by an amount which is, by assumption, small compared to the energy scale on which it varies, and hence this shift can be ignored from the outset. Evaluating the time integral we have

$$\psi_k(t) = i\Omega(k)e^{-i\varepsilon(k)t} \left(\frac{e^{i\omega(k)t}e^{(\gamma-\Gamma)t/2} - 1}{i\omega(k) + \frac{1}{2}(\gamma-\Gamma)} \right), \tag{5.38}$$

leading to

$$P_c(t) = e^{-\gamma t} \int d\omega \, \rho(\omega)\Omega(\omega)^2 \left(\frac{1 + e^{(\gamma-\Gamma)t} - 2\cos(\omega t)e^{(\gamma-\Gamma)t/2}}{\omega^2 + \frac{1}{4}(\gamma-\Gamma)^2} \right). \tag{5.39}$$

It is tempting to evaluate this integral by approximating the Lorentzian as a delta function. While this is OK for the first two terms in the numerator, it fails for the third term because, for times $\sim \Gamma^{-1}$, the cosine term has variations on a scale $\delta\omega \sim \Gamma$. This term, however, can be evaluated as a contour integral, and contributes decaying exponentials of argument $(\gamma - \Gamma)$ as might be guessed from the poles. Doing the contour integral and some further algebra, we finally arrive at an equation governing the time dependence of the continuum population:

$$P_c(t) = \frac{\Gamma}{\gamma - \Gamma} \left(e^{-\Gamma t} - e^{-\gamma t} \right). \tag{5.40}$$

Eqs. (5.34) and (5.40) satisfy the coupled rate equations

$$\dot{P}_d = -\Gamma P_d$$

$$\dot{P}_c = \Gamma P_d - \gamma P_c, \tag{5.41}$$

which justify the rate equations used to model molecule loss in section 5.2. The solutions to these equations for the cases $\gamma \gg \Gamma$ and $\gamma \ll \Gamma$ are plotted in Fig. 7.1 to help emphasize the behavior of the system in these two regimes.

Case III: $\mathcal{D} \ll \gamma(k), \Omega(k)$

In the above we have always assumed that the bandwidth is large compared to all other energy scales, but that will not always be the case. If $\mathcal{D} \ll \Omega(k)$, and $\varepsilon_d - \varepsilon(k) \ll \Omega(k)$, there will be a coherent oscillation between the discrete level and the continuum. To see this, let's take the limit $\mathcal{D} \to 0$ while keeping the continuum levels centered on ε_d. In this case, the Hamiltonian reads

$$\mathcal{H} = \int dk \left[\Omega(k) c_d^\dagger c_k + \Omega(k)^* c_k^\dagger c_d \right]. \tag{5.42}$$

By inspection, unnormalized eigenstates of this Hamiltonian are either of the form

$$|\varphi^\pm\rangle = \left(c_d^\dagger \pm \alpha \int dk \, \Omega(k) c_k^\dagger \right) |vac\rangle \tag{5.43}$$

or of the form

$$|\varphi^\alpha\rangle = \left(\int dk \, f_\alpha(k) c_k^\dagger \right) |vac\rangle, \tag{5.44}$$

where the functions $f_\alpha(k)$ satisfy $\int dk \, f_\alpha(k) \Omega(k) = 0$. Acting on $|\varphi^\pm\rangle$ with the Hamiltonian reveals that $\alpha^{-2} = \int dk \, |\Omega(k)|^2$, which results in eigenvalues for $|\varphi^\pm\rangle$

$$\varepsilon^\pm = \pm \sqrt{\int dk \, |\Omega(k)|^2}. \tag{5.45}$$

Despite the continuum of states coupled to $|d\rangle$, there are only two eigenvectors with any weight in the discrete level. Dynamics are restricted to this two-dimensional Hilbert space, and hence coherent oscillations are observed (between $|d\rangle$ and the continuum).

A clear example of the above scenario is a particle tunneling (with matrix element Ω) from a discrete level into one site of an $\mathcal{N}$-site lattice with vanishing bandwidth. Then $\Omega(k) = \Omega/\sqrt{\mathcal{N}}$, $\varepsilon^{\pm} = \pm\Omega$, and the eigenstates $|\varphi^{\pm}\rangle$ are given by:

$$|\varphi^{\pm}\rangle = \left(c_d^{\dagger} \pm \frac{1}{\sqrt{\mathcal{N}}} \int dk \; c_k^{\dagger}\right) |vac\rangle \tag{5.46}$$

The integral in this expression just generates the localized state into which the particle is tunneling. The physical picture is that the particle hops back and forth between the discrete level and the lattice site to which it couples, and never diffuses out into the lattice, which for vanishing bandwidth is obviously correct. A (perhaps) surprising result is that, even in the presence of a finite bandwidth (i.e. a finite hopping t between sites of the lattice), the particle still does not diffuse out into the lattice over time. The reason is that the coupling of one lattice site to a discrete level shifts its energy by an amount $\Omega \gg t$, and hence the coupling of that one site to the rest of the lattice is energetically suppressed. In other words, strong coupling to the discrete level causes the formation of a localized state within the continuum, which never diffuses. If we now add losses in the continuum, the loss dynamics will proceed as they would for a two level system, and hence we have an effective loss rate $\Gamma \sim \gamma$ when $\gamma \ll \Omega$ and $\Gamma \sim \Omega^2/\gamma$ when $\Omega \ll \gamma$.

Chapter 6

Generation of strong correlations via reactive collisions

Many-body entangled states are known to be useful for quantum computing, quantum teleportation and cryptography protocols [84], and precision metrology [66]. With these applications as motivation, the physics community has invested tremendous effort in preparing, stabilizing, and measuring entangled systems. Much of this effort has relied on coherent (Hamiltonian) dynamics to arrive at entangled states starting from less exotic states with only classical correlations. However, these approaches typically suffer from the necessity to either carefully engineer interactions between particles or to prepare extremely pure and specific initial states (or both). A bottom up implementation of coherent control has yielded entangled states of up to 14 atoms with relatively high fidelity [124] (in ion experiments), and a top down approach has yielded weakly entangled states in a Bose Einstein condensate of $\sim 10^4$ neutral atoms [115]. A promising alternative to coherent control is the collective-nondemolition measurement of some observable with a finite variance in an initially classical state. Such approaches have been used to generate entanglement (in the form of spin squeezing) amongst as many as 10^6 cold thermal atoms [22]. However, collective and coherence preserving measurements are generically difficult to make, and the induced non-classical correlations are typically weak.

In this chapter, we show that two-component *spin-incoherent* fermionic gases can be driven by reactive, *s*-wave, two-body collisions into steady-state spin configurations that—for a given value of the saturated particle number—are pure and highly entangled. The entanglement comes in the form of Dicke states [36], in which the spin-wavefunction is fully symmetric under interchange of

the particles (with the burden of fermionic antisymmetry being taken up entirely by the motional degrees of freedom). Such states have been sought in experiments with ultra-cold bosons for use in Heisenberg-limited phase measurements [82], however these approaches typically suffer from the necessity to reach extremely cold temperatures (for the validity of a two-mode approximation in a double-well potential) or to employ Feshbach resonances [75] (to enhance spin exchange interactions for two-component Bose Einstein condensates). The only requirements to achieve such entanglement in the steady-state of lossy non-degenerate fermions are to have an SU(2) invariant single-particle Hamiltonian (in the pseudo-spin degrees of freedom) and a significant separation of timescales between s-wave and p-wave collisions, with the second requirement typically being satisfied for temperatures in or below the μK range.

Because the desired property (i.e. the Dicke type of spin-entanglement) persists in the steady-state of dissipative dynamics, we do not rely on the highly controlled coherent manipulation that is typical of spin-squeezing experiments with bosons. Driven, dissipative preparation of nontrivial steady-states has been considered before in the context of many-body atomic systems [104, 39, 37], and has been achieved recently in [10, 105]. In contrast to these examples, the mechanism described here is intrinsic and generic to a variety of interesting and experimentally relevant systems, such as fermionic alkaline-earth atoms (AEAs) and fermionic dipolar molecules, and does not require any special engineering of the system-reservoir coupling. After presenting calculations in support of our claims, we discuss the possible realization of such steady states in an experiment. In particular, we will propose a simple proof of principle experiment in which the steady-state entanglement can be revealed via Ramsey spectroscopy of the $^1S_0$ to $^3P_0$ clock transition of an AEA [16, 164]. In this case, we will see that the interferometric precision stays relatively constant even as most of the particles are lost (all but $\sim \sqrt{\mathcal{N}}$ in the long time limit), signaling the development of quantum correlations and the pursuant violation of the standard quantum-limit. The total loss of precision (due to loss of particles) exactly cancels the gain due to the growth of quantum correlations. However, a persistent precision under loss of particles can provide enhanced spectroscopic accuracy. In particular, interrogation of an atomic clock with fewer atoms will reduce $p-$wave elastic[112]

and inelastic[116] collisions, which are a leading source of inaccuracy for states immune to s-wave interactions [11] (e.g. spin-polarized fermions).

Our description of spin-$\frac{1}{2}$ fermions with two-body reactive collisions relies on the formalism detailed in Refs. [43, 62, 165], generalized for fermions, where we assume the temperature to be sufficiently low that losses are dominantly in the s-wave channel. As in Ref. [43], large kinetic energy of fermions in the outgoing channels (which for reactive molecules can correspond to temperatures in the 10K range) guarantees they will be rapidly lost from any typical atom trap, justifying a Born-Markov approximation. Given a density matrix ϱ for the system (fermions, Hilbert space $\mathscr{S}$) plus reservoir (outgoing channels of the inelastic collisions, Hilbert space $\mathscr{R}$), the Born-Markov approximation leads to a master equation for the system reduced density matrix $\rho = \text{Tr}_{\mathscr{R}}[\varrho]$ [62]:

$$\hbar\dot{\rho} = i[\rho, \mathcal{H}] - \frac{\kappa}{2} \int d^3\boldsymbol{r} \left(\mathcal{J}^\dagger \mathcal{J} \rho + \rho \mathcal{J}^\dagger \mathcal{J} - 2\mathcal{J}\rho\mathcal{J}^\dagger \right). \tag{6.1}$$

The system Hamiltonian $\mathcal{H} = \mathcal{H}_0 + g \int d^3\boldsymbol{r} \mathcal{J}^\dagger \mathcal{J}$ is composed of an unspecified single-particle term $\mathcal{H}_0$ and an interaction term with coupling constant $g = 4\pi\hbar^2 a_R/m$, where m is the particle mass and $a = a_R + ia_I$ $(a_I < 0)$ is the complex s-wave scattering length. The jump operators are defined by $\mathcal{J}(\boldsymbol{r}) = \psi_\uparrow(\boldsymbol{r})\psi_\downarrow(\boldsymbol{r})$ (their explicit $\boldsymbol{r}$ dependence is suppressed in the integrals above), where $\psi_\sigma(\boldsymbol{r})$ annihilates a fermion located at position $\boldsymbol{r}$ in internal state $\sigma \in \{\uparrow, \downarrow\}$, and $\kappa = -4\pi\hbar^2 a_I/m$. Assuming without loss of generality that the initial number of particles $\mathcal{N}$ is even, the relevant system Hilbert space can be written as a direct sum over spaces with well defined particle number, $\mathscr{S} = \mathscr{S}^\mathcal{N} \oplus \mathscr{S}^{\mathcal{N}-2} \oplus \cdots \oplus \mathscr{S}^0$, between which coherence never develops. Hence, the density matrix can be decomposed into a sum of density matrices in each particle-number sector, any one of which we label by ρ^n once normalized. Furthermore, any Hilbert space $\mathscr{S}^n$ can be decomposed into a direct product between motional (m) and spin (s) degrees of freedom, $\mathscr{S}^n = \mathscr{S}_m^n \otimes \mathscr{S}_s^n$, and we can define a reduced spin density matrix by $\rho_s^n = \text{Tr}_{\mathscr{S}_m}[\rho^n]$. For what follows, it will be useful to define a fidelity in a given Dicke state[1] of the spin degrees of freedom of n particles, $|S = n/2, S^z\rangle$,

---

[1] The Dicke state of n spins having total z projection of spin S^z is obtained by acting on the state with maximal z-projection of total spin $(n/2 - S^z)$ times with the total spin lowering operator S^-.

given by the population of ρ_s^n in the Dicke state

$$\mathcal{F}_{S,S^z} \equiv \langle S, S^z | \rho_s^n | S, S^z \rangle. \tag{6.2}$$

Here S and S^z are quantum numbers for the total spin and its projection along the z-axis, respectively.

6.1 Simple example with two particles in a double well

To make the physics clear in a simple context, we begin by considering two fermions in a single double well potential (which could be formed in an optical super-lattice [2, 168]). We consider a single wavefunction $\varphi_\alpha(\boldsymbol{r})$ in each well ($\alpha \in \{L, R\}$), denote the creation operator for a fermion in spin state σ and wavefunction φ_α by $\psi_{\sigma\alpha}^\dagger$, and choose an initial state $\psi_{\uparrow L}^\dagger \psi_{\downarrow R}^\dagger | vac \rangle$ without spin correlations. Within a tight binding model for these two wavefunctions, the Hamiltonian is

$$\mathcal{H} = -J \sum_\sigma (\psi_{\sigma L}^\dagger \psi_{\sigma R} + \psi_{\sigma R}^\dagger \psi_{\sigma L}) + U \sum_{\alpha=L,R} \mathcal{J}_\alpha^\dagger \mathcal{J}_\alpha, \tag{6.3}$$

and the master equation reads

$$\hbar\dot{\rho} = i[\rho, \mathcal{H}] - \frac{\gamma}{2} \sum_{\alpha=L,R} \left(\mathcal{J}_\alpha^\dagger \mathcal{J}_\alpha \rho + \rho \mathcal{J}_\alpha^\dagger \mathcal{J}_\alpha - 2\mathcal{J}_\alpha \rho \mathcal{J}_\alpha^\dagger \right). \tag{6.4}$$

Here J is the inter-well hopping, $\mathcal{J}_\alpha = \psi_{\uparrow\alpha} \psi_{\downarrow\alpha}$, $U = g \int d^3\boldsymbol{r} |\varphi_\alpha(\boldsymbol{r})|^4$ is the onsite interaction energy, and $\gamma = \kappa \int d^3\boldsymbol{r} |\varphi_\alpha(\boldsymbol{r})|^4$ is the onsite loss rate. The initial state can be decomposed into an evenly weighted superposition of triplet and singlet $[(\psi_{\uparrow L}^\dagger \psi_{\downarrow R}^\dagger \pm \psi_{\downarrow L}^\dagger \psi_{\uparrow R}^\dagger) | vac \rangle$, with plus for the triplet], and the spin wave function of the triplet is the entangled Dicke state $|1, 0\rangle$. The triplet, $|t\rangle$, having a spin wavefunction that is symmetric under exchange, has an orbital wavefunction that is antisymmetric under exchange, and therefore it is "dark" to s-wave losses, by which we mean simply that $\mathcal{J}_L |t\rangle = \mathcal{J}_R |t\rangle = 0$. It also happens to be an eigenstate of $\mathcal{H}$, and so it is stationary under propagation of the master equation (6.4). On the other hand, there are no dark eigenstates in the singlet sector, and as a result ρ_s^2 is pure at long times and satisfies $\mathcal{F}_{1,0} = 1$. In other words the steady state of our system, when restricted to the subspace with two particles, is the entangled
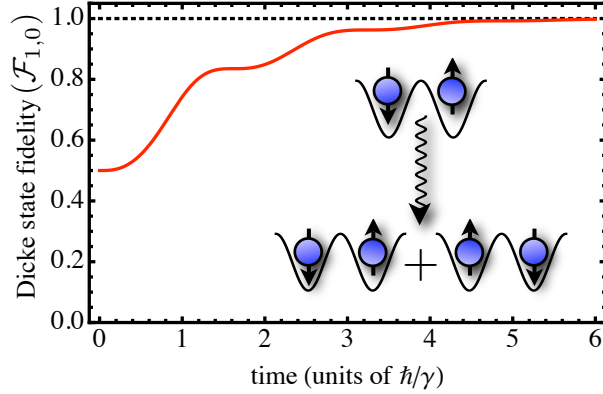
Figure 6.1: The solid red line is the fidelity of the final density matrix (after post-selection for a non-vacant well) with respect to the $S_z = 0$ Dicke state, and approaches 1 (black dotted line) at times long compared to γ^{-1}. The oscillations imposed over the exponential decay are due to the inter-well hopping.

Dicke state $|1,0\rangle$. It should be noted that there is also a 50% probability of obtaining the vacuum, and hence in an array of double wells the entanglement fidelity is only unity after post-selection of the non-vacant wells. In this simple example we see an important general feature of the physics we will discuss, that even purely *local* (intra-well) dissipation, when coexisting with Hamiltonian dynamics that delocalizes the particles, generates *non-local* (inter-well) spin correlations in the steady state.

6.2   Extension to many particles

Solving Eq. (7.20) exactly for initial states with $\mathcal{N} > 2$ initial particles quickly becomes impossible, but strong statements can nevertheless be made regarding the steady state. It is crucial to observe that the jump operators only remove spin singlets from the system, which follows from Fermi statistics combined with the even exchange symmetry of the spatial part of any two-particle wave function susceptible to s-wave scattering. Intuitively, this suggests that losses do not decrease the expectation value of the total spin, $\boldsymbol{S} = \frac{1}{2} \int d^3 \boldsymbol{r} \psi_\sigma^\dagger(\boldsymbol{r}) \boldsymbol{\tau}_{\sigma\sigma'} \psi_{\sigma'}(\boldsymbol{r})$ ($\boldsymbol{\tau}$ being a vector whose components are the Pauli matrices). Mathematically, we say that $\frac{d}{dt}\langle \boldsymbol{S} \cdot \boldsymbol{S} \rangle = \mathrm{Tr}[\rho \boldsymbol{S} \cdot \boldsymbol{S}] = 0$, which can easily be verified in the case when $\mathcal{H}$ is SU(2) invariant by checking that $[\boldsymbol{S} \cdot \boldsymbol{S}, \mathcal{J}(\boldsymbol{r})] = 0$.

A stronger consequence of the commutation of all $\mathcal{J}(\boldsymbol{r})$ with $\boldsymbol{S} \cdot \boldsymbol{S}$ is that population in any sector of total spin, $\mathcal{P}_S$, is also conserved. Because any state with well defined total spin S must have $\langle \hat{N} \rangle \geq 2S$ particles (where $\hat{N} = \int d^3\boldsymbol{r}\,\psi_\sigma^\dagger \psi_\sigma$ is the total number operator), an immediate consequence is that the loss of particles can only yield the vacuum deterministically at long times if the initial state is a total spin-singlet. For an uncorrelated spin state, such as a non-degenerate thermal distribution of $\mathcal{N}$ fermions in a balanced incoherent mixture of $\uparrow$ and $\downarrow$, it can be shown that [6]

$$N(t) \equiv \mathrm{Tr}[\rho \hat{N}] \geq \sum_S 2S\mathcal{P}_S = \frac{\pi^{1/2}\Gamma\left[\frac{\mathcal{N}}{2} + 1\right]}{\Gamma[\frac{\mathcal{N}}{2} + \frac{1}{2}]} - 1, \tag{6.5}$$

which places a lower bound on the steady-state expectation value for the number of particles $N(t)$. This expectation value determines the particle number in a typical steady-state configuration, and is achieved (on average) *without* any post selection, but variations of the steady-state particle number will occur from shot to shot. Taking Stirling's approximation for large $\mathcal{N}$ yields an approximate bound $N(t) \gtrsim \sqrt{\pi\mathcal{N}/2}$. For the chosen restriction on the initial state, the validity of Eq. (6.5) depends only on the SU(2) invariance of $\mathcal{H}$, and not on its precise form. Whether the bound (6.5) is saturated in the steady-state, however, is an important and delicate issue. The bound is only saturated when, in every sector of total spin S, there are *exactly* $\mathcal{N}_S = 2S$ particles. Because the latter condition is only satisfied by Dicke states, saturation of Eq. (6.5) guarantees that all of the ρ_s^n describe pure Dicke states in the steady-state. Demonstrating that this bound is indeed saturated in certain experimentally relevant situations, namely a 1D harmonic trap and a 1D Hubbard chain (optical lattice), is a central technical result of this chapter.

Saturation of the bound in Eq. (6.5) is guaranteed if, for any fixed value of n and S_z, the pure density matrix $|n/2, S_z\rangle\langle n/2, S_z|$ is the *unique* steady-state reduced spin density matrix. This uniqueness, in turn, is equivalent to requiring that any dark-state with quantum numbers n and S_z has a well defined spin wavefunction given by the Dicke state $|n/2, S_z\rangle$. In Appendix F we prove this to be true for a 1D harmonic oscillator potential, and we have verified it numerically for a 1D Hubbard chain (section 6.2.1). It is worth noting at this point that, while the equivalence of
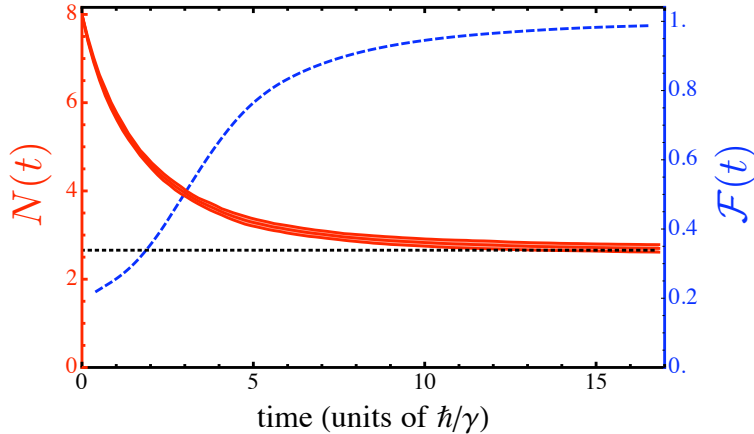
Figure 6.2: Calculation of particle number [$N(t)$, solid red line] and average Dicke state fidelity [$\mathcal{F}(t)$, dashed blue line] for an 8-site Hubbard chain via quantum trajectories. For the number, the shaded region is an estimate of the statistical error from sampling of a finite number of trajectories. The black dotted line is the analytic bound in Eq. (6.5).

dark-states with the Dicke states is intuitive, there are natural Hamiltonians for which this intuition is incorrect. In particular, all Hamiltonians in $D > 1$ that are separable in cartesian coordinates do have dark-states with $\mathcal{F}_{S,S_z} < 1$.

6.2.1 Numerics for a finite Hubbard chain

In order to verify the above statements numerically, we have performed quantum trajectories simulations for an 8-site Hubbard chain with open boundary conditions, an initial filling of one particle per site, and zero polarization ($\mathcal{N} = 8$ and $S_z = 0$). In general we have lower-densities in mind for any experimental application, but using one particle per site allows us to stretch the numerics to the largest $\mathcal{N}$ possible. In Fig. 6.2 we show the calculated particle number and average Dicke state fidelity, $\mathcal{F}(t) = \frac{1}{4} \sum_{S=1}^{4} \mathcal{F}_{S,0}$, and one can see that the former saturates the bound Eq. (6.5) while the latter approach unity at long times. For this calculation we solve for $\mathcal{O}(10^4)$ trajectories with no approximation.

6.3   Experimental implementation

Dicke states are known to be useful for a variety of quantum information protocols, including but not limited to quantum secret sharing [137], teleportation [96], and sub shot-noise limited precision spectroscopy [82]. Here we give a brief description of how the proposed Dicke state preparation could be used in precision spectroscopy of the clock transition in alkaline-earth atoms. For a fixed interrogation time, spectroscopy on $\mathcal{N}$ uncorrelated atoms has a phase sensitivity $\delta\varphi \gtrsim 1/\sqrt{\mathcal{N}}$, a bound known as the standard quantum limit (SQL). This bound can be understood as the minimum tipping angle needed to cause a coherent spin state (CSS) to have an uncertainty cone that precludes its initial position [15] (to one standard deviation). On the other hand, spectroscopy on a Dicke state of $\mathcal{N}$ particles with spin $S_z = 0$ has the potential to approach the Heisenberg limit (HL) of phase sensitivity, $\delta\varphi \sim 1/\mathcal{N}$ [82, 15]. It is important to realize that the production of Dicke states with $\sqrt{\mathcal{N}}$ fermions via two-particle loss does not actually enhance the phase sensitivity relative to the initial state with $\mathcal{N}$ fermions; the enhancement in phase sensitivity between the SQL and HL exactly compensates the reduction of particle number. However, the reduced particle number in the Dicke state and darkness to *real* s-wave interactions (which if present generate clock shifts), can render the accuracy of the final Dicke state superior to that of the initial $\mathcal{N}$ fermion uncorrelated state.

Rather than allowing losses amongst a macroscopic sample of atoms, for which the approach to the steady state could be quite slow, we imagine an array of $\mathcal{T}$ 1D tubes created by a 2D optical lattice. Although there will be variations in the atom number from tube to tube, for simplicity we take each tube to have exactly $\mathcal{N}$ fermionic AEAs in the $^1S_0$ electronic state and $I^z = I$ nuclear-spin state, denoted $|^1S_0, I\rangle$. For the analysis in this chapter to be valid, the temperature should be small compared to the vibrational level-spacing in the transverse tube direction, and also low enough that only the harmonic part of the trapping potential along the tube axis is sampled by the atoms. A $\pi/2$-pulse on the spin degrees of freedom $[|^1S_0, I\rangle \rightarrow \frac{1}{\sqrt{2}}(|^1S_0, I\rangle + |^1S_0, I-1\rangle)]$, followed by single

particle dephasing,[2] generates a statistical mixture of the two spin states ($I^z = I$ and $I^z = I - 1$). Losses can be initiated by applying a π-pulse on the clock transition ($|^1S_0, I^z\rangle \to |^3P_0, I^z\rangle$). We estimate that this π-pulse[3] can be achieved on the $\lesssim 100\mu s$ timescale without exciting transverse excitations in the tubes (which, if present, violate the assumption of a 1D geometry and destroy the uniqueness of the steady-state). Thus the transfer into $^3P_0$ is sufficiently fast that it can be considered instantaneous on the initial timescale of reactive collisions—which, based on universal considerations for a Lieb-Liniger gas, we estimate to be $\gtrsim$ 1ms for experimentally relevant 1D densities [43]—such that it suddenly initiates strong 2-body s-wave losses.

The steady state of the system is a statistical mixture of Dicke states in the different tubes, each having some value of $\mathcal{D}_j$ particles (centered around $\mathcal{D}_0 \approx \sqrt{\mathcal{N}}$) and spin projection S_j^z (centered around zero). Spin selective transfer of $|^3P_0, I-1\rangle$ into $|^1S_0, I\rangle$ maps the spin degree of freedom onto the clock states, leaving a spin-polarized sample, and Ramsey spectroscopy on the clock transition can then be performed [15]. Despite the fluctuation of both $\mathcal{D}_j$ and S_j^z from one tube to another, it can be shown (see Appendix G) that the minimum resolvable rotation angle in a Ramsey experiment scales as

$$\delta\varphi_{\min} \sim 1/\mathcal{D}_0\sqrt{\mathcal{T}}. \tag{6.6}$$

This result can be interpreted as the existence of Heisenberg scaling ($\sim 1/\mathcal{D}_0$) of phase-sensitivity for each tube, which is then combined between tubes in a statistically independent manner (hence the $1/\sqrt{\mathcal{T}}$). In order to utilize this phase sensitivity, the initial value of $S^z = \sum_j S_j^z$ for the entire ensemble must be accurately known. Because S^z is conserved by the losses, it can be measured before transfer to the $^3P_0$, and hence the measurement does not need to preserve any inter-particle correlations (since these develop during the losses). Accurate measurements of this type and precision for $\sim$ 100 atoms in an optical cavity have recently been demonstrated [177].

The primary limitations on the final state fidelity achievable in experiments is likely to be

---

[2] Dephasing of nuclear spins is typically extremely slow, but can be briefly enhanced with large magnetic field gradients or by scattering photons on a cycling transition.

[3] This transfer needs to be of high fidelity, since any atoms remaining in the $^1S_0$ state can undergo s-wave collisions with $^3P_0$ atoms that *do* reduce the system spin. In principle, the purity of this transfer could be enhanced by using an optical pumping scheme.
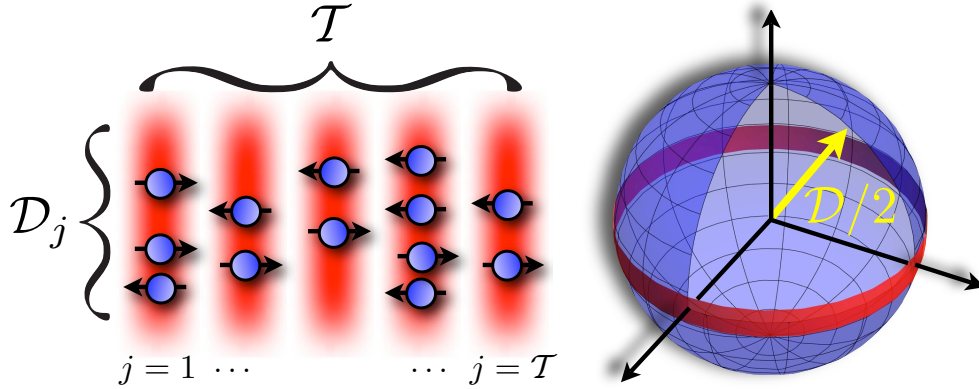
Figure 6.3: (a) An array of $\mathcal{T}$ 1D tubes, each having $\mathcal{D}_j$ atoms in a Dicke state. (b) Bloch sphere representation of a Dicke state in a particular tube.

a combination of finite p-wave losses (which the Dicke states are not dark to) and magnetic field gradients. At sub μK temperatures, the s-wave losses in a spin mixture of ^{87}Sr are expected to be about an order of magnitude faster than the p-wave losses [11]. For reactive molecules (or ^{171}Yb), where the inelastic collisions are expected to more fully saturate the unitarity bound [116], this separation of rates will most likely be even larger. Magnetic field gradients couple sectors of different total S, all of which are separated from the Dicke manifold by a gap for finite systems and nonzero a_R, so in principle their adverse effects can be suppressed to first order [143]. Furthermore, if the two components of the Fermi gas are two nuclear spin states of an AEA, they will be extremely insensitive to magnetic field gradients: We estimate that typical gradients (1mG/cm) will cause spin dephasing on a 100s timescale for a linear system size of 100μm. This timescale is several orders of magnitude longer than the initial two-body loss rate in tightly confined 1D tubes, which we estimate to be on the order of 10ms for ^{87}Sr (assuming a $50E_{\mathrm{R}}$ 2D lattice and scaling the density dependent loss rate from Ref. [11]), and even faster for ^{171}Yb [116]. A more quantitative analysis of the effects of both magnetic field imperfections and finite p-wave losses requires numerical simulations beyond the scope of this work, and is left for future study.

Chapter 7

Long-ranged Ising models with decoherence

7.1   Introduction

In the previous chapter, we specifically sought out atomic and molecular systems with strong dissipation, and we saw a concrete example of how the competition between dissipation and coherent dynamics can result in robust entanglement[104, 37, 52]. However, because *no* physical system is truly closed to the environment, there is a much broader sense in which this competition is important. While decoherence generally tends to degrade correlations in quantum systems, it is now widely appreciated that it can also give rise to many-body physics not possible with strictly coherent dynamics [38, 32, 111]. Regardless of whether one's intention is to minimize or to harness decoherence, determining its effect on interacting many-body systems is central to quantum simulation[12], quantum information [84], and quantum metrology [66].

So far, this understanding has been hindered by the computational complexity of numerical techniques for open systems and the scarcity of exact analytic solutions. Exact solutions for dynamics of interacting quantum systems in dimensions greater than one are rare even in the absence of decoherence, and to our knowledge no such solutions have been obtained in the presence of local decoherence. In this chapter, we describe a comprehensive toolbox for calculating far-from-equilibrium dynamics in open spin-systems with arbitrary Ising interactions. These results are applicable to a broad range of important quantum systems, including trapped ions [17, 97, 87], polar molecules [126, 70], Rydberg atoms [171, 114], neutral atoms in optical cavities [67, 162], optical lattice clocks [164], superconducting qubits[26], quantum dots[77], and nitrogen vacancy centers[136]. In

particular, we will focus on applications of these results to trapped ions because: (1) the relative importance of decoherence and coherently driven quantum correlations is controllable, (2) the tunable long-ranged interactions are generically frustrated, making large-scale numerical simulations impractical, and (3) these experiments are the most developed, with non-equilibrium dynamics already being explored [17].

Taking the Penning trap experiments at NIST [17] as an example, but keeping in mind the generality of these models, the proceeding sections make incremental progress toward an exact solution for both the transverse spin length and spin-spin correlation functions for a spin system that is (1) initialized in an arbitrary uncorrelated state (2) interacting via long-ranged Ising-interactions, and (3) coupled to the environment via the most general form of local Markovian decoherence allowed by nature. The extension to arbitrary initial product states provides significantly more general comparison with the standard Ramsey-type experiments that are used to probe these ions, and the dynamics of correlation functions is crucial to the calculation of spin-squeezing, which is of significant practical importance for precision-metrology. In general, the calculations presented open the possibility of benchmarking trapped-ion quantum simulators—with nearly all of their imperfections accounted for—in parameter regimes where the mean-field description is completely inadequate.

We will begin in Sec. 7.2 by discussing the dynamics of both the transverse (xy-plane) spin-components (the longitudinal spin component is preserved in coherent dynamics) and arbitrary spin-spin correlation functions. In Sec. 7.3, we will describe how (within the Born-Markov approximation) these same observables can be calculated along particular quantum-trajectories, where spontaneous photon-scattering events are taken into account via random applications of "quantum jump operators". Even though these jumps do not commute with the Ising dynamics, we will show how a particular trajectory can nevertheless be dealt with analytically. In Sec. 7.4 stochastic averaging over the occurrences of such jumps will be carried out analytically, yielding a closed-form solution for the spin-length and correlation functions. As an example of the experimental relevance of these calculations, in section 7.5 we discuss how they will enable a careful benchmarking of the

$^9\mathrm{Be}^+$ ion quantum simulator at NIST [17] in the strongly interacting regime. In that experiment, the time scale at which quantum correlations become important, τ_c, typically scales with some power of the ion number $\mathcal{N}$ (e.g. $\sim \mathcal{N}^{1/3}$ for spin-squeezing, or $\sim \mathcal{N}^{1/2}$ for transverse-spin relaxation). And, under current operating conditions, this scaling ensures that quantum fluctuations become important on timescales comparable to the spin-decoherence time. It is crucial, therefore, to approach these experiments with a theory that treats quantum fluctuations and dissipation on an equal footing, and the present work accomplishes precisely that goal.

7.2 Coherent dynamics for arbitrary initial product states

Though our main goal is to study dynamics in the presence of decoherence, we will begin more simply by considering strictly coherent dynamics. Such a strategy will enable us to introduce notation more slowly, and also to gain intuition for why the problem remains tractable when decoherence is included. Moreover, there is quite a bit of new physics to be described even for the strictly coherent evolution; the form of the correlation functions we derive was not previously known, and the types of initial states to which the calculation can be applied are significantly more general than was previously realized [45, 140, 92].

There is also a close connection between coherent and incoherent dynamics which we will exploit throughout the chapter. While we often study decoherence effects by describing the time evolution of a master equation, this is only an ensemble-averaged description of reality. Real dynamics of systems coupled to environments is often better thought of as Hamiltonian-like evolution disrupted by random projective measurements (made by the environment). This point of view is formally encapsulated in the quantum trajectories method, and naturally it would be hard to proceed with a calculation based on this perspective without first developing an understanding of the coherent evolution of the system.

7.2.1   Hamiltonian and initial conditions

We consider dynamics under a Hamiltonian of the form

$$\mathcal{H} = \frac{1}{\mathcal{N}} \sum_{i>j} J_{ij} \hat{\sigma}_i^z \hat{\sigma}_j^z + \sum_j h_j \hat{\sigma}_j^z, \tag{7.1}$$

which arrises naturally in the context of trapped ion experiments. The creation of such a Hamiltonian for ions is an elaborate and beautiful story in its own right, and there are many excellent references for the interested reader [135]. Here we just mention the essential physical ingredients: (1) The spin states correspond to the 2 qubit levels of an alkaline-earth ion, (2) these two spin states can be addressed via Raman lasers in such a way as to create spin dependent forces on the ions, (3) the spin-dependent motion of a single ion couples to the rest of the ions through the coulomb interaction, and hence an effective spin-spin interaction is realized. We consider initial pure states of the form

$$|\psi(0)\rangle = \bigotimes_j \left[\cos\left(\theta_j/2\right) e^{i\varphi_j/2} |\uparrow\rangle_j + \sin\left(\theta_j/2\right) e^{-i\varphi_j/2} |\downarrow\rangle_j \right]. \tag{7.2}$$

When all of the θ_j and φ_j are equal, this state can easily be created in experiments via optical pumping of all ions to the north (or south) pole of the bloch sphere and then applying a strong Rabi drive to rotate the ions into their final configuration. The generalization to spatially dependent angles could be useful in modeling the effects of a slightly inhomogeneous Rabi drive, which would cause the initial spin direction to vary in space. Because it is the simplest non-trivial observable, we will begin by computing the transverse spin-length in the x direction (because of the arbitrary azimuthal angle in the initial state, the restriction of measurements to the x axis causes no loss of generality):

$$\langle S^x(t) \rangle \equiv \sum_j \langle \psi(t) | \hat{\sigma}_j^x | \psi(t) \rangle. \tag{7.3}$$

7.2.2 Calculation of transverse spin length

We're actually going to calculate $\langle\psi(t)|\hat{\sigma}_j^+|\psi(t)\rangle$, and at the end we'll obtain

$$\langle S^x(t)\rangle = \text{Re}\left(\sum_j \langle\psi(t)|\hat{\sigma}_j^+|\psi(t)\rangle\right) \tag{7.4}$$

First some notation, let's write the state of a single spin as

$$|\psi\rangle_j = \sum_{\sigma_j^z} f_j(\sigma_j^z)|\sigma_j^z\rangle, \tag{7.5}$$

where σ_j^z is an index that takes on the eigenvalues of the operator $\hat{\sigma}_j^z$. So $f_j(1) = \cos(\theta_j/2)\,e^{i\varphi_j/2}$ and $f_j(-1) = \sin(\theta_j/2)\,e^{-i\varphi_j/2}$. Now we can write the (time-dependent) wavefunction as

$$|\psi(t)\rangle = \sum_{\sigma_1^z,\ldots,\sigma_\mathcal{N}^z} \exp\left[it\left(\frac{1}{\mathcal{N}}\sum_{i>j}J_{ij}\sigma_i^z\sigma_j^z + \sum_j h_j\sigma_j^z\right)\right] f_1(\sigma_1^z)\times\cdots\times f_\mathcal{N}(\sigma_\mathcal{N}^z)|\sigma_1^z,\ldots,\sigma_\mathcal{N}^z\rangle. \tag{7.6}$$

Let's imagine, in particular, calculating $\langle\psi(t)|\hat{\sigma}_1^+|\psi(t)\rangle$ (there is nothing special about the first spin, this just makes the notation in what follows less confusing). Because the wavefunction enters twice, this would involve two sums like the one in Eq. (7.34), over σ_j^z and $\tilde{\sigma}_j^z$, but very few terms survive: We need $\sigma_1^z = -1$, $\tilde{\sigma}_1^z = 1$, and for all $j \neq 1$ we must have $\sigma_j^z = \tilde{\sigma}_j^z$, so the matrix element is

$$\langle\psi(t)|\hat{\sigma}_1^+|\psi(t)\rangle = f_1^*(1)f_1(-1)\sum_{\sigma_2^z,\ldots,\sigma_\mathcal{N}^z}|f_2(\sigma_2^z)|^2\times\cdots\times|f_\mathcal{N}(\sigma_\mathcal{N}^z)|^2\exp\left[-2it\left(\frac{1}{\mathcal{N}}\sum_{j=2}^\mathcal{N}J_{1j}\sigma_j^z + h_1\right)\right]. \tag{7.7}$$

The exponential simply factors into products

$$\langle\psi(t)|\hat{\sigma}_1^+|\psi(t)\rangle = f_1^*(1)f_1(-1)e^{-2ith_1}\sum_{\sigma_2^z,\ldots,\sigma_\mathcal{N}^z}|f_2(\sigma_2^z)|^2\times\cdots\times|f_\mathcal{N}(\sigma_\mathcal{N}^z)|^2 e^{-2itJ_{12}\sigma_2^z/\mathcal{N}}\times\cdots\times e^{-2itJ_{1\mathcal{N}}\sigma_\mathcal{N}^z/\mathcal{N}}. \tag{7.8}$$

Therefore, we can write

$$\langle S_1^x(t)\rangle = \text{Re}\left(f_1^*(1)f_1(-1)e^{-2ith_1}\prod_{j=2}^\mathcal{N}\sum_{\sigma_j^z}|f_j(\sigma_j^z)|^2 e^{-2itJ_{1j}\sigma_j^z/\mathcal{N}}\right), \tag{7.9}$$

or, for the expectation value $\langle S^x(t)\rangle$,

$$\langle S^x(t)\rangle = \text{Re}\left(\sum_{i=1}^\mathcal{N} f_i^*(1)f_i(-1)e^{-2ith_i}\prod_{j\neq i}\sum_{\sigma_j^z}|f_j(\sigma_j^z)|^2 e^{-2itJ_{ij}\sigma_j^z/\mathcal{N}}\right). \tag{7.10}$$

This expression can easily be evaluated for a large number of spins. In the case when all of the spins point in the $+x$ direction initially, we have $f_i(-1) = f_i(1) = 1/\sqrt{2}$, and this result simplifies to

$$
\begin{aligned}
\langle S^x(t) \rangle &= \frac{1}{2} \mathrm{Re} \left(\sum_{i=1}^{\mathcal{N}} e^{-2ith_i} \prod_{j \neq i} \sum_{\sigma_j^z} \frac{1}{2} e^{-2itJ_{ij}\sigma_j^z/\mathcal{N}} \right), \\
&= \frac{1}{2} \sum_{i=1}^{\mathcal{N}} \cos(2th_i) \prod_{j \neq i} \cos(2tJ_{ij}/\mathcal{N}).
\end{aligned}
\tag{7.11}
$$

7.2.3 Extension to quenched disorder

In many potential realizations of quantum Ising models in cold-atoms context, such as with polar molecules or Rydberg atoms, relatively large defect density will most likely need to be taken into account [78](this is typically not a concern with ions). Shot-to-shot averaging in an experiment (or even a single shot if the observable is self-averaging and the system is large) really measures the disorder average of observables. If the distribution of defects is uncorrelated from site to site, they can be taken into account by assigning probabilities p_j of having a spin on site j and a probability $1 - p_j$ of having no spin on site j. This probability is kept site-dependent; it might arise, e.g. from the spatial variation of chemical potential in an local-density-approximation. We assign a variable to each site, η_j, with $\eta_j = 0$ when the jth site is empty and $\eta_j = 1$ when the jth site is full. We can write discrete probability distributions for the variables η_j, $\mathcal{P}_j(\eta_j)$, such that

$$
\mathcal{P}_j = \begin{cases} p_j & \text{if } \eta_j = 1; \\ 1 - p_j & \text{if } \eta_j = 0. \end{cases}
\tag{7.12}
$$

For a given realization of the η_j, direct application of Eq. (7.10) yields

$$
\langle S^x(\eta_1, \ldots, \eta_{\mathcal{N}}) \rangle = \mathrm{Re} \left(\sum_{i=1}^{\mathcal{N}} \eta_i f_i^*(1) f_i(-1) e^{-2ith_i} \prod_{j \neq i} \sum_{\sigma_j^z} |f_j(\sigma_j^z)|^2 e^{-2itJ_{ij}\sigma_j^z \eta_j/\mathcal{N}} \right).
\tag{7.13}
$$

We have suppressed the explicit time dependence of $\langle S^x(t) \rangle$ in order to emphasize the dependence on the η_j. Notice that the η_i inside the first sum enforces that when summing $\langle S_i^x \rangle$ over all sites only sites with spins on them contribute. The η_j in the exponent enforces that a spin flip on site i

only affects the system energy due to the coupling J_{ij} if there is also a spin on site j. The ensemble averaged spin length is then given by,

$$
\begin{aligned}
\overline{\langle S^x(t)\rangle} &\equiv \sum_{\eta_1,\ldots,\eta_\mathcal{N}} \mathcal{P}_1(\eta_1) \times \cdots \times \mathcal{P}_\mathcal{N}(\eta_\mathcal{N}) \langle S^x(\eta_1,\ldots,\eta_\mathcal{N})\rangle, \\
&= \mathrm{Re}\left(\sum_{\eta_1,\ldots,\eta_\mathcal{N}} \mathcal{P}_1(\eta_1) \times \cdots \times \mathcal{P}_\mathcal{N}(\eta_\mathcal{N}) \sum_{i=1}^{\mathcal{N}} \eta_i f_i^*(1) f_i(-1) e^{-2ith_i} \prod_{j\neq i}\sum_{\sigma_j^z} |f_j(\sigma_j^z)|^2 e^{-2itJ_{ij}\sigma_j^z\eta_j/\mathcal{N}}\right) \\
&= \mathrm{Re}\left(\sum_{i=1}^{\mathcal{N}}\sum_{\eta_i} \mathcal{P}_i(\eta_i)\eta_i f_i^*(1) f_i(-1) e^{-2ith_i} \prod_{j\neq i}\sum_{\sigma_j^z,\eta_j} \mathcal{P}_j(\eta_j)|f_j(\sigma_j^z)|^2 e^{-2itJ_{ij}\sigma_j^z\eta_j/\mathcal{N}}\right) \\
&= \mathrm{Re}\left(\sum_{i=1}^{\mathcal{N}} p_i f_i^*(1) f_i(-1) e^{-2ith_i} \prod_{j\neq i}\sum_{\sigma_j^z,\eta_j} \mathcal{P}_j(\eta_j)|f_j(\sigma_j^z)|^2 e^{-2itJ_{ij}\sigma_j^z\eta_j/\mathcal{N}}\right). \quad (7.14)
\end{aligned}
$$

As before, this expression can easily be evaluated for a large number of spins.

7.2.4 Extension to products of operators (spin-spin correlation functions)

In addition to calculating the spin length, it is useful for a variety of purposes to calculate arbitrary off-diagonal $(i \neq j)$ spin-spin correlation functions of the form

$$
\begin{aligned}
\mathcal{G}_{ij}^{+-} &= \langle\psi(t)|\sigma_i^+\sigma_j^-|\psi(t)\rangle \\
\mathcal{G}_{ij}^{-+} &= \langle\psi(t)|\sigma_i^-\sigma_j^+|\psi(t)\rangle = (\mathcal{G}_{ij}^{+-})^* \\
\mathcal{G}_{ij}^{++} &= \langle\psi(t)|\sigma_i^+\sigma_j^+|\psi(t)\rangle \\
\mathcal{G}_{ij}^{--} &= \langle\psi(t)|\sigma_i^-\sigma_j^-|\psi(t)\rangle = (\mathcal{G}_{ij}^{++})^* \\
\mathcal{G}_{ij}^{+z} &= \langle\psi(t)|\sigma_i^+\sigma_j^z|\psi(t)\rangle \\
\mathcal{G}_{ij}^{-z} &= \langle\psi(t)|\sigma_i^-\sigma_j^z|\psi(t)\rangle = (\mathcal{G}_{ij}^{+z})^* \quad (7.15)
\end{aligned}
$$

Diagonal correlation functions $(i = j)$ can always be rewritten in terms of single-spin expectation values using identities for Pauli matrices, and so we do not calculate them here.

Let's start with $\mathcal{G}_{ij}^{+-}$. In this case, the operators in the expectation value only connect two states if $\tilde{\sigma}_i^z = -\sigma_i^z = 1$, $\tilde{\sigma}_j^z = -\sigma_j^z = -1$, and $\tilde{\sigma}_k^z = \sigma_k^z$ whenever $k \notin \{i,j\}$. Therefore, much as before we

have

$$\mathcal{G}_{ij}^{+-} = f_i^*(1)f_i(-1)f_j^*(-1)f_j(1)e^{-2it(h_i-h_j)} \prod_{k \notin \{i,j\}} \sum_{\sigma_k^z} |f_k(\sigma_k^z)|^2 e^{-2it\sigma_k^z(J_{ik}-J_{jk})/\mathcal{N}} \tag{7.16}$$

Similar considerations lead us to

$$\mathcal{G}_{ij}^{++} = f_i^*(1)f_i(-1)f_j^*(1)f_j(-1)e^{-2it(h_i+h_j)} \prod_{k \notin \{i,j\}} \sum_{\sigma_k^z} |f_k(\sigma_k^z)|^2 e^{-2it\sigma_k^z(J_{ik}+J_{jk})/\mathcal{N}} \tag{7.17}$$

Correlation functions such as $\mathcal{G}_{ij}^{+z}$ are an even simpler extension of the single-spin expectation values from the last section, since they just require an insertion of σ_j^z into the sum

$$\mathcal{G}_{ij}^{+z} = f_i^*(1)f_i(-1)e^{-2ith_i} \left(\sum_{\sigma_j^z} \sigma_j^z |f_j(\sigma_j^z)|^2 e^{-2itJ_{ij}\sigma_j^z/\mathcal{N}} \right) \prod_{k \notin \{i,j\}} \sum_{\sigma_k^z} |f_k(\sigma_k^z)|^2 e^{-2itJ_{ik}\sigma_k^z/\mathcal{N}} \tag{7.18}$$

7.3   Effects of decoherence

7.3.1   Introduction

In addition to considering dynamics induced by the Hamiltonian

$$\mathcal{H} = \frac{1}{\mathcal{N}} \sum_{i>j} J_{ij}\hat{\sigma}_i^z\hat{\sigma}_j^z, \tag{7.19}$$

we would ultimately like to understand spin-dynamics in the presence of both Rayleigh (Γ_{el}) and Raman ($\Gamma_{\mathrm{r}} = \Gamma_{\mathrm{ud}} + \Gamma_{\mathrm{du}}$) decoherence, which are both present and in general non-negligible in the Penning trap experiments. The effect of these different decoherence mechanisms is shown schematically in Fig. 7.1. Because of the decoherence the system-reduced density operator does not remain pure; equivalently, the system becomes entangled with the environment, and any description of the system alone must therefore be statistical in nature (beyond the usual sense in which the system wavefunction has a statistical interpretation). Making the Born-Markov approximation, which physically means that we assume photons leave quickly on the time-scale of system dynamics
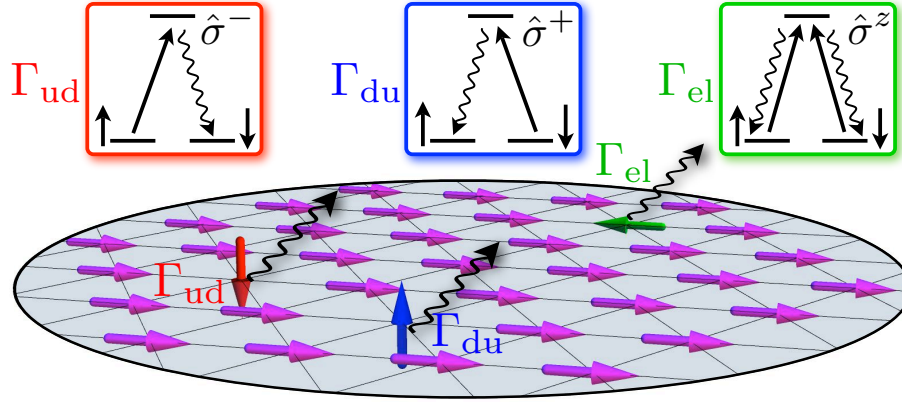
Figure 7.1: Schematic illustration of the NIST experiment, where 100's of $^9\text{Be}^+$ ions reside in a 2D triangular lattice. Off resonant light scattering via intermediate P electronic levels gives rise to both Raman scattering (red and blue arrows, rates Γ_{ud} and Γ_{du}, respectively) and elastic dephasing (green arrow, Γ_{el}).

and never return,[1] the density matrix obeys a master equation in the Lindblad form

$$
\begin{aligned}
\hbar\dot{\rho} &= -i\left[\mathcal{H}, \rho\right] \\
&+ \frac{\Gamma_{\text{du}}}{2} \sum_j \left(2\hat{\sigma}_j^+ \rho \hat{\sigma}_j^- - \rho \hat{\sigma}_j^- \hat{\sigma}_j^+ - \hat{\sigma}_j^- \hat{\sigma}_j^+ \rho \right) \\
&+ \frac{\Gamma_{\text{ud}}}{2} \sum_j \left(2\hat{\sigma}_j^- \rho \hat{\sigma}_j^+ - \rho \hat{\sigma}_j^+ \hat{\sigma}_j^- - \hat{\sigma}_j^+ \hat{\sigma}_j^- \rho \right) \\
&+ \frac{\Gamma_{\text{el}}}{8} \sum_j \left(2\hat{\sigma}_j^z \rho \hat{\sigma}_j^z - 2\rho \right).
\end{aligned}
\tag{7.20}
$$

The second and third lines of Eq. 7.20 account for the effects of spontaneous excitation and spontaneous relaxation, respectively. The fourth line has a similar structure[2] with the jump operators $\hat{\sigma}^\pm$ being replaced by the jump operator $\hat{\sigma}^z$. Because the application of $\hat{\sigma}^z$ to a spin-wavefunction rotates it by π radians in the xy plane, this term gives rise to pure dephasing, i.e. a loss of coherence without any change in population.

We will approach the solution to Eq. 7.20 in the quantum trajectory formalism [133]. Here one imagines a particular trajectory where the system remains in a pure state, but undergoes jumps

---

[1] For spontaneous emission of photons by an atom, this approximation is generally extremely well satisfied. Typical atom sizes are $\lesssim 10^{-10}$m, which means that emitted photons are "gone" in 10^{-10}m$/c \sim 10^{-18}$s, *much* faster than any other relevant atomic-physics timescales.

[2] The difference in structure is superficial, and is remedied be remembering that $\hat{\sigma}^z \hat{\sigma}^z = 1$ and then rewriting $2\rho \to (\rho \hat{\sigma}^z \hat{\sigma}^z + \hat{\sigma}^z \hat{\sigma}^z \rho)$.

(sudden changes to its state-vector) due to the decoherence processes. The desired observable is computed as a function of time along many such trajectories, and then these results are averaged. This procedure yields results that converge (with an error given by statistical fluctuations that vanish in the limit of infinite trajectories) to the exact solution of the master equation.

7.3.2 General prescription for calculating a trajectory

Operational aspects of the quantum trajectories method are described in detail in Ref. [133], but there are some special features of this particular application of the method that warrant discussion. Equation (7.20) is often rearranged as

$$\dot{\rho} = i\left(\mathcal{H}_{\text{eff}}\rho - \rho\mathcal{H}_{\text{eff}}^{\dagger}\right) - \frac{\Gamma_{\text{du}}}{2}\sum_j 2\hat{\sigma}_j^+ \rho\hat{\sigma}_j^- - \frac{\Gamma_{\text{ud}}}{2}\sum_j 2\hat{\sigma}_j^- \rho\hat{\sigma}_j^+ - \frac{\Gamma_{\text{el}}}{8}\sum_j 2\hat{\sigma}_j^z \rho\hat{\sigma}_j^z, \tag{7.21}$$

where the effective (*non-Hermitian*) Hamiltonian $\mathcal{H}_{\text{eff}}$ is given by

$$\mathcal{H}_{\text{eff}} = \mathcal{H} + i\sum_j\left(\frac{\Gamma_{\text{du}}}{2}\hat{\sigma}_j^-\hat{\sigma}_j^+ + \frac{\Gamma_{\text{ud}}}{2}\hat{\sigma}_j^+\hat{\sigma}_j^- + \frac{\Gamma_{\text{el}}}{8}\right). \tag{7.22}$$

$$= \mathcal{H} + i\sum_j\left(\frac{\Gamma_{\text{r}}}{4} + \gamma\hat{\sigma}_j^z + \frac{\Gamma_{\text{el}}}{8}\right). \tag{7.23}$$

Here we have defined $\Gamma_{\text{r}} = \Gamma_{\text{ud}} + \Gamma_{\text{du}}$ and $\gamma = \frac{1}{4}(\Gamma_{\text{ud}} - \Gamma_{\text{du}})$. A quantum trajectory is obtained by time-evolving the initial pure state $|\psi\rangle$ under $\mathcal{H}_{\text{eff}}$, with the time evolution interspersed with sudden applications of the jump operators $\hat{\sigma}_j^-$, $\hat{\sigma}_j^+$, and $\hat{\sigma}_j^z$. The prescription for applying the jump operators is as follows:

(1) Time evolve $|\Psi\rangle$ under $\mathcal{H}_{\text{eff}}$, stopping when $\langle\psi|\psi\rangle = r$, with r a random number between 0 and 1. This defines the time t_1 at which the first jump occurs. Note that this only makes sense because $\mathcal{H}_{\text{eff}}$ is non-Hermitian, and hence the norm of $|\psi\rangle$ decays in time.

(2) To choose which decoherence process occurs, we assign to each jump operator a probability

given by

$$P_j^+ = \frac{\Gamma_{du}}{2} \frac{\langle \psi(t_1)|\hat{\sigma}_j^-\hat{\sigma}_j^+|\psi(t_1)\rangle}{P} \qquad P_j^- = \frac{\Gamma_{ud}}{2} \frac{\langle \psi(t_1)|\hat{\sigma}_j^+\hat{\sigma}_j^-|\psi(t_1)\rangle}{P} \qquad P_j^z = \frac{\Gamma_{el}}{8} \frac{\langle \psi(t_1)|\hat{\sigma}_j^z\hat{\sigma}_j^z|\psi(t_1)\rangle}{P},$$

$$\text{(7.24)}$$

where $P = \sum_j (P_j^+ + P_j^- + P_j^z)$ provides a normalization of the total probability to unity, and then select a jump operator according to this distribution.

(3) Take the jump operator selected in (2), let's call it J, and apply it to $|\psi(t_1)\rangle$ to obtain a new (normalized) wave function immediately after the jump

$$|\psi\rangle(t_1 + \varepsilon)\rangle = \frac{J|\psi(t_1)\rangle}{\sqrt{\langle \psi(t_1 + \varepsilon)|J^\dagger J|\psi(t_1 + \varepsilon)\rangle}}. \qquad \text{(7.25)}$$

This new wavefunction is then fed back into step (1), and the process continues until the final time is reached. It is very important that the jump times and jump operators selected by repeating steps (1) through (3) do not depend on the phases of the wavefunction components in the Ising basis. This is because both $\mathcal{H}_{eff}$ and the operators whose expectation values are calculated in step (2) are diagonal in this basis. As a result, whether or not $\mathcal{H}$ is included in $\mathcal{H}_{eff}$ has no bearing on the selection of jump times or jump operators. Therefore, when choosing trajectories (sets of random jumps) it is perfectly legitimate to ignore the coherent evolution completely. In this case, we truly have a single particle problem: If we want a single trajectory for $\mathcal{N}$ spins, we can create $\mathcal{N}$ trajectories for a single spin, and then assign each trajectory to a particular spin in the lattice. As a result, the time required to select a trajectory scales linearly with the number of ions, and never poses any difficulty.

7.3.3 Analytic calculation of a single trajectory for uniform J_{ij} and $\Gamma_{ud} = \Gamma_{du}$

In this section, we describe how the expectation value $\langle S^x(t)\rangle$ can be calculated analytically along a particular trajectory. To introduce the essential simplifications that allow us to proceed with this calculation, we focus initially on the case of all to all coupling ($J_{ij} = J$), all initial spins

pointed in the x-direction, and $\Gamma_{\mathrm{ud}} = \Gamma_{\mathrm{du}}$. The generalization to arbitrary couplings, arbitrary initial product states, and $\Gamma_{\mathrm{ud}} \neq \Gamma_{\mathrm{du}}$ will be considered in the next section.

From Sec. 7.2 we have an exact solution for the dynamics of $\mathcal{N}$ initially pointing in the $+x$-direction, evolving coherently under the Hamiltonian

$$\mathcal{H}(h, \mathcal{N}) = \frac{J}{\mathcal{N}} \sum_{i>j}^{\mathcal{N}} \hat{\sigma}_i^z \hat{\sigma}_j^z + h \sum_j^{\mathcal{N}} \hat{\sigma}_j^z. \tag{7.26}$$

In particular, the expectation value $\langle S^x(t) \rangle \equiv \mathrm{Re}\left[\sum_j \langle \psi(t) | \hat{\sigma}_j^+ | \psi(t) \rangle \right]$ is given by

$$\langle S^x(t) \rangle = \frac{\mathcal{N}}{2} \cos(2ht) \cos\left(2Jt/\mathcal{N}\right)^{\mathcal{N}-1}. \tag{7.27}$$

It turns out that it is possible to use this expression to calculate the dynamics along a trajectory exactly, which we now show.

A particular trajectory for $\mathcal{N}$ spins consists of a set of jumps due to the Rayleigh and Raman processes (Fig. 7.2(a) for $\mathcal{N} = 2$). The Rayleigh processes involve the application of some $\hat{\sigma}_j^z$ to the
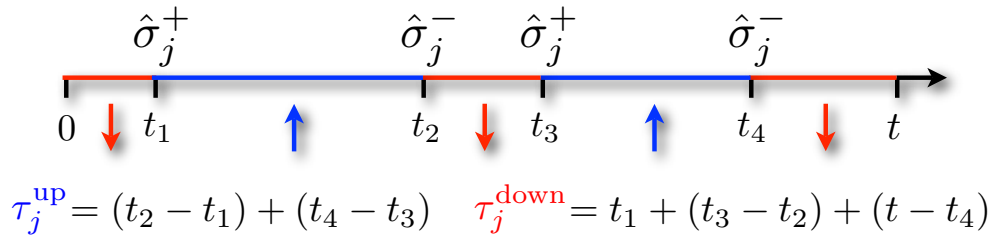
Figure 7.2: A series of Raman flips of the spin on site j can be formally accounted for as a magnetic field of strength $2J_{jk}/\mathcal{N}$ acting for a time $\tau_j^{\mathrm{up}} - \tau_j^{\mathrm{down}}$.

wave function, which changes the sign on any states in the $\sigma^z = -1$ configuration, and hence turns $|+x\rangle$ into $|-x\rangle$. The Raman terms flip spins either from up to down or from down to up (along z). Raman and Raleigh processes on different sites obviously commute, but they do not commute on the same site. However, this turns out to be irrelevant: since a Raman process for spin j projects it either into $|\sigma_j^z = 1\rangle$ or into $|\sigma_j^z = -1\rangle$, whether a Rayleigh process on that site occurs—and

whether it happens before or after the Rayleigh process—can only determine the overall sign of the wavefunction. Hence, if in the trajectory a Rayleigh process occurs on the same site as a Raman process, the Rayleigh process can be ignored completely. All Rayleigh processes that occur on sites for which there is no Raman process commute with the dynamics (both due to Raman flips and the coherent evolution), and hence can be implemented at $t = 0$, yielding an equivalent trajectory.

Now the Raman terms do not commute with the coherent dynamics, and it may seem important to keep track of when they happened, but this is only partially true. Consider the spin flip at time t_1 in Fig. 7.2. The application of $\hat{\sigma}_j^+$ projects out all parts of the wave function that, immediately before t_1, had $\sigma_1^z = 1$, and also enforces that all parts of the wavefunction immediately after t_1 have $\sigma_1^z = 1$. It is as if the spin 1 pointed down before t_1 and down after t_1, and since both states are eigenstates of σ_1^z, this spin has not participated in the coherent dynamics. It does, however, have an influence on the remaining spins, since it couples to them via the spin-spin coupling as an effective magnetic field h, which pointed up before t_1 and down after t_1. Now, the effect of a field along z that switches from down to up is straightforward to take into account: Because at all times the dynamics induced by this field commutes with that induced by the Ising coupling, all that matters is the total time that the field spends pointing in a particular direction. When there are multiple spin flips to spin j [see Fig. 7.2(b)], such as $\hat{\sigma}_j^+(t_1) \times \sigma_j^-(t_2) \times \sigma_j^+(t_3) \times \sigma_j^-(t_4)$, similar reasoning can be applied. Now spin j spends a time $\tau_j^{\text{down}} = t_1 + (t_3 - t_2) + (t - t_4)$ in the down configuration (remember that we can think of it as having pointed down before the first spin flip) and time $\tau_j^{\text{up}} = (t_2 - t_1) + (t_4 - t_3)$ in the up configuration. Assuming that $\tau_j^{\text{up}} - \tau_j^{\text{down}} = -t + 2t_4 - 2t_3 + 2t_2 - 2t_1 > 0$, this is equivalent to a magnetic field of strength $\eta = J/\mathcal{N}$ that has pointed up for a time $\tau_j = \tau_j^{\text{up}} - \tau_j^{\text{down}}$.

The $\mathcal{R}$ spins which have been affected at least once by a Raman process do note contribute to $\langle S^x(t) \rangle$ (since they have a well-defined value of σ^z), and so they are really just spectators that induce dynamics in the remaining $\mathcal{N} - \mathcal{R}$ spins (as time dependent fields of strength $2J/\mathcal{N}$, acting for a total time $\tau = \sum_j \tau_j$). The remaining spins evolve in time according to Eq. 7.27, and therefore

$\langle S^x(t) \rangle$ can be calculated explicitly:

$$\langle S^x(t) \rangle = \frac{\mathcal{N} - \mathcal{R} - 2\mathcal{F}}{2} \cos(2J\tau/\mathcal{N}) \cos\left(2Jt/\mathcal{N}\right)^{\mathcal{N}-\mathcal{R}-1}. \tag{7.28}$$

If we want to obtain $S^x(t) \equiv \text{Tr}\left[S^x\rho\right]$ as given by the master equation, we need to average the result obtained by Eq. (7.28) over many random realizations of these trajectories.

There is one subtlety that hasn't been mentioned yet, which is that time evolution under the effective Hamiltonian in general changes the *magnitude* of the wavefunction coefficients in the Ising basis, whereas the solutions up until now only account for the time evolution of the phases (assuming the magnitudes are constant). For $\Gamma_{\text{ud}} = \Gamma_{\text{du}} = \Gamma_{\text{r}}/2$, this is no problem: The effective Hamiltonian given in Eq. (7.23) simplifies to

$$\begin{aligned} \mathcal{H}_{\text{eff}} &= \mathcal{H} + i\sum_j \left(\frac{\Gamma_{\text{r}}}{4} \overbrace{\left[\hat{\sigma}_j^- \hat{\sigma}_j^+ + \hat{\sigma}_j^+ \hat{\sigma}_j^-\right]}^{\text{Identity}} + \frac{\Gamma_{\text{el}}}{8} \right). \\ &= \mathcal{H} + i\sum_j \left(\frac{\Gamma_{\text{r}}}{4} + \frac{\Gamma_{\text{el}}}{8} \right). \tag{7.29} \end{aligned}$$

The anti-Hermitian part which decays the wavefunction norm is proportional to the identity operator, and hence reduces the magnitude of all wavefunction coefficients at the same rate. Since the wavefunction is always normalized when calculating expectation values along a trajectory, the effect of this decay can be ignored. The situation for $\Gamma_{\text{ud}} \neq \Gamma_{\text{du}}$ is more complicated, but still tractable, as we will discuss in the next section.

Combined with averaging over stochastically generated trajectories, these results constitute an (essentially) exact numerical prescription for calculating $\langle S^x(t) \rangle$ in the presence of Raman and Rayleigh decoherence, which can be evaluated with fairly high precision (relative uncertainties of $\lesssim 10^{-4}$ are feasible). It should be noted, however, that while the scaling of the solution difficulty with ion number is favorable, the scaling with desired precision is not (exponential in the number of digits). Therefore, it could be useful in some situations to have expressions that do not rely on

stochastic sampling of trajectories. The task of obtaining such expressions, by carrying out the stochastic averaging analytically, will be taken up in Sec. 7.4.

7.3.4 Dynamics along a trajectory when $\Gamma_{\mathrm{ud}} \neq \Gamma_{\mathrm{du}}$ and for arbitrary J_{ij}

Now that we have described how $\langle S^x(t) \rangle$ can be calculated for all-to-all coupling and equal up/down Raman flipping rates, we will generalize the calculation to accomodate:

(1) A discrepancy between the up and down scattering rates ($\Gamma_{\mathrm{ud}} \neq \Gamma_{\mathrm{du}}$).

(2) Arbitrary couplings between the various spins (rather than the all-to-all coupling of the previous section).

(3) Arbitrary initial product states.

The considerations of the previous section regarding selection of jump times and jump operators along a trajectory remain valid, so the generalization requires only that we can actually calculate $\langle S^x(t) \rangle$ along an arbitrary trajectory. The effective Hamiltonian for which dynamics must be computed is

$$\mathcal{H}_{eff} = \frac{1}{\mathcal{N}} \sum_{i>j} J_{ij} \hat{\sigma}_i^z \hat{\sigma}_j^z + \sum_j \eta_j \hat{\sigma}_j^z + i \sum_j \left(\frac{\Gamma_{\mathrm{r}}}{4} \overbrace{\left[\hat{\sigma}_j^- \hat{\sigma}_j^+ + \hat{\sigma}_j^+ \hat{\sigma}_j^- \right]}^{\text{Identity}} + \frac{\Gamma_{\mathrm{el}}}{8} \right). \tag{7.30}$$

Here J_{ij} are the arbitrary spin-spin Ising couplings, $\eta_j = \frac{1}{\mathcal{N}t} \sum_k J_{jk} \tau_k$ is an inhomogeneous magnetic field that arrises from the Raman flipped spins and their coupling to the unflipped spins (just as before, but now the field is inhomogeneous because the J_{ij} are inhomogeneous). Dropping anti-Hermitian parts of $\mathcal{H}_{\mathrm{eff}}$ that are proportional to the identity, and defining $\gamma = (\Gamma_{\mathrm{ud}} - \Gamma_{\mathrm{du}})/4$, we can rewrite this as

$$\mathcal{H}_{\mathrm{eff}} = \frac{1}{\mathcal{N}} \sum_{i>j} J_{ij} \hat{\sigma}_i^z \hat{\sigma}_j^z + \sum_j \eta_j \hat{\sigma}_j^z + i\gamma \sum_j \hat{\sigma}_j^z. \tag{7.31}$$

The discrepancy between Γ_{ud} and Γ_{du} shows up as an imaginary magnetic field along z, which causes the spins to drift out of the xy-plane.

Because the couplings (and possibly the initial state) are now inhomogeneous, it will be necessary to keep track of the number of Rayleigh and Raman jumps for each individual site ($\mathcal{F}_j$ and $\mathcal{R}_j$), rather than just the total number of such jumps for the entire system. It will also be useful to define local variables

$$\alpha_j = \delta_{\mathcal{R}_j,0} \qquad \beta_j = (-1)^{\mathcal{F}_j}. \tag{7.32}$$

As before, we write the state of a single spin as $\sum_{\sigma_j^z} f_j(\sigma_j^z)|\sigma_j^z\rangle$, where σ_j^z is an index that takes on the eigenvalues of the operator $\hat{\sigma}_j^z$, $f_j(1) = \cos(\theta_j/2)\, e^{i\varphi_j/2}$, and $f_j(-1) = \sin(\theta_j/2)\, e^{-i\varphi_j/2}$. The initial state of the entire system is taken to be a direct product of states for each individual spin

$$
\begin{aligned}
|\psi(0)\rangle &\equiv \bigotimes_j \sum_{\sigma_j} f_j(\sigma_j)|\sigma_j\rangle && \text{(7.33)} \\
&= \sum_{\sigma_1^z,\ldots,\sigma_{\mathcal{N}}^z} f_1(\sigma_1^z) \times \cdots \times f_{\mathcal{N}}(\sigma_{\mathcal{N}}^z)|\sigma_1^z,\ldots,\sigma_{\mathcal{N}}^z\rangle.
\end{aligned}
$$

Evaluating all or the Rayleigh jumps at $t = 0$ can be accomplished by changing $\varphi_j \to \varphi_j + \pi\mathcal{F}_j$, which rotates the spin on site j by an angle π if it has undergone an odd number of Rayleigh jumps. Raman jumps can be incorporated at $t = 0$ by setting $\theta_j = 0(\pi)$ if the final Raman jump on site j was $\hat{\sigma}_j^+ (\hat{\sigma}_j^-)$. We therefore define $\tilde{f}_j(\sigma_j^z)$ to be the modification of $f_j(\sigma_j^z)$ under those transformations. We also note that, as discussed in Sec. 7.3.3, spins having undergone one or more Raman jumps are treated as an effective magnetic field, and not included in the spin-spin coupling term of the Hamiltonian. In addition to the inclusion of magnetic fields η_j, this requires that we change $J_{ij} \to \alpha_i\alpha_j J_{ij}$ in the Hamiltonian. Therefore, we can write the (time-dependent) wavefunction $|\tilde{\psi}(t)\rangle$ evolving under the effective Hamiltonian as

$$|\tilde{\psi}(t)\rangle = \sum_{\sigma_1^z,\ldots,\sigma_{\mathcal{N}}^z} \exp\left[-it\left(\frac{1}{\mathcal{N}}\sum_{i>j}\alpha_i\alpha_j J_{ij}\sigma_i^z\sigma_j^z + \sum_j(\eta_j - i\gamma)\sigma_j^z\right)\right]\tilde{f}_1(\sigma_1^z) \times \cdots \times \tilde{f}_{\mathcal{N}}(\sigma_{\mathcal{N}}^z)|\sigma_1^z,\ldots,\sigma_{\mathcal{N}}^z\rangle.$$
$$\tag{7.34}$$

Here, and everywhere that follows, the tilde over the wavefunction indicates that the jumps pertaining to some particular trajectory have been applied to the initial state. In order to calculate

the transverse spin-length we will first calculate $\tilde{\sigma}_j^+ = \langle\tilde{\psi}(t)|\hat{\sigma}_j^+|\tilde{\psi}(t)\rangle/\langle\tilde{\psi}(t)|\tilde{\psi}(t)\rangle$, and at the end obtain

$$\tilde{S}^x(t) = \text{Re}\left(\sum_j \tilde{\sigma}_j^+\right) \tag{7.35}$$

Let's imagine, in particular, calculating $\langle\tilde{\psi}(t)|\hat{\sigma}_1^+|\tilde{\psi}(t)\rangle$ (there is nothing special about the first spin, this just makes the notation in what follows less confusing). Because the wavefunction enters twice, this would involve two sums like the one in Eq. (7.34), over σ_j^z and $\sigma_j'^z$, but very few terms survive: We need $\sigma_1^z = -1$, $\sigma_1'^z = 1$, and for all $j \neq 1$ we must have $\sigma_j^z = \sigma_j'^z$, so the matrix element is given by

$$\langle\tilde{\psi}(t)|\hat{\sigma}_1^+|\tilde{\psi}(t)\rangle = \tag{7.36}$$
$$\tilde{f}_1^*(1)\tilde{f}_1(-1)\sum_{\sigma_2^z,\ldots,\sigma_\mathcal{N}^z}|\tilde{f}_2(\sigma_2^z)|^2 \times \cdots \times |\tilde{f}_\mathcal{N}(\sigma_\mathcal{N}^z)|^2\exp\left[2it\left(\eta_1 + \sum_{j=2}^\mathcal{N}\frac{1}{\mathcal{N}}\alpha_1\alpha_j J_{1j}\sigma_j^z + i\alpha_j\gamma\sigma_j^z\right)\right].$$

If $\alpha_j = 0$, the jth spin always has a well defined value of σ_j^z and the choice to include the term $\gamma\sigma_j^z$ in the exponentiated sum (or not) affects only the overall normalization of the wavefunction. By multiplying γ by α_j (in the exponentiated sum), we have chosen to not include the term $\gamma\sigma_j^z$, and this is properly accounted for when normalizing this expectation value below. In order to obtain $\langle\hat{\sigma}_1^+\rangle$ we must divide by the (non-conserved) normalization of the wavefunction $\langle\tilde{\psi}(t)|\tilde{\psi}(t)\rangle$. Defining $g_j(x) = \sum_\sigma |f_j(\sigma)|^2 e^{-\sigma x}$, we obtain

$$\langle\hat{\sigma}_1^+\rangle = \frac{\tilde{f}_1^*(1)\tilde{f}_1(-1)}{g_1(2\gamma t)}\sum_{\sigma_2^z,\ldots,\sigma_\mathcal{N}^z}\frac{|\tilde{f}_2(\sigma_2^z)|^2}{g_2(2\alpha_2\gamma t)} \times \cdots \times \frac{|\tilde{f}_\mathcal{N}(\sigma_\mathcal{N}^z)|^2}{g_\mathcal{N}(2\alpha_\mathcal{N}\gamma t)}$$
$$\times \quad \exp\left[2it\left(\eta_1 + \sum_{j=2}^\mathcal{N}\frac{1}{\mathcal{N}}\alpha_1\alpha_j J_{1j}\sigma_j^z + i\alpha_j\gamma\sigma_j^z\right)\right]. \tag{7.37}$$

This expression can be simplified by making the following set of observations: (1) $\tilde{f}_1^*(1)\tilde{f}_1(-1) = \alpha_1\beta_1 e^{i\varphi_1}\sin(\theta_1)/2$, (2) the α_1 in the exponent is irrelevant, because if it takes the value 0 the entire expression for $\langle\tilde{\psi}(t)|\hat{\sigma}_1^+|\tilde{\psi}(t)\rangle$ vanishes, and (3) the summand factorizes into a product where each term contains only local (i.e. on a single site) variables, and hence the sum of products can be

exchanged for a product of sums. Taking (1-3) into account we obtain

$$\langle \hat{\sigma}_1^+ \rangle = \frac{\sin(\theta_1)e^{i\varphi_1}}{2g_1(2\gamma t)}\alpha_1\beta_1 \prod_{j=2}^{\mathcal{N}} \left(\sum_{\sigma_j^z} \frac{|\tilde{f}_j(\sigma_j^z)|^2}{g_j(2\alpha_j\gamma t)} \exp\left[2it\alpha_j\sigma_j^z\left(J_{1j}/\mathcal{N}+i\gamma\right)\right]e^{2iJ_{1j}\tau_j/\mathcal{N}}\right). \quad (7.38)$$

$$= \frac{\sin(\theta_1)e^{i\varphi_1}}{2g_1(2\gamma t)}\alpha_1\beta_1 \prod_{j=2}^{\mathcal{N}} \left(e^{2iJ_{1j}\tau_j/\mathcal{N}}\frac{g_j[2\alpha_j t(\gamma - iJ_{1j}/\mathcal{N})]}{g_j(2\gamma t\alpha_j)}\right). \quad (7.39)$$

Therefore, we can write

$$\langle \hat{S}^x \rangle = \text{Re} \sum_{j=1}^{\mathcal{N}} \left[\frac{\sin(\theta_j)e^{i\varphi_1}}{2g_j(2\gamma t)}\alpha_j\beta_j \prod_{k\neq j} \left(e^{2iJ_{jk}\tau_k/\mathcal{N}}\frac{g_k[2\alpha_k t(\gamma - iJ_{jk}/\mathcal{N})]}{g_k(2\gamma t\alpha_k)}\right)\right]. \quad (7.40)$$

The calculation of correlation functions follows from extremely similar considerations. For instance, let's consider $\mathcal{G}_{jk}^{-+} \equiv \langle \hat{\sigma}_j^- \hat{\sigma}_k^+ \rangle$. In this case, the operators in the expectation value only connect two states if $-\sigma_j'^z = \sigma_j^z = 1$, $\sigma_k'^z = -\sigma_k^z = 1$, and $\sigma_l'^z = \sigma_l^z$ whenever $l \notin \{j,k\}$. Therefore, much as before we have

$$\mathcal{G}_{jk}^{-+} = \frac{\sin(\theta_j)\sin(\theta_k)e^{i(\varphi_k-\varphi_j)}}{4g_j(2\gamma t)g_k(2\gamma t)}\alpha_j\alpha_k\beta_j\beta_k \prod_{l\notin\{j,k\}} \left(e^{2i(J_{kl}-J_{jl})\tau_l/\mathcal{N}}\frac{g_l[2\alpha_l t(\gamma - i[J_{kl}-J_{jl}]/\mathcal{N})]}{g_l(2\gamma t\alpha_l)}\right). \quad (7.41)$$

Computing correlation functions involving a single $\hat{\sigma}^z$, such as $\mathcal{G}_{jk}^{z+} \equiv \langle \hat{\sigma}_j^z \hat{\sigma}_k^+ \rangle$ can be achieved by inserting σ_j^z into the sum in Eq. (7.37), yielding

$$\mathcal{G}_{jk}^{z+} = \frac{\sin(\theta_k)e^{i\varphi_k}\alpha_k\beta_k}{2g_k(2\gamma t)}\left[\alpha_j\frac{\cos^2(\theta/2)e^{-2\gamma t} - \sin^2(\theta/2)e^{2\gamma t}}{g_j(2\gamma t)} + (1-\alpha_j)\kappa_j\right]$$

$$\times \prod_{l\notin\{j,k\}} \left(e^{2iJ_{kl}\tau_l/\mathcal{N}}\frac{g_l[2\alpha_l t(\gamma - iJ_{kl}/\mathcal{N})]}{g_l(2\gamma t\alpha_l)}\right). \quad (7.42)$$

Assuming one or more Raman flip occurred, the variable κ_j takes on the values ± 1 if the final Raman jump is $\hat{\sigma}_j^\pm$.

7.4   Analytic evaluation of stochastic averages

At this point in the calculation, for clarity of presentation, we set $\varphi_j = 0$ and $\theta_j = \pi/2$ (for all j), so all spins point along the x axis at $t = 0$. Defining $\mathcal{P}(\mathcal{R},\mathcal{F},\tau)$ to be the probability distribution of the variables $\mathcal{R}$, $\mathcal{F}$, and τ on a single site (it is the same on every site), the trajectory averaged

expectation value is given by

$$\overline{\langle \hat{\sigma}_j^+ \rangle} = \sum_{\text{all } \mathcal{R}} \sum_{\text{all } \mathcal{F}} \int d\tau_1 \ldots \int d\tau_{\mathcal{N}} \langle \hat{\sigma}_j^+ \rangle \prod_k \mathcal{P}(\mathcal{R}_k, \mathcal{F}_k, \tau_k). \tag{7.43}$$

To begin, we note that the probability distribution can be decomposed as

$$\mathcal{P}(\mathcal{R}, \mathcal{F}, \tau) = \mathcal{P}_{\text{el}}(\mathcal{F}) \mathcal{P}_{\text{r}}(\mathcal{R}, \tau), \tag{7.44}$$

which is valid because the probability of Rayleigh jump is independent of whether a Raman jump has occurred (and vice versa). The occurrence of random processes follows a Poissonian distribution, so

$$\mathcal{P}_{\text{el}}(\mathcal{F}) = e^{-\Gamma_{\text{el}}t/4} (\Gamma_{\text{el}}t/4)^{\mathcal{F}} / \mathcal{F}!, \tag{7.45}$$

and we have also calculated $\mathcal{P}_{\text{r}}$. The result depends on whether $\mathcal{R}$ is even or odd (the proof is simple but requires some careful reasoning, and we do not give it here). We parameterize the $\mathcal{R}$-odd solution by $\mu = (\mathcal{R} - 1)/2$ (which will run over all non-negative integers), and we parameterize the $\mathcal{R}$-even solutions by $\mu = (\mathcal{R} - 2)/2$ (once again running μ over all nonnegative integers), and obtain

$$\mathcal{P}_{\text{r}}^{\text{odd}}(\mu, \tau) = \frac{\Gamma_{\text{r}}}{4} e^{-\Gamma_r t/2} \frac{(\Gamma_{\text{ud}}\Gamma_{\text{du}}/4)^{\mu}}{(\mu!)^2} e^{-2\tau\gamma}(t^2 - \tau^2)^{\mu} \tag{7.46}$$

$$\mathcal{P}_{\text{r}}^{\text{even}}(\mu, \tau) = \frac{\Gamma_{\text{ud}}\Gamma_{\text{du}}t}{4} e^{-\Gamma_r t/2} \frac{(\Gamma_{\text{ud}}\Gamma_{\text{du}}/4)^{\mu}}{\mu!(\mu+1)!} e^{-2\tau\gamma}(t^2 - \tau^2)^{\mu}. \tag{7.47}$$

By evaluating the sum

$$\sum_{\mathcal{F}=0}^{\infty} \mathcal{P}_{\text{el}}(\mathcal{F}) e^{i\pi\mathcal{F}} = e^{-\Gamma_{\text{el}}t/2}, \tag{7.48}$$

we obtain

$$\overline{\langle \hat{\sigma}_j^+ \rangle} = \frac{e^{-\Gamma_{\text{el}}t/2}}{2\cosh(2\gamma t)} \sum_{\mathcal{R}_1, \ldots \mathcal{R}_{\mathcal{N}}} \int d\tau_1 \ldots \int d\tau_{\mathcal{N}} \tag{7.49}$$

$$\times \left[\mathcal{P}(\mathcal{R}_j, \tau_j) \alpha_j \prod_{k \neq j} e^{2iJ_{jk}\tau_k/\mathcal{N}} \frac{\cosh[2\alpha_k t(\gamma - iJ_{jk}/\mathcal{N})]}{\cosh(2\gamma t\alpha_k)} \mathcal{P}_{\text{r}}(\mathcal{R}_k, \tau_k) \right]$$

$$= \frac{e^{-\Gamma_{\text{el}}t/2}}{2\cosh(2\gamma t)} \left[\sum_{\mathcal{R}_j} \int d\tau_j \alpha_j \mathcal{P}(\mathcal{R}_j, \tau_j) \right] \tag{7.50}$$

$$\times \left[\prod_{j \neq k} \sum_{\mathcal{R}_k} \int d\tau_k e^{2iJ_{jk}\tau_k/\mathcal{N}} \frac{\cosh[2\alpha_k t(\gamma - iJ_{jk}/\mathcal{N})]}{\cosh(2\gamma t\alpha_k)} \mathcal{P}_{\text{r}}(\mathcal{R}_k, \tau_k) \right].$$

Because α_j gives 1 if there have not been any Raman flips at site j and 0 otherwise, the term in the first square bracket is just the probability that there has been no Raman flip on site j, which is given by $e^{-\Gamma_r t/2} \cosh(2\gamma t)$ [this comes from evolving the wavefunction of a single spin pointing along x with the effective Hamiltonian Eq. (7.30)]. Defining $\Gamma = \frac{1}{2}(\Gamma_{\mathrm{el}} + \Gamma_r)$, we have

$$\overline{\langle \hat{\sigma}_j^+ \rangle} = \frac{1}{2} e^{-\Gamma t} \times \left[\prod_{j \neq k} \sum_{\mathcal{R}_k} \int d\tau_k e^{2iJ_{jk}\tau_k/\mathcal{N}} \frac{\cosh[2\alpha_k t(\gamma - iJ_{jk}/\mathcal{N})]}{\cosh(2\gamma t\alpha_k)} \mathcal{P}_{\mathrm{r}}(\mathcal{R}_k, \tau_k) \right] \tag{7.51}$$

Defining $s = 2i\gamma + 2J/\mathcal{N}$, the trick is now to evaluate the quantity

$$\begin{aligned}
\Phi(J, t) &= \sum_{\mathcal{R}} \int d\tau \mathcal{P}(\mathcal{R}, \tau) e^{2iJ\tau/\mathcal{N}} \frac{\cosh(ist\alpha)}{\cosh(2\gamma t\alpha)} \tag{7.52} \\
&= e^{-\Gamma_r t/2} \cosh(ist) + \sum_{\mathcal{R}=1}^{\infty} \int d\tau \mathcal{P}(\mathcal{R}, \tau) e^{2iJ\tau/\mathcal{N}}.
\end{aligned}$$

The second equality follows from pulling off the $\mathcal{R} = 0$ term in the sum, which represents the probability of having no Raman flip (and so we can set $\tau = 0$ and $\alpha = 1$ in this term). The second term represents the probability for any finite number of Raman flips, and hence we must keep τ arbitrary but can set $\alpha = 0$. The integral over τ can be evaluated by using the identity

$$\int_{-t}^{t} d\tau (t^2 - \tau^2)^{\mu} e^{-ix\tau} = (2t)^{\mu+1} \frac{j_\mu(xt)\mu!}{(x)^\mu}, \tag{7.53}$$

where j is a spherical Bessel function. The remaining sum over $\mathcal{R}$ can be recognized as a generating function for the spherical Bessel functions (or a derivative thereof). Defining parameters $\lambda = \Gamma_r/2$ and $r = \Gamma_{\mathrm{ud}}\Gamma_{\mathrm{du}}$, and functions

$$\begin{aligned}
F(x, y) &= \mathrm{sinc}(\sqrt{x^2 - y}) \tag{7.54} \\
G(x, y) &= \frac{\cos(\sqrt{x^2 - y}) - \cos(x)}{x}, \tag{7.55}
\end{aligned}$$

we obtain

$$\begin{aligned}
\Phi(J, t) &= e^{-\lambda t} \cos(st) + \lambda t e^{-\lambda t} F(st, rt) + st e^{-\lambda t} G(st, rt) \tag{7.56} \\
&= e^{-\lambda t} \left[\cos\left(t\sqrt{s^2 - r}\right) + \lambda t \mathrm{sinc}\left(t\sqrt{s^2 - r}\right) \right] \tag{7.57}
\end{aligned}$$
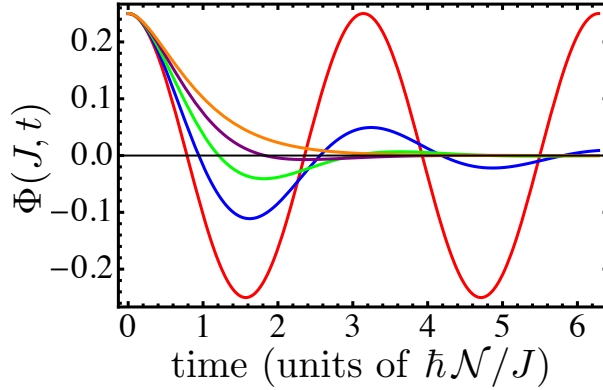
Figure 7.3: Plots of $\Phi(J, t)$ for $\gamma = 0$ and $\Gamma_{\mathrm{r}}/\Gamma_{\mathrm{r}}^{\mathrm{c}} \in \{0, 1/4, 1/2, 3/4, 1\}$, showing a transition from oscillatory to damped behavior.

We can now write out the exact solution

$$\overline{\langle \hat{S}^x \rangle} = \frac{e^{-\Gamma t}}{2} \mathrm{Re} \sum_j \prod_{k \neq j} \Phi(J_{jk}, t). \tag{7.58}$$

For spin-spin correlation functions, similar calculations to those described above lead us to obtain us to obtain

$$\langle \hat{\sigma}_j^a \hat{\sigma}_k^b \rangle = \frac{1}{4} e^{-2\Gamma t} \prod_{l \notin \{j,k\}} \Phi(aJ_{jl} + bJ_{kl}, t) \tag{7.59}$$

$$\langle \hat{\sigma}_j^a \hat{\sigma}_k^z \rangle = \frac{1}{2} e^{-\Gamma t} \Psi(aJ_{jk}, t) \prod_{l \notin \{j,k\}} \Phi(aJ_{jl}, t), \tag{7.60}$$

where $a, b = \pm 1$ and

$$\Psi(J, t) = e^{-\lambda t} (is - 2\gamma) t \, \mathrm{sinc}(t\sqrt{s^2 - r}). \tag{7.61}$$

These correlation functions, along with similar ones obtained by interchange of the site indices, completely determine the spin-spin correlations. Each instance of $\hat{\sigma}^x$ or $\hat{\sigma}^y$ in an observable generates an overall multiplicative factor of $e^{-\Gamma t}$; this is the effect of decoherence at the single-particle level. The structure of $\Phi(J, t)$ captures the effect of decoherence on the many-body physics, and could not have been deduced without our exact treatment.

We note that for $\gamma = 0$ the function $\Phi(J, t)$ undergoes a qualitative transition from oscillatory ($s^2 > r$) to damped ($s^2 < r$) behavior when $\Gamma_r = \Gamma_{\mathrm{r}}^{\mathrm{c}} \equiv 4J/\mathcal{N}$ [Fig. 7.3]. Therefore, when there

is only one coupling strength J, for instance in the case of all-to-all or nearest-neighbor couplings, dynamics of the transverse spin-length and correlation functions undergoes the same transition. More generally, for nonzero γ and any ζ, correlation functions exhibit a series of Hopf bifurcations as Γ_{r} is tuned. We note that the factors of $e^{-\Gamma t}$ in Eqs. (7.58-7.60) may make this transition difficult to observe experimentally, since the correlations are rapidly suppressed at the critical $\Gamma_{\mathrm{r}}^{\mathrm{c}}$.

7.5   Application to trapped-ion experiments

Trapped ion systems can simulate the Hamiltonian in Eq. (7.1), and can accurately measure the decoherence rates Γ_{el}, Γ_{ud}, and Γ_{du}. We note that both the Born-Markov approximation and the assumption of uncorrelated decoherence processes are extremely well justified for trapped ion systems [170]. Sample averaged spin-length and spin-spin correlation functions are easily measured in these experiments by looking at the length (and its shot-to-shot fluctuations) of various projections of the Bloch vector. In the trapped ion experiments discussed in Ref. [17], when $\zeta = 0$ the time scale at which quantum correlations become important for these observables, τ_c, scales with some power of the ion number: $\tau_c \sim \mathcal{N}^{1/3}$ for spin-squeezing, $\sim \mathcal{N}^{1/2}$ for transverse-spin relaxation, and $\sim \mathcal{N}$ for the creation of macroscopic superposition states (MSS's). Taking $\mathcal{N} = 100$ and $\Gamma = 0.06J$, as is typical in that experiment, we expect the proper incorporation of decoherence to be quantitatively important even for spin-squeezing, despite it being a relatively short-time indication of entanglement.

Equations (7.59) and (7.60) allow us to exactly calculate the effect of decoherence and the finite range of interactions on the maximum spin squeezing achievable in experiment. Figure 7.4(a) shows the expected maximal squeezing and anti-squeezing as a function of angle ψ in the yz plane for $\zeta = 0, 3$, with $\Gamma = 0.06J$ and $\Gamma_{\mathrm{el}} = 8\Gamma_{\mathrm{ud}} = 8\Gamma_{\mathrm{du}}$ (typical experimental numbers in [17]). The effects of decoherence are more pronounced for shorter range interactions due to the longer time scales for maximal squeezing. For this calculation the spins are assumed to be initialized (prior to the Ising dynamics) in a coherent state pointing along the x-axis, and we define the spin squeezing
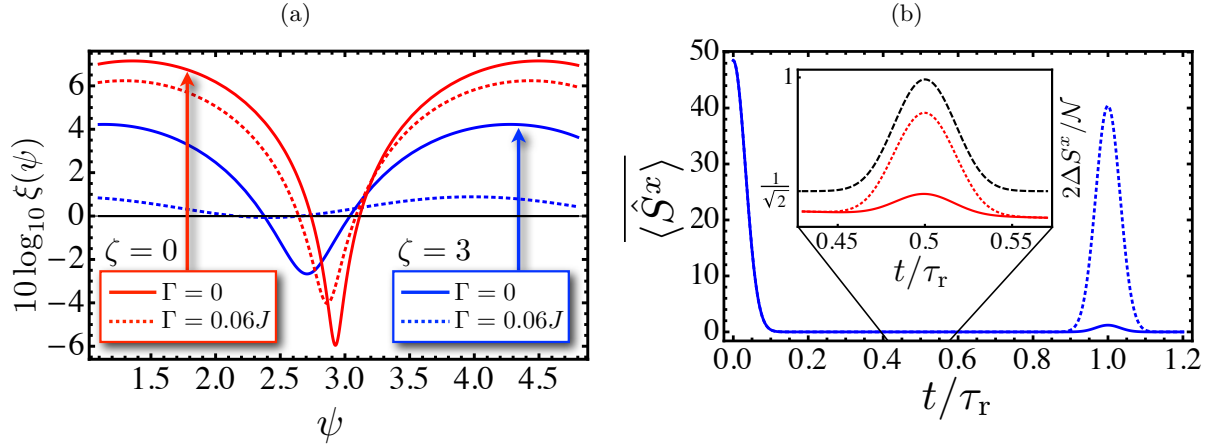
Figure 7.4: (a) Example of how spin squeezing is affected by decoherence (dashed lines are $\Gamma = 0.06J$, solid lines are for $\Gamma = 0$) for long-ranged (red, $\zeta = 0$) and short-ranged (blue, $\zeta = 3$) interactions. (b) Transverse spin relaxation and revivals for $\zeta = 0$, with parameters corresponding to expected experimental capabilities in [17] (blue solid line). The dotted blue line is obtained by treating decoherence at the single-particle level, and underestimates the detrimental effect of Raman decoherence by about a factor of 35. Inset: transverse-spin fluctuations peaking at time $\tau_r/2$. Experimental parameters, exact treatment (red solid line); experimental parameters, single-particle treatment (red-dotted line); no decoherence (black dashed line).

parameter

$$\xi(\psi) = \frac{\sqrt{\mathcal{N}}\Delta S^\psi}{\overline{\langle \hat{S}^x \rangle}}, \tag{7.62}$$

with

$$\Delta A = \sqrt{\overline{\langle \hat{A}^2 \rangle} - \overline{\langle \hat{A} \rangle}^2}, \tag{7.63}$$

$$\hat{S}^\psi = \frac{1}{2}\sum_j \hat{\sigma}_j^\psi, \tag{7.64}$$

and

$$\hat{\sigma}_j^\psi = \cos(\psi)\hat{\sigma}_j^y + \sin(\psi)\hat{\sigma}_j^z. \tag{7.65}$$

For the current experimental parameters there is essentially no spin revival, and no indication of a MSS at $\tau_r/2$. However, assuming 97 ions and expected improvements in the experiment [17] (a roughly 50-fold increase in the ratio J/Γ), in Fig. 7.4(b) we show that transverse spin revivals begin to appear. In that figure, the dotted line is obtained by treating the decoherence at the single-particle level, which amounts to attaching a decaying exponential $e^{-\Gamma t}$ to the operators

$\hat{\sigma}^x$ and $\hat{\sigma}^y$. We note that this treatment would be exact if the decoherence were only of the Rayleigh type ($\Gamma_\mathrm{r} = 0$). The solid line is the full solution from Eq. (7.58); the large ($\sim$ 35-fold) discrepancy between the single-particle and exact results indicates that our theory will be essential for understanding the behavior of this experiment.[3]   In the inset of Fig. 7.4(b) we plot the transverse spin fluctuations ΔS^x at times near $\tau_\mathrm{r}/2$. The peak in these fluctuations (which would achieve unity in the absence of decoherence) is a result of strong transverse-spin correlations in an emerging MSS, indicating that the expected improvements to the experiments will bring within reach the production of MSS's of ~ 100 ions in the near future.

---

[3] The significant additional decoherence beyond what is predicted at the single-particle level can be understood from a simple physical picture: We have said that the Raman flipped spins couple to the unflipped spins as a longitudinal magnetic field, but this magnetic field is "fluctuating" (in the sense that its strength varies from trajectory to trajectory). This fluctuating longitudinal magnetic field gives rise to additional dephasing, beyond what is induced by the Rayleigh decoherence.

Bibliography

[1] Ehud Altman, Walter Hofstetter, Eugene Demler, and Mikhail D. Lukin. New Journal of Physics, 5:113.1, 2003.

[2] M. Anderlini, P. J. Lee, B. L. Brown, J. Sebby-Strabley, W. D. Phillips, and J. V. Porto. Nature, 448:452, 2007.

[3] P. W. Anderson. Localized magnetic states in metals. Phys. Rev., 124:41–53, Oct 1961.

[4] N. Andrei, K. Furuya, and J. H. Lowenstein. Solution of the kondo problem. Rev. Mod. Phys., 55:331–402, Apr 1983.

[5] K. Andres, J. E. Graebner, and H. R. Ott. $4f$-virtual-bound-state formation in ceal$_3$ at low temperatures. Phys. Rev. Lett., 35:1779–1782, Dec 1975.

[6] F. T. Arecchi, Eric Courtens, Robert Gilmore, and Harry Thomas. Atomic coherent states in quantum optics. Phys. Rev. A, 6:2211–2237, Dec 1972.

[7] F. F. Assaad. Phys. Rev. Lett, 83:796, 1999.

[8] Waseem S. Bakr, Jonathan I. Gillen, Amy Peng, Simon Fölling, and Markus Greiner. Nature, 462:74–77, 2009.

[9] J. Bardeen, L. N. Cooper, and J. R. Schrieffer. Microscopic theory of superconductivity. Phys. Rev., 106:162–164, Apr 1957.

[10] J. T. Barreiro, M. Müller, P. Schindler, D. Nigg, T. Monz, M. Chwalla, M. Hennrich, C. F. Roos, P. Zoller, and R. Blatt. Nature, 470:486, 2011.

[11] M. Bishof, M. J. Martin, M. D. Swallows, C. Benko, Y. Lin, G. Quéméner, A. M. Rey, and J. Ye. Inelastic collisions and density-dependent excitation suppression in a ^{87}sr optical lattice clock. Phys. Rev. A, 84:052716, Nov 2011.

[12] Immanuel Bloch, Jean Dalibard, and Wilhelm Zwerger. Many-body physics with ultracold gases. Rev. Mod. Phys., 80:885–964, Jul 2008.

[13] D. Blume and Chris H. Greene. Fermi pseudopotential approximation: Two particles under external confinement. Phys. Rev. A, 65:043613, Apr 2002.

[14] S. N. Bose. Z. Phys., 26:178, 1924.

[15] P. Bouyer and M. A. Kasevich. Phys. Rev. A, 56:1083(R), 1997.

[16] Martin M. Boyd, Tanya Zelevinsky, Andrew D. Ludlow, Seth M. Foreman, Sebastian Blatt, Tetsuya Ido, and Jun Ye. Optical atomic coherence at the 1-second time scale. Science, 314(5804):1430–1433, 2006.

[17] Joseph W Britton, Brian C Sawyer, Adam C. Keith, C.-C. Joseph Wang, James K Freericks, Hermann Uys, Michael J Biercuk, and John J Bollinger. Nature, 484:489, 2012.

[18] G. Campbell, J. Mun, M. Boyd, and P. Medley. Science, 313:649, 2006.

[19] Gretchen K. Campbell, Jongchul Mun, Micah Boyd, Patrick Medley, Aaron E. Leanhardt, Luis G. Marcassa, David E. Pritchard, and Wolfgang Ketterle. Imaging the mott insulator shells by using atomic clock shifts. Science, 313(5787):649–652, 2006.

[20] Howard J. Carmichael. Satistical methods in quantum optics. 1999.

[21] M. A. Cazalilla, A. F. Ho, and M. Ueda. New J. Phys., 11:103033, 2009.

[22] Zilong Chen, Justin G. Bohnet, Shannon R. Sankar, Jiayan Dai, and James K. Thompson. Conditional spin squeezing of a large ensemble via the vacuum rabi splitting. Phys. Rev. Lett., 106:133601, Mar 2011.

[23] Marc Cheneau, Peter Barmettler, Dario Poletti, Manuel Endres, Peter Schaub, Takeshi Fukuhara, Christian Gross, Immanuel Bloch, Corinna Kollath, and Stefan Kuhr. Nature, 481:484–487, 2012.

[24] Cheng Chin, Rudolf Grimm, Paul Julienne, and Eite Tiesinga. Rev. Mod. Phys., 82:1225–1286, Apr 2010.

[25] Cheng Chin, Rudolf Grimm, Paul Julienne, and Eite Tiesinga. Feshbach resonances in ultracold gases. Rev. Mod. Phys., 82:1225–1286, Apr 2010.

[26] I. Chiorescu, Y. Nakamura, C. J. P. M. Harmans, and J. E. Mooij. Coherent quantum dynamics of a superconducting flux qubit. Science, 299(5614):1869–1871, 2003.

[27] Amodsen Chotia, Brian Neyenhuis, Steven A. Moses, Bo Yan, Jacob P. Covey, Michael Foss-Feig, Ana Maria Rey, Deborah S. Jin, and Jun Ye. Long-lived dipolar molecules and feshbach molecules in a 3d optical lattice. Phys. Rev. Lett., 108:080405, Feb 2012.

[28] P. Coleman. Phys. Rev. B, 28:5255, 1983.

[29] P. Coleman. Handbook of Magnetism and Adacanced Magnetic Materials, 1:95, 2007.

[30] Elbio Dagotto. Correlated electrons in high-temperature superconductors. Rev. Mod. Phys., 66:763–840, Jul 1994.

[31] A. J. Daley, M. M. Boyd, J. Ye, and P. Zoller. Phys. Rev. Lett., 101:170504, 2008.

[32] E.G. Dalla Torre, E. Demler, T. Giamarchi, and E. Altman. Nat. Phys., 6:802, 2010.

[33] Andrea Damascelli, Zahid Hussain, and Zhi-Xun Shen. Angle-resolved photoemission studies of the cuprate superconductors. Rev. Mod. Phys., 75:473–541, Apr 2003.

[34] L. de Forger de Parny, F. Hebert, V. G. Rousseau, R. T. Scalettar, and G. G. Batrouni. arXiv[cond-mat.quant-gas], 1105.6141, 2011.

[35] B. J. DeSalvo, M. Yan, P. G. Mickelson, Y. N. Martinez de Escobar, and T. C. Killian. Degenerate fermi gas of ^{87}Sr. Phys. Rev. Lett., 105:030402, Jul 2010.

[36] R. H. Dicke. Coherence in spontaneous radiation processes. Phys. Rev., 93:99–110, Jan 1954.

[37] S. Diehl, A. Micheli, A. Kantian, B. Kraus, H. P. Büchler, and P. Zoller. Nat. Phys., 4:878, 2008.

[38] S. Diehl, E. Rico, M.A. Baranov, and P. Zoller. Nat. Phys., 7:971, 2011.

[39] S. Diehl, W. Yi, A. J. Daley, and P. Zoller. Dissipation-induced d-wave pairing of fermionic atoms in an optical lattice. Phys. Rev. Lett., 105:227001, Nov 2010.

[40] S. Doniach. Physica B, 91:231, 1977.

[41] L.-M. Duan, E. Demler, and M. D. Lukin. Controlling spin exchange interactions of ultracold atoms in optical lattices. Phys. Rev. Lett., 91:090402, Aug 2003.

[42] L.M. Duan. Europhys. Lett., 67:721, 2004.

[43] S. Dürr, J. J. García-Ripoll, N. Syassen, D. M. Bauer, M. Lettner, J. I. Cirac, and G. Rempe. Lieb-liniger model of a dissipation-induced tonks-girardeau gas. Phys. Rev. A, 79:023614, Feb 2009.

[44] A. Einstein. Sitzungberichte der Preussischen Akademie der Wissenschaften, Physikalisch-mathematische Klasse, page 261, 1924.

[45] Gérard G. Emch. J. Math Phys., 7:1198, 1966.

[46] P. Fazekas and E. Müller-Hartmann. Z. Phys. B, 85:285, 1991.

[47] E Fermi. Nuovo Cimento, 11:157, 1934.

[48] C. D. Fertig, K. M. O'Hara, J. H. Huckans, S. L. Rolston, W. D. Phillips, and J. V. Porto. Phys. Rev. Lett., 94:120403, 2005.

[49] R. P. Feynman. Simulating physics with computers. Int. Jour. of Theor. Phys., 21:467–488, 1982.

[50] Matthew P. A. Fisher et al. Boson localization and the superfluid-insulator transition. Phys. Rev. B, 40(1):546–570, Jul 1989.

[51] S. Fölling, A. Widera, T. Müller, F. Gerbier, and I. Bloch. Phys. Rev. Lett., 97:060403, 2006.

[52] M. Foss-Feig, M. Hermele, and A. M. Rey. Phys. Rev. A, 81:051603(R), 2010.

[53] Michael Foss-Feig, Andrew Daley, James K. Thompson, and Ana Maria Rey. Steady-state many-body entanglement of hot reactive fermions. arXiv:1207.4741 [cond-mat.quant-gas], 2012.

[54] Michael Foss-Feig, Kaden R. A. Hazzard, John J. Bollinger, and Ana Maria Rey. Non-equilibrium dynamics of ising models with decoherence: an exact solution. arXiv:1209.5795 [cond-mat.quant-gas], 2012.

[55] Michael Foss-Feig, Michael Hermele, Victor Gurarie, and Ana Maria Rey. Heavy fermions in an optical lattice. Phys. Rev. A, 82:053624, Nov 2010.

[56] Michael Foss-Feig, Michael Hermele, and Ana Maria Rey. Probing the kondo lattice model with alkaline-earth-metal atoms. Phys. Rev. A, 81:051603, May 2010.

[57] Michael Foss-Feig and Ana Maria Rey. Phase diagram of the bosonic kondo-hubbard model. Phys. Rev. A, 84:053619, Nov 2011.

[58] E. Fradkin. Field theories of condensed matter systems. Frontiers in Physics, Addison-Wesley, 1991.

[59] J. K. Freericks, M. M. Maśka, Anzi Hu, Thomas M. Hanna, C. J. Williams, P. S. Julienne, and R. Lemański. Improving the efficiency of ultracold dipolar molecule formation by first loading onto an optical lattice. Phys. Rev. A, 81:011605, Jan 2010.

[60] T. Fukuhara, S. Sugawa, and Y. Takahashi. Phys. Rev. A, 76:051604(R), 2007.

[61] T. Fukuhara, Y. Takasu, M. Kumakura, and Y. Takahashi. Phys. Rev. Lett., 98:030401, 2007.

[62] J. J. Garcia-Ripoll, S. Dürr, N. Syassen, D. M. Bauer, M. Lettner, G. Rempe, and J. I. Cirac. New J. Phys., 11:013053, 2009.

[63] M Gaudin. J. Physique, 37:1087, 1976.

[64] S. Giorgini, L. P. Pitaevskii, and S. Stringari. Rev. Mod. Phys., 80:1215, 2008.

[65] Stefano Giorgini, Lev P. Pitaevskii, and Sandro Stringari. Theory of ultracold atomic fermi gases. Rev. Mod. Phys., 80:1215–1274, Oct 2008.

[66] Vittorio Giovannetti, Seth Lloyd, and Lorenzo Maccone. Quantum-enhanced measurements: Beating the standard quantum limit. Science, 306(5700):1330–1336, 2004.

[67] Sarang Gopalakrishnan, Benjamin L. Lev, and Paul M. Goldbart. Frustration and glassiness in spin models with cavity-mediated interactions. Phys. Rev. Lett., 107:277201, Dec 2011.

[68] A. V. Gorshkov, M. Hermele, V. Gurarie, P. S. Julienne, P. Zoller, E. Demler, M. D. Lukin, and A. M. Rey. Nat. Phys., 6:289, 2010.

[69] A. V. Gorshkov, P. Rabl, G. Pupillo, A. Micheli, P. Zoller, M. D. Lukin, and H. P. Büchler. Suppression of inelastic collisions between polar molecules with a repulsive shield. Phys. Rev. Lett., 101:073201, Aug 2008.

[70] Alexey V. Gorshkov, Salvatore R. Manmana, Gang Chen, Jun Ye, Eugene Demler, Mikhail D. Lukin, and Ana Maria Rey. Tunable superfluidity and quantum magnetism with ultracold polar molecules. Phys. Rev. Lett., 107:115301, Sep 2011.

[71] M. Greiner, O. Mandel, T. W. Hänsch, and I. Bloch. Nature, 419:51, 2002.

[72] M. Greiner, C. A. Regal, and D. S. Jin. Nature, 426:537, 2003.

[73] M. Greiner, C. A. Regal, and D. S. Jin. Probing the excitation spectrum of a fermi gas in the bcs-bec crossover regime. Phys. Rev. Lett., 94:070403, Feb 2005.

[74] M. Gring, M. Kuhnert, T. Langen, T. Kitagawa, B. Rauer, M. Schreitl, I. Mazets, D. Adu Smith, E. Demler, and J. Schmiedmayer. Relaxation and prethermalization in an isolated quantum system. Science, 337(6100):1318–1322, 2012.

[75] C. Gross. pHD tutorial, 2012.

[76] M. Gulacsi. Advances in Physics, 53(7):769, 2004.

[77] R. Hanson, L. P. Kouwenhoven, J. R. Petta, S. Tarucha, and L. M. K. Vandersypen. Spins in few-electron quantum dots. Rev. Mod. Phys., 79:1217–1265, Oct 2007.

[78] Kaden R. A. Hazzard, Salvatore Manmana, Michael Foss-Feig, and Ana Maria Rey. Far from equilibrium quantum magnetism with ultracold polar molecules. arXiv:1209.4076 [cond-mat.quant-gas], 2012.

[79] M. Hermele, V. Gurarie, and A. M. Rey. Phys. Rev. Lett., 103:135301, 2009.

[80] A. C. Hewson. The kondo problem to heavy fermions. 1993.

[81] T. Ho and S. Zhang. arXiv[cond-mat.quant-gas], 1007.0650, 2010.

[82] M. J. Holland and K. Burnett. Phys. Rev. Lett., 71:1355, 1993.

[83] C. Hooley and J. Quintanilla. Phys. Rev. Lett., 93:80404, 2004.

[84] Ryszard Horodecki, Paweł Horodecki, Michał Horodecki, and Karol Horodecki. Quantum entanglement. Rev. Mod. Phys., 81:865–942, Jun 2009.

[85] K. Huang and C. N. Yang. Phys. Rev., 105:767, 1957.

[86] A. Isacsson and S. M. Girvin. Multiflavor bosonic hubbard models in the first excited bloch band of an optical lattice. Phys. Rev. A, 72(5):053604, Nov 2005.

[87] R. Islam, E.E. Edwards, K. Kim, S. Korenblit, C. Noh, H. Carmichael, G.-D. Lin, L.-M. Duan, C.-C. Joseph Wang, J.K. Freericks, and C. Monroe. Nature Comm., 2:377, 2011.

[88] D Jaksch, V. Venturi, J. I. Cirac, C. J. Williams, and P. Zoller. Phys. Rev. Lett., 89:040402, 2002.

[89] Robert Jördens, Niels Strohmaier, Kenneth Günter, Henning Moritz, and Tilman Esslinger. Nature, 455:204, 2008.

[90] K. Kanjilal and D. Blume. Phys. Rev. A, 70:042709, 2004.

[91] K. Kanjilal and D. Blume. Nondivergent pseudopotential treatment of spin-polarized fermions under one- and three-dimensional harmonic confinement. Phys. Rev. A, 70:042709, Oct 2004.

[92] Michael Kastner. Diverging equilibration times in long-range quantum spin models. Phys. Rev. Lett., 106:130601, Mar 2011.

[93] T. Kasuya. <u>Prog. Theo. Phys.</u>, 16:45, 1956.

[94] W. Ketterle and N. J. Van Druten. <u>Advances in Atomic, Molucular, and Optical Physics.</u>, 37:181, 1996.

[95] Alexander V. Khaetskii, Daniel Loss, and Leonid Glazman. Electron spin decoherence in quantum dots due to interaction with nuclei. <u>Phys. Rev. Lett.</u>, 88:186802, Apr 2002.

[96] N. Kiesel, C. Schmid, G. Tóth, E. Solano, and H. Weinfurter. Experimental observation of four-photon entangled dicke state with high fidelity. <u>Phys. Rev. Lett.</u>, 98:063604, Feb 2007.

[97] K. Kim, M.-S. Chang, S. Korenblit, R. Islam, E.E. Edwards, J.K. Freericks, G.-D. Lin, L.-M. Duan, and C. Monroe. <u>Nature</u>, 465:590–593, 2010.

[98] Toshiya Kinoshita, Trevor Wenger, and David S. Weiss. <u>Nature</u>, 440:900–903, 2006.

[99] Thorsten Köhler, Krzysztof Góral, and Paul S. Julienne. Production of cold molecules via magnetically tunable feshbach resonances. <u>Rev. Mod. Phys.</u>, 78:1311–1361, Dec 2006.

[100] W. Kohn. Analytic properties of bloch waves and wannier functions. <u>Phys. Rev.</u>, 115:809–821, Aug 1959.

[101] W. Kohn. <u>Phys. Rev.</u>, 123:1242, 1961.

[102] Jun Kondo. <u>Prog. Theor. Phys.</u>, 32:37, 1964.

[103] S. Kraft, F. Vogt, O. Appel, F. Riehle, and U. Sterr. <u>Phys. Rev. Lett.</u>, 103:130401, 2009.

[104] B. Kraus, H. P. Büchler, S. Diehl, A. Kantian, A. Micheli, and P. Zoller. Preparation of entangled states by quantum markov processes. <u>Phys. Rev. A</u>, 78:042307, Oct 2008.

[105] Hanna Krauter, Christine A. Muschik, Kasper Jensen, Wojciech Wasilewski, Jonas M. Petersen, J. Ignacio Cirac, and Eugene S. Polzik. Entanglement generated by dissipation and steady state entanglement of two macroscopic objects. <u>Phys. Rev. Lett.</u>, 107:080503, Aug 2011.

[106] Werner Krauth, Nandini Trivedi, and David Ceperley. Superfluid-insulator transition in disordered boson systems. <u>Phys. Rev. Lett.</u>, 67:2307–2310, Oct 1991.

[107] T. D. Kühner and H. Monien. Phases of the one-dimensional bose-hubbard model. <u>Phys. Rev. B</u>, 58:R14741–R14744, Dec 1998.

[108] C. Lacroix. <u>Solid State Communications</u>, 54:991, 1985.

[109] C. Lacroix and M. Cyrot. <u>Phys. Rev. B</u>, 20:1969, 1979.

[110] Patrick A. Lee, Naoto Nagaosa, and Xiao-Gang Wen. Doping a mott insulator: Physics of high-temperature superconductivity. <u>Rev. Mod. Phys.</u>, 78:17–85, Jan 2006.

[111] Tony E. Lee, H. Häffner, and M. C. Cross. Collective quantum jumps of rydberg atoms. <u>Phys. Rev. Lett.</u>, 108:023602, Jan 2012.

[112] N. D. Lemke, J. von Stecher, J. A. Sherman, A. M. Rey, C. W. Oates, and A. D. Ludlow. p-wave cold collisions in an optical lattice clock. <u>Phys. Rev. Lett.</u>, 107:103902, Aug 2011.

[113] Seth Lloyd. Universal quantum simulators. Science, 273(5278):1073–1078, 1996.

[114] Robert Löw, Hendrik Weimer, Ulrich Krohn, Rolf Heidemann, Vera Bendkowsky, Björn Butscher, Hans Peter Büchler, and Tilman Pfau. Universal scaling in a strongly interacting rydberg gas. Phys. Rev. A, 80:033422, Sep 2009.

[115] B. Lücke, M. Scherer, J. Kruse, L. Pezz, F. Deuretzbacher, P. Hyllus, O. Topic, J. Peise, W. Ertmer, J. Arlt, L. Santos, A. Smerzi, and C. Klempt. Twin matter waves for interferometry beyond the classical limit. Science, 334(6057):773–776, 2011.

[116] A. D. Ludlow, N. D. Lemke, J. A. Sherman, C. W. Oates, G. Quéméner, J. von Stecher, and A. M. Rey. Cold-collision-shift cancellation and inelastic scattering in a yb optical lattice clock. Phys. Rev. A, 84:052724, Nov 2011.

[117] J. M. Luttinger. Phys. Rev., 119:1153, 1960.

[118] Olaf Mandel, Markus Greiner, Artur Widera, Tim Rom, Theodor W. Hänsch, and Immanuel Bloch. Coherent transport of neutral atoms in spin-dependent optical lattice potentials. Phys. Rev. Lett., 91:010407, Jul 2003.

[119] Olaf Mandel, Markus Greiner, Artur Widera, Tim Rom, Theodor W. Hänsch, and Immanuel Bloch. New Journal of Physics, 12:055013, 2010.

[120] R. M. Martin. Phys. Rev. Lett., 48:362, 1982.

[121] Y. N. Martinez de Escobar et al. Phys. Rev. Lett., 103:200402, 2009.

[122] D. McKay and B. DeMarco. New Journal of Physics, 12:055013, 2010.

[123] D. McKay, M. White, M. Pasienski, and B. DeMarco. Nature, 453:76, 2008.

[124] Thomas Monz, Philipp Schindler, Julio T. Barreiro, Michael Chwalla, Daniel Nigg, William A. Coish, Maximilian Harlander, Wolfgang Hänsel, Markus Hennrich, and Rainer Blatt. 14-qubit entanglement: Creation and coherence. Phys. Rev. Lett., 106:130506, Mar 2011.

[125] Torben Müller, Simon Fölling, Artur Widera, and Immanuel Bloch. State preparation and dynamics of ultracold atoms in higher lattice orbitals. Phys. Rev. Lett., 99(20):200405, Nov 2007.

[126] K.-K. Ni, S. Ospelkaus, M. H. G. de Miranda, A. Pe'er, B. Neyenhuis, J. J. Zirbel, S. Kotochigova, P. S. Julienne, D. S. Jin, and J. Ye. A high phase-space-density gas of polar molecules. Science, 322(5899):231–235, 2008.

[127] K.-K. Ni, S. Ospelkaus, D. Wang, G. Quéméner, B. Neyenhuis, M. H. G. de Miranda, J. L. Bohn, J. Ye, and D. S. Jin. Dipolar collisions of polar molecules in the quantum regime. Nature (London), 464:1324–1328, 2010.

[128] M. Ogata and H. Shiba. Phys. Rev. B, 41:2326, 1990.

[129] M. Olshanii. Atomic scattering in the presence of an external confinement and a gas of impenetrable bosons. Phys. Rev. Lett., 81:938–941, Aug 1998.

[130] B. Paredes, C. Tejedor, and J. I. Cirac. Phys. Rev. A, 71:063608, 2005.

[131] B. M. Peden, D. Meiser, M. L. Chiofalo, and M. J. Holland. Phys. Rev. A, 80:043803, 2009.

[132] H. Pichler, A. J. Daley, and P. Zoller. Nonequilibrium dynamics of bosonic atoms in optical lattices: Decoherence of many-body states due to spontaneous emission. Phys. Rev. A, 82:063605, Dec 2010.

[133] M. B. Plenio and P. L. Knight. The quantum-jump approach to dissipative dynamics in quantum optics. Rev. Mod. Phys., 70:101–144, Jan 1998.

[134] A. Polkovnikov, S. Sachdev, and S. M. Girvin. Phys. Rev. A, 66:053607, 2002.

[135] D. Porras and J. I. Cirac. Effective quantum spin systems with trapped ions. Phys. Rev. Lett., 92:207901, May 2004.

[136] Steven Prawer and Andrew D. Greentree. Diamond for quantum computing. Science, 320(5883):1601–1602, 2008.

[137] R. Prevedel, G. Cronenberg, M. S. Tame, M. Paternostro, P. Walther, M. S. Kim, and A. Zeilinger. Experimental realization of dicke states of up to six qubits for multiparty quantum networking. Phys. Rev. Lett., 103:020503, Jul 2009.

[138] Goulven Quéméner and John L. Bohn. Electric field suppression of ultracold confined chemical reactions. Phys. Rev. A, 81:060701, Jun 2010.

[139] Goulven Quéméner and John L. Bohn. Strong dependence of ultracold chemical rates on electric dipole moments. Phys. Rev. A, 81:022702, Feb 2010.

[140] Charles Radin. J. Math Phys., 11:2945, 1970.

[141] N. Read, D. M. Newns, and S. Doniach. Phys. Rev. B, 30:3841, 1984.

[142] C. A. Regal, C. Ticknor, J. L. Bohn, and D. S. Jin. Nature, 424:47, 2003.

[143] A. M. Rey, A. V. Gorshkov, and C. Rubbo. Many-body treatment of the collisional frequency shift in fermionic atoms. Phys. Rev. Lett., 103:260402, Dec 2009.

[144] A. M. Rey, G. Pupillo, C. W. Clark, and C. J. Williams. Phys. Rev. A, 72:033616, 2005.

[145] M. Rigol and A. Muramatsu. Phys. Rev. A, 70:043627, 2004.

[146] M. A. Ruderman and C. Kittel. Phys. Rev., 78:275, 1950.

[147] H. R. Sadeghpour, J. L. Bohn, M. J. Cavagnero, B. D. Esry, I. I. Fabrikant, J. H. Macek, and A. R. P. Rau. Collisions near threshold in atomic and molecular physics. J. Phys. B: At. Mol. Opt. Phys., 33:R93–R140, 2000.

[148] M. P. Sarachik, E. Corenzwit, and L. D. Longinotti. Resistivity of mo-nb and mo-re alloys containing 1Phys. Rev., 135:A1041–A1045, Aug 1964.

[149] T. A. Savard, K. M. O'Hara, and J. E. Thomas. Laser-noise-induced heating in far-off resonance optical traps. Phys. Rev. A, 56:R1095–R1098, Aug 1997.

[150] Richard T. Scalettar, Ghassan George Batrouni, and Gergely T. Zimanyi. Localization in interacting, disordered, bose systems. Phys. Rev. Lett., 66:3144–3147, Jun 1991.

[151] U. Schneider, L. Hackermller, S. Will, Th. Best, I. Bloch, T. A. Costi, R. W. Helmes, D. Rasch, and A. Rosch. Metallic and insulating phases of repulsively interacting fermions in a 3d optical lattice. 322(5907):1520–1525, 2008.

[152] J. R. Schrieffer and P. A. Wolff. Phys. Rev., 149:491, 1966.

[153] J. Sebby-Strabley, M. Anderlini, P. S. Jessen, and J. V. Porto. Lattice of double wells for manipulating pairs of cold atoms. Phys. Rev. A, 73(3):033605, Mar 2006.

[154] Jacob. F. Sherson, Christof Weitenberg, Manuel Endres, Marc Cheneau, Immanuel Bloch, and Stefan Kuhr. Nature, 467:68–72, 2010.

[155] M. Sigrist, H. Tsunetsuga, and K. Ueda. Phys. Rev. Lett., 67:2211, 1991.

[156] Manfred Sigrist, Hirokazu Tsunetsugu, Kazuo Ueda, and T. M. Rice. Ferromagnetism in the strong-coupling regime of the one-dimensional kondo-lattice model. Phys. Rev. B, 46:13838–13846, Dec 1992.

[157] I. B. Spielman, P. R. Johnson, J. H. Huckans, C. D. Fertig, S. L. Rolston, W. D. Phillips, and J. V. Porto. Collisional deexcitation in a quasi-two-dimensional degenerate bosonic gas. Phys. Rev. A, 73:020702, Feb 2006.

[158] F. Steglich, J. Aarts, C. D. Bredl, W. Lieke, D. Meschede, W. Franz, and H. Schäfer. Superconductivity in the presence of strong pauli paramagnetism: $Cecu_2si_2$. Phys. Rev. Lett., 43:1892–1896, Dec 1979.

[159] S. Stellmer, M. K. Tey, B. Huang, R. Grimm, and F. Schreck. Phys. Rev. Lett., 103:200401, 2009.

[160] G. R. Stewart. Rev. Mod. Phys., 56:755, 1984.

[161] J. T. Stewart, J. P. Gaebler, and D. S. Jin. Nature, 454:744–747, 2008.

[162] Philipp Strack and Subir Sachdev. Dicke quantum spin glass of atoms and photons. Phys. Rev. Lett., 107:277202, Dec 2011.

[163] N. Strohmaier et al. Phys. Rev. Lett., 99:220601, 2007.

[164] Matthew D. Swallows, Michael Bishof, Yige Lin, Sebastian Blatt, Michael J. Martin, Ana Maria Rey, and Jun Ye. Suppression of collisional shifts in a strongly interacting lattice clock. 331(6020):1043–1046, 2011.

[165] N. Syassen, D. M. Bauer, M. Lettner, T. Volz, D. Dietze, J. J. Garcia-Ripoll, J. I. Cirac, G. Rempe, and S. Dürr. Strong dissipation inhibits losses and induces correlations in cold molecular gases. Science, 320(5881):1329–1331, 2008.

[166] S. Taie et al. arXiv[cond-mat.quant-gas], 1005.3760, 2010.

[167] Shintaro Taie, Rekishu Yamazaki, Seiji Sugawa, and Yoshiro Takahashi. Nature Physics (advanced online publication), 2012.

[168] S. Trotzky, P. Cheinet, S. Flling, M. Feld, U. Schnorrberger, A. M. Rey, A. Polkovnikov, E. A. Demler, M. D. Lukin, and I. Bloch. Time-resolved observation and control of superexchange interactions with ultracold atoms in optical lattices. Science, 319(5861):295–299, 2008.

[169] H. Tsunetsugu, M. Sigrist, and K. Ueda. <u>Rev. Mod. Phys.</u>, 69(3):809, 1997.

[170] H. Uys, M. J. Biercuk, A. P. VanDevender, C. Ospelkaus, D. Meiser, R. Ozeri, and J. J. Bollinger. Decoherence due to elastic rayleigh scattering. <u>Phys. Rev. Lett.</u>, 105:200401, Nov 2010.

[171] Hendrik Weimer, Markus Müller, Igor Lesanovsky, Peter Zoller, and Hans Peter Büchler. <u>Nat. Phys.</u>, 6:382–388, 2010.

[172] S. Will, Th. Best, U. Schneider, L. Hackermüller, D.-S. Lühmann, and I. Bloch. <u>Nature</u>, 465:197, 2010.

[173] Kenneth G. Wilson. The renormalization group: Critical phenomena and the kondo problem. <u>Rev. Mod. Phys.</u>, 47:773–840, Oct 1975.

[174] Georg Wirth, Matthias Olschlager, and Andreas Hemmerich. <u>Nat. Phys. (Advanced online publication)</u>, 2010.

[175] C. Xu and C. Wu. <u>Phys. Rev. B</u>, 77:134449, 2008.

[176] K. Yosida. <u>Phys. Rev.</u>, 106:896, 1957.

[177] Hao Zhang, Robert McConnell, Senka Ćuk, Qian Lin, Monika H. Schleier-Smith, Ian D. Leroux, and Vladan Vuletić. <u>ArXiv:1203.3160 [physics.atom-ph]</u>, 2012.

Appendix A

Second quantization

In this thesis we will need to describe the behavior of large collections of atoms, and therefore will work almost exclusively in the notation of second-quantization. There are many excellent references that derive the equivalence between second-quantization and first-quantization, and here we only make some very general statements to clarify notation and motivate its use. Just as in first quantization, we choose some convenient set of single particle wavefunctions $\varphi_\alpha(\boldsymbol{r})$ to span the relevant Hilbert space. An $\mathcal{N}$ particle state having n_α particles in each wavefunction $\varphi_\alpha(\boldsymbol{r})$ is created from the vacuum by applying creation operators $\hat{\varphi}_\alpha^\dagger$ to the vacuum state (which has no particles)[1]

$$|\Psi\rangle = \frac{\left(\hat{\varphi}_1^\dagger\right)^{n_1}}{\sqrt{n_1!}} \times \frac{\left(\hat{\varphi}_2^\dagger\right)^{n_2}}{\sqrt{n_2!}} \times \ldots |vac\rangle. \tag{A.1}$$

Note that if we take $\hat{\psi}^\dagger(\boldsymbol{r})$ to create a particle at the point $\boldsymbol{r}$, we can create a particle in state $\varphi_\alpha(\boldsymbol{r})$ by taking an appropriate linear superposition of states with a particle in a well defined location, i.e.

$$\hat{\psi}_\alpha^\dagger = \int d^3\boldsymbol{r}\,\hat{\psi}^\dagger(\boldsymbol{r})\varphi_\alpha^*(\boldsymbol{r}). \tag{A.2}$$

This generalizes in the obvious way to any other change of basis. If we also want to describe some internal degrees of freedom of these particles, we give these creation operators an additional index to specify what internal state a particle is created in. For instance, we might want to describe alkaline earth atoms in one of two electronic states, denoted g (ground) and e (excited), so now we

---

[1] The factors of $\sqrt{n_j!}$ in the denominators are necessary for proper normalization, as can easily be checked by explicitly evaluating $\langle\Psi|\Psi\rangle$ using the commutation relations.

can create atoms in the single particle state $\varphi_\alpha(\boldsymbol{r})$ and internal electronic state $g(e)$ by applying $\hat{\varphi}^\dagger_{\alpha g}(\hat{\varphi}^\dagger_{\alpha e})$ to the vacuum.[2]   The key piece of mathematics that causes bosons to have symmetrized wavefunctions and fermions to have anti-symmetrized wavefunctions are the defining commutation (anti-commutation) relations for bosonic (fermionic) operators. Writing these in the position basis, and including an index for possible internal degrees of freedom, we have

$$\left[\hat{\psi}^\dagger_\alpha(\boldsymbol{r}), \hat{\psi}_\beta(\boldsymbol{r}')\right] = \delta_{\alpha\beta}\delta(\boldsymbol{r} - \boldsymbol{r}'), \tag{A.3}$$

$$\left[\hat{\psi}_\alpha(\boldsymbol{r}), \hat{\psi}_\beta(\boldsymbol{r}')\right] = 0. \tag{A.4}$$

for bosons and

$$\left\{\hat{\psi}^\dagger_\alpha(\boldsymbol{r}), \hat{\psi}_\beta(\boldsymbol{r}')\right\} = \delta_{\alpha\beta}\delta(\boldsymbol{r} - \boldsymbol{r}'), \tag{A.5}$$

$$\left\{\hat{\psi}_\alpha(\boldsymbol{r}), \hat{\psi}_\beta(\boldsymbol{r}')\right\} = 0. \tag{A.6}$$

for fermions, where $\{a, b\} = ab + ba$ and $[a, b] = ab - ba$.

We point out, in passing, that just because second-quantization is often used to describe many-body systems, it should not be misconstrued as containing any essential ingredients of many-body physics. It is strictly a notation, and it does not describe anything that can't also be (and historically often was) described with first-quantization. One way of viewing its notational advantage is that it explicitly incorporates the symmetrization requirements imposed on a wavefunction by the Bose- or Fermi- statistics of the particles being described. In the notation of first quantization, each particle is assigned an index, and one can try to describe $\mathcal{N}$ particles by associating with each particle index a well defined state. But this would simply be wrong; a proper bosonic wavefunction should be symmetric under interchange of any two particle indices. The problem is that first quantization naturally describes *too big* a Hilbert space, and we need to go out of our way (through explicit symmetrization of the wavefunctions) to constrain it to the physical (symmetric) Hilbert space. In second quantization, there is simply no way of making the above mistake.

---

[2] Because any n level system has a formal connection to a spin-$n/2$ object, we might refer to this two level atom as being a spin-1/2 particle. It's important to remember that, because our description of atoms is non-relativistic, there is no difficulty caused by violating the spin-statistics connection. We will regularly talk about spinless fermions, spin-1/2 bosons, etc., all of which would be nonsense in relativistic field theory.

Appendix B

Effective Hamiltonians

For systems that are only weakly interacting, it is common to take interactions into account perturbatively. In lattice physics, however, we often encounter the situation where interactions are the largest energy scale in the problem, and there is no reason to expect such a (weak-coupling) perturbative treatment to be useful, or even correct. In this strongly interacting regime, the problem can be simplified by recognizing that large parts of the Hilbert space are inaccessible at low energies. For example, for spin-$\frac{1}{2}$ fermions in an optical lattice, at unit filling and with $U \gg J$, the low lying eigenstates of the system should have almost no weight in any many-body state where two fermions reside on the same site. This motivates defining a low-energy Hilbert space, $\mathscr{H}_g$, consisting of only the many-body states with one fermion per site (for a lattice with L sites, there are 2^L such states, since each fermion can occupy one of two spin states). The high energy Hilbert space $\mathscr{H}_e$ consists of everything else, and the full Hilbert space is a direct sum of these $\mathscr{H} = \mathscr{H}_g \oplus \mathscr{H}_e$.

In the above example, for U finite and $J = 0$, $\mathscr{H}_g$ is the degenerate groundstate manifold of $\mathcal{H}$. A natural question to ask is: If we add in a small $J \ll U$ as a perturbation, how is this degeneracy lifted? In particular, we might want to know what the spectrum looks like, or whether the groundstate develops any interesting correlations. These questions can be answered by deriving an effective Hamiltonian. Because the low-energy Hilbert space $\mathscr{H}_g$ is formally identical to that of a spin$-\frac{1}{2}$ lattice model, it is natural to expect that the effective Hamiltonian will describe interacting spins, and we will verify this below.

Motivated by the above example, here we will consider situations where the first-order energy

shifts vanish (this happens at unit filling because the hopping does not connect states in $\mathcal{H}_g$ to first order), and one must proceed to second-order. There are a number of ways to derive the effective Hamiltonian to second-order, for instance by using Brillouin-Wigner perturbation theory [58] or a canonical transformation [152]. But here, we will just motivate the correct result by analogy to something more familiar: first-order degenerate perturbation theory. When doing first-order degenerate perturbation theory in a perturbation $\mathcal{V}$, the lesson learned is that we can't just choose some arbitrary basis for $\mathcal{H}_g$, denoted $|g_\alpha\rangle$, and then write down the first-order energy shifts $E_\alpha^{g(1)} = \langle g_\alpha|\mathcal{V}|g_\alpha\rangle$. Instead, we must compute the matrix elements $\mathcal{V}_{\alpha\beta} \equiv \langle g_\alpha|\mathcal{V}|g_\beta\rangle$, and then find the eigenvalues of the matrix $\mathcal{V}_{\alpha\beta}$. An unnecessarily complicated perspective would be to define an effective Hamiltonian $\mathcal{H}_{\text{eff}}$ as the (unique) operator acting in $\mathcal{H}_g$ with matrix elements given by $\langle g_\alpha|\mathcal{H}_{\text{eff}}|g_\beta\rangle = \mathcal{V}_{\alpha\beta}$. Note that $\mathcal{H}_{\text{eff}}$ is really just the projection of the operator $\mathcal{V}$ onto the low energy Hilbert-space. Now the first(zeroth)-order perturbative result for the energies (eigenstates) in $\mathcal{H}_g$ are the same as the exact eigenvalues (eigenstates) of $\mathcal{H}_{\text{eff}}$.

When the perturbation doesn't have any matrix elements between states in $\mathcal{H}_g$, and if the states $|g_\alpha\rangle$ were non-degenerate, then we would calculate the ground state energy shift to second order by summing over all states $|e_\beta\rangle$ in $\mathcal{H}_e$ as

$$E_\alpha^{g(2)} = \sum_\beta \frac{\langle g_\alpha|\mathcal{V}|e_\beta\rangle\langle e_\beta|\mathcal{V}|g_\alpha\rangle}{E_\alpha^{g(0)} - E_\beta^{e(0)}} \tag{B.1}$$

$$= \langle g_\alpha| \left[\sum_\beta \frac{\mathcal{V}|e_\beta\rangle\langle e_\beta|\mathcal{V}}{E_\alpha^{g(0)} - E_\beta^{e(0)}} \right] |g_\alpha\rangle. \tag{B.2}$$

The second line has been written in a suggestive way: If the states $|g_\alpha\rangle$ are all degenerate, and we define $E_\alpha^{g(0)} = E^{g(0)}$, then (just like in first-order degenerate perturbation theory) in order to find the energy splitting due to the perturbation we define an effective Hamiltonian

$$\mathcal{H}_{\text{eff}} = \sum_\beta \frac{\mathcal{V}|e_\beta\rangle\langle e_\beta|\mathcal{V}}{E^{g(0)} - E_\beta^{e(0)}} \tag{B.3}$$

and find its eigenvalues. This formalism allows us to derive, for instance, a superexchange Hamiltonian in the strong coupling limit of the Hubbard model, or the Kondo Hamiltonian in the strong coupling limit of the Anderson model (see Chapter 3 for a discussion).

B.1   Application to the Hubbard model at large U/J

As a concrete example of the above procedure, we imagine a two-site Hubbard model, with two spin-$\frac{1}{2}$ atoms in the strong coupling limit $U/J \gg 1$ (for now, these can be either Bosons or Fermions). The Hamiltonian is given by $\mathcal{H} = \mathcal{H}_0 + \mathcal{V}$, with

$$\mathcal{H}_0 = U \sum_{j=1,2} \sum_{\sigma\sigma'} \hat{a}_{j\sigma}^\dagger \hat{a}_{j\sigma'}^\dagger \hat{a}_{j\sigma'} \hat{a}_{j\sigma} \qquad \text{and} \qquad \mathcal{V} = -J \sum_\sigma \left(a_{1\sigma}^\dagger a_{2\sigma} + a_{2\sigma}^\dagger a_{1\sigma} \right). \tag{B.4}$$

When $J = 0$, our low energy Hilbert space $\mathscr{H}_g$ contains just four vectors, $|\uparrow\uparrow\rangle$, $|\downarrow\downarrow\rangle$, $|\uparrow\downarrow\rangle$, and $|\downarrow\uparrow\rangle$, all of which have zero energy. The high energy Hilbert space $\mathscr{H}_e$ consists of states where one well has two atoms in it and the other has none, all of which have an energy U. Exactly what states are available depends on whether the atoms are bosons or fermions, and in order to leave this unspecified we will just denote these states by $|e_\alpha\rangle$, as before.

According to Eq. (B.3), the effective Hamiltonian is (to second order in J)

$$\mathcal{H}_{\text{eff}} = \sum_\beta \frac{\mathcal{V}|e_\beta\rangle\langle e_\beta|\mathcal{V}}{0 - U} \tag{B.5}$$

$$= -\frac{J^2}{U} \sum_\beta \sum_{\sigma,\sigma'} \left(a_{1\sigma}^\dagger a_{2\sigma} + a_{2\sigma}^\dagger a_{1\sigma} \right) |e_\beta\rangle\langle e_\beta| \left(a_{1\sigma'}^\dagger a_{2\sigma'} + a_{2\sigma'}^\dagger a_{1\sigma'} \right) \tag{B.6}$$

$$= -\frac{J^2}{U} \sum_{\sigma,\sigma'} \left(a_{1\sigma}^\dagger a_{2\sigma} + a_{2\sigma}^\dagger a_{1\sigma} \right) \left(a_{1\sigma'}^\dagger a_{2\sigma'} + a_{2\sigma'}^\dagger a_{1\sigma'} \right) \tag{B.7}$$

$$= -\frac{J^2}{U} \sum_{\sigma,\sigma'} \left(a_{1\sigma}^\dagger a_{1\sigma'} a_{2\sigma} a_{2\sigma'}^\dagger + a_{2\sigma}^\dagger a_{2\sigma'} a_{1\sigma} a_{1\sigma'}^\dagger \right) \tag{B.8}$$

The third equality follows because $\sum_\beta |e_\beta\rangle\langle e_\beta|$ is just a completeness identity in $\mathscr{H}_e$ (note that this simplification only occurred because all intermediate states in this example have the same energy), and the fourth equality follows from recognizing that two of the four terms from the previous line annihilate all states $\mathscr{H}_g$, and then doing some rearranging of the operators (which, in this case, is valid for either bosons or fermions). Now we can switch the operators around so that they are normal ordered on each site (using the commutation relations for bosons or anticommutation

relations for fermions)

$$\mathcal{H}_{\text{eff}} = -\frac{J^2}{U} \sum_{\sigma,\sigma'} \left(a^\dagger_{1\sigma} a_{1\sigma'} \left[\delta_{\sigma\sigma'} \pm a^\dagger_{2\sigma'} a_{2\sigma} \right] + a^\dagger_{2\sigma} a_{2\sigma'} \left[\delta_{\sigma\sigma'} \pm a^\dagger_{1\sigma'} a_{1\sigma} \right] \right) \tag{B.9}$$

$$= \pm \frac{-J^2}{U} \sum_{\sigma,\sigma'} \left(a^\dagger_{1\sigma} a_{1\sigma'} a^\dagger_{2\sigma'} a_{2\sigma} + a^\dagger_{2\sigma} a_{2\sigma'} a^\dagger_{1\sigma'} a_{1\sigma} \right). \tag{B.10}$$

Here the $+$ is for bosons, $-$ is for fermions, and in the last line we have dropped terms that just amount to an overall energy shift in $\mathcal{H}_g$. At this point, one can just evaluate all of the matrix elements by brute force. However, knowing in advance what we're looking for, we can do a little better. Using the convention that repeated indices are summed over, and changing some indices, we can rewrite the last line above as

$$\mathcal{H}_{\text{eff}} = \pm \frac{-J^2}{U} \left(a^\dagger_{1\alpha} a_{1\beta} a^\dagger_{2\gamma} a_{2\delta} \right) 2\delta_{\alpha\delta}\delta_{\beta\gamma} \tag{B.11}$$

$$= \pm \frac{-J^2}{U} \sum_i \left(a^\dagger_{1\alpha} \sigma^i_{\alpha\beta} a_{1\beta} \right) \left(a^\dagger_{2\gamma} \sigma^i_{\gamma\delta} a_{2\delta} \right). \tag{B.12}$$

In the second line, $\sigma^i_{\alpha\beta}$ are Pauli matrices (with α, β the matrix indices), we have used the common identity $\sum_i \sigma^i_{\alpha\beta} \sigma^i_{\gamma\delta} = 2\delta_{\alpha\delta}\delta_{\beta\gamma} - \delta_{\alpha\beta}\delta_{\gamma\delta}$, and again dropped terms that are constant when acting in $\mathcal{H}_g$. Now, we recognize that $\frac{1}{2} a^\dagger_{j\alpha} \boldsymbol{\sigma}_{\alpha\beta} a_{j\beta}$ can be rewritten as a spin operator $\boldsymbol{s}_j$ (switching from index notation to bold font for vectors). There's nothing obvious about that; the equivalence can be viewed as a statement that the above operators (in terms of bosons or fermions) have the same matrix elements as the spin-$\frac{1}{2}$ operators when restricted to $\mathcal{H}_g$. Alternatively, one can view the equivalence as a statement that the spin operators and the quadratic bosonic or fermionic operators obey the same (Pauli algebra) commutation relations.[1] Now we can rewrite the effective Hamiltonian as

$$\mathcal{H}_{\text{eff}} = -\frac{4J^2}{U} \boldsymbol{s}_1 \cdot \boldsymbol{s}_2 \text{ for bosons} \qquad \text{OR} \qquad \mathcal{H}_{\text{eff}} = \frac{4J^2}{U} \boldsymbol{s}_1 \cdot \boldsymbol{s}_2 \text{ for fermions}, \tag{B.13}$$

and we call this the Heisenberg Hamiltonian. If we were to say something like: "*The antiferro-magnetic Heisenberg model governs the low energy physics of the spin-$\frac{1}{2}$ Fermi-Hubbard model, at a*

---

[1] For bosons, this equivalence is an example of the Schwinger boson representation of spin. For fermions, I think this representation goes by the name of Abrikosov-pseudo fermion representation. It's not surprising that the spin representation works for fermions just as well as for bosons. When applying the operators $\hat{a}^\dagger_{j\sigma} \hat{a}_{j\sigma'}$ to singly occupied sites, double occupancies never occur (even between applications of the two operators involved), and hence it just doesn't matter whether the particles are bosons or fermions.
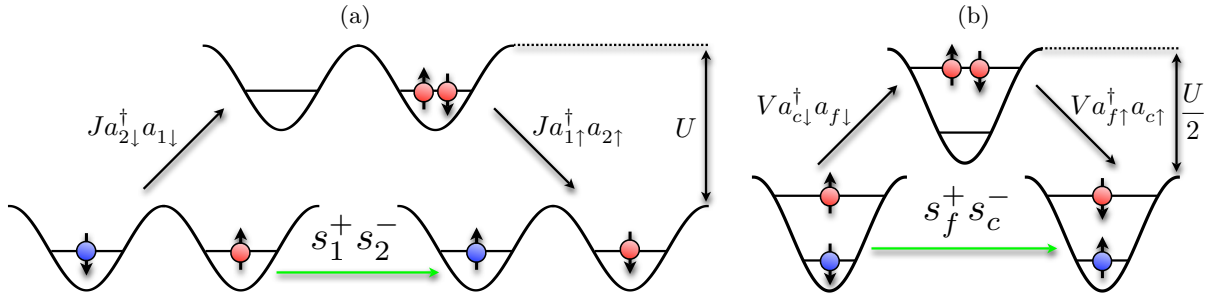
Figure B.1: Diagrammatic illustration of the types of perturbative process contributing to $\mathcal{H}_{\text{eff}}$ for the Hubbard model (a) and the Anderson model (b), illustrating their formal similarity. The spin operators and green arrow are meant to show the corresponding action of the effective Hamiltonian, which directly couples the two low-energy states.

filling of one particle per site, and in the limit $U/J \to \infty$", the above equivalence is what we have in mind. Notice that, had we chosen a model with many sites, we would have arrived instead at

$$\mathcal{H}_{\text{eff}} = \pm \frac{4J^2}{U} \sum_{\langle i,j \rangle} \boldsymbol{s}_i \cdot \boldsymbol{s}_j. \tag{B.14}$$

This is still a highly non-trivial model (in general, groundstate properties for $+$ cannot be obtained analytically in $D > 1$), but at least it alerts that, for fermions, we should expect anti-ferromagnetic ordering in the groundstate, whereas for bosons we should expect ferromagnetic ordering.

It's worth pointing out that, up to the overall factor of 4 and the correct sign, we could have guessed this result. The J^2/U comes from the general structure of second order perturbation theory, and the product $\boldsymbol{s}_1 \cdot \boldsymbol{s}_2$ is the only combination of spin operators that is SU(2) invariant [since $\mathcal{H}$ is SU(2) invariant, we expect the effective Hamiltonian to preserve this symmetry order-by-order in perturbation theory], quartic in the underlying creation and annihilation operators (as it should be from second order perturbation theory in J), and not proportional to the identity operator.[2]

In fact, we could *even* have guessed the sign on physical grounds: For fermions, the energy is lowered to second-order by virtual transitions through doubly occupied states which, thanks to the Pauli exclusion principle, can only occur if the two spins are anti-aligned. For bosons, these virtual transitions lower the energy more when the two spins are aligned than when they aren't, due to

---

[2] We dropped overall energy shifts anyway, so we're not getting the ground-state energy right, but we are getting the energy splittings in the low energy spectrum correct, which is much more important.

Bose enhancement of the tunneling.

B.2   Application to the Anderson model at large U/V

In chapter 3 we consider the Kondo lattice model, which in some situations arrises from the periodic Anderson model as an effective Hamiltonian (just as the Heisenberg model emerges from the Hubbard model). On a single site, the periodic Anderson model describes the hybridization (V) of two orbitals, labeled f and c, when one of those orbitals has a large interaction energy U.

The single-site Hamiltonian can be written

$$\mathcal{H}_{\mathrm{A}} = U \sum_{\sigma\sigma'} \hat{a}^{\dagger}_{f\sigma} \hat{a}^{\dagger}_{f\sigma'} \hat{a}_{f\sigma'} \hat{a}_{f\sigma} + V \sum_{\sigma} \left(a^{\dagger}_{c\sigma} a_{f\sigma} + a^{\dagger}_{f\sigma} a_{c\sigma} \right) + \varepsilon_f \sum_{\sigma} a^{\dagger}_{f\sigma} a_{f\sigma}. \tag{B.15}$$

If we choose $\varepsilon_f = -U/2$ (sometimes called the *symmetric condition*), and $V = 0$, and there is one atom per orbital, we find a low energy Hilbert space consisting of $|\uparrow\uparrow\rangle$, $|\downarrow\downarrow\rangle$, $|\uparrow\downarrow\rangle$, and $|\downarrow\uparrow\rangle$, where here the first entry indicates the spin of the atom in the f-orbital and the second entry indicates the spin of the atom in the c-orbital. All of these states are degenerate with an energy $-U/2$, whereas the two states in $\mathscr{H}_e$ (two atoms in either the f-orbital or the c-orbital) have an energy 0. This problem has the exact same structure as the one we just solved! Mapping $J \to V$, and $U \to U/2$, we can read the effective Hamiltonian directly from the result for the Hubbard model:

$$\mathcal{H}_{\mathrm{eff}} \equiv \mathcal{H}_{\mathrm{K}} = \pm \frac{8V^2}{U} \boldsymbol{s}_f \cdot \boldsymbol{s}_c. \tag{B.16}$$

This Hamiltonian describes (one site of) the Kondo lattice model, and in transition metal oxides exhibiting heavy-fermion behavior (see chapter 3), this is *exactly* how it emerges. It was first derived by Schrieffer and Wolff [152] using a canonical transformation.

Appendix C

Implementation of local constraints in mean-field theory

For the initialization of the self-consistent diagonalization procedure used in Section 3.4, and anytime during the procedure immediately after the $\tilde{V}_i$ have been updated, it is necessary to determine the μ_{ie} that satisfy the local constraint on the e atom density ($n_{ei} = 1$). Finding the correct μ_{ie} amounts to finding a root of the vector-valued function:

$$\Delta_j \left(\mu_{ie}\right) = 1 - 2 \sum_k \sum_{q<q_F^k} \left| v_{qk}^j \right|^2, \tag{C.1}$$

since Δ_j is the deviation from 1 of the number of localized atoms at site j. The dependence of Δ on the chemical potentials is implicit in the v_{qk}^j, because they are obtained by diagonalizing the $\mathcal{H}_k$, in which the μ_{ie} appear explicitly. We proceed to solve $\Delta_j \left(\mu_{ie}\right) = 0$ via Newton's method, where the gradient is calculated in first order perturbation theory (this is just linear response theory)[79]:

$$\frac{\partial \Delta_j}{\partial \mu_{ie}} = \frac{2}{L_t} \sum_k \sum_{q<q_F^k} \sum_{q'>q_F^k} \Re \left[\frac{\bar{v}_{qk}^i v_{q'k}^i \bar{v}_{q'k}^j v_{qk}^j}{\epsilon_q - \epsilon_q'} \right], \tag{C.2}$$

$\Re$ being the real part. Newton's method amounts to making successive linear approximations to the nonlinear equation $\Delta_j \left(\mu_{ie}\right) = 0$: we choose a starting point μ_{ie}^0 from the local density approximation, and then solve

$$\Delta_j \left(\mu_{ie}^0\right) - \sum_i \delta\mu_{ie} \left. \left(\frac{\partial \Delta_j}{\partial \mu_{ie}} \right) \right|_{\mu_e^0} = 0 \tag{C.3}$$

for the $\delta\mu_{ie}$ by inverting the matrix $\partial \Delta_j / \partial \mu_{ie}$. We then change $\mu_{ie}^0 \to \mu_{ie}^0 + \delta\mu_{ie}$, and repeat until the constraints are satisfied to within a desired tolerance.

This procedure works wherever the hybridizations $\tilde{V}_i$ are finite, but breaks down, for instance, near the edge of the trap. In general, we initiate the self-consistent diagonalization with a trap strength that is sufficiently weak to allow finite g atom density at the trap edges, and then turn up the trap slowly throughout the iteration. Whenever the hybridization at the edges begins to vanish, the Fermi level is flanked by two nearly degenerate combinations of a single e atom at the leftmost or rightmost lattice site. The gradient defined in Eq. (C.2) becomes badly behaved at this point, because the degenerate states split the Fermi level, and they must be excluded from the sum (one can avoid the resulting divergences by exploiting the reflection symmetry about the center of the trap, but inclusion of these degenerate states nevertheless increases the precision necessary to reliably invert the gradient matrix).

Appendix D

Scattering between P and D bands in a separable optical lattice

Here we explain in more detail the problem of having 2D Kondo-like physics in a separable lattice $\mathcal{I}(\boldsymbol{r}) = \mathcal{I}_x(x) + \mathcal{I}_y(y)$; these considerations also apply to the $D > 1$ multi-flavor models discussed in Ref. [86]. Though we are interested in spin-$\frac{1}{2}$ bosons, for simplicity we will ignore the spin degree of freedom (or alternatively restrict ourselves to the fully polarized states in our spin-$\frac{1}{2}$ model). Projecting the spinless version of the Hamiltonian in Eq. (4.1) onto the Hilbert space of a single site, we obtain

$$\tilde{\mathcal{H}} = \sum_\alpha E_\alpha \hat{n}_\alpha + \sum_\alpha \frac{U_\alpha}{2} \hat{n}_\alpha(\hat{n}_\alpha - 1) + 2 \sum_{\alpha > \beta} V_{\alpha\beta} \hat{n}_\alpha \hat{n}_\beta + \sum_{\{\alpha,\beta\} \neq \{\gamma,\delta\}} W_{\alpha\beta\gamma\delta} \alpha^\dagger \beta^\dagger \gamma \delta, \qquad (\text{D.1})$$

where the site index has been dropped and the mean band energies E_α have been accounted for.

Because the noninteracting part of the Hamiltonian is separable in x-y coordinates, a generic Wannier function can be labeled by independent band indices for the x and y directions, and so we introduce a vector band index $\boldsymbol{\alpha} = \{\alpha_x, \alpha_y\}$. In this notation, a Wannier function is given by

$$w_{\boldsymbol{\alpha}}(\boldsymbol{r}) = w_{\alpha_x}^x(x) w_{\alpha_y}^y(y), \qquad (\text{D.2})$$

and has single-particle energy $E_{\boldsymbol{\alpha}} = \epsilon_{\alpha_x}^x + \epsilon_{\alpha_y}^y$, where

$$\epsilon_{\alpha_x}^x = \int dx\, w_{\alpha_x}^x(x) \left[\mathcal{I}_x(x) - \frac{\hbar^2 \partial_x^2}{2m} \right] w_{\alpha_x}^x(x) \qquad (\text{D.3})$$

(and likewise for $\epsilon_{a_y}^y$). We assume all of these Wannier functions to be real. The lowest energy single particle state $|00\rangle$, with $\boldsymbol{\alpha} = \{0, 0\}$, is both the most stable (against vibrational decay) and the least mobile, and hence is the obvious candidate for the localized spins in the Kondo-Hubbard

model. The lowest energy state that has an enhanced hopping in *both* spatial directions is $|11\rangle$, with $\boldsymbol{\alpha} = \{1, 1\}$, and we choose it for the conduction atoms.

The two-particle state with one boson in $|00\rangle$ and one boson in $|11\rangle$ is, at the single particle level, degenerate with the two-particle state in which one boson is in $|10\rangle$ ($\boldsymbol{\alpha} = \{1, 0\}$) and one boson is in $|01\rangle$ ($\boldsymbol{\alpha} = \{0, 1\}$), both states having energy $E_0 = \epsilon_0^x + \epsilon_1^x + \epsilon_0^y + \epsilon_1^y$. Therefore, the minimal Hilbert space for an interacting model that contains both $|00\rangle$ and $|11\rangle$ must also contain $|10\rangle$ and $|01\rangle$. Defining the two particle states $|1\rangle = |00\rangle \otimes |11\rangle$ and $|2\rangle = |10\rangle \otimes |01\rangle$, it is straightforward to check that $\langle 1|\tilde{\mathcal{H}}|1\rangle = \langle 2|\tilde{\mathcal{H}}|2\rangle = 2V$, where

$$V = \frac{4\pi\hbar^2 a_s \chi}{m} \int d^2\boldsymbol{r} w_0^x(x)^2 w_0^y(y)^2 w_1^x(x)^2 w_1^y(y)^2 \tag{D.4}$$

is the same Kondo exchange defined in the manuscript. In other words, in addition to having the same single particle energy, the states $|1\rangle$ and $|2\rangle$ have the same interaction energy, and remain degenerate at the *many-body* level. Furthermore, $|1\rangle$ and $|2\rangle$ are connected by the W terms in $\tilde{\mathcal{H}}$, with matrix element $\langle 1|\mathcal{H}|2\rangle = 2V$. Because $|1\rangle$ and $|2\rangle$ are degenerate at the many-body level, and are connected by an interaction with the same strength as the Kondo exchange, a site initially in state $|1\rangle$ will scatter into the state $|2\rangle$ in a characteristic time $\tau = \pi/V$.

For implementation of the multi-flavor models of Ref. [86] in D > 1, some non-separability of the lattice would need to be present in order to prevent the above mentioned collision channels from populating states outside of the Hilbert space considered (which includes the state $|2\rangle$ but excludes the state $|1\rangle$).

Appendix E

Derivation of the weak coupling Hamiltonian for the boson Kondo Hubbard model

Here we derive the second order weak-coupling effective Hamiltonian via perturbation theory in the Kondo term $\mathcal{H}_V = 2V\sum_j \boldsymbol{S}_{ja} \cdot \boldsymbol{S}_{jb}$

$$\mathcal{H}_{\mathrm{wc}}^{(2)} = \sum_{n,\Sigma} \frac{\mathcal{H}_V |n,\Sigma\rangle\langle n,\Sigma| \mathcal{H}_V}{\varepsilon_0 - \varepsilon_n}. \tag{E.1}$$

The state $|n,\Sigma\rangle$ above has one conduction boson in the single particle state $\psi_n(j)$, the rest of the conduction bosons in $\psi_0(j)$, and a spin configuration labeled by the index Σ; only states of this form contribute at this order. Because the energy denominators have no dependence on Σ, the sum over Σ is a completeness identity in spin space and can be dropped. Using the basis transformation $a_{j\sigma}^\dagger = \sum_m a_{m\sigma}^\dagger \psi_m(j)$ we can rewrite the Kondo coupling as

$$\mathcal{H}_V = 2V \sum_{jmn} \boldsymbol{S}_j^b \cdot \boldsymbol{S}_{mn}^a \psi_m(j)\psi_n(j), \tag{E.2}$$

where $\boldsymbol{S}_{mn}^a = \sum_{\sigma\sigma'} a_{m\sigma}^\dagger \boldsymbol{\tau}_{\sigma\sigma'} a_{n\sigma'}$. For expectation values within the degenerate ground state manifold we have the equivalence

$$\mathcal{H}_{\mathrm{wc}}^{(2)} = 4V^2 \sum_{mjl} \frac{\left(\boldsymbol{S}_j^b \cdot \boldsymbol{S}_{0m}^a\right)\left(\boldsymbol{S}_l^b \cdot \boldsymbol{S}_{m0}^a\right) \mathcal{G}_{jl}^0 \mathcal{G}_{jl}^m}{\varepsilon_0 - \varepsilon_m}. \tag{E.3}$$

Taking advantage of common identities for Pauli matrices, within the ground state manifold we can rewrite

$$\left(\boldsymbol{S}_j^b \cdot \boldsymbol{S}_{0m}^a\right)\left(\boldsymbol{S}_l^b \cdot \boldsymbol{S}_{m0}^a\right) = \frac{\mathcal{N}_a}{4}\boldsymbol{S}_j^b \cdot \boldsymbol{S}_l^b - \frac{\delta_{jl}}{2}\boldsymbol{S}_{00}^a \cdot \boldsymbol{S}_j^b, \tag{E.4}$$

which leads to

$$
\begin{aligned}
\mathcal{H}_{\text{wc}}^{(2)} &= -n\mathcal{N}V^2 \sum_{j,l} \mathcal{R}_{jl} \boldsymbol{S}_{jb} \cdot \boldsymbol{S}_{lb} \\
&+ 2V^2 \boldsymbol{S}_a \cdot \sum_{j} \mathcal{R}_{jj} \boldsymbol{S}_{jb}.
\end{aligned}
\tag{E.5}
$$

Appendix F

Uniqueness of the steady state

Here we show that for a 1D harmonic oscillator, in a particular sector of Hilbert space $\mathscr{S}^n$ and for a particular value of S^z, the unique steady-state reduced spin density matrix is given by

$$\rho_s^n = |n/2, S^z\rangle\langle n/2, S^z|. \tag{F.1}$$

The extension of what follows to the 1D Hubbard chain is fairly straightforward, and will be described in more detail in future work. As discussed in the text, it is sufficient to prove that all dark eigenstates of the non-interacting Hamiltonian

$$\mathcal{H}_{HO} = \int dx \, \psi_\sigma^\dagger(x) \left(\frac{\partial_x^2}{2m} + \frac{1}{2}m\omega^2 x^2 \right) \psi_\sigma(x) \tag{F.2}$$

have a maximally symmetric spin wavefunction. To understand the properties of its dark eigenstates under particle exchange, we will actually work in first quantization writing an eigenstate for $\mathcal{N}$ particles as

$$\Psi = \sum_{\vec{\sigma}} \mathcal{A}_{\vec{\sigma}} \, \Phi_{\vec{\sigma}}(r_1, \ldots, r_{\mathcal{N}})|\vec{\sigma}\rangle. \tag{F.3}$$

Here the jth component of the vector $\vec{\sigma}$, $\sigma_j \in \{\uparrow, \downarrow\}$, labels the spin orientation of the jth particle (along some arbitrary quantization axis, which we'll call z), and the total spin wavefunction in any term of the sum is

$$|\vec{\sigma}\rangle = |\sigma_1\rangle \otimes |\sigma_2\rangle \otimes \cdots \otimes |\sigma_{\mathcal{N}}\rangle. \tag{F.4}$$

The sum over $\vec{\sigma}$ should be understood as independent summations over each index

$$\sum_{\vec{\sigma}} = \sum_{\sigma_1} \sum_{\sigma_2} \cdots \sum_{\sigma_{\mathcal{N}}}, \tag{F.5}$$

the coefficients $\mathcal{A}_{\vec{\sigma}}$ are arbitrary, and $\Phi_{\vec{\sigma}}$ is a normalized orbital wavefunction for the $\mathcal{N}$ particles.

Dark states of s-wave losses have zero expectation value in the interaction operator

$$\mathcal{U} = \sum_{m<n} \mathcal{U}_{mn} = g \sum_{m<n} \delta(r_m - r_n), \tag{F.6}$$

and this expectation value can be evaluated as

$$\begin{aligned} U &= \int \mathscr{D}r \, \Psi^* \mathcal{U} \, \Psi \\ &= \sum_{\vec{\sigma}} |\mathcal{A}_{\vec{\sigma}}|^2 \int \mathscr{D}r \, \Phi_{\vec{\sigma}}^* \mathcal{U} \, \Phi_{\vec{\sigma}}, \end{aligned} \tag{F.7}$$

with $\mathscr{D}r \equiv \prod_j dr_j$. The last equality holds because the interaction is spin-independent. It is crucial to realize that the operator $\mathcal{U}$ is positive-semidefinite, which means that satisfying $U = 0$ actually implies the stricter constraint

$$\int \mathscr{D}r \, \Phi_{\vec{\sigma}}^* \mathcal{U} \, \Phi_{\vec{\sigma}} = 0 \quad \forall \vec{\sigma}. \tag{F.8}$$

In addition to the operator $\mathcal{U}$ being positive-semidefinite, the constituent pairwise interaction operators are as well. Hence, the condition $\int \mathscr{D}r \, \Phi_{\vec{\sigma}}^* \mathcal{U} \, \Phi_{\vec{\sigma}} = 0$ actually implies that

$$\int \mathscr{D}r \, \Phi_{\vec{\sigma}}^* \mathcal{U}_{mn} \, \Phi_{\vec{\sigma}} = 0 \quad \forall \, m \neq n. \tag{F.9}$$

The above set of equalities can now be used to pin down properties regarding the exchange symmetry of the wave functions $\Phi_{\vec{\sigma}}$.

F.1 Implications for the exchange symmetry of the orbital wave functions

Let's choose two particles, say particle 1 and particle 2, and define relative and center-of-mass coordinates for them as $r = r_1 - r_2$ and $R = (r_1 + r_2)/2$. We can then expand the wavefunction $\Phi_{\vec{\sigma}}$ in a way that makes the symmetrization with respect to exchange of particles 1 and 2 explicit:

$$\Phi_{\vec{\sigma}} = \sum_{\beta s} \mathcal{B}_{\vec{\sigma}\beta s} \times \varphi_{\alpha(\beta,s)}(r)\varphi_\beta(R)\psi_s(r_3, \ldots, r_N). \tag{F.10}$$

In the above φ_α are harmonic oscillator wavefunctions, the ψ_s are a complete and orthonormal set of eigenfunctions for the remaining $\mathcal{N} - 2$ particles, and the notation $\alpha(\beta, s)$ implies that the

relative wavefunction of particles 1 and 2 is uniquely determined by β and s. This point is crucial, and relies on the observation that for Ψ to be an eigenstate, when expanded in terms of eigenstates Φ_σ all of the eigenstates must have the same eigenvalue. Hence the energies of states α, β, and s are constrained to add to some fixed value. From now on we'll drop this explicit dependence. The interaction energy between particles 1 and 2 is given by

$$
\begin{aligned}
U_{12} &= \int \mathscr{D}r \; \Phi_{\vec{\sigma}}^* \mathcal{U}_{12} \, \Phi_{\vec{\sigma}} \\
&= g \sum_{\beta s} \mathcal{B}_{\vec{\sigma}\beta s} \varphi_\alpha(0) \times \mathcal{B}_{\vec{\sigma}\beta s}^* \varphi_\alpha^*(0) \\
&= \sum_{\beta s} \left| \mathcal{B}_{\vec{\sigma}\beta s} \varphi_\alpha(0) \right|^2,
\end{aligned}
\tag{F.11}
$$

and hence $U_{12} = 0$ implies that

$$
\mathcal{B}_{\vec{\sigma}\beta s} \varphi_\alpha(0) = 0 \quad \forall \, \beta, s
\tag{F.12}
$$

So $\mathcal{B}_{\vec{\sigma}\beta s}$ must be zero for all even wave functions (all of which are finite at the origin), implying that $\Phi_{\vec{\sigma}}$ is strictly odd under interchange of particles 1 and 2. By repeating the above argument for two arbitrary particles m and n, it is easy to see that $\Phi_{\vec{\sigma}}$ is strictly odd under interchange of *any* two particles.

F.2   Implications for the spin wavefunction

We can now ask what the antisymmetry of $\Phi_{\vec{\sigma}}$ implies for the full wave function

$$
\Psi = \sum_{\vec{\sigma}} \mathcal{A}_{\vec{\sigma}} \, \Phi_{\vec{\sigma}}(r_1, \ldots, r_N) |\vec{\sigma}\rangle.
\tag{F.13}
$$

Under interchange of two arbitrary particles we have $|\vec{\sigma}\rangle \rightarrow |\vec{\sigma}'\rangle$, and we obtain the new wave function

$$
\begin{aligned}
\Psi' &= -\sum_{\vec{\sigma}} \mathcal{A}_{\vec{\sigma}} \, \Phi_{\vec{\sigma}}(r_1, \ldots, r_N) |\vec{\sigma}'\rangle \\
&= -\sum_{\vec{\sigma}} \mathcal{A}_{\vec{\sigma}'} \, \Phi_{\vec{\sigma}'}(r_1, \ldots, r_N) |\vec{\sigma}\rangle \\
&= -\Psi \\
&= -\sum_{\vec{\sigma}} \mathcal{A}_{\vec{\sigma}} \, \Phi_{\vec{\sigma}}(r_1, \ldots, r_N) |\vec{\sigma}\rangle,
\end{aligned}
\tag{F.14}
$$

implying that

$$\mathcal{A}_{\vec{\sigma}}\,\Phi_{\vec{\sigma}}(r_1,\ldots,r_N) = \mathcal{A}_{\vec{\sigma}'}\,\Phi_{\vec{\sigma}'}(r_1,\ldots,r_N). \tag{F.15}$$

The second equality follows because switching $\sigma \leftrightarrow \sigma'$ in the summand just changes the order of the terms in the sum, and the third equality follows from the antisymmetry of the total wavefunction under particle exchange. By repeated permutations of various particles, this chain of logic can be used to demonstrate that all of the $\mathcal{A}_{\vec{\sigma}}\,\Phi_{\vec{\sigma}}(r_1,\ldots,r_N)$ are equal, and hence we have

$$\Psi = \mathcal{A}\Phi(r_1,\ldots,r_N)\sum_{\vec{\sigma}}|\vec{\sigma}\rangle. \tag{F.16}$$

Now $\mathcal{A}$ is just some normalization, which is related to the total z projection of the spin, and it is clear that Ψ breaks up into the product of a completely antisymmetric orbital wavefunction multiplied by a completely symmetric spin wavefunction.

Appendix G

Phase sensitivity of the steady-state

In order to estimate the phase measurement sensitivity of an array of 1D tubes in the steady state, we begin by considering just the jth tube, with initial particle number $\mathcal{N}$, final particle number $\mathcal{D}_j$ after relaxing to steady state via collisional loss, and initial (and final) spin projection S_j^z. The initial $\mathcal{N}$ atoms can most easily be prepared in an incoherent mixture of spin up and spin down by simply allowing a coherent state initially prepared along the x-direction to undergo single particle dephasing (which could be briefly enhanced via a myriad of methods). For the coherent state, the probability of a given S_j^z is given by a binomial distribution, which for large $\mathcal{N}$ is approximated by the continuous probability distribution

$$\mathcal{P}(S_j^z) = \sqrt{\frac{2}{\mathcal{N}\pi}} e^{-2(S_j^z/\sqrt{\mathcal{N}})^2}. \tag{G.1}$$

Note that without dephasing into a mixture, a coherent state of fermions does not undergo s-wave collisions. In the sense that such a distribution is easily prepared experimentally, we take this to be a worst-case scenario; a distribution of S_j^z more sharply peaked around $S_j^z = 0$ will enhance the phase sensitivity. The probability distribution of steady-state particle numbers in the jth tube, conditioned on a particular value of S_j^z, is given by

$$\mathcal{P}(\mathcal{D}_j|S_j^z) = \Theta(\mathcal{D}_j - |2S_j^z|) \frac{2\mathcal{D}_j}{\mathcal{N}} e^{-(\mathcal{D}_j/\sqrt{2\mathcal{N}})^2} e^{2(S_j^z/\sqrt{\mathcal{N}})^2}. \tag{G.2}$$

For $S_j^z = 0$, this distribution is peaked around $\mathcal{D}_0 \approx \sqrt{\mathcal{N}}$ (giving the expected value of $n(\infty)$ quoted in the text). For $|S_j^z| > 0$, the step function Θ reflects the fact that as particles are lost (remember that S_j^z is conserved by the losses), the remaining particles are maximally spin polarized once

$\mathcal{D}_j = 2|S_j^z|$. The second exponential provides the proper normalization, $\frac{1}{2} \int_0^\infty d\mathcal{D}_j \, \mathcal{P}(\mathcal{D}_j|S_j^z) = 1$, where the factor of $\frac{1}{2}$ comes from converting sums into integrals while respecting our assumption of even particle number.

For this single tube, small rotations about the x-axis by an angle $\delta\varphi$ cause a standard deviation in the final distribution of S_j^z given by [15]

$$\sigma(\delta\varphi, \mathcal{D}_j, S_j^z) \approx \delta\varphi \sqrt{\frac{(\mathcal{D}_j - 2S_j^z)(\mathcal{D}_j + 2S_j^z)}{8}}. \tag{G.3}$$

for large $\mathcal{D}_j$. For $S_j^z = 0$ (before the rotation), this demonstrates that a discrepancy in S_j^z (after the rotation) of order unity is expected for $\delta\varphi \sim 1/\mathcal{D}_j$, hence the Heisenberg scaling of phase-sensitivity (about $\varphi = 0$) within a single tube. The phase uncertainty for arbitrary φ can be determined by the more general criterion [115, 82]

$$\delta\varphi = \frac{\sqrt{\langle (S_j^z)^4 \rangle - \langle (S_j^z)^2 \rangle^2}}{\partial \langle (S_j^z)^2 \rangle / \partial\varphi}, \tag{G.4}$$

and reproduces the previous result in the limit of small rotations.

Our estimation of the phase sensitivity for an array of tubes relies only on the assumption that the *initial* (i.e. before the losses) value of $S^z = \sum_j S_j^z$ is known to within an uncertainty Σ, but does not require any knowledge of S_j^z in the individual tubes, greatly relaxing the experimental requirements. This uncertainty Σ guarantees that, in principle, rotations causing deviations in S^z of order Σ can be detected. For $\mathcal{T}$ tubes with well defined (i.e. measured) total spin projection S^z, the expected standard deviation in S^z (denoted σ_{tot}) due to a rotation by angle φ about the x-axis satisfies

$$\sigma_{\text{tot}}^2 = \overbrace{\int_{-\infty}^\infty \cdots \int_{-\infty}^\infty}^{\mathcal{T} \text{ times}} \prod_j dS_j^z \overbrace{\int_0^\infty \cdots \int_0^\infty}^{\mathcal{T} \text{ times}} \prod_j d\mathcal{D}_j \prod_j \left[\frac{1}{2} \mathcal{P}(\mathcal{D}_j|S_j^z) \mathcal{P}(S_j^z) \right] \times \tag{G.5}$$

$$\sum_j \sigma(\delta\varphi, \mathcal{D}_j, S_j^z)^2 \, \delta(S^z - \sum_j S_j^z). \tag{G.6}$$

Here δ is the Dirac δ-function, reflecting the correlations established between the various S_j^z by the knowledge of S^z, and the factors of $\frac{1}{2}$ again come from converting sums into integrals while

respecting the assumption of even particle number. If we ignore this δ-function constraint, which is valid in the large $\mathcal{T}$ limit, the integral simplifies greatly to

$$\sigma_{\text{tot}}^2 \approx \frac{\mathcal{T}}{2} \int_{-\infty}^{\infty} dS_j^z \int_0^{\infty} d\mathcal{D}_j \mathcal{P}(\mathcal{D}_j|S_j^z)\mathcal{P}(S_j^z)\, \sigma(\delta\varphi, \mathcal{D}_j, S_j^z)^2. \tag{G.7}$$

Equation (G.7) can be evaluated explicitly to reveal

$$4\sigma_{\text{tot}}^2 \approx \mathcal{T}\mathcal{N}\delta\varphi^2 \approx \mathcal{T}\mathcal{D}_0^2\delta\varphi^2. \tag{G.8}$$

Setting the total standard deviation to Σ gives a minimum phase sensitivity of

$$\delta\varphi_{\text{min}} \approx \frac{2\Sigma}{\mathcal{D}_0\sqrt{\mathcal{T}}}. \tag{G.9}$$

As has been demonstrated recently in Ref. [177], $\Sigma \sim 1$ is possible for ~ 100 atoms in an optical cavity, as long as measurements that do not preserve coherence between the atoms are acceptable. Such measurements certainly are acceptable before the losses take place, since we require no inter-particle correlations in the initial state (they develop dynamically due to the losses). Therefore, as quoted in Sec. 6.3, we expect a minimum phase sensitivity that scales as $\delta\varphi_{\text{min}} \sim \frac{1}{\mathcal{D}_0\sqrt{\mathcal{T}}}$ to be achievable in experiment.

Appendix H

Derivation of distribution functions $\mathcal{P}(\mathcal{R}, \mathcal{F}, \tau)$

In Section 7.4, we gave the probability distributions $\mathcal{P}(\mathcal{R}, \mathcal{F}, \tau)$ of trajectories with (1) $\mathcal{R}$ Raman jumps and (2) $\mathcal{F}$ Rayleigh jumps, and (3) satisfying $\tau^{\mathrm{up}} - \tau^{\mathrm{down}} = \tau$. We showed that $\mathcal{P}(\mathcal{R}, \mathcal{F}, \tau)$ can be decomposed as

$$\mathcal{P}(\mathcal{R}, \mathcal{F}, \tau) = \mathcal{P}_{\mathrm{r}}(\mathcal{R}, \tau) \times \mathcal{P}_{\mathrm{el}}(\mathcal{F}) \tag{H.1}$$

$$= \mathcal{P}_{\mathrm{r}}(\mathcal{R}, \tau) \times \frac{e^{-\Gamma_{\mathrm{el}} t/4} (\Gamma_{\mathrm{el}} t)^{\mathcal{F}}}{\mathcal{F}!}. \tag{H.2}$$

Here we derive the distribution $\mathcal{P}_{\mathrm{r}}(\mathcal{R}, \tau)$ in detail.

We will divide trajectories up into two categories, those with $\mathcal{R}$ odd and those with $\mathcal{R}$ even, and we'll treat the odd case first. We assume that the spin initially points in the x direction, in which case the probability of pointing up or down at $t = 0$ is equal. Let's imagine the spin points up at $t = 0$ (with probability $\frac{1}{2}$), then the probability of a sequence of $\mathcal{R}$ (time labeled) jumps such as

$$\hat{\sigma}^-(t_1)\hat{\sigma}^+(t2) \times \cdots \times \hat{\sigma}^+(t_{\mathcal{R}-1})\hat{\sigma}^-(t_{\mathcal{R}}) \tag{H.3}$$

is given by

$$P(t_1, t_2, \ldots, t_{\mathcal{R}}) = \frac{1}{2} e^{-\Gamma_{\mathrm{ud}} t_1} (dt_1 \Gamma_{\mathrm{ud}}) e^{-\Gamma_{\mathrm{du}}(t_2 - t_1)} (dt_2 \Gamma_{\mathrm{du}}) \times \cdots \times e^{-\Gamma_{\mathrm{ud}}(t_{\mathcal{R}} - t_{\mathcal{R}-1})} (\Gamma_{\mathrm{ud}} dt_{\mathcal{R}}) e^{-\Gamma_{\mathrm{du}}(t - t_{\mathcal{R}})}$$

$$= \frac{1}{2} e^{-\Gamma_{\mathrm{ud}} \tau^{\mathrm{up}}} e^{-\Gamma_{\mathrm{du}} \tau^{\mathrm{down}}} (dt_1 \times \cdots \times dt_{\mathcal{R}}) \Gamma_{\mathrm{ud}}^{(\mathcal{R}+1)/2} \Gamma_{\mathrm{du}}^{(\mathcal{R}-1)/2}. \tag{H.4}$$

$$\tag{H.5}$$

We can now obtain $\mathcal{P}_{\mathrm{r}}^{\mathrm{odd}}(\mathcal{R}, \tau)$ by integrating $P(t_1, \ldots, t_{\mathcal{R}})$ over the time variables $t_1, \ldots, t_{\mathcal{R}}$, under the constraints that $\tau^{\mathrm{up}} - \tau^{\mathrm{down}} = \tau$ and $dt_1 < dt_2 < \cdots < dt_{\mathcal{R}-1} < dt_{\mathcal{R}}$. Defining $\mu = (\mathcal{R} - 1)/2$,
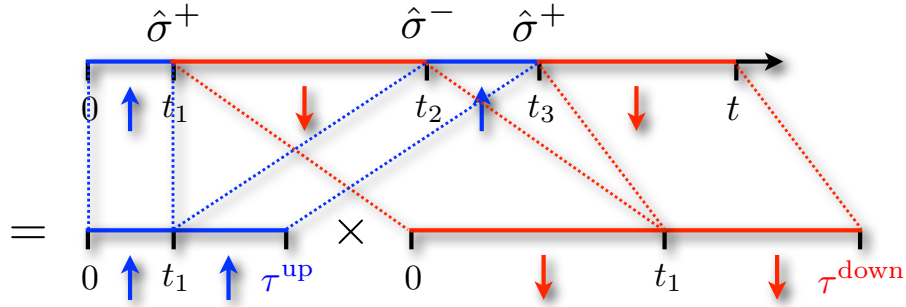
Figure H.1: Diagrammatic representation for the factorization of the integral in Eq. (H.8) for a trajectory with three spin flips. The key point is that the total volume of configuration space spanned by changing the location of times t_1, t_2, and t_3, subject to the constraint on τ. is the same as the product of the unconstrained volumes accessible to the configurations on the bottom.

and also adding in the contribution from trajectories where the spin starts pointed down (which is obtained by switching $\Gamma_{\mathrm{ud}} \leftrightarrow \Gamma_{\mathrm{du}}$ in the expressions above) we obtain

$$\mathcal{P}_{\mathrm{r}}^{\mathrm{odd}}(\mathcal{R}, \tau) = \frac{1}{2}\Gamma_{\mathrm{r}} e^{-\Gamma_{\mathrm{ud}}\tau^{\mathrm{up}}} e^{-\Gamma_{\mathrm{du}}\tau^{\mathrm{down}}} (\Gamma_{\mathrm{ud}}\Gamma_{\mathrm{du}})^{\mu} \int_0^t dt_1 \int_{dt_1}^t dt_2 \ldots \int_{dt_{\mathcal{R}-1}}^t dt_{\mathcal{R}} \delta(\tau^{\mathrm{up}} - \tau^{\mathrm{down}} - \tau). \tag{H.6}$$

The key step is to realize that the constraint renders this chain of integrals a product between two ordered volume integrals:

$$\int_0^t dt1 \int_{dt_1}^t dt_2 \ldots \int_{dt_{\mathcal{R}-1}}^t dt_{\mathcal{R}} P(t_1, t_2, \ldots, t_{\mathcal{R}}) \delta(\tau^{\mathrm{up}} - \tau^{\mathrm{down}} - \tau) \tag{H.7}$$

$$= \left(\int_0^{\tau^{\mathrm{up}}} dt_1 \ldots \int_{t_{\mu-1}}^{\tau^{\mathrm{up}}} dt_{\mu} \right) \times \left(\int_0^{\tau^{\mathrm{down}}} dt_1 \ldots \int_{t_{\mu-1}}^{\tau^{\mathrm{down}}} dt_{\mu} \right). \tag{H.8}$$

The above equality is shown schematically in Fig. H.1. Ordered volume integrals can easily be taken on symmetry grounds as

$$\int_0^{\tau^{\mathrm{up}}} dt_1 \ldots \int_{t_{\mu-1}}^{\tau^{\mathrm{up}}} dt_{\mu} = \frac{(\tau^{\mathrm{up}})^{\mu}}{\mu!}, \tag{H.9}$$

and hence we have

$$\mathcal{P}_{\mathrm{r}}^{\mathrm{odd}}(\mu, \tau) = \frac{1}{2}\Gamma_{\mathrm{r}} e^{-\Gamma_{\mathrm{ud}}\tau^{\mathrm{up}}} e^{-\Gamma_{\mathrm{du}}\tau^{\mathrm{down}}} (\Gamma_{\mathrm{ud}}\Gamma_{\mathrm{du}})^{\mu} \frac{(\tau^{\mathrm{up}})^{\mu}}{\mu!} \frac{(\tau^{\mathrm{down}})^{\mu}}{\mu!} \tag{H.10}$$

$$= \frac{\Gamma_{\mathrm{r}}}{2} e^{-\Gamma_{\mathrm{r}}t/2} e^{-2\gamma\tau} (\Gamma_{\mathrm{ud}}\Gamma_{\mathrm{du}}/4)^{\mu} \frac{(t^2 - \tau^2)^{\mu}}{(\mu!)^2}. \tag{H.11}$$

When $\mathcal{R}$ is even, we instead define $\mu = (\mathcal{R}+1)/2$, and from extremely similar considerations obtain

$$\mathcal{P}_{\mathrm{r}}^{\mathrm{even}}(\mu, \tau) = \frac{\Gamma_{\mathrm{ud}}\Gamma_{\mathrm{du}}t}{2} e^{-\Gamma_{\mathrm{r}}t/2} e^{-2\gamma\tau} (\Gamma_{\mathrm{ud}}\Gamma_{\mathrm{du}}/4)^{\mu} \frac{(t^2 - \tau^2)^{\mu}}{\mu!(\mu + 1)!}. \tag{H.12}$$